

Contents

1	The History of Radar Technology	1
2	Electromagnetic field theory & wave propagation basics	7
2.1	Fields and Waves in Free Space	8
2.2	Reflection on Perfect Conducting Bodies	9
2.3	Reflection on Dielectric Interfaces	10
3	The Radar Equation	13
3.1	Radar Equation for Point Targets	13
3.2	Radar Equation for Extended Targets	15
3.3	The Radar Horizon	16
3.4	Bistatic Radar Equation	17
4	Information Content in Radar Signals.....	19
4.1	Range	19
4.2	Velocity	21
4.3	Direction (Azimuth, Elevation)	21
4.4	Polarization Characteristics of the Target	21
5	Resolution and Accuracy	23
5.1	Measurement Accuracy and Sine Wave Oscillations.....	23
5.2	Accuracy and Range Measurement	24
5.3	Range Resolution of Two Neighbouring Targets.....	25
5.4	Angular Resolution.....	26
6	Radar Receiver Noise and Target Detection	28
6.1	Thermal Noise	28
6.2	Cosmic and Background Noise	29
6.3	Atmospheric Absorption Noise	32
6.4	System Noise Temperature	33
6.5	False Alarm Rate and Probability of Detection.....	35
6.6	Radar Detectors	38
7	CW- and FM-CW Radar	41
7.1	CW Doppler Radar	41
7.1.1	The Doppler Frequency	41
7.1.2	Quadrature Modulation	42
7.1.3	Range Measurement with CW Radar.....	43
7.2	FM CW-Radar	44
7.2.1	Range Measurement with FM CW Radar	44
7.2.2	Range Resolution with FM CW Radar	46
8	Pulse Radar	49

8.1	The History of Pulse Radar	49
8.2	Transmission Types of Pulse Radar	49
8.3	Simple Pulse Radar	51
8.4	Coherent Pulse Radar	52
8.5	MTI Radar (Moving Target Indication)	54
8.5.1	MTI with Delay-Line Canceller	54
8.6	Filterbank Procedure	56
8.7	Impulse Integration for Increasing the Sensitivity	58
8.7.1	Incoherent Integration	58
8.7.2	Examples for Incoherent Integration.....	60
8.8	Pulse Compression for Improving the Resolution	62
8.8.1	Compression of a frequency modulated pulse (chirp)	62
8.8.2	Digital Pulse Compression	66
8.8.3	Digital Pulse Compression with Barker Code	67
9	Beamforming	71
10	Synthetic Aperture Radar	75
10.1	Resolution Limits of Conventional Radar Devices	75
10.2	Procedures for Improving the Resolution	75
10.2.1	Range Resolution with Pulse Compression	75
10.2.2	Improvement of the Azimuth Resolution.....	76
10.3	Basic Principle of SAR	77
10.4	Theoretical Basics of SAR.....	79
10.5	Maximum Resolution Capability	82
10.6	Analysis Procedures.....	82
10.7	PRF Determination	85
11	Characteristics of Radar Targets	87
11.1	Definition of the Radar Backscattering Cross-Section	87
11.2	Fundamentals of Radar polarimetry	89
11.2.1	Polarization	89
11.2.2	Polarization Scattering Matrix	90
11.3	Complex Radar Cross-Section and RCS Matrix	91
11.4	RCS Measurement Techniques.....	93
11.4.1	Measurement of the Scalar Radar Cross-Section σ	93
11.4.2	Measurement of The Complex Polarization Scattering Matrix	93
11.4.3	Calibration and Error Correction for Polarimetric RCS Measurements	95
11.5	Radar Cross-Section of Simple Objects	100
11.5.1	Sphere.....	100

11.5.2	Circular Disks	102
11.5.3	Arbitrary Flat Disk	103
11.5.4	Radar Cross-Section of Further Simple Bodies	103
11.6	Calibration Standards for Free Space Measurements	105
11.6.1	Luneburg Lenses	105
11.6.2	Corner Reflectors	106
11.7	RCS of Complex Objects.....	109
11.8	Reduction of the Radar Backscattering Cross-Section	110
11.8.1	Optimization of Shape and Style	110
11.8.2	Covering with Radar absorbing material	111
11.8.3	Layering of the Outer-Surface Materials	111
12	Selected Areas in Radar Signal Processing.....	113
12.1	Constant False Alarm Rate (CFAR)	113
12.1.1	Introduction	113
12.1.2	The CAGO-CFAR	113
12.1.3	The OS-CFAR.....	115
12.1.4	CAOS-CFAR	116
12.1.5	The CASH-CFAR	117
12.1.6	MAMIS-CFAR	118
12.1.7	Quality of the CFAR Threshold and CFAR Loss	118
12.1.8	Conclusions	123
12.2	Design of Low Side Lobe Chirp Pulse Compression	123
12.2.1	Introduction	123
12.2.2	Linear and Nonlinear Chirp Waveforms.....	125
12.2.3	Nonlinear Chirp Based on the Circle- ϕ Function.....	127
12.2.4	Receiver and Signal Processor Considerations	129
12.2.5	Design Example	130
12.2.6	Results	132
13	Selected Radar Applications	135
13.1	Tracking Radar	135
13.2	Monopulse Radar	135
13.3	Automotive Radar (ACC).....	141
13.3.1	History	141
13.3.2	Automobile Radar System Parameters	143
13.3.3	Circuit and Switching Concepts.....	146

13.3.4	Modulation Procedures	148
13.3.5	Processing	149
13.3.6	Reflection Cross-Section in Street Traffic at 76 GHz.....	149
13.3.7	Power Budget	151
13.3.8	ACC Sensor System Specification.....	153
13.3.9	MMIC Integration	153
13.3.10	Problem Areas	156
13.3.11	Literature	157
13.3.12	Exercises for ACC Radar	157
13.4	Phased-Array Radar	158
14	Future Radar Systems	162
14.1	The Transmit Subsystem	162
14.2	The Receiver Subsystem.....	163
14.3	SDRS and SD-SAR System Aspects	164
15	Bibliography	167
15.1	Fundamental Literature	167
15.2	Automotive Radar	167
15.3	Synthetic Aperture Radar	167
15.4	Antennas general	167
15.5	Antennenarrays	168
15.6	RCS	168
15.7	Digital Beamforming	169
15.8	General and Supporting Literature	169

1 The History of Radar Technology

Much has been composed on the history of Radar technology, particularly since it is possible to find sections about it in almost every book on the theme of Radars. With some reservation one can say that Radar technology became 100 years old in 1988. It was Heinrich Hertz, who with his underlying and groundbreaking Experiments in 1887/88 was able to demonstrate for electromagnetic waves, that they are reflected by metals and dielectric objects. The above reservation is appropriate because Heinrich Hertz truly determined an effect of the reflection, but whose application thereof was not further considered. At the beginnings of Radar technology the breakthrough of this field of engineering was not successful and quick. One must even modestly state, that apart from a few exceptions, Radar was ignored for almost over 40 years.

After Heinrich Hertz, it was first the German engineer, Christian Hülsmeyer (1881-1957), who employed himself with the mentioned reflection effect and registered his patent in 1904 (shown in Figure 1.1). The instrumentation was introduced on the International Navigation Association in Rotterdam, but nevertheless interest in the technology failed to appear. They pursued their ideas for another few years without economic or financial success. Discouraged by the lack of interest, Hülsmeyer and his investor, Heinrich Mannheim, gave up a few years later.

The next person, who recognized the importance of the Radar effect, was Marconi. As a young man Marconi had exhaustively pursued the work of Heinrich Hertz and had constructed his communication experiments upon it. In 1922 he gave a fiery speech before the *Institute of Radio Engineers* (IRE) in London. Several lines can be read in Figure 1.2. Nevertheless not even he was in a position to awake enthusiasm and interest for Radar technology.

Beginning in 1922 successful Radar experiments with a wooden ship using 600 MHz were carried out by Tayler and Young of the US Naval Research Laboratory (NRL). Their work was also abandoned after a short while.

Then in the years 1925/26 Breit and Tuve conducted investigations on the earth's Ionosphere. From this time on the importance of Radar for Navigation, especially at sea, became increasingly recognized. At the same time research work became heavily promoted and supported in many countries, like the USA, England, France and last, but not least, Germany.

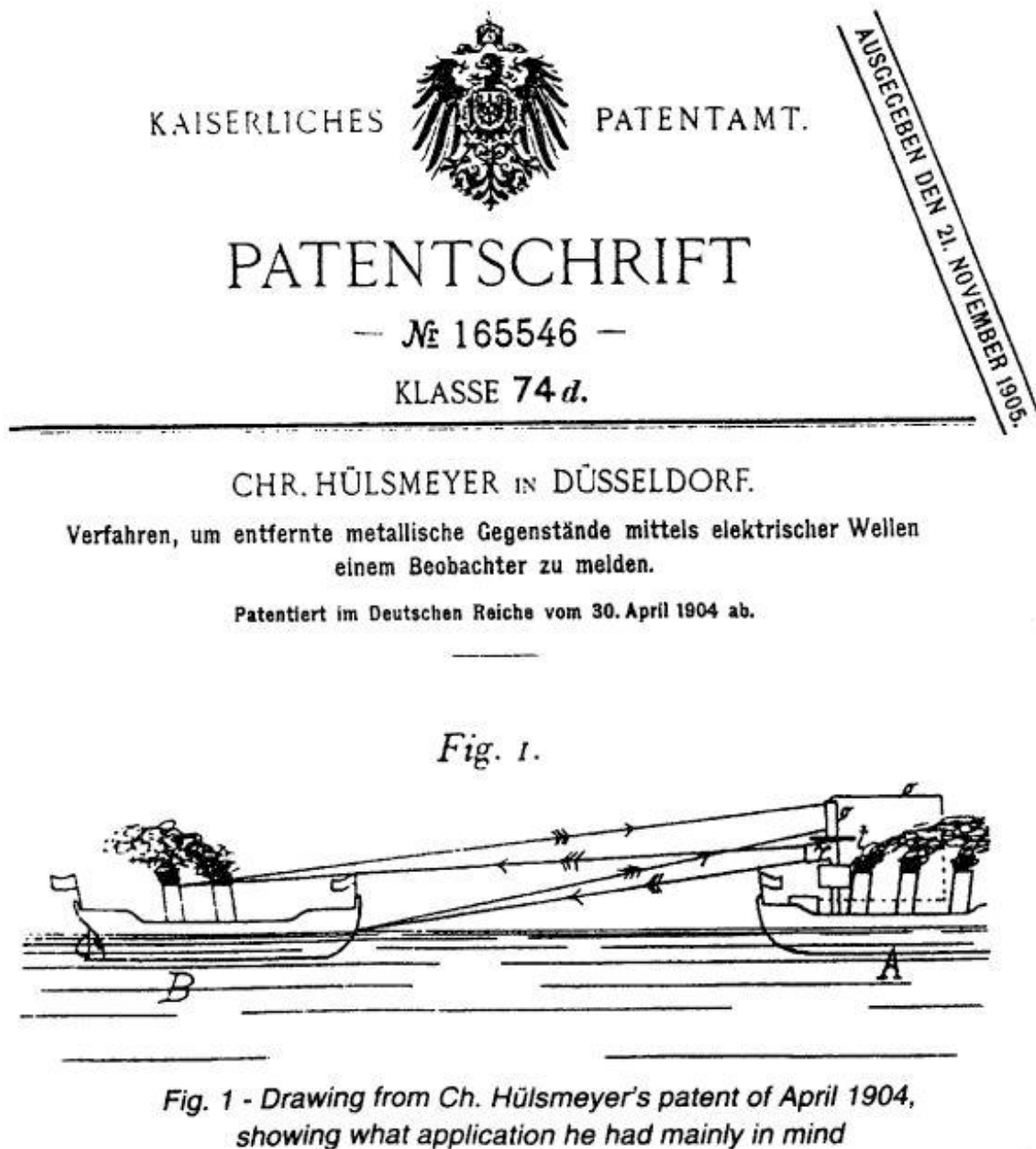


Figure 1.1 Cover page of Hülsmeier's patent specification

As was first shown by Hertz, electric waves can be completely reflected by conducting bodies. In some of my tests I have noticed the effects of reflection and detection of these waves by metallic objects miles away. It seems to me that it should be possible to design apparatus by means of which a ship could radiate or project a divergent beam of these rays in any desired direction, which rays, if coming across a metallic object, such as another steamer or ship, would be reflected back to a receiver screened from the local transmitter on the sending ship, and thereby, immediately reveal the presence and bearing of the other ship in fog or thick weather.

Figure 1.2 Section of the Marconi Speech in 1922 before the IRE

In Germany it was the GEMA (Gesellschaft für Elektrische und Mechanische Apparate), Pinsch, and Telefunken, which became known for their work on Radar systems. The first instruments were very simple and operated with relatively low frequencies. The following lists a few important dates:

1930 US NRL (L.A. Hyland) locates an airplane, 33 MHz, 2 Miles

1933 French Marine locates an Iceberg, 1800 MHz

1933 Pinsch locates a Ship, 0.3 W, 2200 MHz, 2 km

1934 GEMA locates a Ship 500 t, 150 MHz, 12 km

A large advancement in innovation brought the employment of pulsable Magnetrons¹ and the Braun Cathode Ray Tube², as the following data shows:

1935 In England Sir Watson Watt submitted a proposal for the Radar defense of England. Already in 1937 five systems exist with a range of 100 km.

1936 Telefunken (preceeding Freya) locates Junkers W34, 60 km

1937 Telefunken, Freya, 125 MHz, 150 km (Figure 1.3)

1938 Patent for Fundamental of Pulse Radar Technology (US - SC Col. William Blair) USA, NRL XAF Ship Radar 200 MHz, 6 kW, 50 Miles.

Radar technology underwent rapid development during the years of the Second World War. An example for this is the founding of the Radiation Laboratory at MIT (Massachusetts Institute of Technology). Until 1945 there were 3000 engineers and scientists employed there.

Listed below are simply a few more important dates from Germany's Radar development:

1940 "Würzburg C", 200 MHz, 3 m ϕ , 4000 Unit

1941 "Würzburg Riese" 7,5 m ϕ , $\pm 10'$, 1500 Unit (Figure 1.4)

1942 "Mannheim", 12 kW, automatic analysis

1942 "BordRadar Lichtenstein", 150 MHz, 15000 Unit

After the war year the development of Radar systems entered a long pause. Noteworthy however, is that in 1946 the USA succeeded in reception of echoes from the Moon with a modified apparatus from the "Würzburg Riese" series.

¹ Varian brothers, Palo Alto, ca. 1935

² Karl Ferdinand Braun, 1850 – 1918, Braun Cathode Ray Tube 1896, Nobelpize 1909

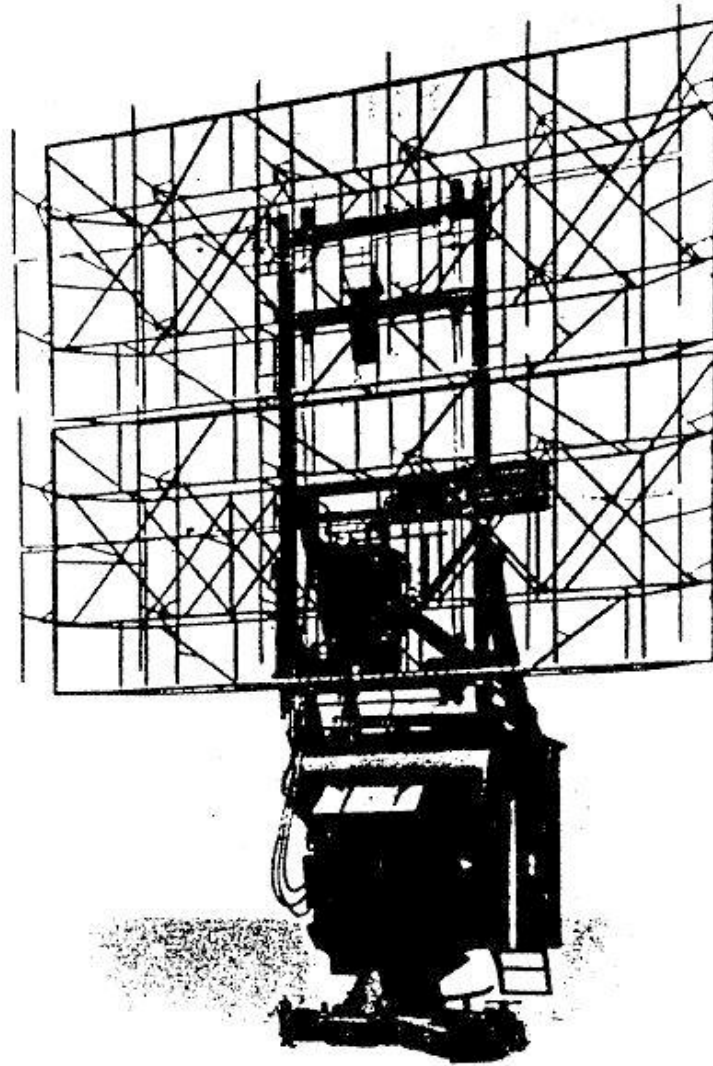


Figure 1.3 Radar apparatus Freya, Telefunken 1937

Beginning at the end of the 50's Radar technology also saw increasing innovation in the component and signal processing sectors. In Radar receivers as well as in the signal analysis circuitry, vacuum tubes were replaced by semiconductors. Despite these improvements the technological development of Radar technology was slower than in the consumer goods industry until the 70's. The reason can be seen from the very long development phases needed for larger systems, particularly in the military field. Often it happened that more than 10 years would pass from the definitions phase until the deployment-ready apparatus would be realized. Only after the 70's did Radar technology experience comparably rapid phase of development through the opening of new fields of usage, as in the fields of sensors and remote sensing.

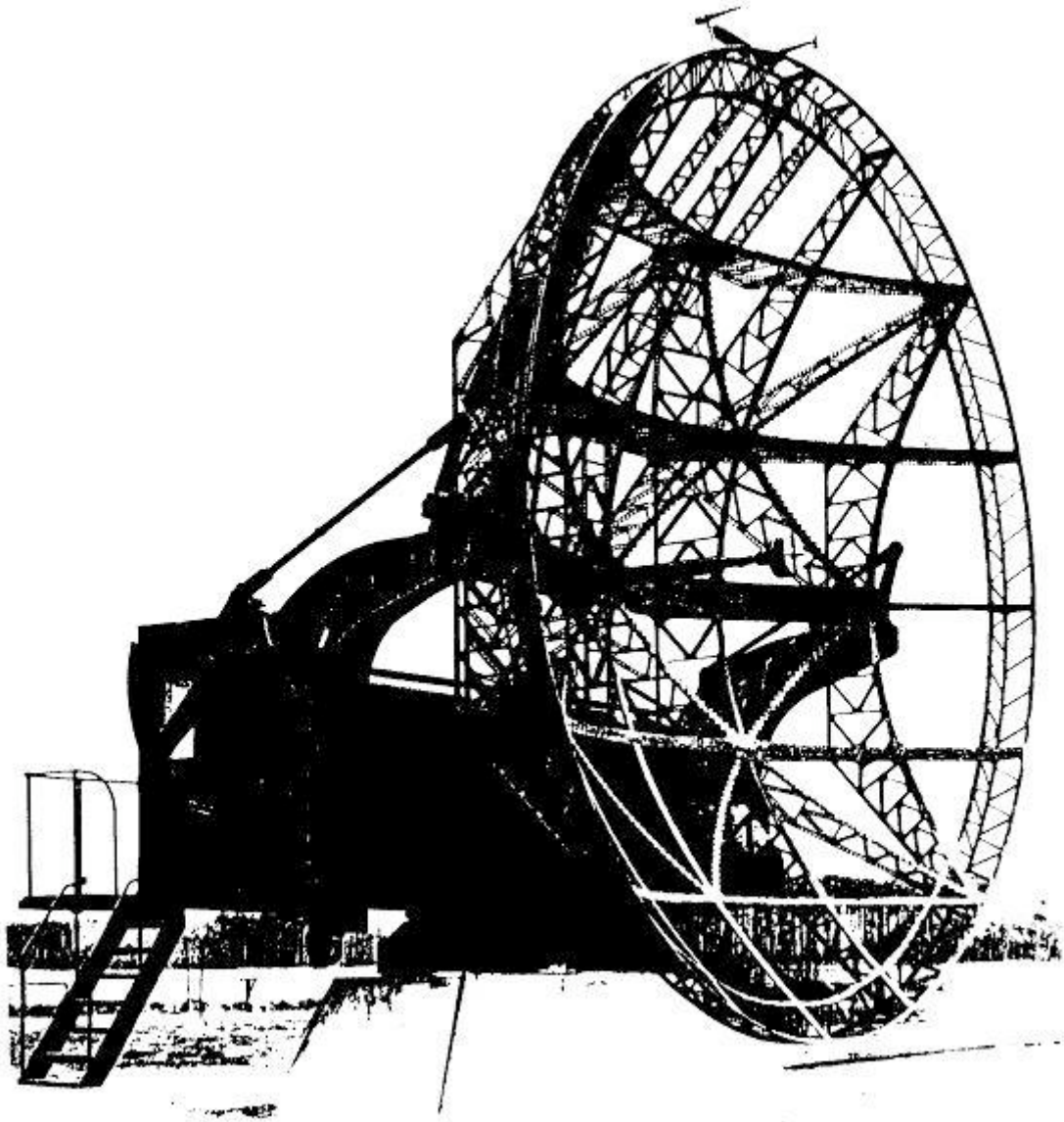


Figure 1.4 Radar apparatus “Würzburg Reise”, Telefunken 1941

The available script presents the principles used today and the current status of the technology. Further relevant Literature on the history of Radar can be found in [4, 5, 11, 12].

2 Electromagnetic field theory & wave propagation basics

Through the analysis of the fundamental procedures of Radar technology one can normally assume that the transmitter/receiver and the target object are in the mutual far-field. This makes the inspection of plane waves at the equipment site (e.g. antenna) and the reflecting objects according to Figure 2.1 possible.

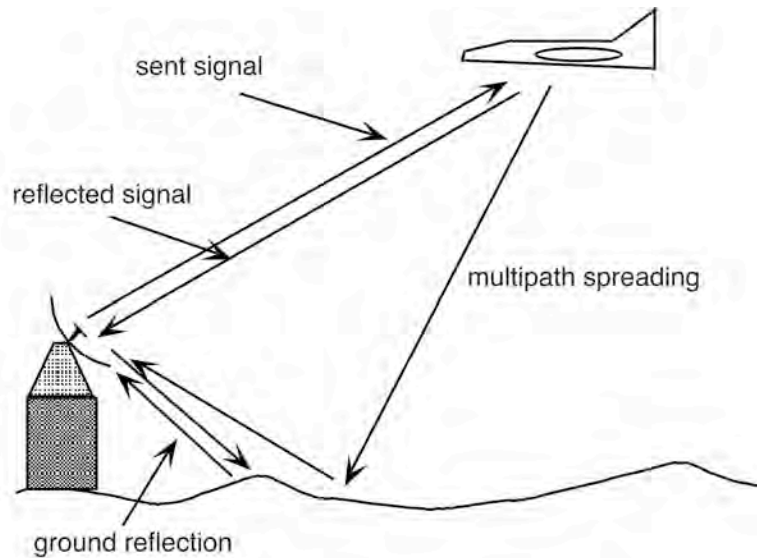


Figure 2.1 Diagram of the basic function of Radar: sent signal, reflected signal from object, multipath spreading, ground reflection.

The essence of Radar technology lies in the use of a wave reflected by an object.

Important for the performance are:

- Frequency
- Polarization
- Target properties
- Equipment performance
- Intervisibility (how well equipment and object can “see“ one another)
- Distance

Below the theoretical constraints for the reflection of plane waves on metallic and dielectric bodies will be shown. Quantitative analysis will follow later.

2.1 Fields and Waves in Free Space

The foundation of all wave behaviour is described by Maxwell's Equations:

$$\text{rot} \vec{H} = \frac{\partial \vec{D}}{\partial t} + \vec{j} \quad (2.1)$$

$$\text{rot} \vec{E} = -\frac{\partial \vec{B}}{\partial t} \quad (2.2)$$

$$\text{div} \vec{B} = 0 \quad (2.3)$$

$$\text{div} \vec{D} = \rho \quad (2.4)$$

The solutions of these equations are so varied that general and task specific restrictions must be made and boundary conditions are defined.

Restrictions:

Time-harmonic processes:

$$\underline{e}(t) = \underline{E} \cdot e^{j\omega t} \quad (2.5)$$

$$\frac{\partial}{\partial t} = j\omega \quad (2.6)$$

Charge density of free space:

$$\rho = 0 \quad (2.7)$$

Current in free space:

$$\vec{i} = 0 \quad (2.8)$$

Homogeneous and isotropic field densities:

$$\vec{D} = \epsilon \vec{E} = \epsilon_0 \epsilon_r \vec{E} \quad (2.9)$$

$$\vec{B} = \mu \vec{H} = \mu_0 \mu_r \vec{H} \quad (2.10)$$

$$c = \frac{1}{\sqrt{\mu\epsilon}} = \frac{c_0}{\sqrt{\mu_r \epsilon_r}} \quad (2.11)$$

Spreading of the field in the z-direction:

$$\vec{e}(x, y, z, t) = \text{Re} \left\{ \vec{E}(x, y) \cdot e^{\gamma z + j\omega t} \right\} \quad (2.12a)$$

$$\vec{h}(x, y, z, t) = \text{Re} \left\{ \vec{H}(x, y) \cdot e^{\gamma z + j\omega t} \right\} \quad (2.12b)$$

$$y = \alpha + j\beta$$

$$\frac{\partial}{\partial z} = y \approx j\beta (\text{lossless}) \quad (2.13b)$$

From Maxwell’s equations it follows that all cartesian components of the field in a homogenous, isotropic, charge and current free medium ($\text{grad } \epsilon = 0, \text{grad } \mu = 0$) and namely the instantaneous values satisfy the Wave Equation:

$$\Delta A = \frac{1}{c^2} \frac{\partial^2 A}{\partial t^2} \tag{2.14}$$

The free-space propagation in the far field of the antenna is described by plane waves with the Poynting vector $\vec{S} = \vec{E} \times \vec{H}$. \vec{E} and \vec{H} are in phase and they lie perpendicular to each other.

Of interest for Radar technology is the position of the field components \vec{E} and \vec{H} regarding the media, on which they impinge. One distinguishes the wave by the position of the electrical field components based upon the direction of propagation and spreading. Should \vec{E} and \vec{S} stretch in a vertical plane, this is vertical polarization. Should they stretch in a horizontal plane, this is horizontal polarization.

2.2 Reflection on Perfect Conducting Bodies

The behaviour of reflecting objects is demonstrated on perfect conducting bodies. On conducting bodies certain field conditions are enforced, which are signified as boundary conditions:

- Upon perfect conducting surfaces there can exist no tangential electrical field strengths:

$$E_{\text{tan}} \equiv 0 \tag{1.15}$$

- For frequencies in the microwave range there exists an extreme Skin Effect and consequently the penetration depths of all fields disappear. Therefore only tangential magnetic field components appear on conducting surfaces.

$$H_{\text{norm}} \equiv 0 \tag{2.16}$$

- Due to the consistency of the electric field Maxwell’s equations yield the following:

$$\frac{\partial H_{\text{tan}}}{\partial n} = 0 \tag{2.17}$$

Where $\partial/\partial n$ demonstrates an identified existing tangential field H_{tan} from the derivation according to measuring standards. In Figure 2.2 the boundary conditions for the time independent components are illustrated.

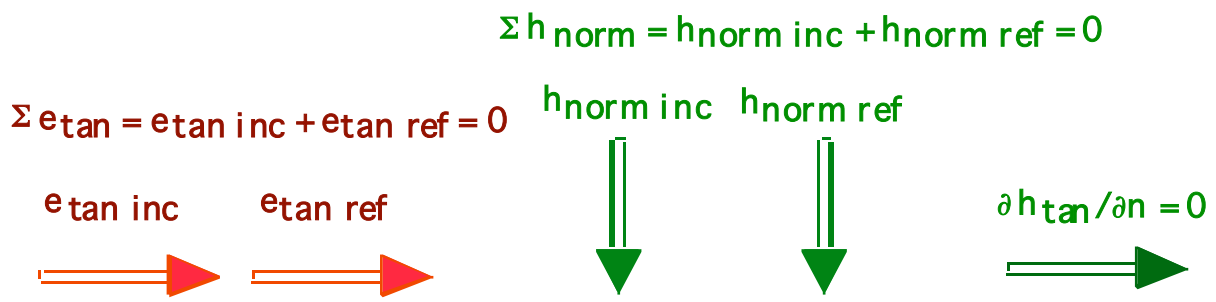


Figure 2.2 Boundary conditions on a perfectly conducting surface (inc = incident, ref = reflected)

These boundary conditions lead to total reflection with a shift in phase ($r = -1$) of the electromagnetic waves of a perfect conducting body. The direction of the reflection depends upon the incident angle and the geometry of the body. Complex bodies show a more complex reflection characteristic.

2.3 Reflection on Dielectric Interfaces

In Radar technology, in addition to metallic objects like airplanes, dielectric objects are also of interest. Examples are the Earth’s surface, plants, water, etc. The waves penetrate, as will be shown, into the dielectric. There are losses of the dielectric (e.g. water, where the penetrating waves quickly dissipate), whereby this attenuation due to losses is proportional to the frequency and the loss angle of the material.

When a wave from free space, as in Figure 2.3, encounters a infinitely extended dielectric surface with relative permittivity ϵ_r , then a coherent wave is dispersed in the entire, which has varying characteristics in the two subsections and whose electrical field lines experience a break when crossing the interface, if the field line does not arise perpendicularly. With linear polarization, the polarization is defined by the situation of the electrical field vector in the incident plane.

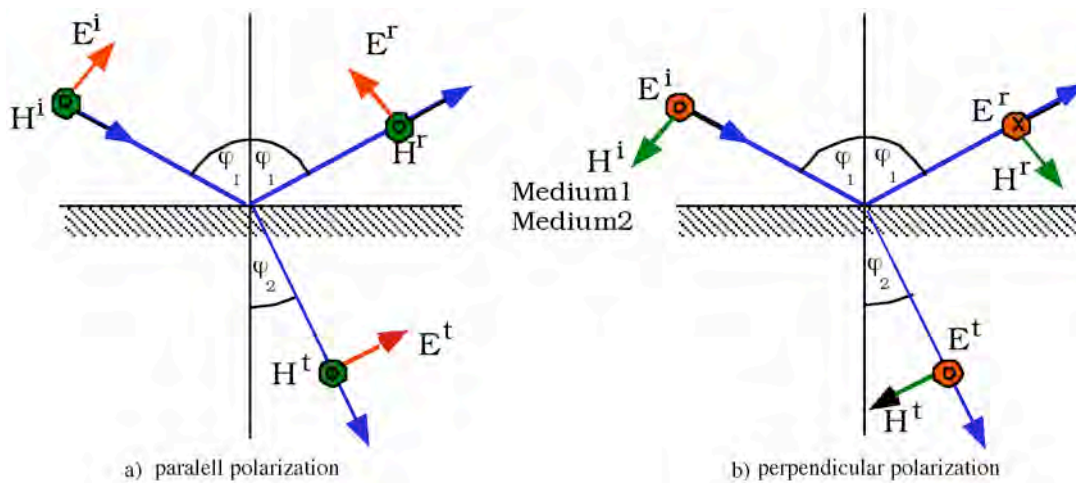


Figure 2.3 Polarization defined incident Waves. (a) Parallel Polarization (b) Perpendicular Polarization

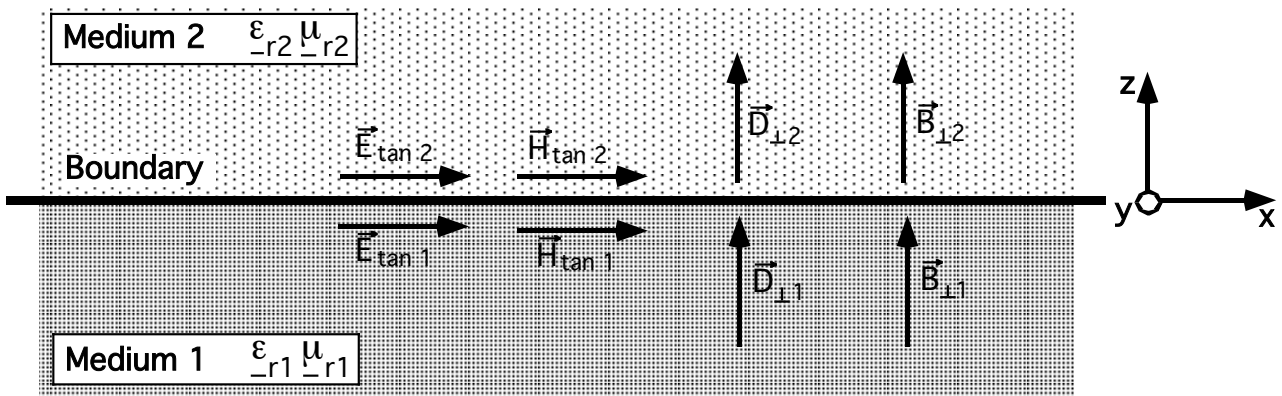
The electric field can show a tangential component E_{1tan} and a perpendicular component E_{1norm} in regard to the interface. In the dielectric exist the corresponding components E_{2tan} and E_{2norm} . The following applies for the instantaneous values at the interface:

$$e_{1tan} = e_{2tan}, e_{1norm} = \epsilon_r \cdot e_{2norm} \tag{2.18}$$

The tangential electric field strengths are constant at the interface and the orthogonal electric field strengths undergo a shift or “jump” in the transition at the interface. When the dielectric is void of magnetic effects (thus $\mu_r = 1$), the magnetic field strengths pass unchanged through the interface. The following applies for the instantaneous values:

$$h_{1tan} = h_{2tan}, h_{1norm} = h_{2norm} \tag{2.19}$$

Figure 2.4 shows the boundary conditions in diagrammatic form.



$$\begin{aligned} \vec{E}_{\text{tan } 1} &= \vec{E}_{\text{tan } 2} & \vec{J}_F &= \vec{n}_{12} \times (\vec{H}_{\text{tan } 1} - \vec{H}_{\text{tan } 2}) \\ \vec{D}_{\text{norm } 1} &= \vec{D}_{\text{norm } 2} & \longrightarrow & \epsilon_{r1} \vec{E}_{\text{norm } 1} = \epsilon_{r2} \vec{E}_{\text{norm } 2} \\ \vec{B}_{\text{norm } 1} &= \vec{B}_{\text{norm } 2} & \longrightarrow & \mu_{r1} \vec{H}_{\text{norm } 1} = \mu_{r2} \vec{H}_{\text{norm } 2} \end{aligned}$$

Figure 2.4 Boundary conditions at dielectric interfaces.

With help from these boundary conditions (2.18) and (2.19) can yield the effects and/or the influences of the dielectrics and, in particular, the characteristics of the reflected waves [14]. Below the complex reflection coefficients for E-Waves and H-Waves are arranged according to how they impinge upon the expanded dielectric surfaces. The wave originates from medium 1 and encounters medium 2.

E parallel to the plane, Figure 2.3a:

$$r_{\parallel} = \frac{Z_1 \cdot \cos \varphi_1 - Z_2 \cdot \cos \varphi_2}{Z_1 \cdot \cos \varphi_1 + Z_2 \cdot \cos \varphi_2} \tag{2.20}$$

E perpendicular to the plane, Figure 2.3b:

$$r_{\perp} = \frac{Z_2 \cdot \cos \varphi_1 - Z_1 \cdot \cos \varphi_2}{Z_2 \cdot \cos \varphi_1 + Z_1 \cdot \cos \varphi_2} \tag{2.21}$$

$$\frac{\sin \varphi_2}{\sin \varphi_1} = \frac{\sqrt{\mu_{r1} \epsilon_{r1}}}{\sqrt{\mu_{r2} \epsilon_{r2}}} \quad \cos \varphi_2 = \sqrt{1 - \frac{\epsilon_{r1}}{\epsilon_{r2}} \cdot \sin^2 \varphi_1} \tag{2.22}$$

Z_1 and Z_2 are the impedances for the field waves in the respective media.

In Table 2.1 the boundary conditions for various materials have been assembled into their vector forms.

Field intensity	General	Finite conductivity media, no sources or charges $\sigma_1, \sigma_2 \neq \infty$ $J_s = M_s = 0$ $q_{es} = q_{ms} = 0$	Medium 1 of infinite electric conductivity $\sigma_1 = \infty; \sigma_2 \neq \infty$ $M_s = 0$ $q_{ms} = 0$	Medium 1 of infinite magnetic conductivity ($H_{1t} = 0$) $J_s = 0$ $q_{es} = 0$
Tangential electric field	$\vec{n} \times (E_2 - E_1) = -M_s$	$\vec{n} \times (E_2 - E_1) = 0$	$\vec{n} \times E_2 = 0$	$\vec{n} \times E_2 = -M_s$
Tangential magnetic field	$\vec{n} \times (H_2 - H_1) = J_s$	$\vec{n} \times (H_2 - H_1) = 0$	$\vec{n} \times H_2 = J_s$	$\vec{n} \times H_2 = 0$
Normal electric flux	$\vec{n} \cdot (D_2 - D_1) = q_{es}$	$\vec{n} \cdot (D_2 - D_1) = 0$	$\vec{n} \cdot D_2 = q_{es}$	$\vec{n} \cdot D_2 = 0$
Normal magnetic flux	$\vec{n} \cdot (B_2 - B_1) = q_{ms}$	$\vec{n} \cdot (B_2 - B_1) = 0$	$\vec{n} \cdot B_2 = 0$	$\vec{n} \cdot B_2 = q_{ms}$

Table 2.1 Boundary conditions on interfaces

3 The Radar Equation

3.1 Radar Equation for Point Targets

The general Radar equation found in Literature is derived for point targets. Point targets are objects whose dimensions D are small compared to the illumination $R \cdot \gamma_{BW}$ (Range * Half-power beamwidth) by the Radar at the target site. This is illustrated in Figure 3.1.

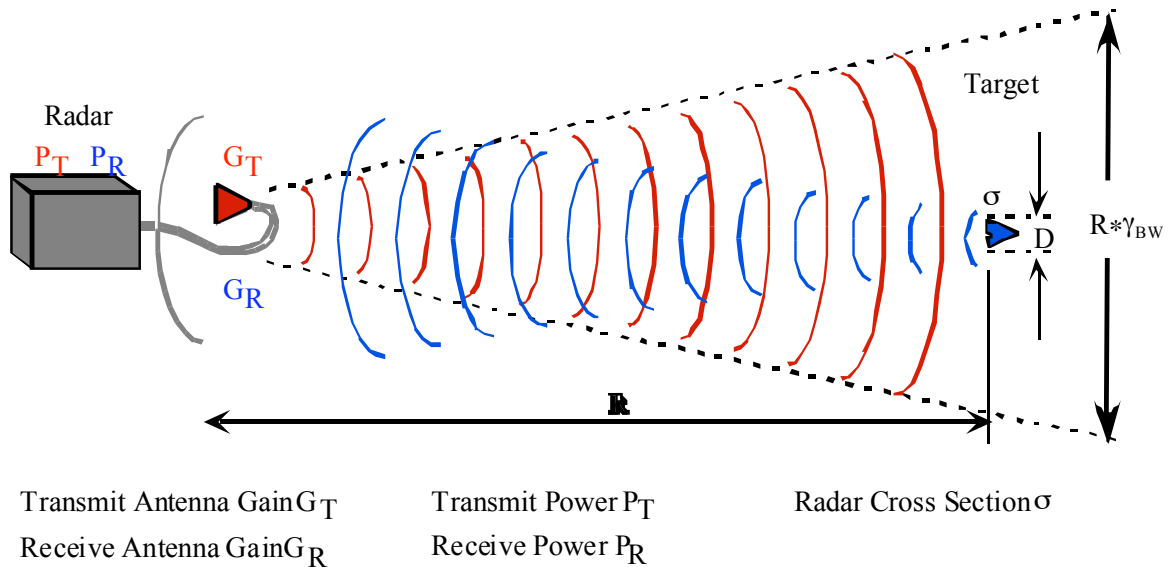


Figure 3.1 Illustration of the principle of Radar.

For better understanding the Radar equation will be progressively derived in this section. Peripheral effects and environmental influences, as well as sensitivity, will be dealt with later. On the sender-side of the Radar a power P_T will be radiated. With a range R from the transmitter a power density at the target S_i results from isotropic (spherical) radiation

$$S_i = \frac{P_T}{4\pi R^2} \tag{3.1}$$

This is the power density of an omni-directional antenna with a range R . Since in Radar technology one, almost exclusively, directs the radiation, the power density at the range R increases with the antenna gain G_T :

$$S_i = \frac{P_T \cdot G_T}{4\pi R^2} \tag{3.2}$$

The following can be considered: The transmitting antenna gain G_T relates only to the maximum of the antenna main lobe. Consequently, G_T indicates the increase of the power density at a distance R through Radar antennas based upon isotropic emitters with the same sending power. G comprises the antenna losses and is calculated with the directivity D and the antenna efficiency η :

$$G = \eta \cdot D \tag{3.3}$$

The impinging radiated power is scattered by the target object and is dependent on shape, size, material or orientation of the object. The measure of scattered power in direction of the Radar is the scattering cross section σ/m^2 of the object. With this, from the target to the transmitter the power P_t is scattered.

$$P_t = S_t \cdot \sigma = \frac{P_T \cdot G_T}{4\pi R^2} \cdot \sigma \quad (3.4)$$

At the location of the transmitter/receiver antenna the scatter power P_t generates the power density S_R .

$$S_R = \frac{P_t}{4\pi R^2} = \frac{P_T \cdot G_T \cdot \sigma}{(4\pi R^2)^2} \quad (3.5)$$

The receiving antenna has an effective area A_R , and it absorbs the power out of the power density S_R .

$$P_R = S_R A_R = \frac{P_T G_T \sigma A_R}{(4\pi R^2)^2} \quad (3.6)$$

The effective area A_R is also used in direct relationship to the gain G [9].

$$G = \frac{4\pi A_R}{\lambda^2} \quad (3.7)$$

This then yields:

$$P_R = P_T \cdot \frac{G_T \cdot G_R \cdot \lambda^2}{(4\pi)^3 \cdot R^4} \cdot \sigma = P_T \cdot \frac{A_T \cdot A_R}{4\pi \lambda^2 \cdot R^4} \cdot \sigma \quad (3.8)$$

Under the assumption that a postulated signal-to-noise ratio S/N gives the received power P_{Rmin} , one obtains the maximum range of coverage R_{max} .

$$R_{max} = \sqrt[4]{P_T \cdot \frac{A_T A_R}{4\pi \lambda^2 P_{Rmin}} \cdot \sigma} = \sqrt[4]{P_T \cdot \frac{G_T G_R \lambda^2}{(4\pi)^3 P_{Rmin}} \cdot \sigma} \quad (3.9)$$

P_{Rmin} = minimum received power (see section “Noise and Detection“)

The dependence of the transmitted power P_T and the Radar cross-section σ is proportional by $(\sqrt[4]{\quad})$ the 4th root. The dependence of the wavelength is essentially more complicated since the scattering cross section can be heavily frequency dependent. Furthermore in G_T , the frequency over the effective area of the antenna is contained quadratically. Consequently, for the estimation of the frequency dependence of the range of coverage, the influence of frequency on the following characteristics must be considered:

- Antenna gain
- Propagation attenuation
- Cross-section of the reflection

3.2 Radar Equation for Extended Targets

For extended targets, meaning targets that are located in the far field, R_{max} is proportional $\sqrt[3]{}$ to $\sqrt{}$, depending on the distance and characteristics of the target. An example of a flat, two-dimensional target with an extension $D \gg R \cdot \Theta_H$ will be shown by Figure 3.2 on the basis of geometric optics.

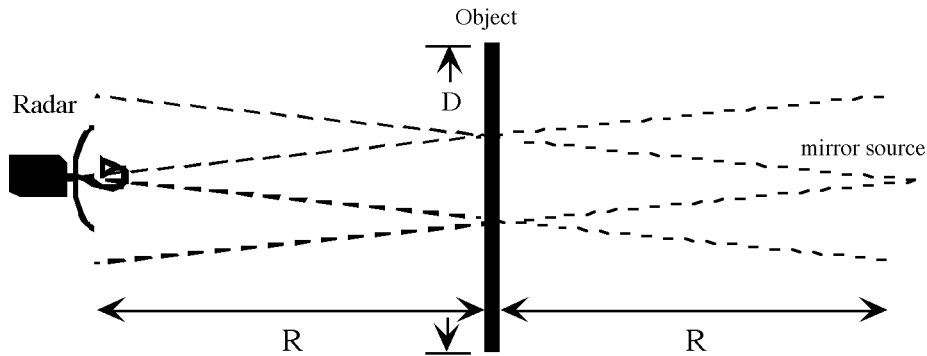


Figure 3.2 Reflection on a flat, extended target.

The mirrored reflection is in relation to a “virtual” source from a distance R behind the target. The power density at the receiver then becomes:

$$S_R = \frac{P_T \cdot G_T}{4\pi(2R)^2} \tag{3.10}$$

From this follow the received power P_R

$$P_R = S_R A_R = \frac{P_T G_T G_R \cdot \lambda^2}{4 \cdot (4\pi)^2 \cdot R^2} \tag{3.11}$$

And the range of coverage is yielded by

$$R_{max} = \sqrt{\frac{P_T G_T G_R \cdot \lambda^2}{P_{Rmin} 4 \cdot (4\pi)^2}} \tag{3.12}$$

For extended concave targets (e.g. Parabolic) will be $\sim \sqrt[3]{}$ with $p < 2$ (focused) and for extended targets with $R_{max} \sim \sqrt[3]{}$ and $p > 2$ (unfocussed). The assumption is in all cases that the reflection over the entire surface area of the extended object is well correlated, meaning, for example, that no scattering appears. Such “smooth” surfaces can be, for example, the sides of trucks of the extended hulls of ships.

3.3 The Radar Horizon

The range of coverage of Radar equipment can be limited due to minimum received power P_{Rmin} and as well due to the visibility (i.e. the Radar horizon). The Radar horizon is given by the Earth's curvature and the height of the Radar equipment & the target object, as shown in Figure 3.3.

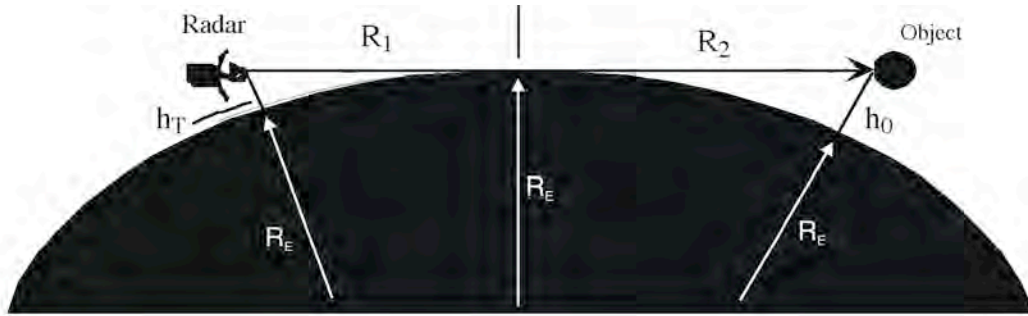


Figure 3.3 Location determination of an object under the horizon ($R_E = \text{Earth's radius}$)

Considering the geometry & optics, the following estimation for the range of coverage is yielded by:

$$\begin{aligned}
 R_{geom} &= R_1 + R_2 = \sqrt{(h_T + R_E)^2 - R_E^2} + \sqrt{(h_0 + R_E)^2 - R_E^2} \\
 &\approx \sqrt{2h_T R_E} + \sqrt{2h_0 R_E} = \sqrt{2R_E} \cdot (\sqrt{h_T} + \sqrt{h_0})
 \end{aligned}
 \tag{3.13}$$

This estimation is derived under the following requirements:

- $R_E \gg h_T, h_0$
- Earth is flat and void of various elevations
- Refraction of the electromagnetic waves in the atmosphere is neglected

This estimation of the neglect of the refraction leads to an under-estimation of the range of coverage. While passing through atmosphere (expected to be thinner at each higher elevation) the wave will be refracted towards the Earth as demonstrated in Figure 3.4.

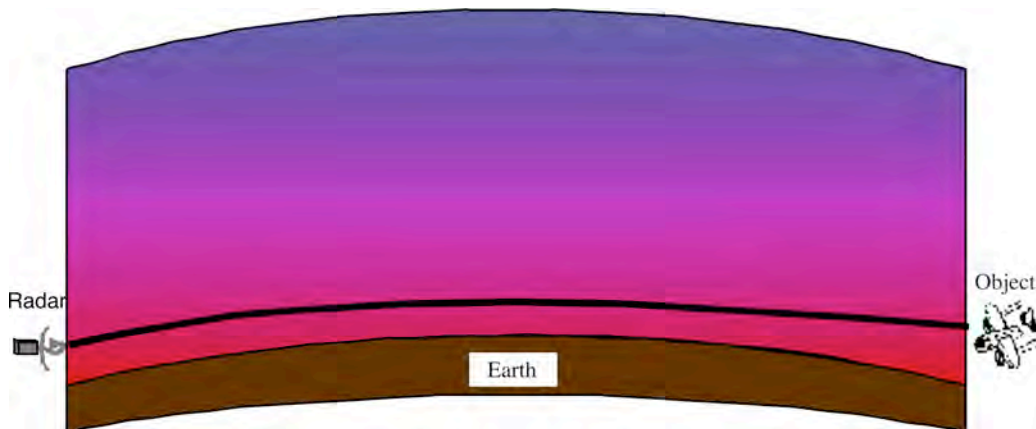


Figure 3.4 Refraction of waves in the inhomogeneous atmosphere and the enlargement of the range of coverage.

Through this bending, as it is taken into account in physical optics, the visibility & view under the horizon will be expanded. The ray path is bent to the Earth. A correction factor k is used in the calculation of the range of coverage.

$$R_{phys} = R_{geom} \sqrt{k} = \sqrt{2kR_E} (\sqrt{h_T} + \sqrt{h_0}) \quad (3.14)$$

For a linear running refractive index profile, k follows as:

$$k = \frac{1}{1 + R_E \cdot \frac{dn}{dh}} \quad (3.15)$$

Here dn/dh indicates the differential change of the refractive index n with height/altitude h . For the standard atmosphere $dn/dh \approx -40 \cdot 10^{-6} / km$ and for the correction factor:

$$k \approx 1,34 = 4/3 \quad (3.16)$$

One speaks of a 4/3 Earth radius. With that the range of coverage is enlarged by approximately 15.7%.

3.4 Bistatic Radar Equation

In the previously derived Radar equation it presupposes that transmitters and receivers are at the same place (i.e. the Radar is monostatic). There are, however, many reasons for transmitters and receivers to be separate spatially:

- Reduction of the antenna coupling in order to measure the smallest of signals
- Use of a single transmitter for several receivers
- Use of other or foreign transmitters (transmitter of opportunity)
- Protection of the receiver from discovery (and possible destruction)
- Protection of the receiver from electrical interference (electronic warfare)

In all cases there is a reference for the receiver and, as a rule, a direct connection to the transmitter is required, as demonstrated in Figure 3.5.

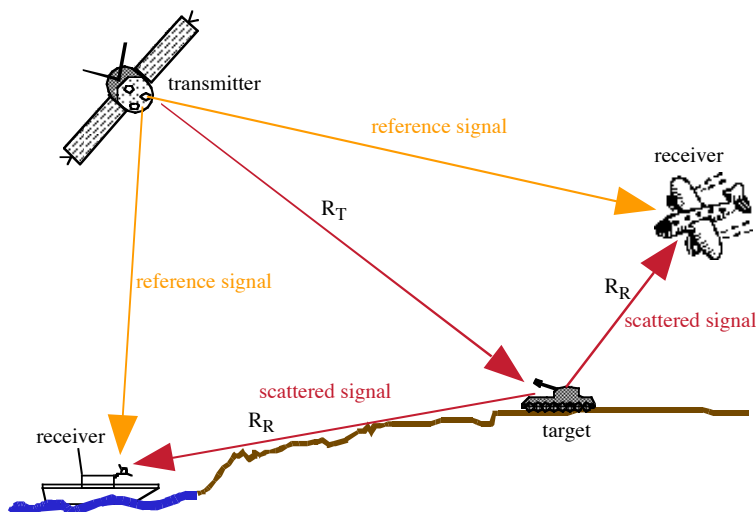


Figure 3.5 Bistatic Radar scenario: Satellite as the sender and 2 receivers.

The derivation of the Radar equation for bistatic Radar is as with monostatic Radar. Simply the grouping of terms is different.

$$\begin{aligned}
 P_R &= P_T G_T \cdot \frac{1}{4\pi R_T^2} \cdot \sigma_B \cdot \frac{1}{4\pi R_R^2} \cdot \frac{\lambda^2}{4\pi} G_R \\
 &= P_T \cdot \frac{G_T G_R \lambda^2}{(4\pi)^3 R_T^2 R_R^2} \sigma_B
 \end{aligned}
 \tag{3.17}$$

Here meaning:

P_R = receiver power

P_T = transmitter power

R_T = distance from the transmitter to the target

R_R = distance from the receiver to the target

σ_B = bistatic radar cross – section of the target

G_T = transmitter gain

G_R = receiver gain

For the analysis of the receiver signal the direct, coherent reception of the transmitter signal (*illuminator*) is necessary. From the propagation time and the directions the Radar picture is generated with relatively elaborate trigonometry.

Of interest is particularly the use of available transmitters (e.g. TV satellites as illuminators). Development in this direction is strongly enforced and not only in the military.

4 Information Content in Radar Signals

In the section for the Radar Equation the realizable information content of Radar was implicitly demonstrated. Depending on the principle that is put to use, the following information can be obtained from a Radar signal and/or a series of signals:

Distance or Range R ,

Velocity and/or Speed (change in distance over time) $\frac{dR}{dt}$,

Azimuth ψ , change of the Azimuth over time $\frac{d\psi}{dt}$

Elevation ϑ , change in elevation over time $\frac{d\vartheta}{dt}$

Size of the target s ,

Shape of the target $\frac{d\sigma}{d\psi}$,

Polarization of the target s_{vv} & s_{hh} ,

Signature (information about the target) $[\sigma]$.

The most important and most often evaluated information would be:

Distance or Range,

Velocity and/or Speed,

Direction.

In the following their determination and analysis will be discussed as well as procedures for their measurement to be shown.

4.1 Range

The range is measured as the time difference between the echo-signal and a corresponding reference. As a reference the transmission signal is normally marked and the timestamp between is saved at the receiver. The range can be calculated from the duration Δt and the speed of propagation c_0 :

$$c_0 \cdot \Delta t = 2R \Rightarrow R = c_0 \cdot \frac{\Delta t}{2} \quad (4.1)$$

For very precise range measurements the genuine speed of propagation (influenced by air pressure, moisture, etc.) is to be used instead of c_0 . The resolution in the range depends on the time steps of the timer (e.g. 1 ns = 30 cm).

Three magnitudes are used for resolving the timestamp, as is shown in Figure 4.1:

- Amplitude A → Pulse Modulation → Pulse Radar
- Frequency f → Frequency Modulation → FM-CW Radar
- Phase φ → Phase Modulation → Phase Interferometer

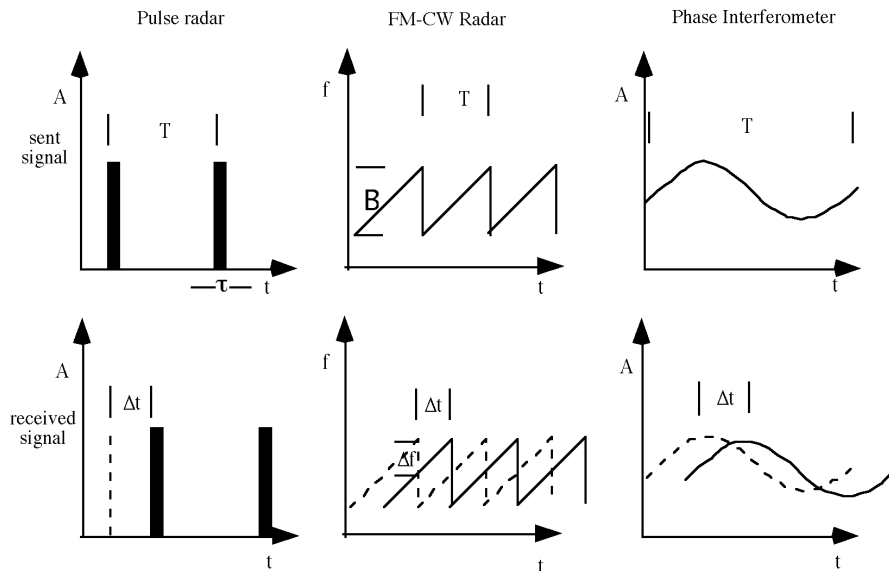


Figure 4.1 Procedure to measure range: T = Period duration, B = Frequency shift, Δf = frequency difference, Δt time difference, τ = Pulse duration.

With pulse Radar the time difference can be measured directly. With FM-CW Radar the duration will be determined from the difference in frequency as received from the target and of the current transmitter. For the simple case of linear frequency modulation, referring to Figure 4.1, Δt is as follows:

$$\Delta t = \Delta f \frac{T}{B} \Rightarrow R = \Delta f \frac{T}{2B} C_o \tag{4.2}$$

Along with the analysis of the frequency difference Δf, with FM-CW Radar the range to reflecting objects can also be calculated from a Fourier transform of the complex frequency signal in the time domain.

The unambiguous range of coverage is limited by the pulse repetition frequency PRF = 1/T of the selection. For the repetition period T follows the unambiguous range of coverage:

$$R_{unamb} = \frac{c_0 \cdot T}{2} = \frac{c_0}{2PRF} \tag{4.3}$$

The resolution, meaning the distance separation of two targets, is in all case inversely proportional to the bandwidth B, which will be employed. As a good approximation the following can be applied:

$$\Delta R_{min} > \frac{c}{2B} \tag{4.4}$$

In the last few years several *Super-Resolution Algorithms*, as ESPRIT, have been developed, with which the resolution under certain conditions can be considerably improved.

4.2 Velocity

In the case of continuous observation of the target (CW Radar) its radial velocity produces a phase shift of the received signal, known as Doppler effect, from which follows:

$$\omega_d = \frac{d\varphi}{dt} \quad (4.5)$$

$$f_d = \frac{\omega_d}{2\pi} = \frac{1}{2\pi} \frac{d\varphi}{dt} = -\frac{2}{\lambda_0} \frac{dr}{dt} = -\frac{2v_r}{\lambda_0} = -\frac{2v_r f_0}{c_0} \quad (4.6)$$

$f_d = \text{Doppler frequency}$

$v_r = \text{radial velocity}$

$f_0, \lambda_0 = \text{transmission frequency, wavelength}$

$c_0 = \text{propagation velocity}$

As a rule $f_d [\text{Hz}] = 55,5 \cdot v [\text{km/h}] / \lambda [\text{cm}]$. With a movement diagonally for the direction of propagation of the wave only the radial component from v is to be considered v_r . The Doppler effect is clear with CW Radar devices, in contrast to the coherent pulse Radar. With this the ambiguity develops if the phase shift through Doppler in a pulse interval becomes larger than 2π . With the non-coherent pulse Radar, i.e. no phase reference from pulse to pulse, the radial velocity is measured over the change of distance, however substantially more inaccurately. The coherent procedures require a good short-time stability of the transmission signals (see pulse Radar, chapter 8).

4.3 Direction (Azimuth, Elevation)

Antennas generate a plane wave in the far field. They also mainly receive the plane wave from the far field, which corresponds to the alignment of the antenna. The target direction therefore can be determined from the antenna position. This does apply, however, only so long, as on the propagation path no deviations from straight rays by inhomogeneities arise (*Duct*). The attainable accuracy depends on the half power beam-width of the antenna characteristic. Another procedure for the measurement of direction uses several receiving antennas, at which the phase difference of the received signal is used for the direction finding. Examples are mono-pulse Radar (section 11,1,1) and interferometers, as used in astronomy.

4.4 Polarization Characteristics of the Target

The polarization of a target is rarely considered. However, it offers the possibility of determining and/or of differentiating between structures. As an example, vegetation (trees, plants, etc.) normally reflects with vertical polarization substantially more strongly than with horizontal polarization, since vegetation is usually aligned vertically. However, de-polarization on the propagation path represents a problem (therefore the use of polarization diversity with communications satellites). The choice of the correct polarization offers, among other advantages, the possibility of suppressing disturbances (weather). Thus precipitation disturbs less with circular polarization. The knowledge around the evaluation of polarization characteristics is called Radar polarimetry.

5 Resolution and Accuracy

Resolution is a measurement for how close or dense targets may be to each other, while still being able to separately detect them. Under the term resolution the ability is therefore understood for the separation of neighbouring objects. Accuracy is a measure for how large the tolerances for the determination of the information parameters, such as distance, speed, etc. are. The accuracy describes thus, with which relative or absolute errors the measured variable can be determined. Measurement uncertainty result from:

- Imprecise measurement equipment
- Quantization errors
- Noise
- Signal distortion.

For an example a sine wave oscillation will be analyzed.

5.1 Measurement Accuracy and Sine Wave Oscillations

As shown in Figure 5.1, when one observes a sine wave, with superimposed noise $n(t)$, so differs the observed amplitude from the true amplitude around $\Delta U = n(t)$

$$u(t) = U_0 \sin(\omega t + \varphi_0) + n(t) \quad (5.1)$$

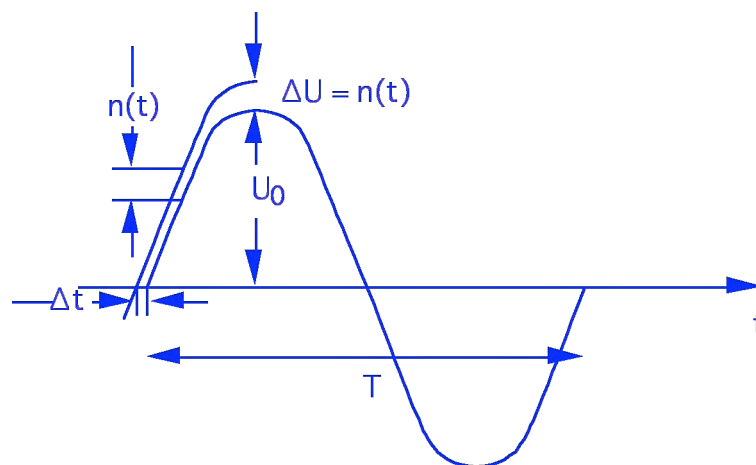


Figure 5.1 Sine wave oscillation with superimposed noise.

Amplitude measurement error: The root-mean-square error is

$$\partial U = \sqrt{\overline{n^2}} \quad (5.2)$$

The relative error then becomes

$$\frac{\partial U}{U} = \frac{\sqrt{\overline{n^2}}}{\sqrt{U_0^2}} = \frac{1}{\sqrt{\frac{(\sqrt{2}U_{eff})^2}{n^2}}} = \frac{1}{\sqrt{2S/N}} \quad (5.3)$$

Time measurement error: The time error Δt according to Figure 5.1 is

$$\Delta t = \frac{n(t)}{\text{slope}} \tag{5.4}$$

For the sine function this is (at zero crossover crucial for the measurement) ωU_o , from which follows:

$$\partial t = \sqrt{\Delta t^2} = \frac{\sqrt{n^2}}{\omega U_o} = \frac{\sqrt{n^2}}{\omega \sqrt{2U_{eff}}} = \frac{1}{\omega \sqrt{2S/N}} \tag{5.5}$$

Phase error: The phase error results directly:

$$\partial \phi = 2\pi f \cdot \partial t = \frac{1}{\sqrt{2S/N}} \tag{5.6}$$

Period error: The period error ∂T (RMS) is larger than ∂t by around a factor of $\sqrt{2}$, since two passes are to be measured.

$$\partial T = \frac{\sqrt{2}}{\omega \sqrt{2S/N}} = \frac{T}{2\pi \sqrt{S/N}} \tag{5.7}$$

The relative errors for the period and the frequency are then:

$$\frac{\partial T}{T} = \frac{1}{2\pi \sqrt{S/N}} \tag{5.8}$$

$$\frac{\partial f}{f} = \frac{1}{2\pi \sqrt{S/N}} \tag{5.9}$$

5.2 Accuracy and Range Measurement

For calculating the accuracy of the range measurement one replaces the sine wave with a video pulse as in Figure 5.2.

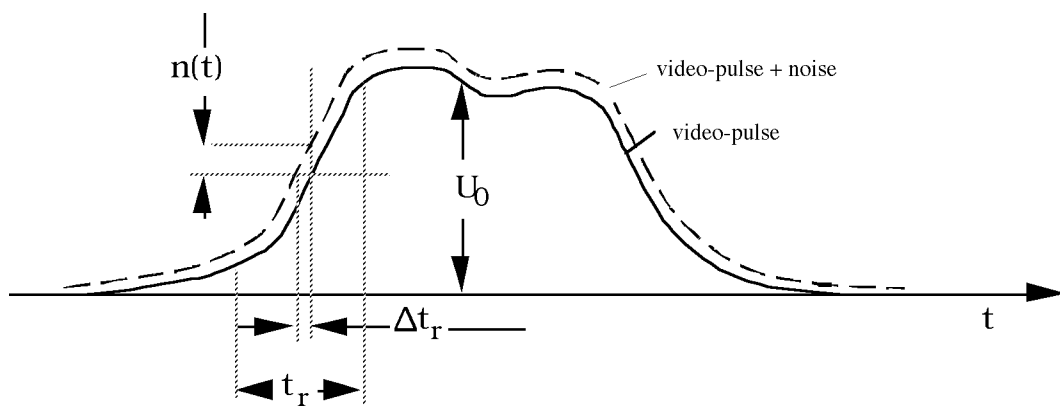


Figure 5.2 Video pulse and added noise with edge triggering.

The calculation of Δt_r is performed similar to equation (5.5)

$$\Delta t_r = \frac{t_r}{\sqrt{U_0^2/n^2}} = \frac{t_r}{\sqrt{2S/N}} \quad (5.10)$$

t_r is the linear rise time from 10% up to 90% of U_0 . Δt_r is the measurement accuracy for the edge triggering. With that yields the range accuracy:

$$\Delta R = c_0 \cdot \Delta t_r / 2 \quad (5.11)$$

The other equations from above can be applied in analogous way.

5.3 Range Resolution of Two Neighbouring Targets

By the term resolution it is understood the differentiation of targets, which are in very close proximity to on another, as shown in Figure 5.3

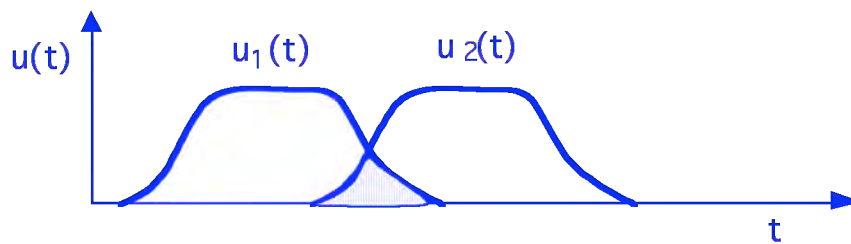


Figure 5.3 Echoes of two neighbouring objects.

$u_1(t)$ indicates the echo of target 1 and $u_2(t)$ the echo of target 2. Then for resolution optimization the integral must become a maximum.

$$\int (u_1(t) - u_2(t))^2 dt = \int [u_1^2(t) - 2u_1(t)u_2(t) + u_2^2(t)] dt \quad (5.12)$$

The integral will become a maximum when the negative part becomes minimum, thus

$$\int u_1(t)u_2(t) = \text{minimum} \quad (5.13)$$

Assuming that both signals result from the same or similar shape (same reflection cross section) then their transit times being t_1 & t_2 yield on the left side of the equation (5.13):

$$\int u(t - t_1)u(t - t_2) \quad (5.14)$$

This integral represents the auto-correlation function of the signal with itself. For optimizing the resolution, the shape of the pulse should be optimized. The ideal result would be:

$$\int = 0 \text{ für } t_1 \neq t_2; \int = 1 \text{ für } t_1 = t_2 \quad (5.15)$$

If the targets are different in size, then one should bear equation (5.14) in mind. The auto-correlation will then become a cross-correlation.

With typical specifications of the threshold value for the cross-correlation, the range resolution ΔR can be approximately calculated as illustrated in Figure 5.4

$$\Delta R = c_0 \cdot \tau / 2 \tag{5.16}$$

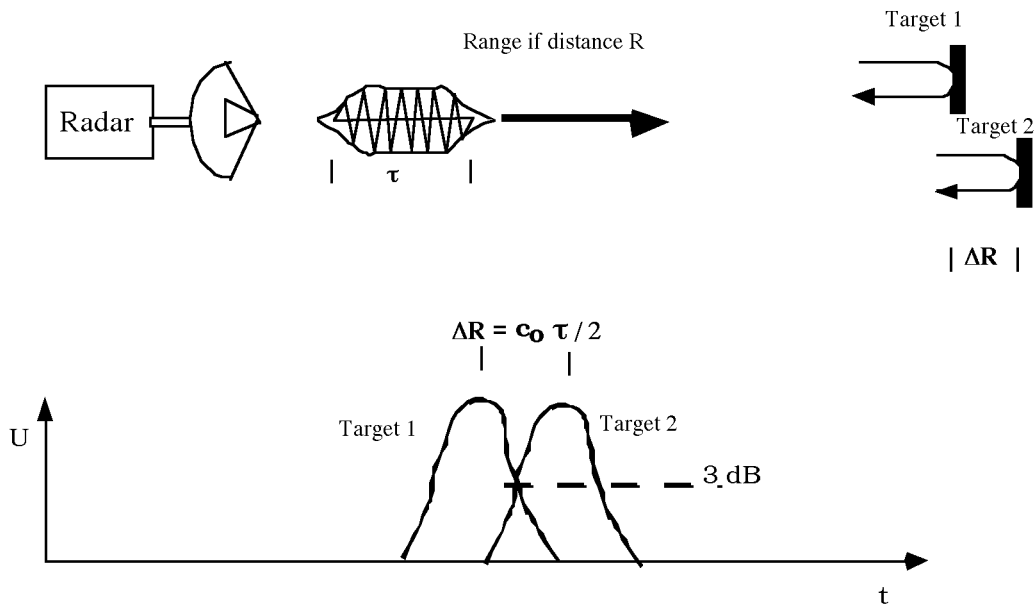


Figure 5.4 Range resolution of two targets.

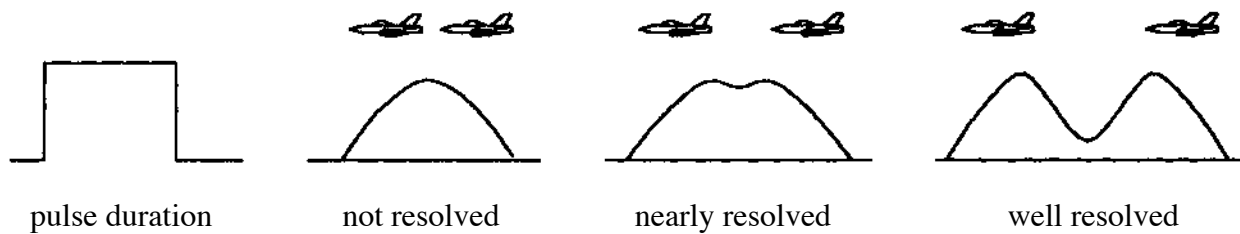


Figure 5.5 Example for the ability to resolve objects at differing ranges & separation distances.

5.4 Angular Resolution

The angular resolution can be calculated in a similar way as the range resolution, if pulse echoes are replaced with the maximum of the directivity. As a good approximation the half-power beamwidth γ_{BW} of the antenna can be utilized. This is illustrated in Figure 5.6.

$$\Delta x = R \cdot \gamma_{BW} \tag{5.17}$$

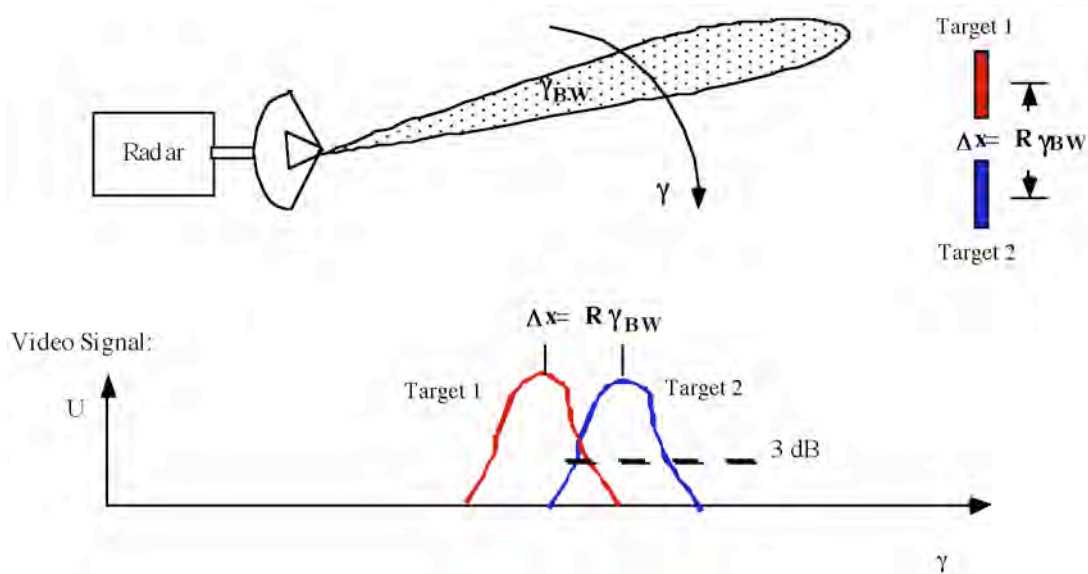


Figure 5.6 Angular resolution of two targets.

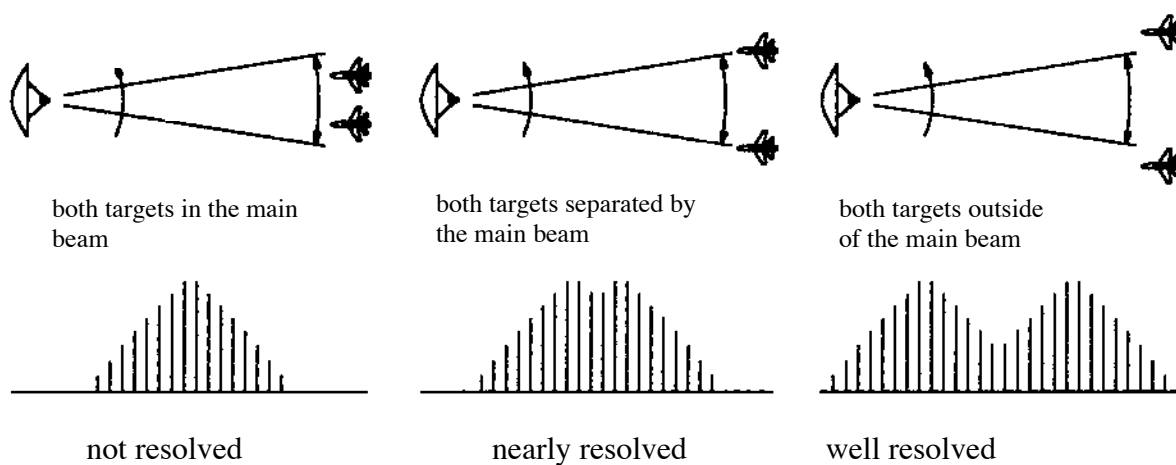


Figure 5.7 Further examples for angular resolution.

6 Radar Receiver Noise and Target Detection

The maximum range of coverage has been determined in Chapter 3 with the minimum receiving power $P_{R \min}$. This will again be determined with the required signal-to-noise ratio S/N and the noise P_N power at the receiver input.

The fundamental contributions to P_N yield:

- thermal noise
- cosmic noise
- atmospheric absorption noise
- Man made noise.

In the following section the system inherent noise contribution and the contributions of the communication path will be dealt with.

6.1 Thermal Noise

The thermal (ohmic) noise is inherent to the system and is determined by the temperature and the bandwidth. The theories of noisy dipoles and quadripoles are to be found in [10]. The thermal noise power P_N results from:

$$P_N = N_T \cdot B_N = k \cdot T \cdot B_N \quad (6.1)$$

$$k = 1,38 \cdot 10^{-23} \text{ J/}^\circ\text{K Boltzmann's constant}$$

$$B_N = \text{Noise bandwidth of the receiver (3dB bandwidth)}$$

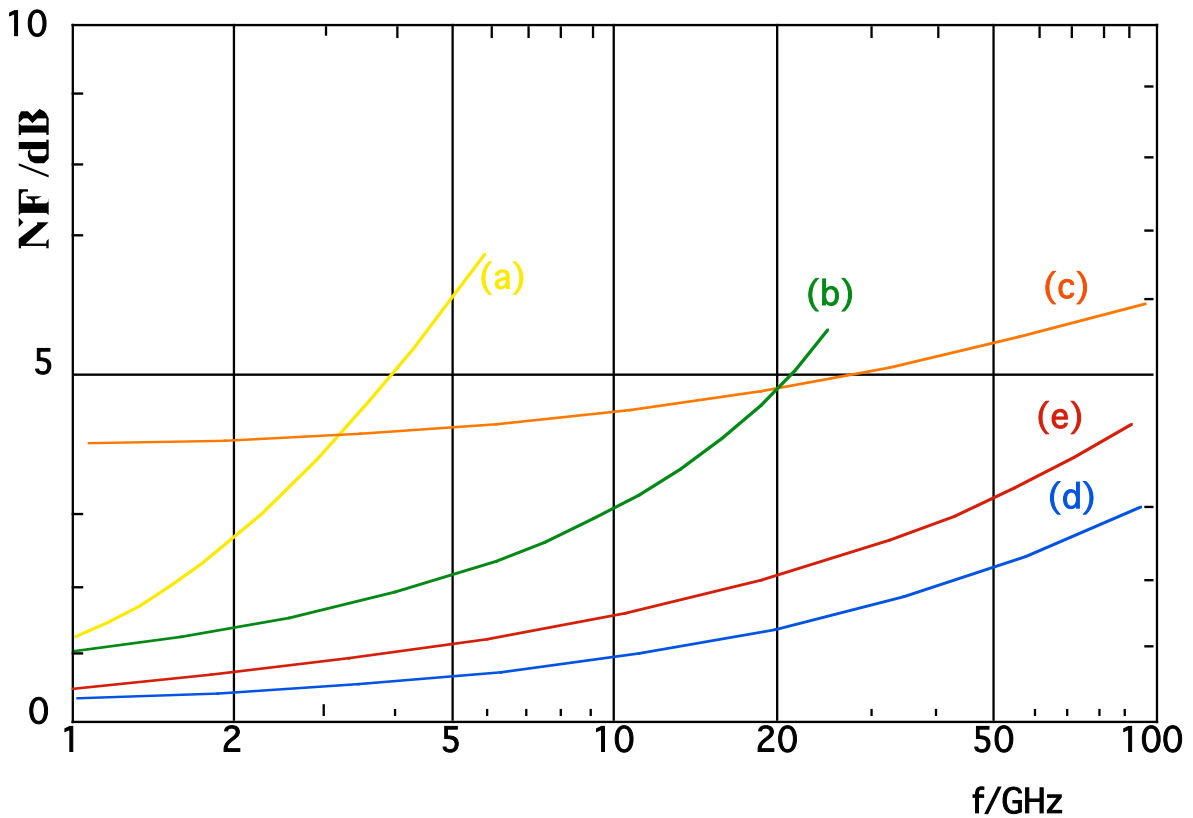
$$N_T = \text{Noise power density}$$

$$\text{For } T = 300^\circ\text{K: } N_T = -114 \text{ dBm/MHz bandwidth} \quad (6.1a)$$

In practice the thermal noise will be increased due to flicker and spot noise of the receiver input stages. This increase will be indicated as the noise figure NF.

If the output noise power of the receiver amounts to N_A and if the total gain is G, then we have the following:

$$NF = \frac{N_A}{N_T \cdot G} = \frac{N_A}{kTB \cdot G} \quad (6.2)$$



- a) Bi-polar Transistor-Amplifier
- b) FET-Amplifier
- c) GaAs-Schottky-Mixer,
- d) Parametric Amplifier
- e) P-HEMT Amplifier

Figure 6.1 Noise measurement (dB) of various receiver input stages

The gain is able to be expressed as a quotient of the signal power at the output P_A and input P_E of the receiver.

$$G = \frac{P_A}{P_E} = \frac{P_{A \min}}{P_{E \min}} \tag{6.3}$$

The minimum receiver input power is calculated with equation (6.4):

$$P_{R \min} = NF \cdot kTB \frac{P_A}{N_A} = NF \cdot kTB_N (S/N) = NF \cdot N_T (S/N) \tag{6.4}$$

S/N is the required Signal-to-Noise ratio for further analysis.

6.2 Cosmic and Background Noise

Broadband noise comes from outer space in the form of plane waves. The antennas then always receive this noise if the directivity of the main or side lobes points to outer space. The noise results from our galaxy, the Milky Way, other galaxies, “Radio Stars and Clusters”, and from the Sun.

The antenna noise temperature T_{Ant} , which takes these noise contributions into consideration, can be calculated, with help from (6.5), by the convolution of the background temperature T_B with the squared directivity $C(\theta, \psi)$.

Figure 6.2 shows the convolution.

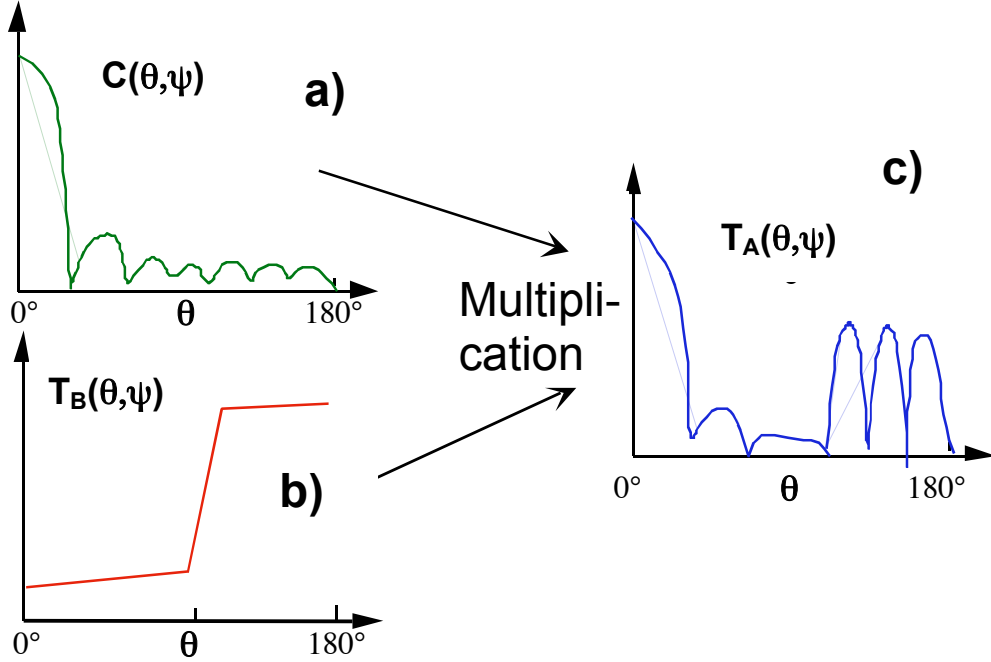


Figure 6.2 Noise contributions as a function of the elevation: a) Directivity, b) Noise temperature as a function of the elevation, c) Noise temperature of the antenna as a convolution of a) & b).

$$T_{Ant} = \frac{G}{4\pi} \oint_{4\pi} C^2(\theta, \psi) T_B(\theta, \psi) d\Omega \tag{6.5}$$

There are two interesting special cases. In the first case, only a slight variation of the background temperature T_B for varying θ and ψ in the main beam of the antenna is assumed. Then T_B can be taken as a constant factor for the integral in equation (6.5).

The remaining integral can be calculated with equation (6.7), with the acceptance of a high degree of efficiency ($G \approx D$), and with the utilization of equation (6.6):

$$G = \frac{4\pi}{\oint_{4\pi} C^2(\theta, \psi) d\Omega} \tag{6.6}$$

$$T_{Ant} = \frac{GT_B}{4\pi} \oint_{4\pi} C^2(\theta, \psi) d\Omega = T_B \tag{6.7}$$

The noise of extended sources can be described by the brightness B_C . The brightness B_C is defined as the noise power, which is received per unit of area (m^2), per bandwidth (Hz), and per solid angle $\Omega_B(rad)$.

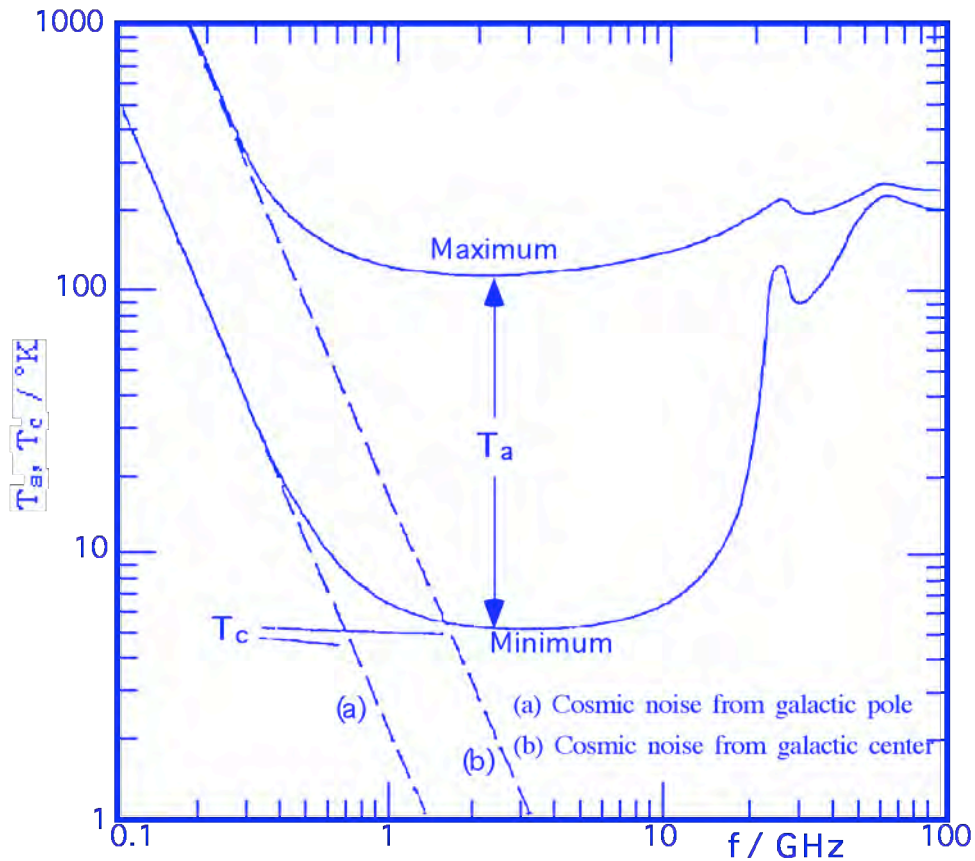


Figure 6.3 Noise temperature of outer space T_c in Kelvin (cosmic temperature, extended noise sources) seen from the earth for linear polarization, as well as the temperature of the atmospheric absorption noise T_a .

The brightness B_c is associated with the noise temperature T_B by the Rayleigh-Jeans Formula:

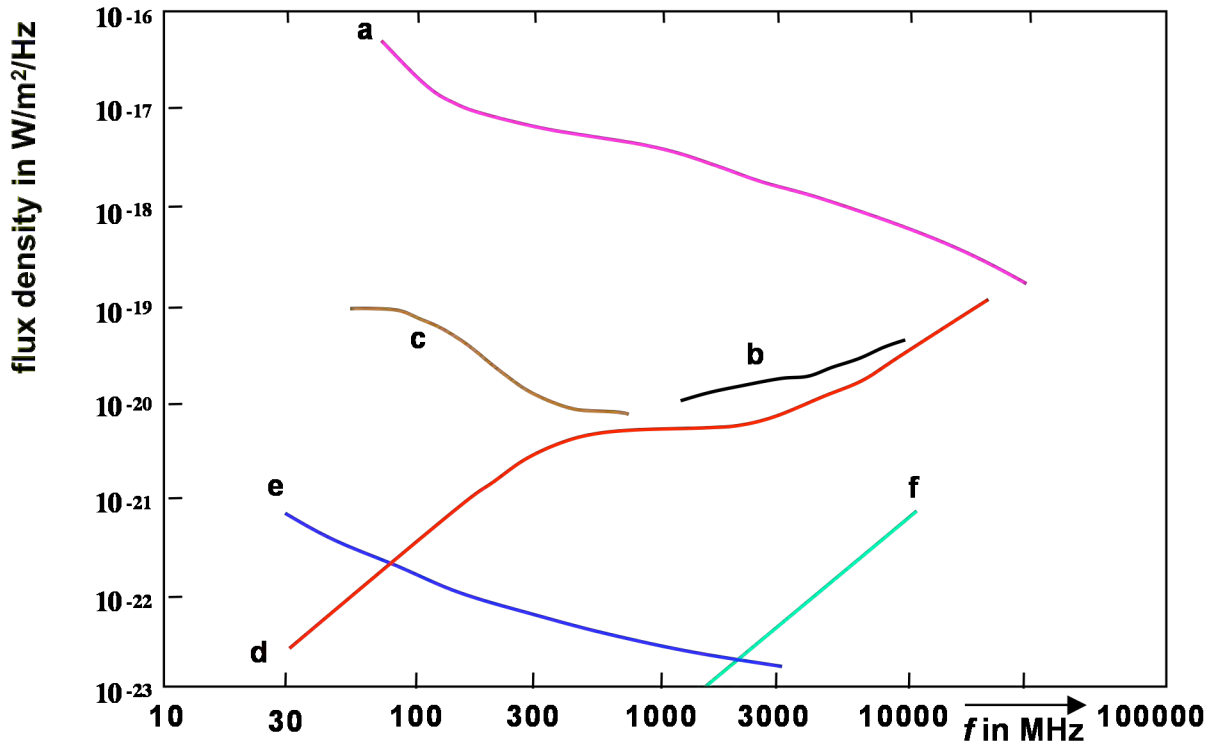
$$B_c = \frac{2kT_B}{\lambda^2} \frac{W}{m^2Hz \text{ Steradian}} \tag{6.8}$$

The second special case demonstrates a semi-discrete noise source of the temperature in a narrow area of the solid angle Ω_B . The background radiation is to be neglected. The equivalent solid angle of the antenna $\Omega_{Ant} = 4 \pi/G$ is $\gg \Omega_B$. By aligning the antenna to the noise source, the antenna noise temperature T_{Ant} can be calculated within good approximation according to equation (6.9):

$$T_{Ant} = T_B \frac{\Omega_B}{\Omega_{Ant}} \tag{6.9}$$

An example for such a discrete noise source is the sun $\Omega_H = 6,5 \cdot 10^{-5}(sr)$ (solid angle in steradian). The noise temperature of the sun lies in the frequency range from 2GHz at approximately $10\,000^\circ K$. With $\Omega_{Ant} = 0,08 \text{ sr}$ (from 22dBi) the antenna noise temperature results in $T_{Ant} = 8,2^\circ K$. Higher antenna noise temperature values T_{Ant} result from higher antenna gains.

For the Sun and the Moon the aspect angles from the Earth are approximately $1/2^\circ$ each. Figure 6.3 shows the Sun, Moon, and Cassiopeia.



- (a) Maximum peak intensities of enhanced solar noise
- (b) Region of solar slowly varying component
- (c) Region of solar noise storms
- (d) Solar thermal noise
- (e) Cassiopeia (radio star)
- (f) Moon

Figure 6.4 Noise from radio stars and bodies: Sun, Moon, and Cassiopeia.

The first case is for that reason the most interesting. When aligning the antenna to the sky, the resulting noise temperature is $T_{Ant} \approx 40^\circ K$ due to the cosmic background noise. When aligning the antenna along the Earth (in the direction of the horizon) the resulting noise temperature is around $200^\circ K$, i.e., the average from the “warm” Earth and the “cold” sky.

6.3 Atmospheric Absorption Noise

In a stationary condition all bodies, which absorb energy, re-radiate the same energy as noise power. This is the radiation theory of black bodies. Would this not be the case then some objects would warm themselves and others would cool themselves down. The transmitting power of the Radar will partially be absorbed by the atmosphere and will be re-radiated as noise. With absorption noise as a function of the surrounding temperature of the atmosphere $T_u = 260^\circ K$ and with the atmospheric attenuation L_a , the effective noise temperature T_a is as follows:

$$T_a = T_u(L_a - 1); \text{ where } T_u = 260^\circ K \tag{6.7}$$

L_a/dB	1,3	3	10
$T_a/^\circ K$	67	260	2340

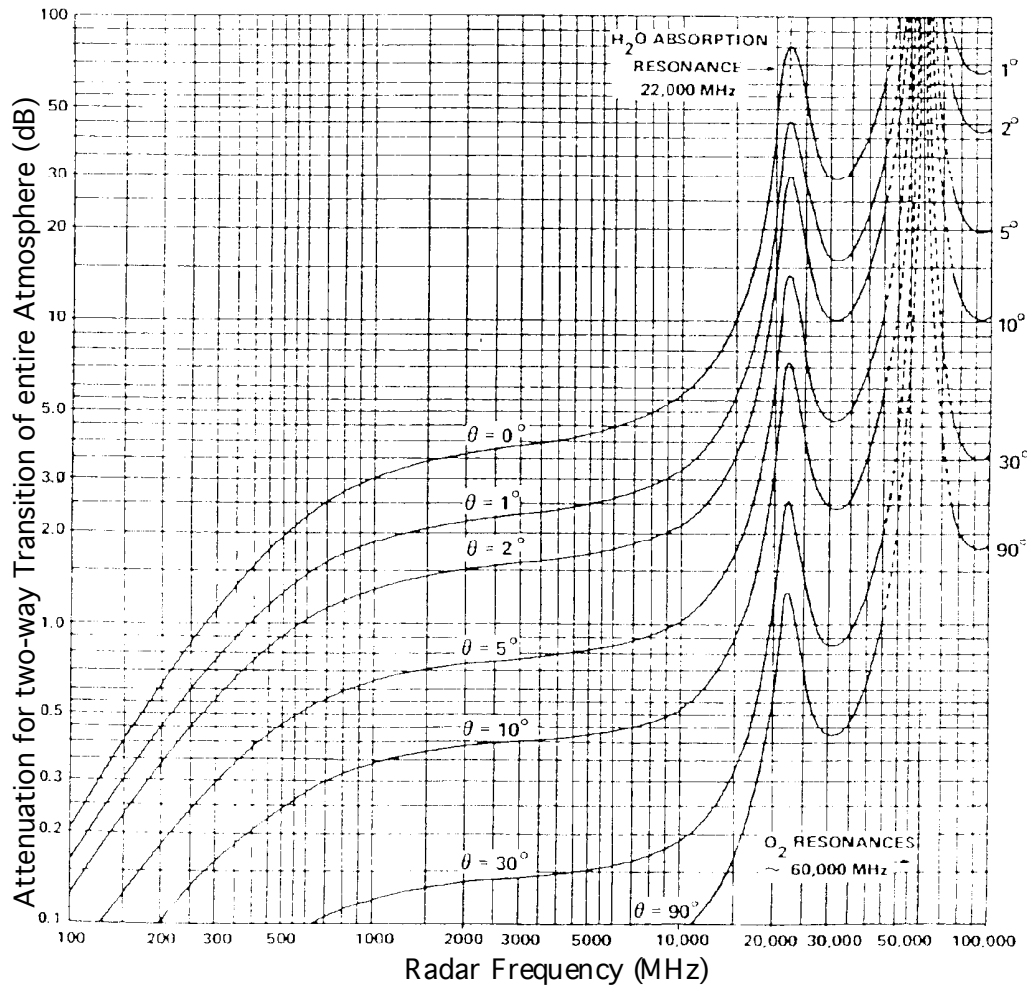


Figure 6.5 Two-way atmospheric attenuation.

Since the atmospheric noise rises with the attenuation, the maximum occurs for Earth-tangential radiation, the minimum for perpendicular radiation ($\Theta = 90^\circ$ in Figure 6.5). The atmospheric noise has a broad minimum between 1 and 10 GHz, within which the up-to-now chosen frequencies for Radar instrumentation for Earth exploration from outer space have also been defined. The two-way attenuation in the atmosphere is illustrated with the incident angle as a parameter in Figure 6.5. From this the atmospheric absorption noise can be computed directly.

6.4 System Noise Temperature

When calculating the system noise temperature all noise contributions, which are fed into the input stages of the antenna, must be considered according to power and without any phase correlation. Generally the contributions for system noise temperature can be divided into three groups:

Cosmic noise and atmospheric absorption noise,
 Increase of the noise figure due to losses and attenuation of the input systems
 (antenna, waveguide, switch, circulator, etc.),
 Effective noise temperature of the receiver (amplifier, mixer, etc.).
 Figure 6.6 shows the individual contributions with their identifiers.

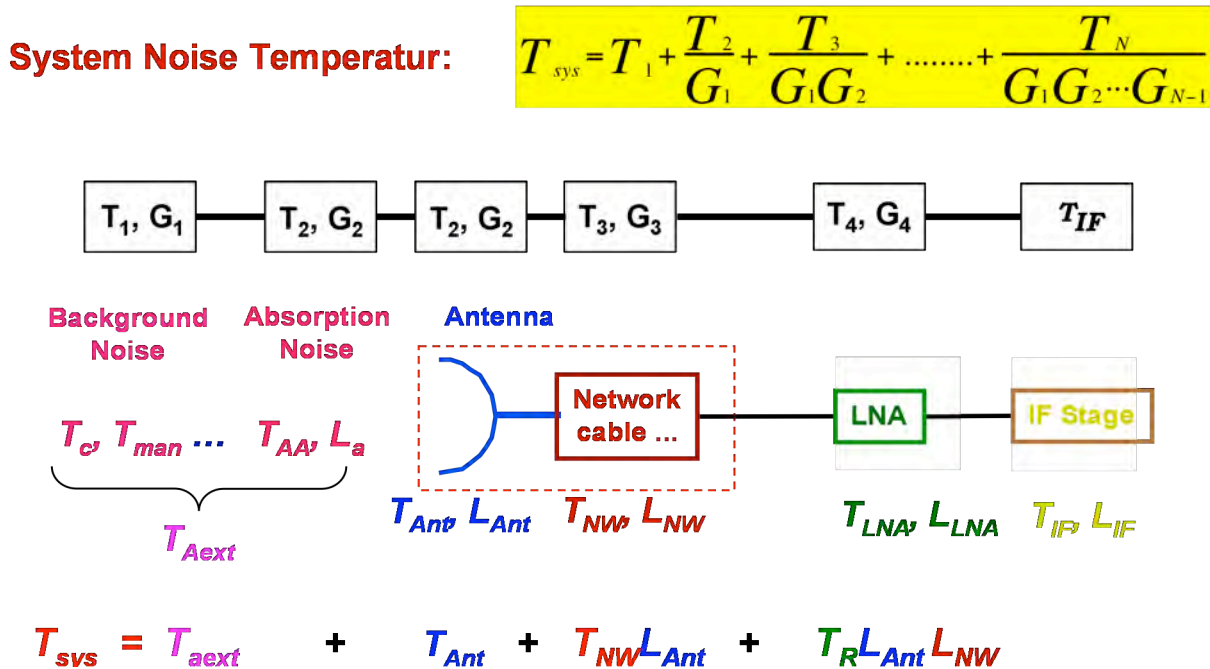


Figure 6.6 Contributions of system noise temperature

The noise temperature is calculated exactly as the noise figure as a contribution of the individual stages divided by the product of the gains G_i of all preceding stages i .

$$T_{ges} = T_1 + \frac{T_2}{G_1} + \frac{T_3}{G_1 G_2} + \dots + \frac{T_N}{G_1 G_2 G_{n-1}} \tag{6.10}$$

Here it is assumed that the respective entrance reflection factors are negligible.

$$T_1 = T_{Ant} \quad T_2 = T_a \quad T_3 = T_{RF} \quad T_4 = T_E$$

$$G_1 = 1 \quad G_2 = 1/L_a \quad G_3 = 1/L_{RF} \quad G_4 = V$$

With the identifiers from Figure 6.6 the following is obtained:

$$T_{total} = T_{Ant} + T_a + T_{RF}L_a + T_E L_{RF}L_a \tag{6.11}$$

The noise bandwidth B_N for white noise is not identical to the 3 dB bandwidth of the in-between frequency filters (IF bandwidth) B_{IF} . It can be calculated from,

$$B_N = \frac{\int_{-\infty}^{\infty} |H(f)|^2 df}{|H(f_0)|^2} \tag{6.12}$$

$H(f)$ = IF frequency channel & $H(f_0)$ = max of the IF filter curve.

In B_N it is considered that the noise through the HF and IF circuitry (especially the filter) will be weighted according to the frequency. Only for rectangular filters is B_N identical to the IF bandwidth B_{IF} . From the noise temperature T_{total} , one obtains the noise power:

$$N_{total} = k \cdot T_{total} \cdot B_N \tag{6.13}$$

6.5 False Alarm Rate and Probability of Detection

Since the received of a Radar signal is always distorted by noise, for the detection of Radar targets one can only make a compromise between a “false alarm rate” and the probability of detection. Crucial are the specifications of a detection threshold (figure 6.7), which are compared to the measured signal and it is determined whether the signal is to be interpreted as noise or as a target. The optimal threshold must be determined dependent upon the respective application. For example, a high threshold value leads to a small “false alarm rate”, however, at the same time leads to a reduced probability of detection.

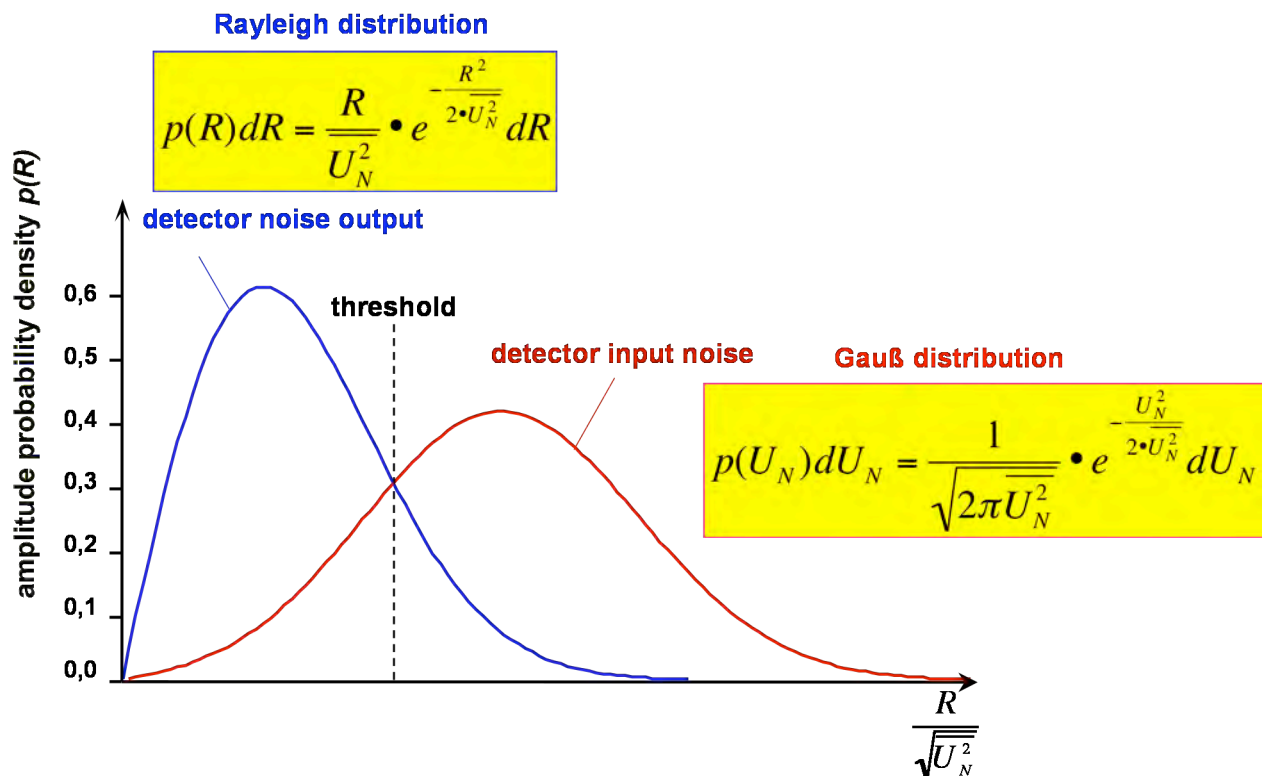


Figure 6.7 “False alarm rate” dependent upon the position of the detection threshold.

If one would like to obtain quantitative predictions dependent upon the threshold and upon the noise power density, then generally the probability density $p(U_N)$ of the noise voltage U_N is

accepted to be a Gaussian distribution. As shown in Figure 6.8, a probability density $p(R)$ of the noise envelope R , which is a Rayleigh distribution, is the result at the output of the video amplifier.

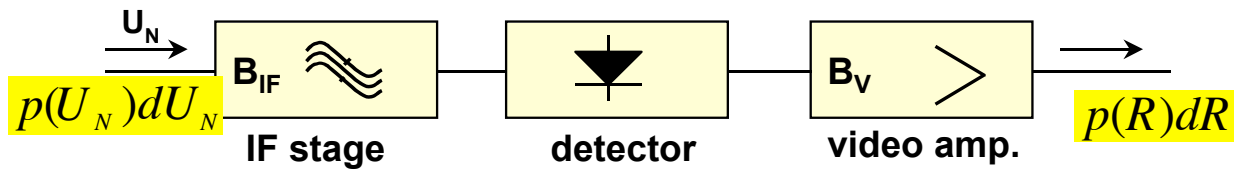


Figure 6.8 IF Stage, detector and video amplifier of a Radar.

If one now sets the threshold and calculates the probability with integration, so that the noise crosses the threshold, then the result is the false alarm rate P_{fa} .

$$p(U_T \leq R \leq \infty) = \int_{U_T}^{\infty} \frac{R}{U_N^2} e^{-\frac{R^2}{U_N^2}} dR = e^{-\frac{U_T^2}{2U_N^2}} = P_{fa} \tag{6.14}$$

The P_{fa} is shown in Fig 6.9. From equation (6.14), one obtains the time between two false alarms T_{fa} for various cases, which are shown in Figure 6.9

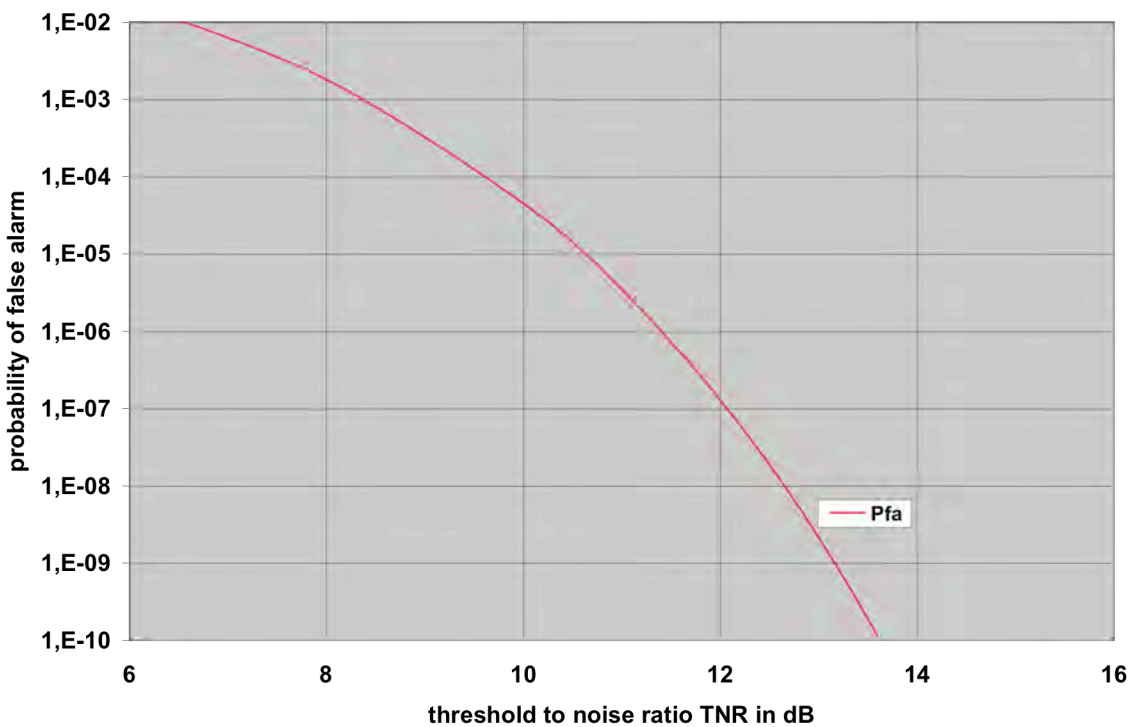


Figure 6.9 Probability of False alarm P_{fa} as a function of the detection threshold.

In a comparable approach for the detection of a distorted signal, the result is the curves in Figure 6.10.

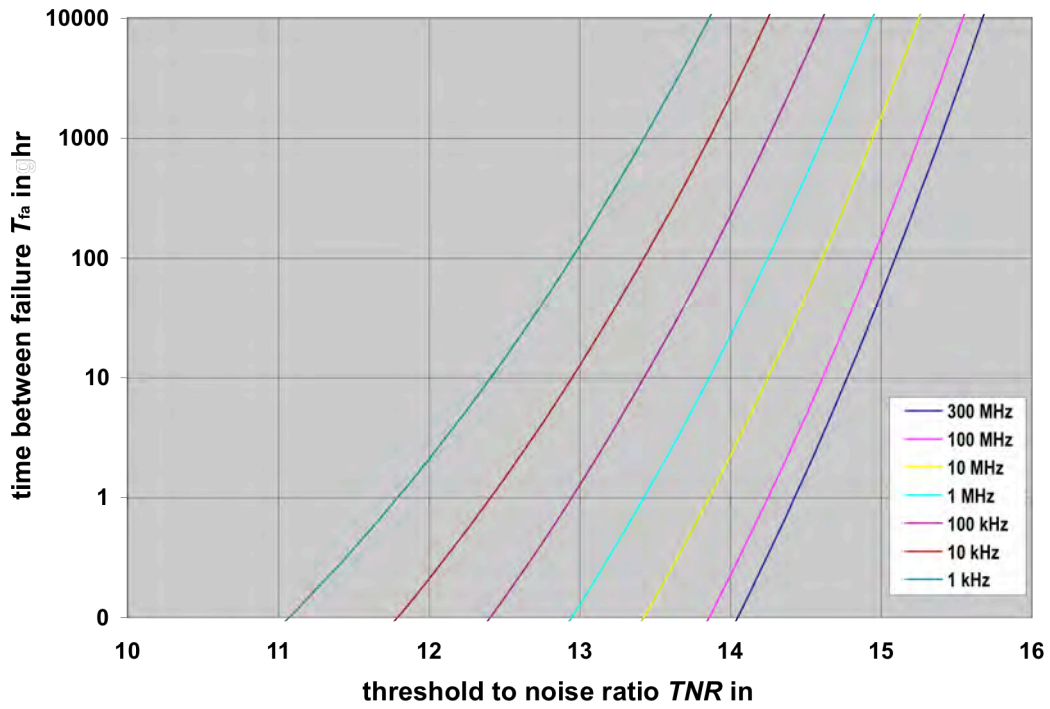


Figure 6.9 Time between failure T_{fa} as a function of the detection threshold.

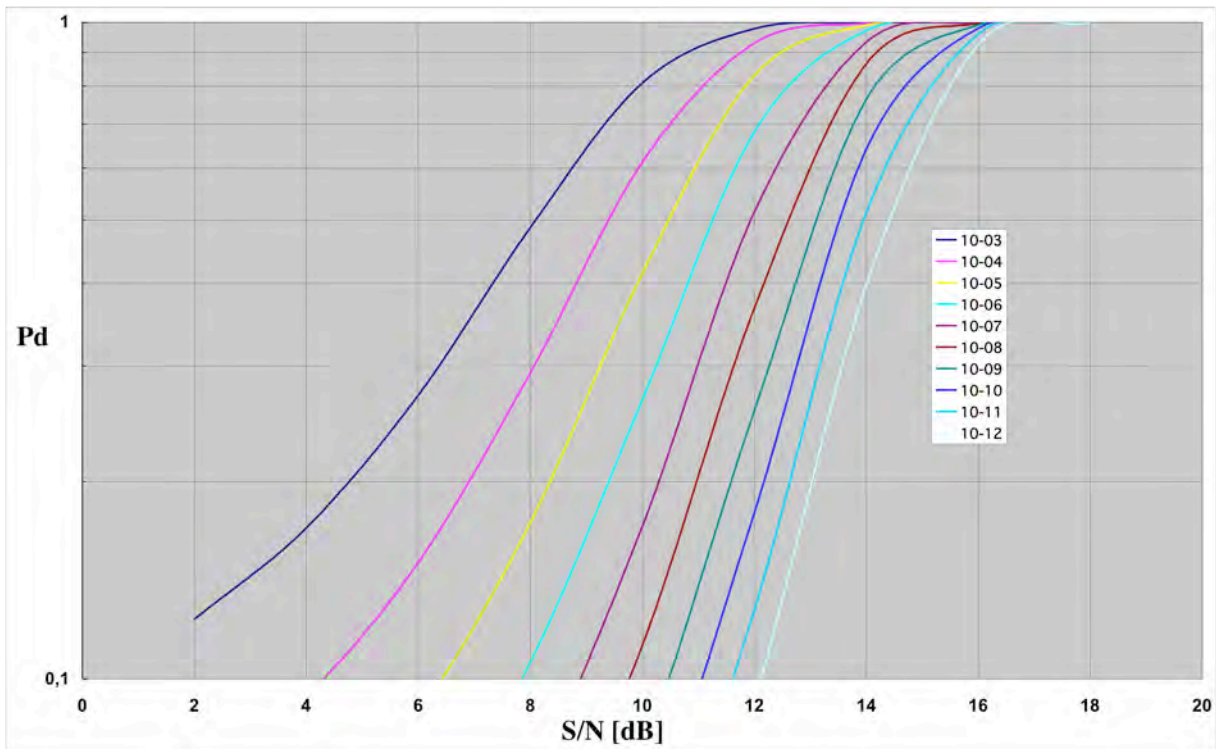


Figure 6.10 Probability of Detection P_d , as a function of the detection threshold.

6.6 Radar Detectors

In practice essentially two detector procedures are used, the envelope detector and the I/Q detector. The advantages of the envelope detector, illustrated in Figure 6.11, whose central element can, for example, exhibit a linear, a square or a logarithmic characteristic, lie in its simple feasibility.

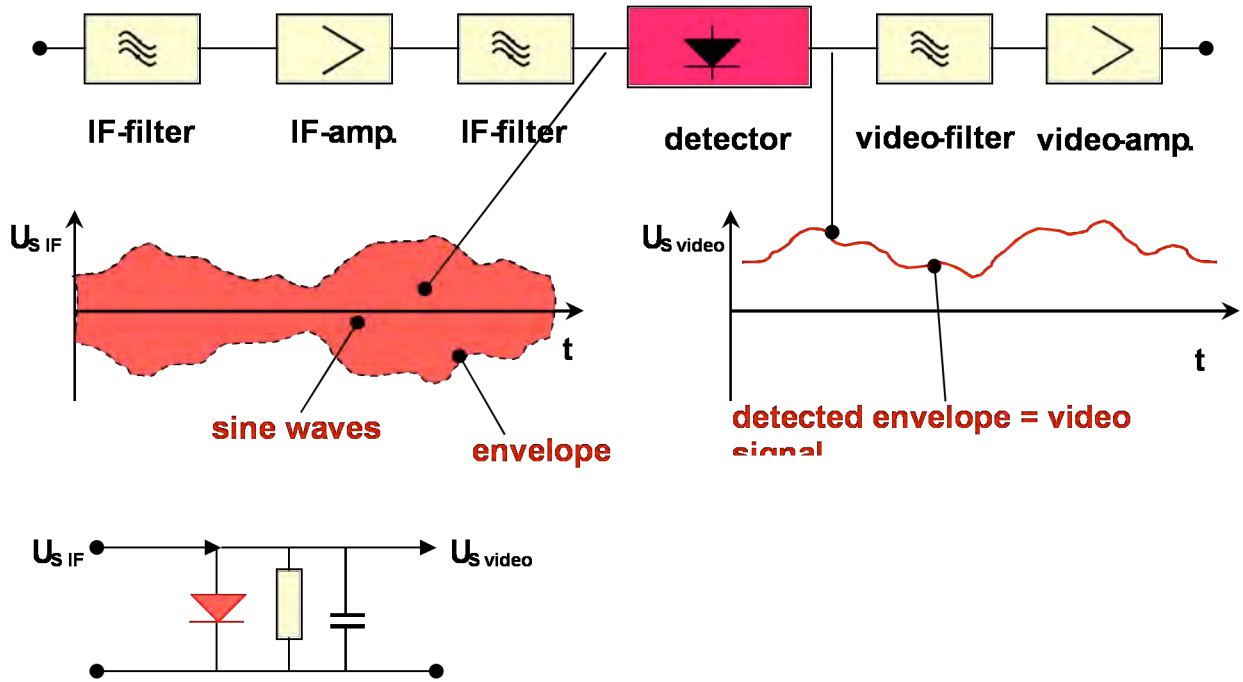


Figure 6.11 Receiver stages of a Radar with envelope detector.

- **square law detector:** $U_{s\ video} \sim (U_0 + U_{SIF} \cdot \cos \omega_{IF} t)^2 \sim 2U_0 U_{SIF}$
- **linear detector** $U_{s\ video} \sim U_{SIF}$
- **logarithmic detector:** $U_{s\ video} \sim \log(U_0 + U_{SIF} \cdot \cos \omega_{IF} t)$

By these simple detectors only the amplitude is preserved, the phase information is destroyed. The bandwidth of the video signal is $B_v = B_{IF}/2$. However, for this simplicity the phase information is destroyed if the Radar signal was coherent before. For coherent systems therefore the I/Q detector, shown in Figure 6.12, is available (see section 7.1.2).

The amplitude of the I/Q detector output is:

$$U_0 = \sqrt{I^2 + Q^2} = \sqrt{I^2 \cos^2 \varphi + Q^2 \sin^2 \varphi}$$

$$\varphi = \arctan \frac{I}{Q}$$

$$f = \frac{d\varphi}{2\pi dt}$$

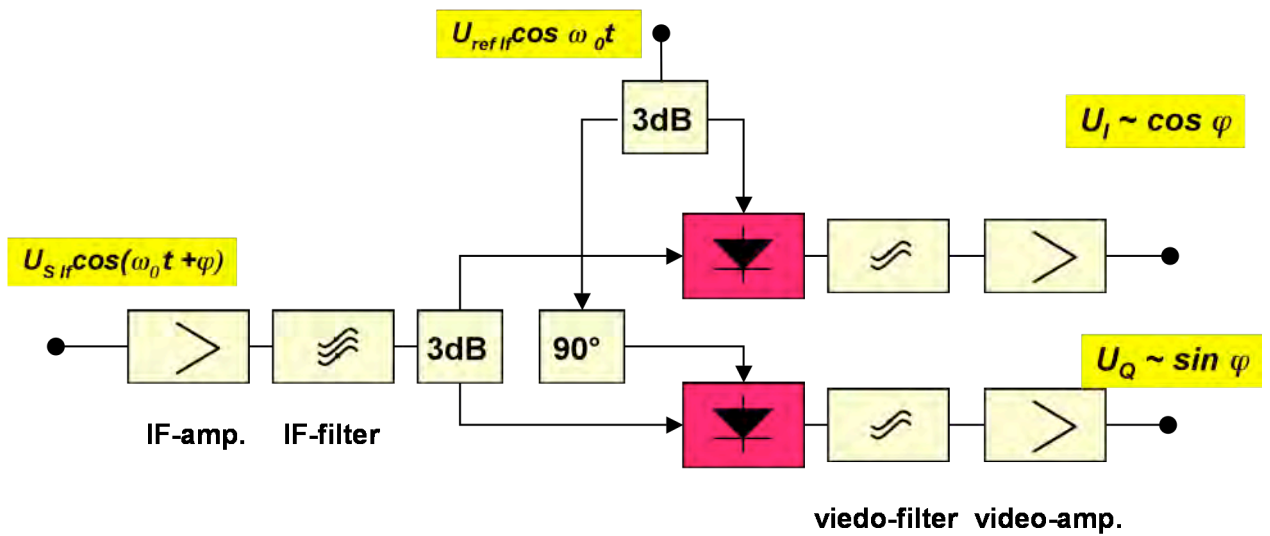


Figure 6.12 Receiver stages of a Radar of with I/Q detector.

7 CW- and FM-CW Radar

The CW (*continuous wave*) Radar continuously radiates with the power P_T . A reflective object leads to a receiving power P_R at the Radar. The relationship P_R/P_T amounts up to 10^{-20} . The small receiving signal becomes overlapped by the transmitting signal. The separation of transmitting and receiving antenna (a bistatic construction) yields to an insufficient uncoupling (e.g. 80 dB). 3 procedures have been developed, through which CW Radar can become operational:

- Measurement of the frequency modulation due to the Doppler Shift.
⇒ CW Doppler Radar, only moving targets,
- Measurement of the phase shift of the receiving signal.
⇒ Interferometry
- Frequency modulation of the transmitting signal.
⇒ FM CW Radar.

7.1 CW Doppler Radar

7.1.1 The Doppler Frequency

The Doppler effect is caused by a relative movement between Radar and reflecting objects, identical to acoustics when there is a velocity difference between hearer and the sound source (police car). The Doppler Frequency ω_D is calculated from:

$$\omega_D = 2\pi f_D = \frac{d\Theta}{dt} = \frac{2\pi}{\lambda} \frac{dr}{dt} = \frac{4\pi v_r}{\lambda} \tag{7.1}$$

$$f_D = \frac{2v_r}{\lambda} \approx 55,5 \cdot \frac{v_r(km/h)}{\lambda(cm)} (Hz) \tag{7.2a}$$

$$f_D = 1,85 f_T (GHz) v_r(km/h) (Hz) \tag{7.2b}$$

where λ is the wavelength and v_r is the radial velocity. Figure 7.1 shows a simple CW Radar schematic. One obtains the baseband around the zero frequency directly by mixing the oscillator and receiving signal. The lower frequency limit is critical with this method, since it determines the smallest measurable velocity. Additionally, the baseband is influenced by the FM noise of the oscillator and by the sensitivity to spot & flicker noise.

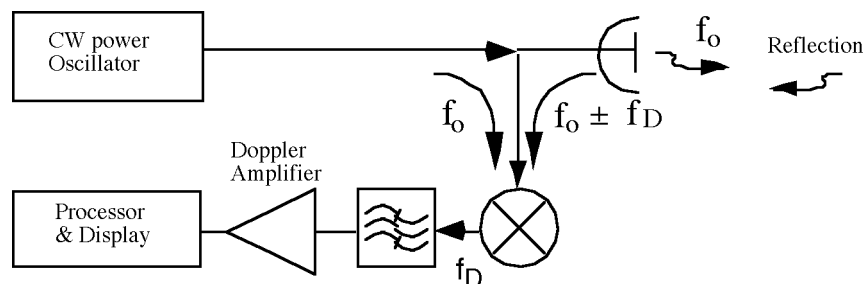


Figure 7.1 Block circuit diagram of a simple CW Radar.

The mixture on an IF Band in MHz range gives some relief, since the NF noise of the semi-conductors approximately decreases by $1/f$. Figure 7.2 shows an example for this.

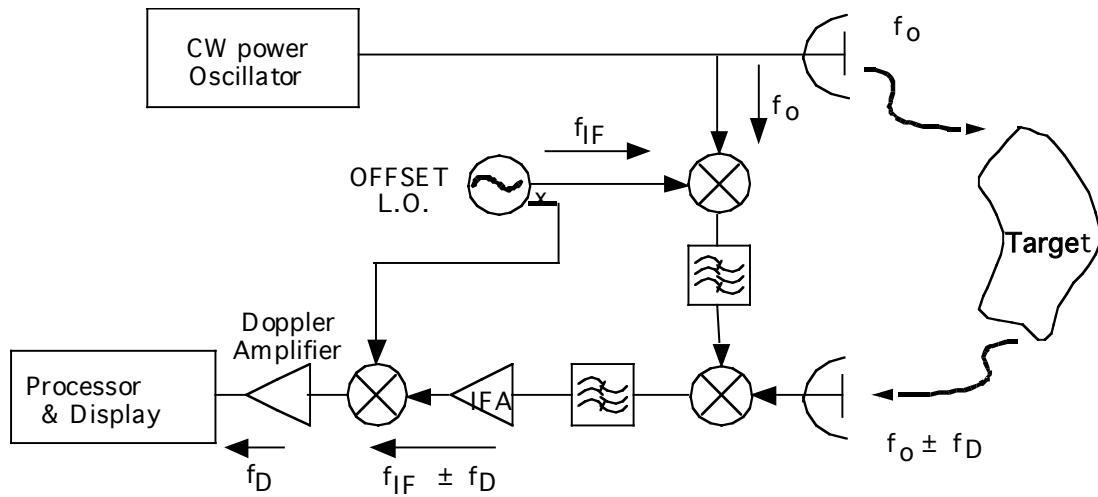


Figure 7.2 Block circuit diagram of Radar with IF.

For analyzing the velocity, the Doppler Frequency will be enumerated or filtered out by a filterbank. A typical Doppler signal is shown in Figure 7.3.

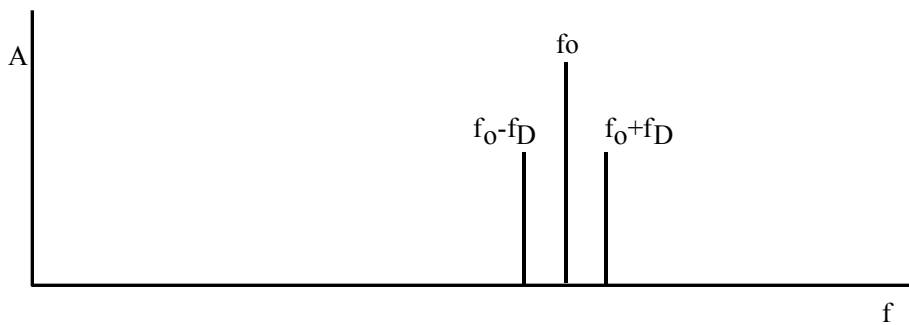


Figure 7.3 Typical Doppler signal of CW Radar.

7.1.2 Quadrature Modulation

Through the application of two mixers, which is practiced in quadrature modulation (phase difference of 90° for the oscillator), the sign (+/-) of the Doppler Frequency can be evaluated. A quadrature demodulator (I/Q-Demodulator) determines the allocation of the receiving signal, which is indicated with reference in-phase (I) or quadrature (Q) (meaning perpendicular), as shown in Figure 7.4.

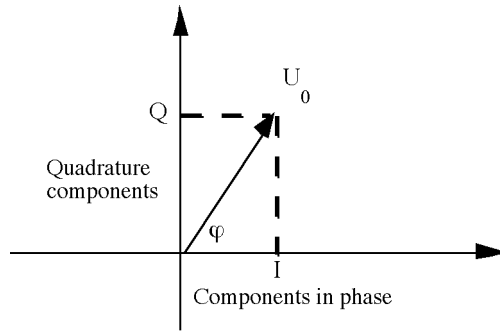


Figure 7.4 Quadrature signal.

From this, the parameters follow:

$$U_0 = \sqrt{I^2 + Q^2} \tag{7.3}$$

$$\varphi = \arctan \frac{Q}{I}$$

$$f = \frac{d\varphi}{2\pi dt}$$

For a departing object f_D is negative. The block diagram for a circuit for quadrature detection is shown in Figure 7.5

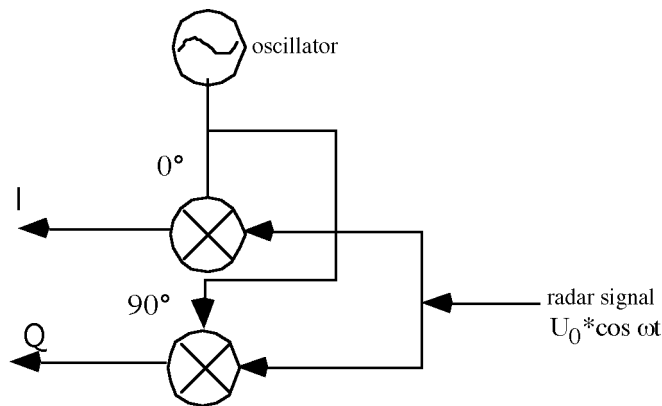


Figure 7.5 Quadrature demodulator

One obtains the same result if the receiving signal is fed into the two mixers with a phase difference of 90° .

7.1.3 Range Measurement with CW Radar

Range measurement with CW Radar is only possible over the range of the uniqueness of the signal (meaning the range $\lambda/2$), however, when in this range, quite exact. Thus CW Radar is suitably outstanding for position control and/or range measurement in automatic control engineering. As an example, the measurement of the wear of a brake disc of a passenger car is represented in Figure 7.6.

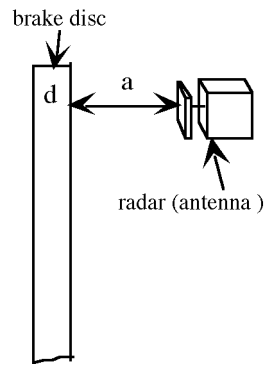


Figure 7.6 Distance measurement with CW Radar

The phase shift of the reflected wave received at the Radar amounts to:

$$\Delta\varphi = 2\pi \frac{2a}{\lambda_0} = 2\pi \frac{2(a_0 + \text{friction wear})}{\lambda_0} \quad (7.4)$$

Here is the a_0 initial setting. The phase measurement with a precision of 3° to 5° is quite possible. As an example, a sensor is regarded with 24 GHz, with which 5° correspond to the change in phase of a of distance variation of approximately $40 \mu\text{m}$. Thus the wear due to friction can be controlled very exactly.

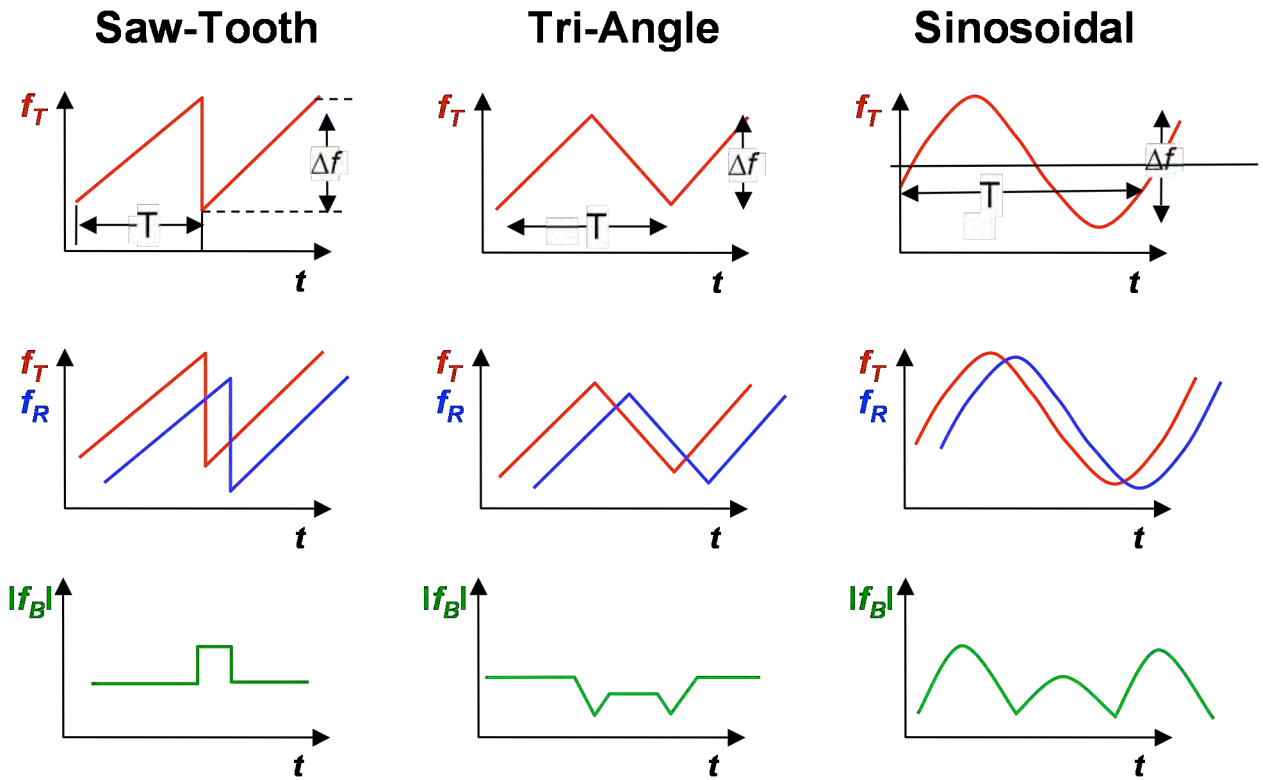
For the measurement of larger ranges and distances, an amplitude modulation (AM) can be modulated on the CW signal and for the analysis, the phase of the AM can be determined. The use of two or more sequential CW signals, with a frequency offset of Δf , is also possible (stepped frequency CW Radar).

7.2 FM CW-Radar

The simple CW Radar in section 7.1 is not in the position to clearly measure a range $>\lambda/2$ to an object, since referencing timestamps of any kind are not present over the entire signal. These timestamps can be generated through the frequency modulation of the transmitting signal. The result is FW CW Radar.

7.2.1 Range Measurement with FM CW Radar

In the early years of Radar technology simple modulation processes were selected, such as will be used for explanation and instruction in the following sections. Today, with the use of synthesizers, nearly any frequency process is possible. Figure 7.7 shows 3 examples.



$T = \text{Period}, \Delta f = \text{Frequency sample},$
 $f_T(t) = \text{Transmit frequency}$
 $f_R(t) = \text{Receiving frequency} = f_T(t - \tau) \pm f_D,$
 $f_B = \text{"Beatfrequency" (Mixeroutput)} = f_T - f_R$

Figure 7.7 FM CW modulation schemes.
a Sawtooth modulation, **b** Triangular modulation, **c** Sinusoidal modulation

The figure shows the transmitting signal in the upper lines, in the middle row the transmitting and receiving signals, and on the bottom the difference from both. The transmitting frequency is, as follows, time-dependent for the sawtooth modulation.

$$f_T = f_0 + \Delta f \cdot \frac{t}{T} \tag{7.5}$$

For the symmetric triangular modulation results in:

$$f_T = f_0 + \Delta f \cdot \frac{2t}{T} \tag{7.6}$$

In the following the sawtooth modulation will be further considered. During the run time $\Delta t = 2R/c_0$ for the signal to the target and back, the transmitting frequency is altered corresponding to Δt :

$$f_T = f_0 + \Delta f \cdot \frac{t + \Delta t}{T} \tag{7.7}$$

The mixing of the received signal with the current transmitting signal takes place in the Radar receiver. From this the result is, among other things, the difference frequency f_B , also known as the “beat frequency”:

$$f_B = (f_0 + \Delta f \cdot \frac{t + \Delta t}{T}) - (f_0 + \Delta f \cdot \frac{t}{T}) = \Delta f \frac{\Delta t}{T} \quad (7.8)$$

The range R follows from this:

$$R = c_0 \cdot \frac{f_B}{2\Delta f} \cdot T \quad (7.9)$$

The beat frequency is proportional to the target range R. More complex frequency processes can be calculated analogously.

7.2.2 Range Resolution with FM CW Radar

The measurement period t_{meas} and the utilized bandwidth Δf are crucial for the range resolution. For targets, for which $\Delta t \ll T$ applies, nearly the complete period is available for the measurement:

$$t_{meas} \approx T \quad (7.10)$$

Two targets with the ranges R_1 and R_2 have a difference in frequency of:

$$\Delta f_B = |f_{B1} - f_{B2}| = \frac{2\Delta f}{c_0 T} \cdot |R_1 - R_2| = \frac{2\Delta f}{c_0 T} \cdot \Delta R \quad (7.11)$$

From the measurement period T comes the minimum resolvable beat frequency $f_{B \min} = 1/T$. Thus the result is the minimum range resolution:

$$\Delta f_{B \min} = \frac{1}{T} = \frac{2\Delta f}{c_0 T} \cdot \Delta R_{\min} \Rightarrow \Delta R_{\min} = \frac{c_0}{2\Delta f} \quad (7.12)$$

This is inversely proportional to the bandwidth. For this purpose, the target must be analyzed throughout the entire frequency pass. A reduction of the measurement period reduces the resolution. In practice a degradation of nearly 30% can be expected:

$$\Delta R_{\min} = 1,3 \cdot \frac{c_0}{2\Delta f} \quad (7.13)$$

The maximum range R_{\max} determines the period duration. The signal duration $\Delta t = 2R_{\max}/c_0$ must be considerably smaller than the period T , since the resolution, as shown above, will otherwise not be reached:

$$T \gg \frac{2}{c_0} \cdot R_{\max} \quad (7.14)$$

For the determination of the S/N , the proper bandwidth is the Radar bandwidth Δf .

The precision will be determined by the frequency counter for f_B , the linearity of the pass, and by the run-time errors in the Radar equipment & during the signal propagation. The required transmission powers are small because of the length of the analysis time. FM CW Radar in-

strumentation is very often employed for the altitude measurement of airplanes, helicopters, and balloons. In recent years they have also dominated the automobile Radar sensors market. A superimposed Doppler signal f_D increases the IF-frequency (beat frequency) f_B when the target is approaching (up-ramp) while decreasing it when the target is departing (down-ramp). With Figure 7.8 this is demonstrated for an approaching target using triangular modulation.

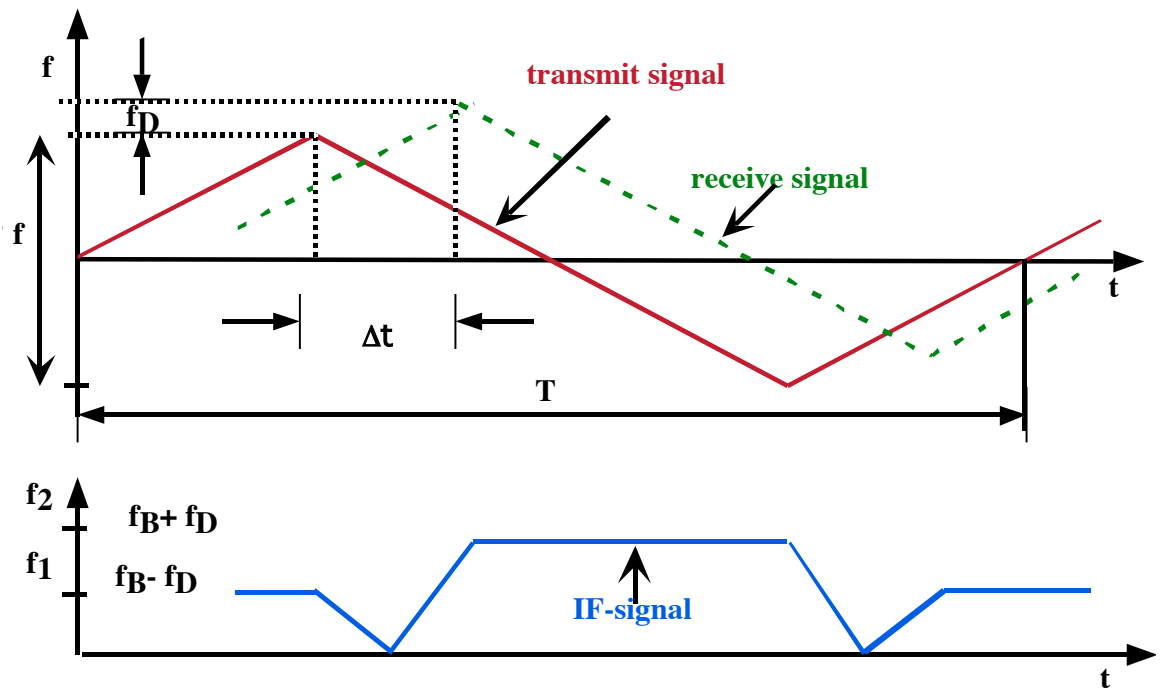


Figure 7.8 Triangular modulation with superimposed Doppler. Doppler frequency = f_D , beat frequency = f_B , frequency pass = B , period duration = T .

Both pieces of information, range and velocity, can be simple separated after the determination of f_1/f_2 from the IF signal.

$$f_B = \frac{1}{2}(f_2 + f_1) ; f_D = \frac{1}{2}(f_2 - f_1) \tag{7.15}$$

A typical FM CW Radar instrument is demonstrated in Figure 7.9. The frequency modulation is triangular in form. The Radar has separate transmitting and receiving antennas. On the reception side a low-noise pre-amplifier (LNA) is built in. The IF signal is converted to base-band with an I/Q demodulator. Typical IF frequencies are anywhere between 500 kHz and 10,7 MHz.

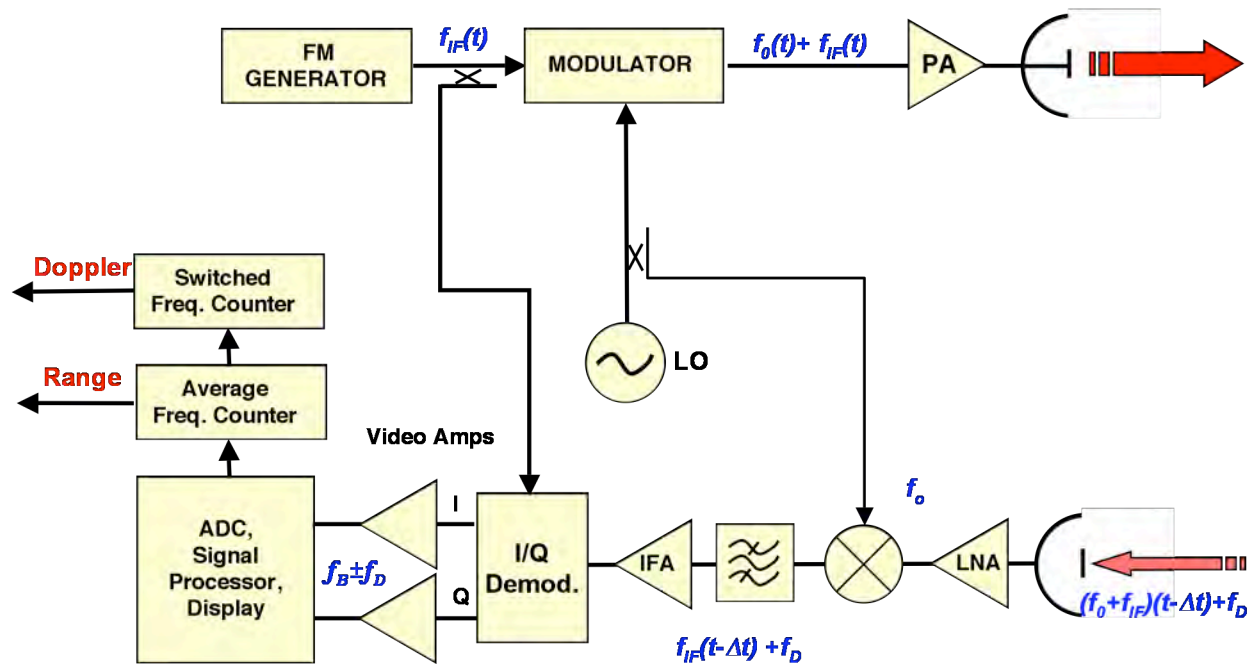


Figure 7.9 FM CW Radar system – block diagram

Figure 7.10 shows a microwave door opener, which has become implemented as CW Doppler Radar.

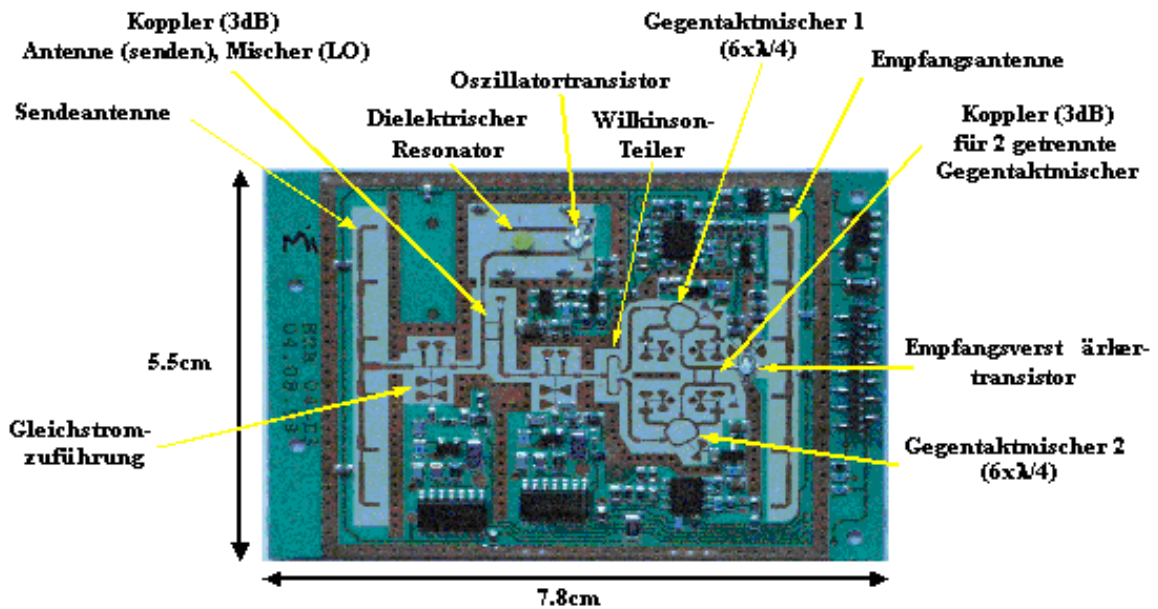


Figure 7.10 Microwave door opener: 24 GHz CW Doppler Radar.

8 Pulse Radar

8.1 The History of Pulse Radar

The first pulse Radars had a very low pulse repetition rate. On one side, one could not create a higher pulse rate and on the other side, one could not process it. After the Second World War the pulse repetition rate could be incrementally increased as much as the demanded, unique range of coverage permitted. The until today valid fundamentals of pulse Radar technology had been laid down by Colonel Blair of the US Signal Corps in a patent from 1938.

8.2 Transmission Types of Pulse Radar

Pulse Radar instruments can, in principle, be divided into four categories, of which however, not all are suitable for each application. The subdivision takes places once after the existence of the phase preservation between the transmitting and receiving signal according to:

- Coherent Radar (phase preservation),
- Incoherent Radar (arbitrary phase from pulse to pulse),

as well according to the pulse repetition frequency $PRF = f_p$:

- Low PRF (< 1000 Hz),
- High PRF (> 30000 Hz).

In Figure 8.1 the various transmission types in the time and frequency domain are represented. Figure 8.1a shows a simple CW Radar instrument in the time and frequency domain. A moved target shifts the line in the frequency domain for the receiving signal of f_0 to $f_0 + f_d$. At the output of the mixer one obtains:

$$\pm f_d = f_s - f_E \quad (8.1)$$

With pulse Radar the behavior is different. Figure 8.1b demonstrates time and frequency domain for Radars with low PRF:

$$f_p = 1/T \quad (T = \text{Period}) \quad (8.2)$$

The pulse duration is until today, in most cases, considerably larger than the period duration of the microwave carriers. Through pulse modulation, a signal of duration τ and periodic in cycle to the PRF will be sent from the microwave carrier. With the Fourier transform of the envelope of the pulses, an envelope of the spectrum results in the frequency domain. For a rectangular pulse the result is the $\sin x/x$ function in the frequency domain. The linear spacing is reciprocal to the period T . Additional, Doppler shift superimposes with $\pm f_d$.

Coherent Radar devices could be developed only after accurate phase preserving high-gain amplifiers were available. Today the transmission signal is usually derived from quartz crystal and/or from synthesizers. The nonlinear distortions of the available amplifiers can be usually neglected. In Figure 8.1d the signals in the time and frequency domain for non-coherent pulse

Radar are represented. Since there exists no phase reference from pulse to pulse, the signal is spread and/or “smeared” over the spectrum. The envelope of the spectrum is determined through the Fourier transform of the pulses.

A low PRF (Figure 8.1b and 8.2) allows a large unambiguous range of coverage, however this leads to a very small unambiguous range of the Doppler frequency due to the dense linear frequency spacing in the spectrum, i.e. ambiguities in the Doppler frequency develop if f_d becomes $> 1/T$. By higher PRF, as shown in Figure 8.1c, the opposite problem of unambiguity in the range to target exists, since the period duration $\Delta t_{max} = T = c_0/2R_{max}$ is very small, while the Doppler frequency is now unambiguous over a large velocity range. In Figure 8.3 are represented the spectra of the enlarged transmission and receiving signals.

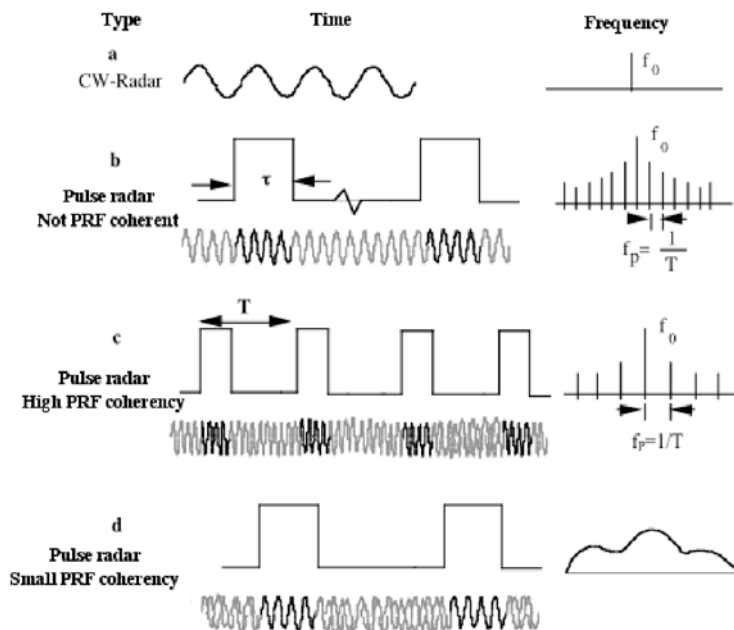


Figure 8.1 Transmission types - Pulse Radar.

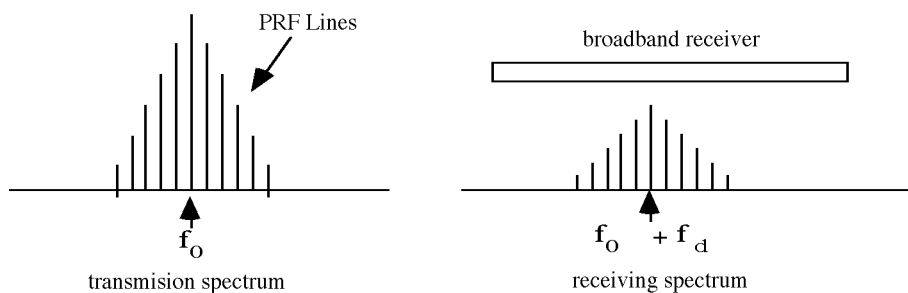


Figure 8.2 Transmitting and receiving signals with low PRF.

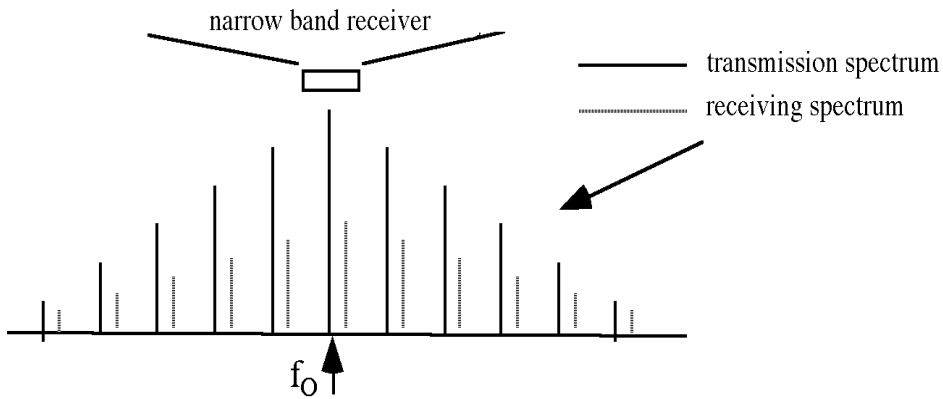


Figure 8.3 Transmission and receiving spectrum with high PRF.

The details of the respective fundamental principles will be discussed following.

8.3 Simple Pulse Radar

The problem associated with CW Radar devices regarding the de-coupling from transmission path to reception path is solved by pulse Radar through the temporal separation of transmission and reception. For the suppression of very strongly cross-talking transmission pulses into the receiving system, the receiver input is short-circuited or decoupled by a circulator. Figure 8.4 shows a typical, simple pulse Radar system. To produce the pulses either magnetrons or switched amplifiers are employed. There is no reference from the transmission oscillator to the receiver, therefore non-coherent pulse Radar cannot measure Doppler and thus only the distance and not the speed of a target can be determined.

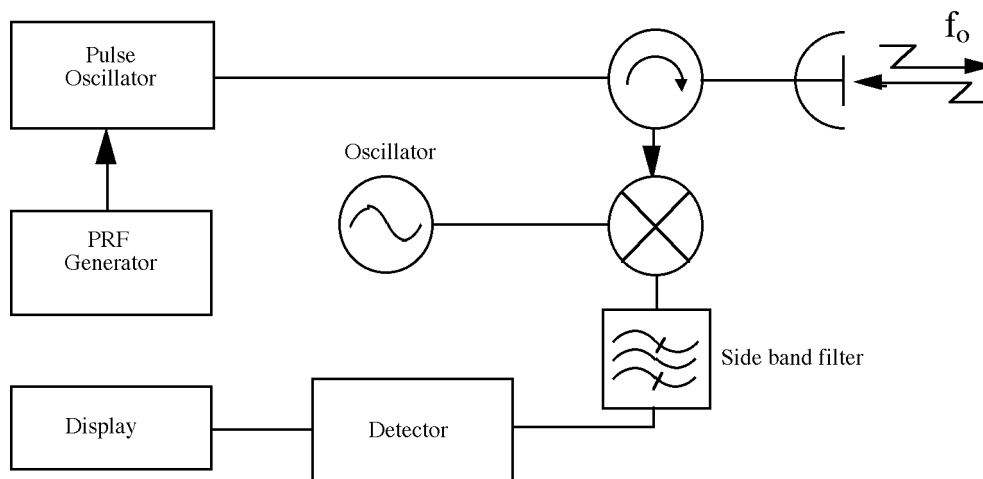


Figure 8.4 Simple, non-coherent Radar.

8.4 Coherent Pulse Radar

Coherent pulse Radar is in the position to deliver information regarding the range as well as Doppler information, i.e. the velocity and/or speed of an object. Here a coherent oscillator (COHO) is introduced on the transmission side, which also delivers the phase reference for the receiving signal. The transmitting oscillator (LO for Local Oscillator) is added on the transmitting end and is again taken out at the receiving end. In comparison to the Doppler frequency, which can be measured, both oscillators must be sufficiently stable for the entire time. In Figure 8.5, an example of coherent pulse Radar, a quadrature modulator is employed to additionally determine the direction of the target movement.

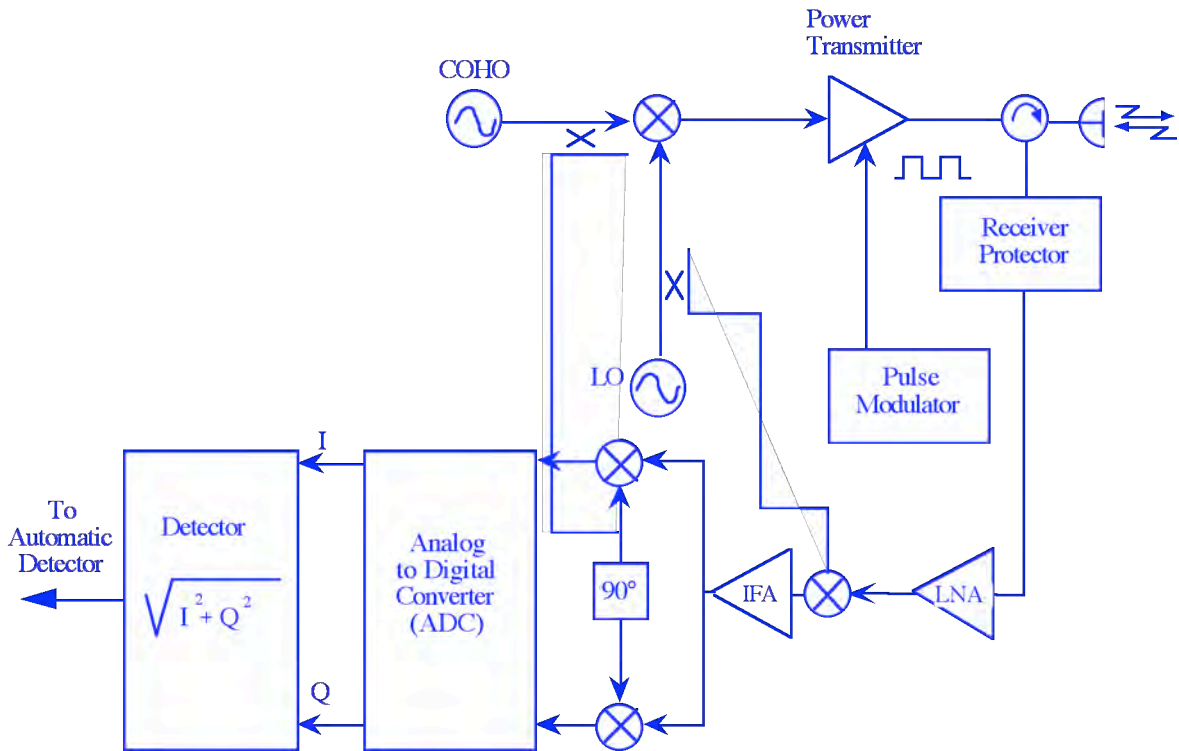


Figure 8.5 Coherent pulse Radar.

Two various fundamental methods of Doppler analysis are known and will be subsequently and shortly introduced. [7].

The transmitting signal for pulse Radar is:

$$U_s = A_s \sin \omega_0 t \tag{8.3}$$

The reference signal:

$$U_{ref} = A_{ref} \sin \omega_0 t + \varphi_{ref} \tag{8.4}$$

$\varphi_{ref} = \text{constant}$, e.g. $\varphi_{ref} = 0$. The receiving signal from a target at range R becomes:

$$U_E = A_E \cdot \sin \left[(\omega_0 + \omega_d) t - \frac{2\omega_0 R}{c} \right] \tag{8.5}$$

After combining one obtains:

$$U_{diff} = U_d = A_d \cdot \sin\left[2\pi f_d t - \frac{4\pi f_0 R}{c}\right] \tag{8.6}$$

By demonstrating a video signal at the indicator it is possible to distinguish two cases:

$$\begin{aligned} f_d &> 1/\tau \\ f_d &< 1/\tau \end{aligned} \tag{8.7}$$

From which the illustrations according to Figure 8.6 result.

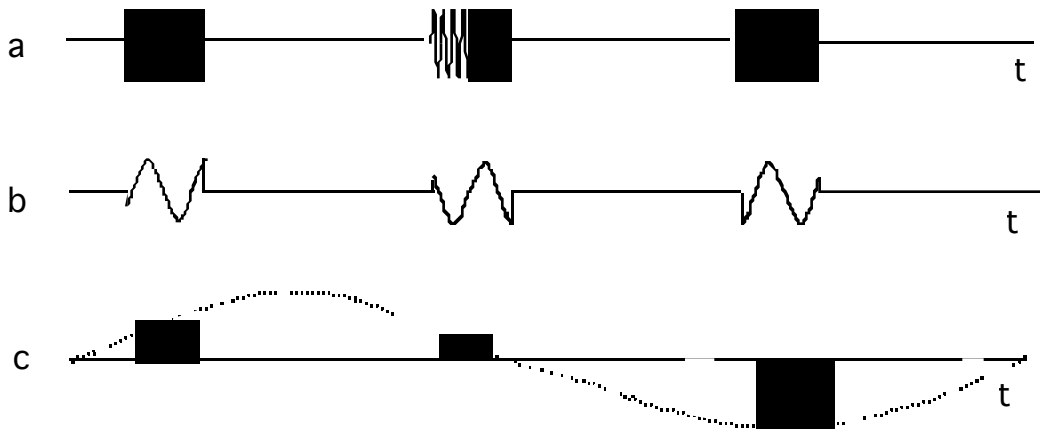


Figure 8.6 a) Transmitting signal b) Video signal $f_d > 1/\tau$, c) Video signal $f_d < 1/\tau$.

The pulsing is identical to a sample of the Doppler oscillation. For uniqueness the sampling theorem must be fulfilled, meaning at minimum each half period of the Doppler oscillation must be sampled.

$$PRF = \frac{4 \cdot v_{max}}{\lambda_0} \tag{8.8}$$

The resolution is a result of the observation period, meaning of the number of the used sample values N_{FFT} of the Fourier transform.

$$\Delta v = \frac{\lambda_0 \cdot PRF}{2N_{FFT}} \tag{8.9}$$

One speaks about blind frequencies for the phase differences between the transmitting and receiving signal of $\pm n2\pi$. For blind frequencies $f_d = n \cdot \frac{1}{T} = n \cdot f_{blind}$ results in a non-detectable Doppler frequency.

Figure 8.7 Blind speed.

8.5 MTI Radar (Moving Target Indication)

Moved or shifted targets can be detected in many ways and with many methods and particularly due to:

- Doppler shift
- Range change from scan to scan
- Direction change from scan to scan

At first glance it is not therefore so necessary to integrate the elaborate Doppler signal processing. In practice it is however so that the echoes from moved targets are not received alone, but are rather surrounded by clutter, the echoes of all the reflecting objects found in the resolution region. This clutter mostly masks the echoes of moved objects. By analyzing the Doppler shift, targets, which lay 20 – 30 dB under the clutter level, can be discovered and selected. There are even examples for the detection of signals smaller by 70 - 90 dB. Circuits, which distinguish these echoes of moved targets from the clutter, are designated as Moving Target Indicators (MTI).

8.5.1 MTI with Delay-Line Cancellor

By being given a video signal of a pulse Doppler Radar on a display terminal with sweep (A-Scope) according to Figure 8.8c and then successively representing the echoes of the following pulses, then one can obtain the curves a-e in Figure 8.8. If one uses a display terminal with memory and “writes” the echoes on top of one another, then one obtains Figure 8.8Σ. Fixed targets deliver constant echo amplitudes, while moving targets deliver sine-shaped amplitudes as in Figure 8.8c.

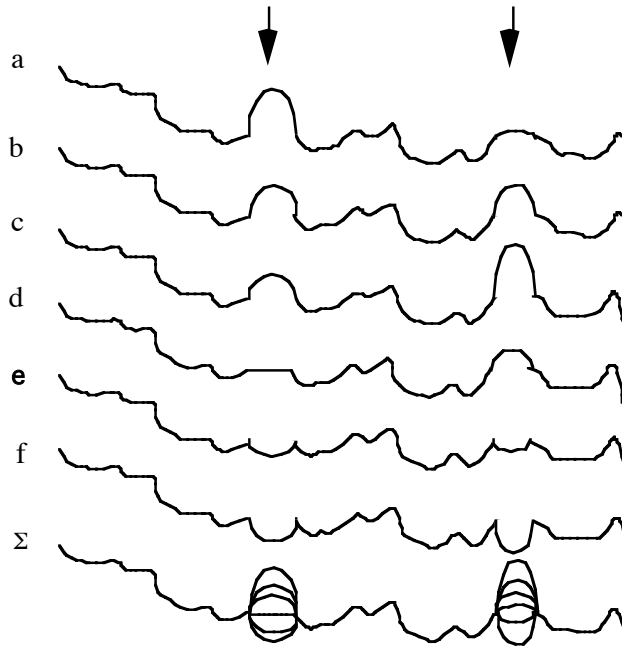


Figure 8.8 Time behaviour of moving targets (↓) on an oscilloscope.

For automatic analysis the fact that fixed-target echoes are constant from pulse to pulse is used. Bipolar video signals are separated into two channels, from which one is delayed by the pulse duration $T = 1/f_p$. Then both are subtracted. The procedure is illustrated in Figure 8.9.

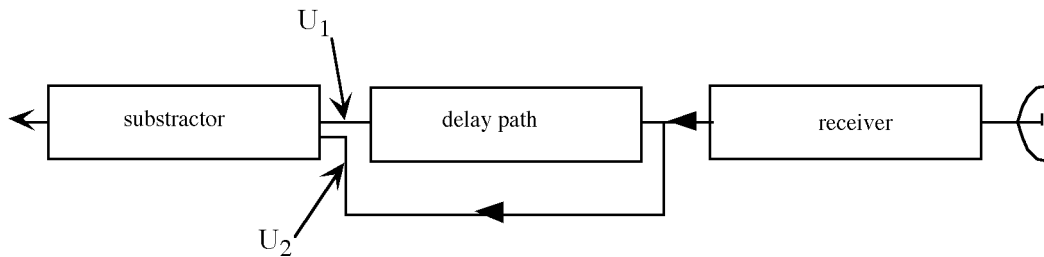


Figure 8.9 MTI with Delay-Line Cancellor.

The output of the subtractor can be utilized for the brightness modulation of a PPI scope (Plane Position Indicator). The delay time is equal to the period T of the signal. With electromagnetic waves the necessary delay times within the $\mu s - ms$ range cannot be reached. Instead one converts the signal into an acoustic wave and thereby achieves a larger delay time around a factor of 10^5 . For some years digital delay methods have been used in addition to the analog methods. The signal is sampled and read into a shift register. The “range gates” determine the cycling (see section 8.6). Examples for MTI Radar and Delay Line Cancellers are shown in Figures 8.10 and 8.11. A single Delay Line Cancellor shows a sine characteristic for the suppression of the clutters. If one sets two Single Delay Line Cancellers one behind the other, then a squared sine characteristic results. In continuation, all well-known filter structures (Butterworth, Chebyshev, Bessel, Elliptical, etc.) can be realized. In addition the MTI

function can be obtained on the IF side. The equations from above apply with the substitution $\omega_d \rightarrow \omega_{ZF} \pm \omega_d$. Good circuits suppress fixed targets to 1% (voltage).

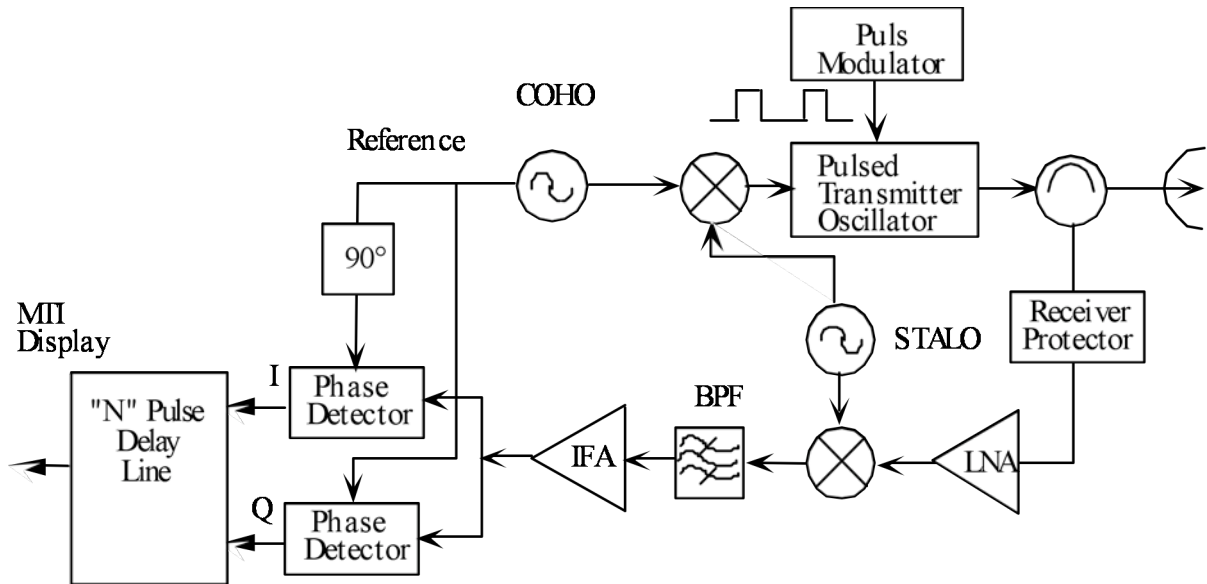


Figure 8.10 Block diagram of MTI Radar.

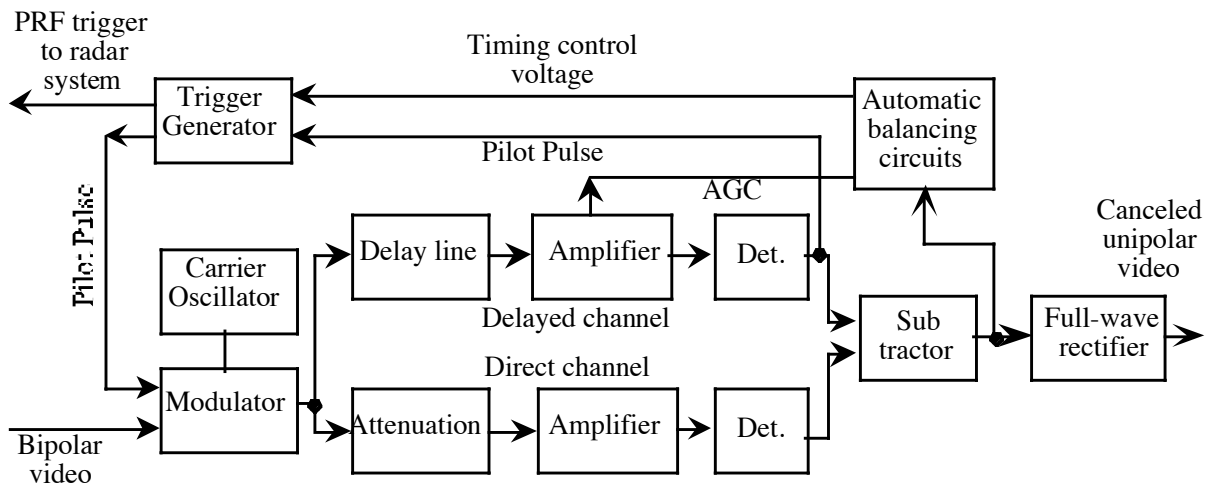


Figure 8.11 Block diagram of a Delay Line Canceller.

8.6 Filterbank Procedure

Here, identified as the filterbank analysis procedure, digital signal processing was quickly developed and put to use. Range and Doppler frequency regions are divided into sub-regions, which are processed separately. Figure 8.12 shows this division into sub-regions for the range.

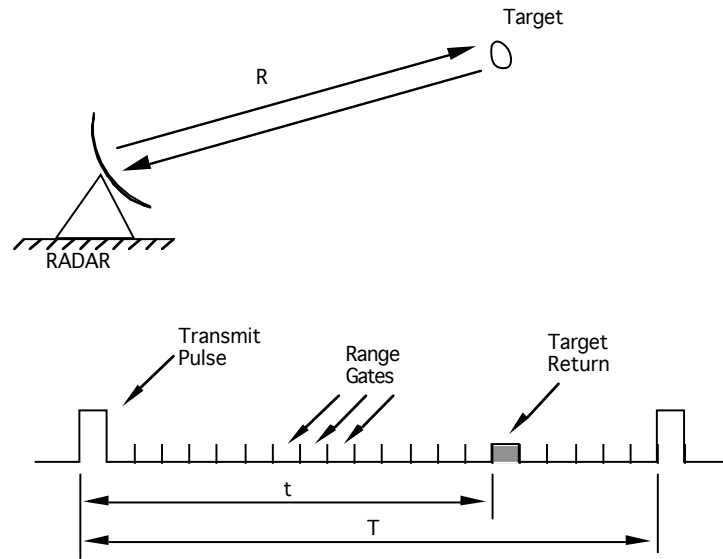


Figure 8.12 Range sub-regions of pulse Radar (range gates).

The earlier "range gates" were digitally switched analog paths. The Doppler frequency is similarly subdivided into frequency regions. A block diagram of the entire arrangement is shown in Figure 8.13.

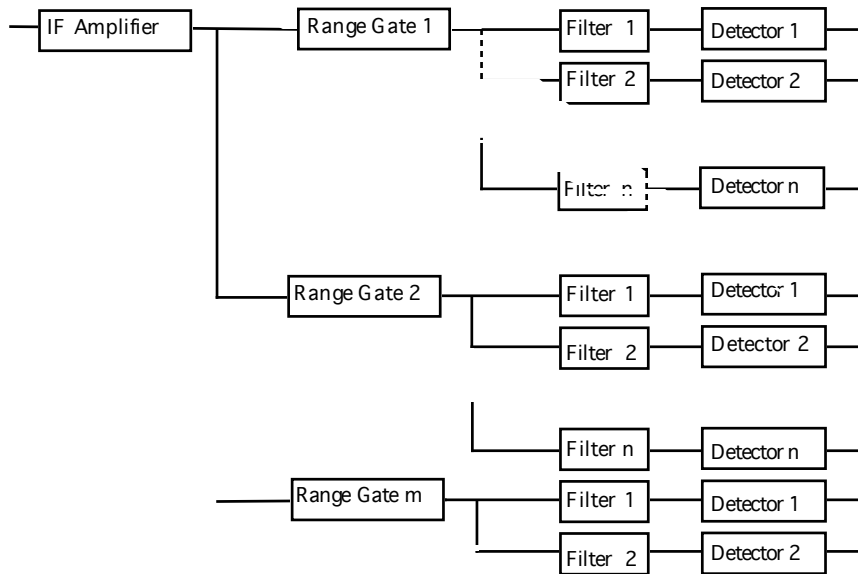


Figure 8.13 Range gates and Doppler filter arrays.

The false alarm rate with this procedure is considerably lower than MTI with delay line cancellation because of the low bandwidth of the filter. With new devices the video signal (bipolar) is sampled and processed by computer. Here, the Fourier transform replaces the filter.

8.7 Impulse Integration for Increasing the Sensitivity

With all Radar devices, which are not agile from pulse to pulse, several pulses are reflected from a target with each sample instance. One identifies the summation of all pulses from a target as integration. The detection becomes even better the more reflected energy from the target is received and integrated. From the Radar equation possibilities for an apparent energy increase can be seen. They each exist only for only one pulse. In this section the dwell time for a target will also be considered. It results in the hits per scan n_B and depends on the following:

- Pulse repetition rate f_p [Hz],
- Half-power bandwidth of the antenna θ_B [Grad],
- Scan-rate of the antenna $\dot{\Theta}_S$ [Grad/sec].

$$n_B = \frac{\Theta_B f_p}{\dot{\Theta}_S} \quad (8.10)$$

Common by rotating Radar systems:

$$10 < n_B < 15 \quad (8.11)$$

For systems with high PRF (Pulse Doppler for short ranges), values of a few hundred for n_B can be obtained. The integration can always take place at two different places in the signal path:

- IF Integration \Rightarrow Pre-detection or Coherent integration,
- Video Integration \Rightarrow Post-detection or Incoherent integration.

Coherent integration (pre-detection) is only seldom used, since it assumes a constant phase between transmission and receiving for the pulses to be integrated. The integration can then, for example, take place through a narrow IF filter, whose bandwidth is inversely proportional to the target dwell time. A sample rate of 360°/sec and a 2° half-power bandwidth result in a dwell time of 1/180 sec. That means that the integration filter has a bandwidth of 180 Hz. The integration effect is obtained by the energy storage in the filter. The quality of the filter determines the integration efficiency. In the following the non-coherent integration will be described in more detail.

8.7.1 Incoherent Integration

For incoherent integration the following considerations apply. If n pulses are summed in an ideal integration, then the S/N ratio at the output of the integrator improves by a factor n . This practically cannot be achieved by incoherent integration, since additional noise develops when rectifying. The improvement, which can be achieved by an operator with a storage tube, is approximately proportional to \sqrt{n} . From Marcum [6] the achievable improvement, henceforth identified as integration efficiency, is calculated.

The efficiency for n pulses is defined by:

$$E(n) = \frac{(S/N)_1}{n(S/N)_n} \tag{8.12}$$

$(S/N)_1 = S/N$ for one pulse.

$(S/N)_n = S/N$ for one pulse of the same probability of detection P_d and false alarm rate P_{fa} with the integration of n pulses.

$$(8.13)$$

Then one obtains:
$$n \cdot E(n) = I(n) = \frac{(S/N)_1}{(S/N)_n}$$

$I(n)$ is the integration factor. Near this factor the power of the Radar can be reduced by the integration in relation to the case, which is not integrated. $I(n)$ is represented in Figure 8.14. The probability of detection P_d and the false alarm rate P_{fa} are of minor influence. Often the integration loss (Equation 8.14) is also stated as demonstrated in Figure 8.15.

$$L(n) = 10 \log\left(\frac{1}{E(n)}\right) \tag{8.14}$$

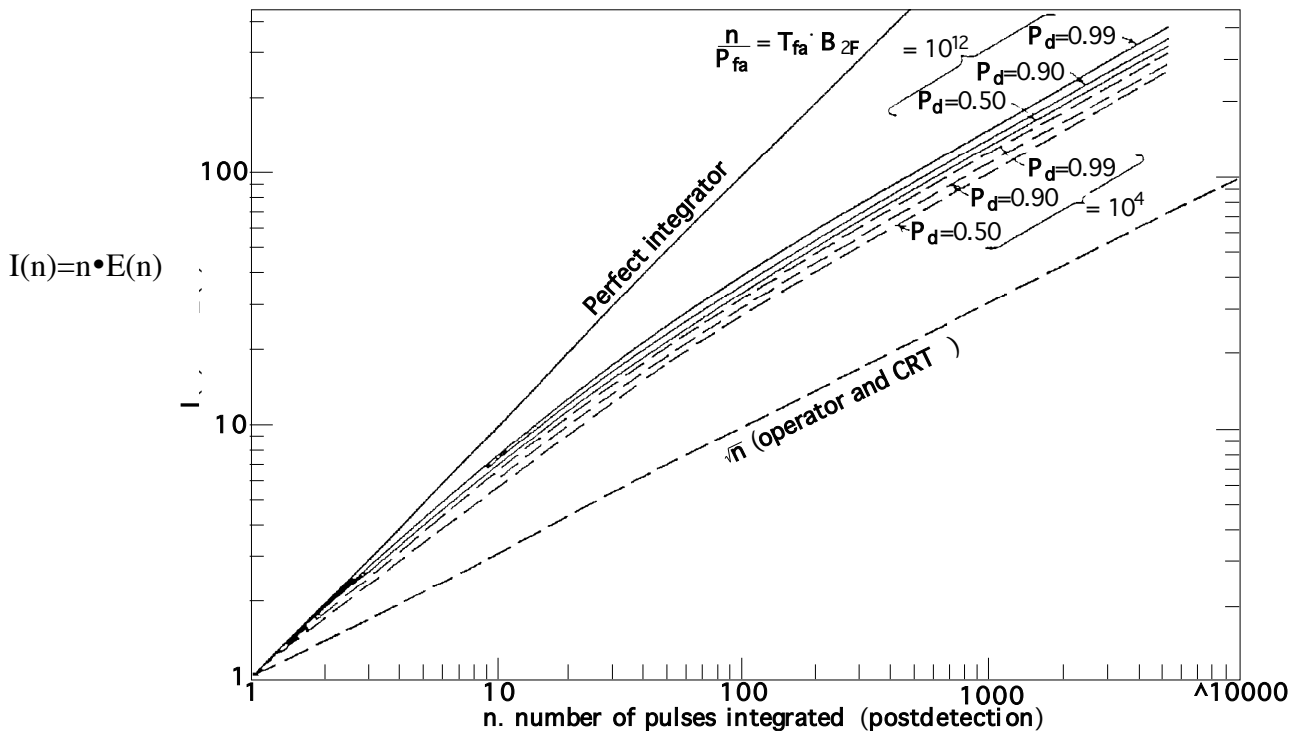


Figure 8.14 Integration factor as a function of the number of the integrated pulses n for non-coherent integration.

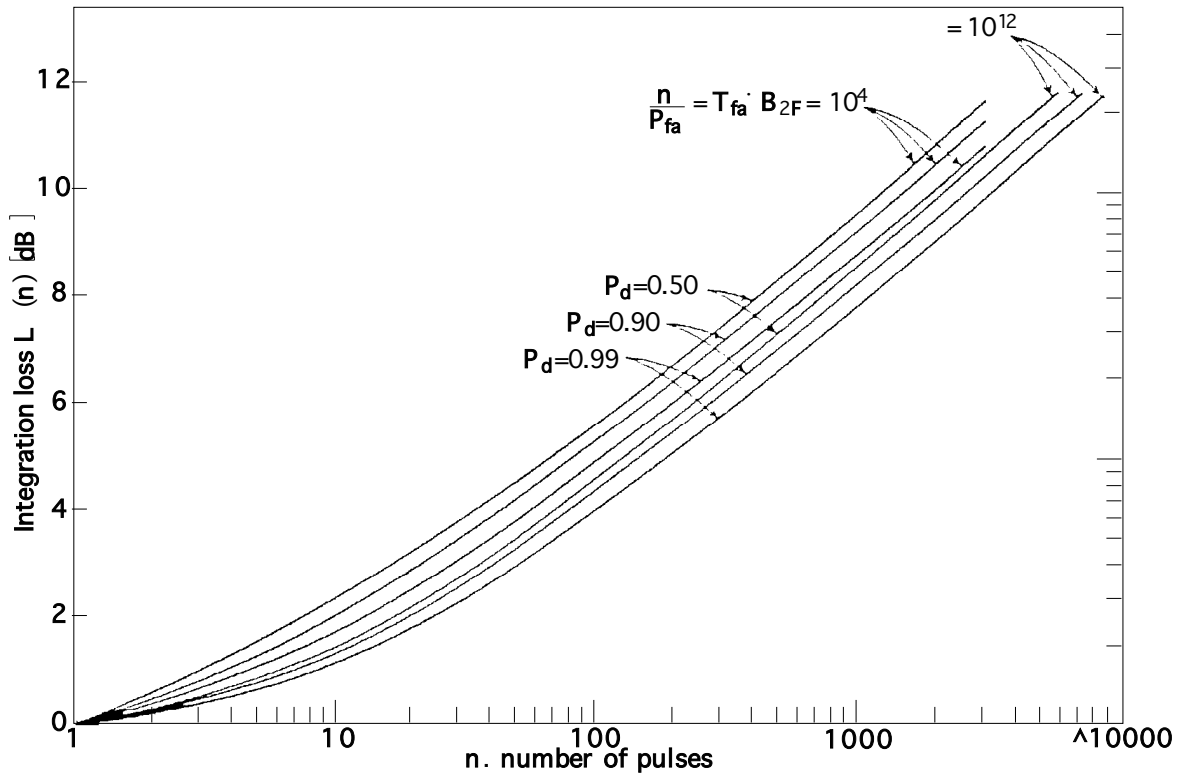


Figure 8.15 Integration loss as a function of the integrated pulses n for non-coherent integration.

With a given false alarm rate and detection probability the increase in the range of coverage can be calculated by integration with the modified Radar equation according to equation (3.8) and the integration gain (Figure 8.14 and/or Equation 8.10). In the Radar equation the following is replaced:

$$P_{R_{\min}} = kTB_n L(S/N)_1 \tag{8.15}$$

T = Temperature in Kelvin, $(S/N)_1$ = required signal-to-noise ration for a pulse, B_n = noise bandwidth, L = system losses. Through Equation (3.9), Equation (8.16) results:

$$P_{R_{\min}} = \frac{kTB_n L(S/N)_1}{nE(n)}$$

$$\Rightarrow R_{\max}^4 = \frac{P_s G_s G_e \lambda^2 \sigma}{(4\pi)^3 kTB_n L(S/N)_1} nE(n) \tag{8.16}$$

8.7.2 Examples for Incoherent Integration

Different procedures have been developed for integration, from which three will be quickly presented:

- Tapped delay line integration
- Looped integration

- Binary integration

With tapped delay line integration, according to Figure 8.16, analog or digital signals are fed into a tapped delay line, whose length corresponds to the number of hits per scan n_B . At the output one obtains a maximum if n successive echoes are received from a target. The execution of an analog tapped delay line can be realized by RLC bandpass resonators, RC elements, static memory elements or mechanically circulating samplers. Shift registers are used for digital integration. The advantage of the tapped delay line is that any weighting of the taps is possible, for example, in order to strengthen the wanted pulses or weaken the older pulses.

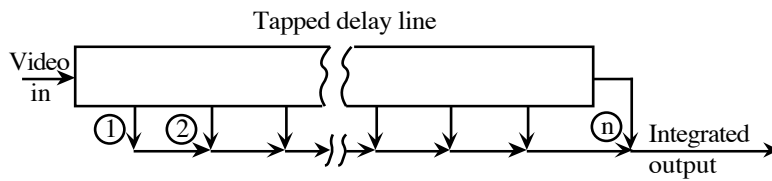


Figure 8.16 Incoherent integrator with a tapped delay line.

The loop integration, as shown in Figure 8.17, as a rule has a poor efficiency as discussed earlier. This is due to the fact that the loop gain k must be smaller than 1 in order to hinder an oscillation. Single-step arrangements make possible a loop gain of up to .9, dual-step up to .98. The loop gain is dependent upon the number of the pulses that must be integrated. A weighting is not possible.

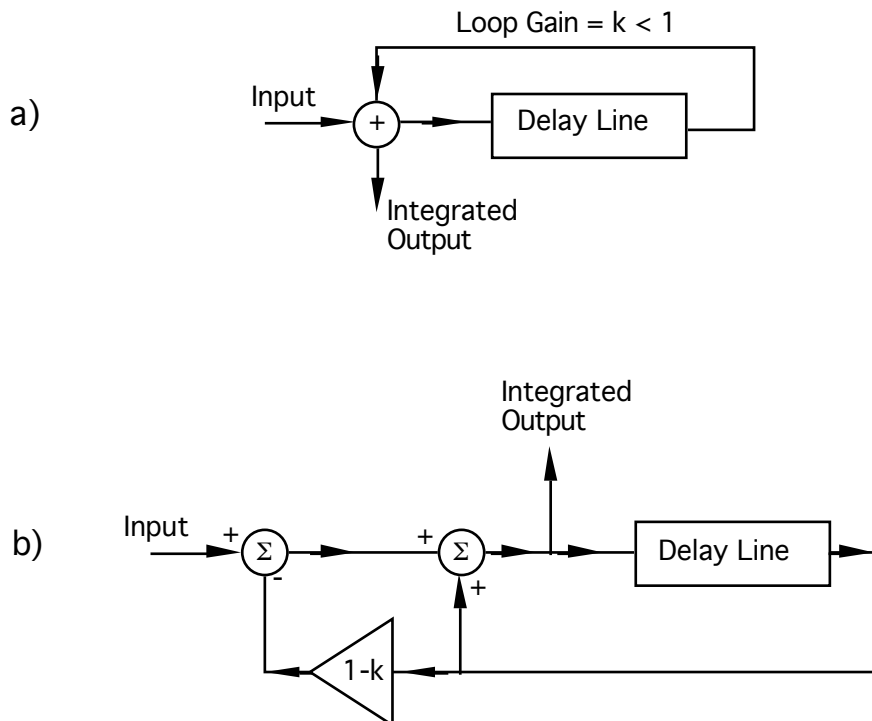


Figure 8.17 Loop integration: a) single-step ($k < .9$) b) dual-step ($k < .98$)

The third version of non-coherent integration is binary integration and it digitally analyzes the number of occurrences in a windowed range. Figure 8.18 shows a corresponding arrangement.

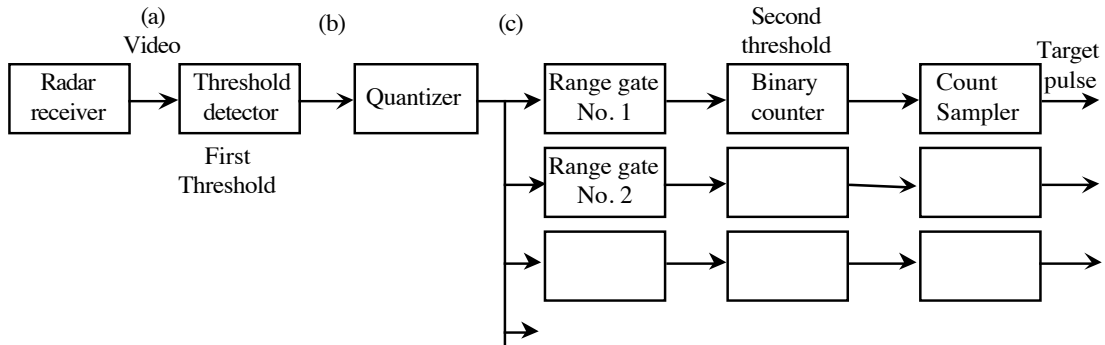


Figure 8.18 Block diagram of a binary integrator.

A target is identified if m echoes are counted from a possible number n , all within a certain time interval.

8.8 Pulse Compression for Improving the Resolution

As has been already said in the previous section, the range of coverage is determined primarily by the total energy, which is received from a target. There the energy has been increased through the integration of several pulses. The same effect can be achieved by the increase of the pulse duration τ . The precision of the range measurement is independent upon the pulse duration so that there are no given restrictions here. The resolution of two neighbouring targets, as has been shown in section 2.6, is calculated with the autocorrelation function and/or with the cross-correlation. Thus the resolution is directly dependent upon the pulse duration. According to this, the signal at the receiver must be temporally shortened (i.e. compressed) when dealing with longer pulses, this in order to improve the range resolution as well as the precision and the sensitivity. Procedures of this type have been developed in communication theory long before they found use in Radar technology. In order to make possible this compression the transmitting signal must be modulated in the pulse (intra-pulse modulation), again in order to obtain marks within the pulse duration. Digital and analog procedures will be described in the following.

8.8.1 Compression of a frequency modulated pulse (chirp)

One of the first procedures for the realization of pulse compression involved the frequency modulation of the transmitting pulses. The procedure is clearly demonstrated in Figure 8.19. The transmitting pulse, which is represented by a rectangle in Figure 8.19a is, as shown in Figure 8.19b, linearly frequency modulated between f_1 and f_2 . Figure 8.19c illustrates the time procedure. The signal re-received over the signal path is fed into a frequency dependent filter, according to Figure 8.19e. The first arriving low frequency f_1 is delayed around t_2 , and the

later, higher frequencies delayed only around t_1 . Through this it is achieved that the entire power of the long transmitting pulses “simultaneously” leave the compression filter within a very short pulse, according to Figure 8.19d.

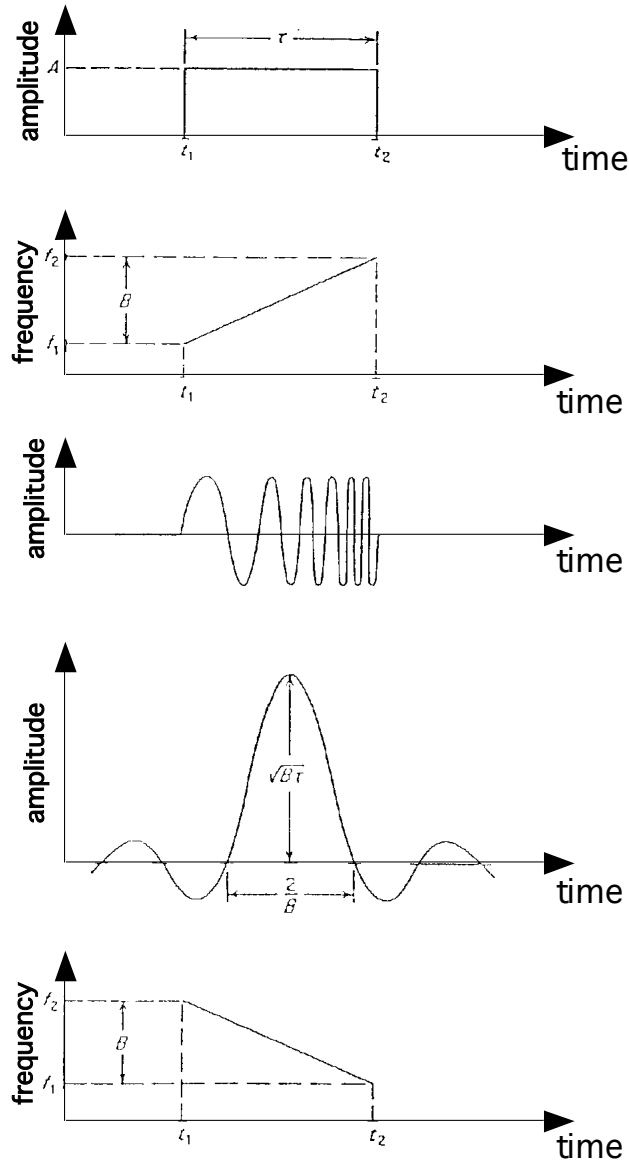


Figure 8.19 Frequency modulated pulse compression.

Figure 8.20 shows how the high resolution is regained. There is no time separation possible before the compression. After the compression the possibility for time separation depends upon the amplitudes of the target echoes and the side lobes of the compressed function.

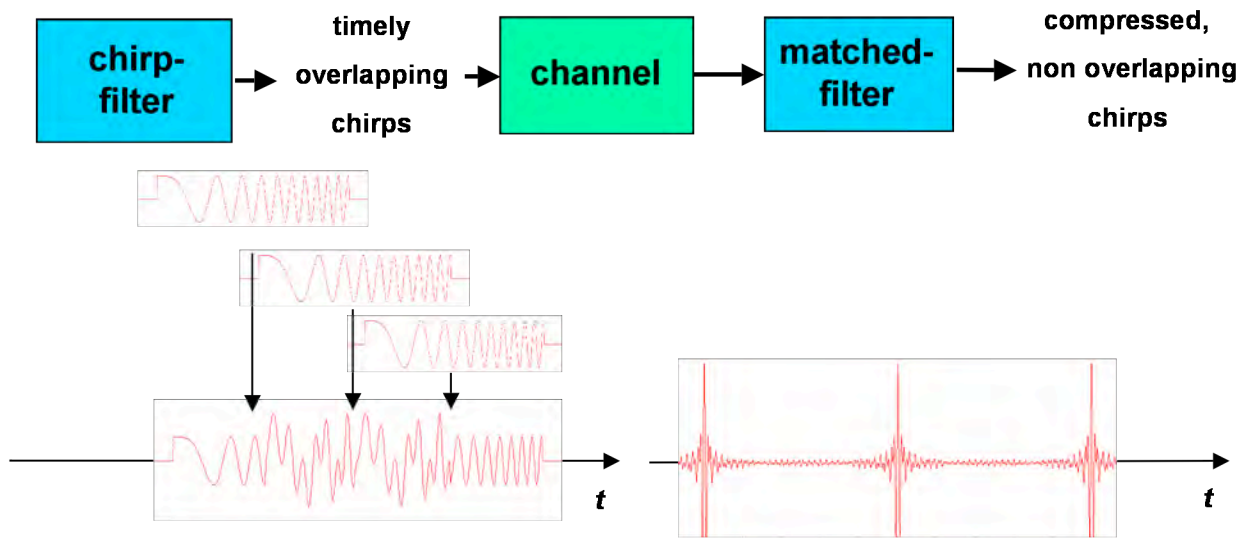


Figure 8.20 Echoes of neighboring targets: left: before the compression, right: after the compression.

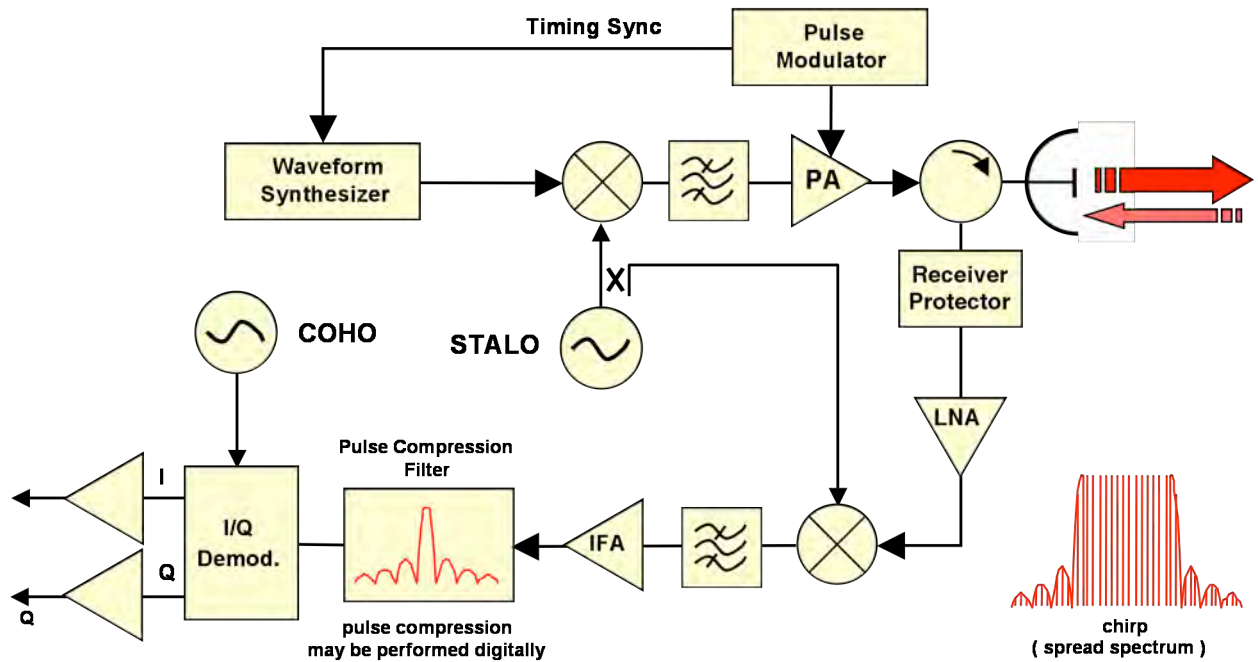


Figure 8.21 Typical block diagram for Radar with FM pulse compression.

All filters with frequency dependent delay times are suitable for use as compression filters. For the case on hand a high-pass filter, as a waveguide, would be suitable. If the higher frequencies are to be delayed, opposite of the example in Figure 8.19, then low-pass filters can be

used. With newer devices acoustic delay lines (surface and material waves) are used. It is important that the filter is adapted to the frequency pass (i.e. matched filters). If it delays too little, the compression is not fully reached. If it delays too much, then the pulse is again dispersed, not compressed. Today the employment of FM pulse compression no longer serves to increase the energy of a pulse. In fact, broad spectra are used in order reduce the coded spectral energy density and thus avoid that Radar-warning stations & receivers discover any activity. The procedures range even to Spread Spectrum and coded noise (PN-Codes = *Pseudo Noise Codes*).

In Figure 8.19 a rectangular pulse and a linear FM and compression were assumed. From that results a compressed pulse shape of $\sin x/x$. If one identifies the frequency pass with B and the pulse duration with τ , then the amplitude of the pulse is proportional to $\sqrt{B\tau}$ and the width to $2/B$. Under these conditions the Fourier transform of the compressed pulse of the entrance pulse has the form:

$$\frac{\sin(\pi Bt)}{\pi Bt} \tag{8.17}$$

The overshoot of Function (8.17) would interfere with the video detection. In practice a rectangular pulse is not realizable and this problem does not arise. In fact almost any frequency modulation and pulse form is used, only if the compression filter is adapted to it, meaning that it is a matched filter. Following this the envelope of the compressed FM pulse is briefly described and derived.

If it is defined that the impulse response of the impulse function $\delta(t)$ equals $h(t)$, then one can obtain the response of any function $x(t)$ if one divides the function into durations of $\Delta\tau$, as shown in Figure 8.22.

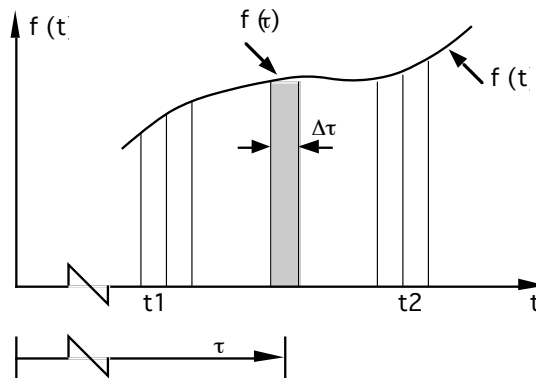


Figure 8.22 Division of the pulse function.

The impulse function $\delta(t)$ with the duration $\Delta\tau$ has the amplitude $x(t)$. The response $g(t)$ of the entire input function $x(t)$ results from the summation of all impulse functions.

$$g(t) = \sum_{\tau=t_1}^{t_2} x(\tau) \cdot h(t - \tau) \cdot \Delta\tau \tag{8.18}$$

In the limit the following is obtained:

$$g(t) = \int_{t_1}^{t_2} x(\tau) \cdot h(t - \tau) d\tau \tag{8.19}$$

As shown by Figure 8.19, the chosen example of linear FM is the normalized time function of the pulse.

$$x(t) = \cos(2\pi f_0 t + \frac{1}{2} b t^2)$$

$$b = \frac{2\pi B}{\tau} \text{ (FM - Rate) =}$$

$$\cos(\omega_0 t + \frac{1}{2} b t^2) ; -\frac{\tau}{2} < t < \frac{\tau}{2} \tag{8.20}$$

$$x(t) = 0 \text{ otherwise}$$

The matched filter, which represents the ideal compression filter, has the function:

$$h(t) = \sqrt{\frac{2b}{\pi}} \cdot \cos(\omega_0 - \frac{1}{2} b t^2); -\frac{\tau}{2} < t < +\frac{\tau}{2} \tag{8.21}$$

With a normalizing factor of $\sqrt{2b/\pi}$, Equation (8.19) results in:

$$g(t_0) = \sqrt{\frac{2b}{\pi}} \int_{-\frac{\tau}{2}}^{+\frac{\tau}{2}} \cos(\omega_0 t + \frac{1}{2} b t^2) \cdot \cos(\omega_0(t_0 - t) - \frac{1}{2} b(t_0 - t)^2) dt \tag{8.22}$$

The result is obtained after many transformations.

$$g(t_0) = \sqrt{\frac{2b}{\pi}} \cos(\omega_0 t_0) \cdot \frac{\sin(\frac{bt_0}{2}(\tau - |t_0|))}{bt_0/2} \tag{8.23}$$

A comparison of compressed pulses with short pulses of the same bandwidth shows that the same precision and resolution cannot be achieved with FM compression. The deterioration is identified as compression loss.

8.8.2 Digital Pulse Compression

With digital technology for pulse compression the transmitting signal is either amplitude or phase modulated, where as a rule the phase modulation is preferred because of the larger total energy content of the signal. The two most used procedures employ the:

Binary Phase Coding (BPC) e.g.⇒ Barker Code
 or
 Multiphase Coding e.g.⇒ Frank Code

8.8.3 Digital Pulse Compression with Barker Code

The Barker Code consists of a special sequence binary phase encoded signal with the duration τ , as demonstrated in Figure 8.23.

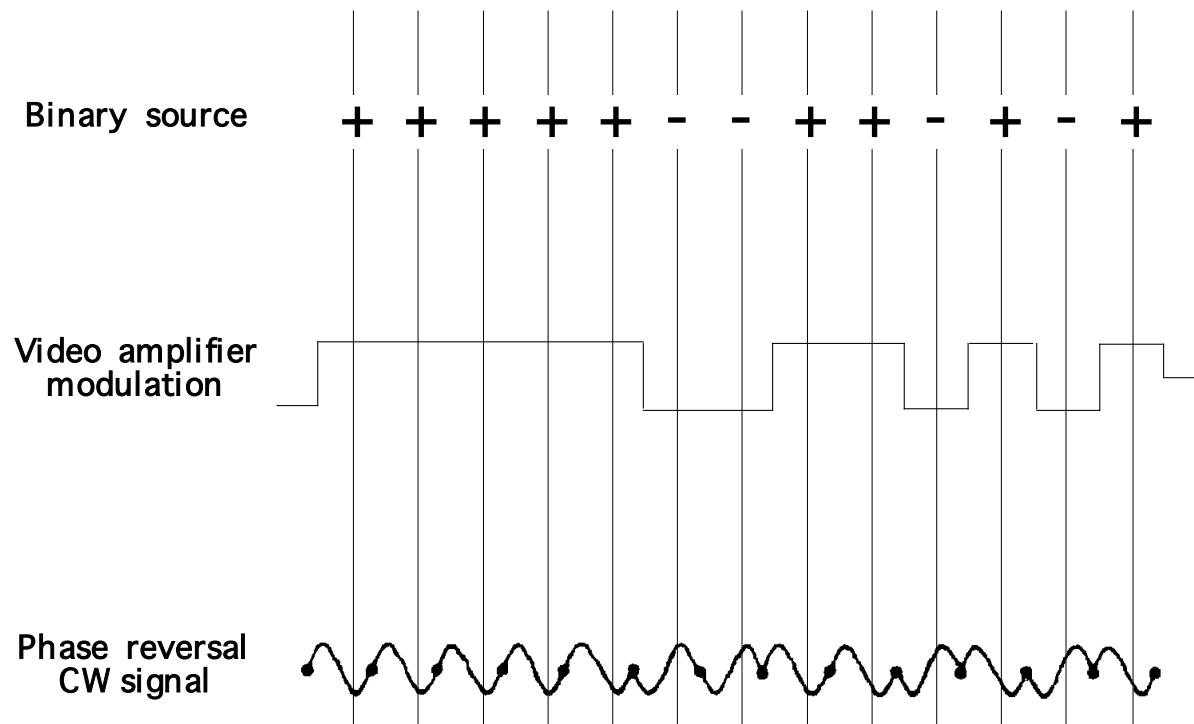


Figure 8.23 Barker Code of length 13.

The phases in the signal are altered by 180° at each sign change. The entire duration of the signal is $N\tau$. The largest bandwidth is $1/\tau$. At the receiver the signals run through a series of digital delay lines with a run-time delay τ . The signal is sampled after each delay gate and is then fed into a summing unit. Figure 8.24 shows an arrangement of this type. Each of the individual signals rests at the summing unit in such a way that all values are positive when the last bit arrives.

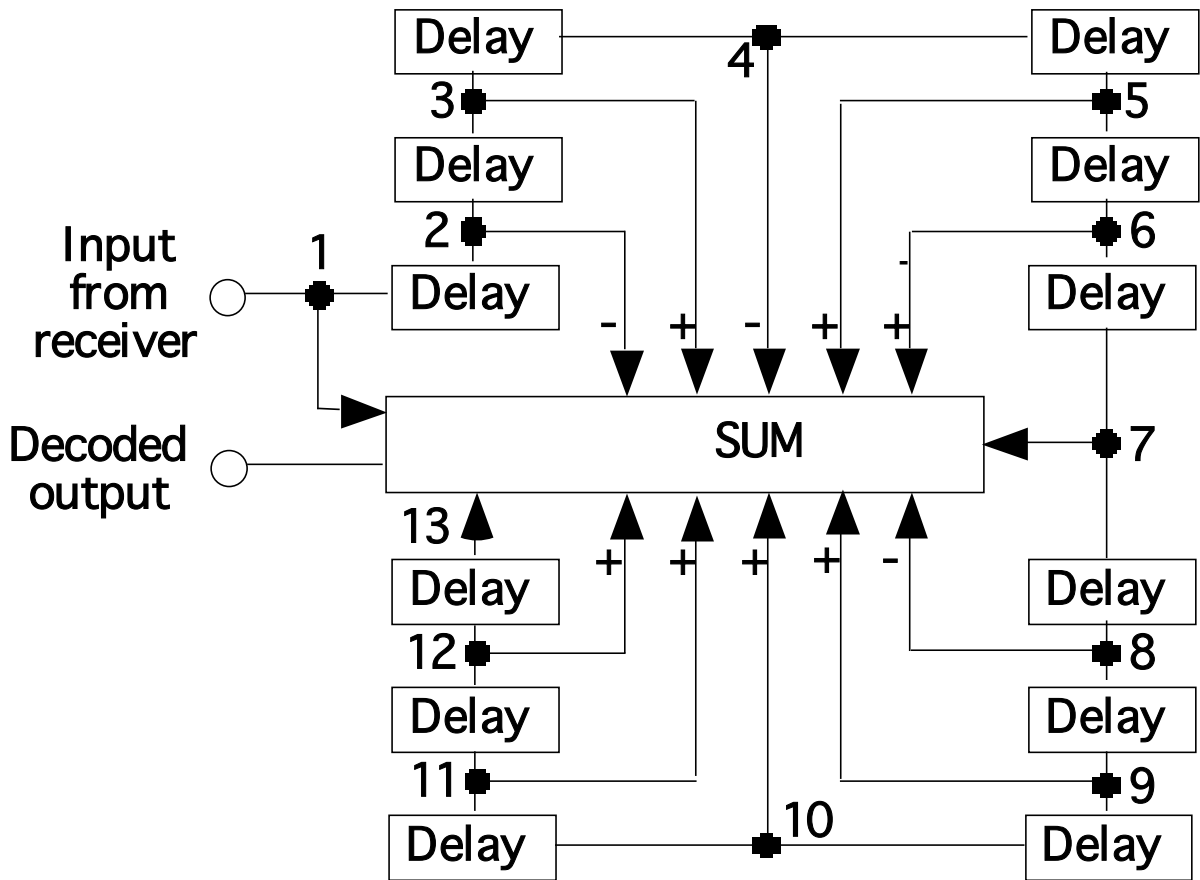


Figure 8.24 Barker Decoder for $N = 13$.

Characteristic of the Barker Code up to $N=13$ is that all side lobes are ≤ 1 , while the main lobe is equal to N . Figure 8.25 shows the mathematical process of the circuit in Figure 8.24. The output delivers $2 \times N$ elements, as demonstrated in Figure 8.26.

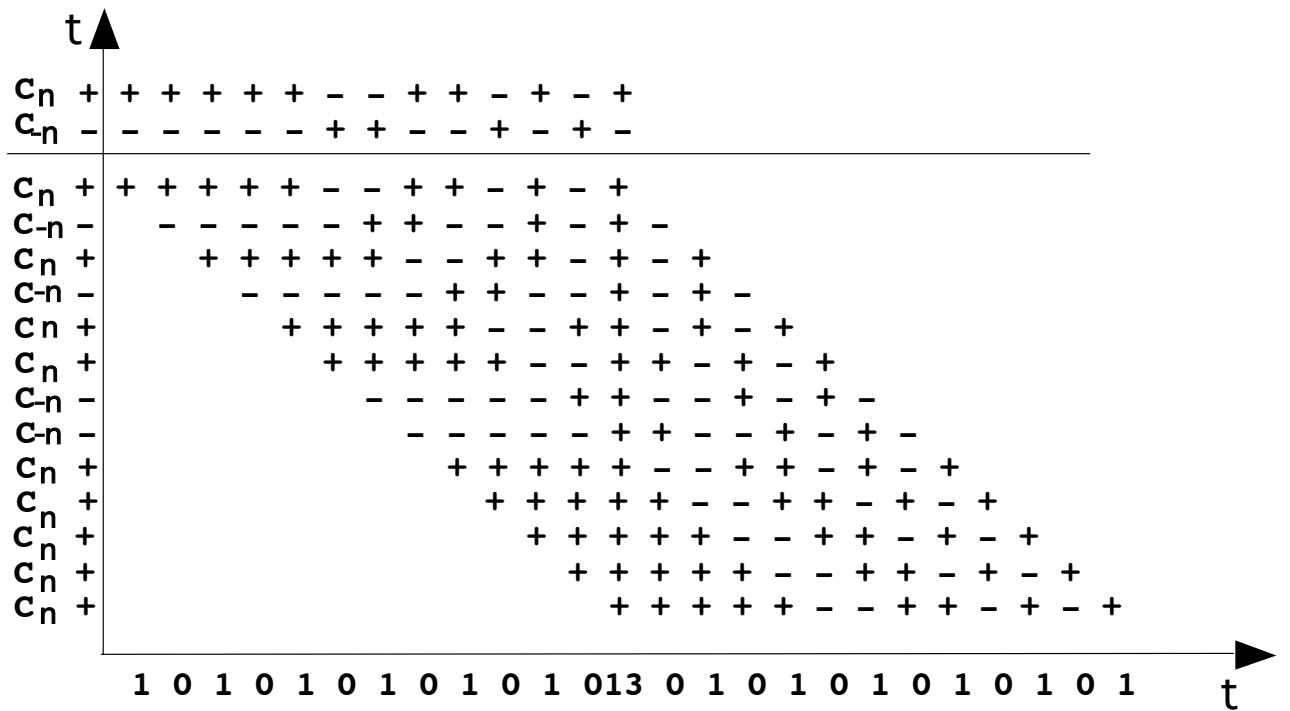


Figure 8.25 Signals at the summing unit of the Barker Decoder for N=13.

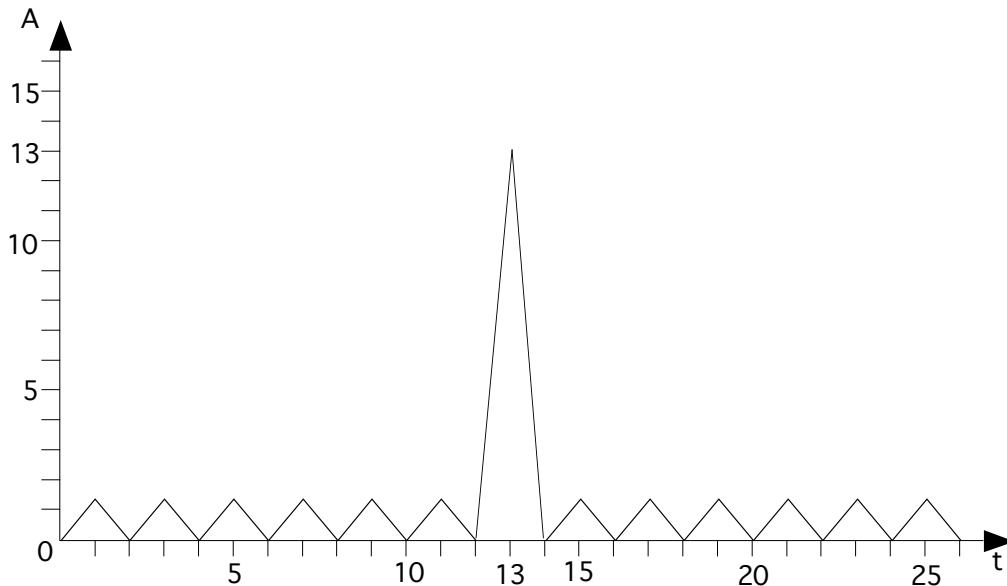


Figure 8.26 Decoded Barker Code for N=13.

Until today Barker Codes up to N=150 are known, whose side lobes are less than or equal to 7. In addition to the Barker Code there are today several synthetic, well correlating codes.

9 Beamforming

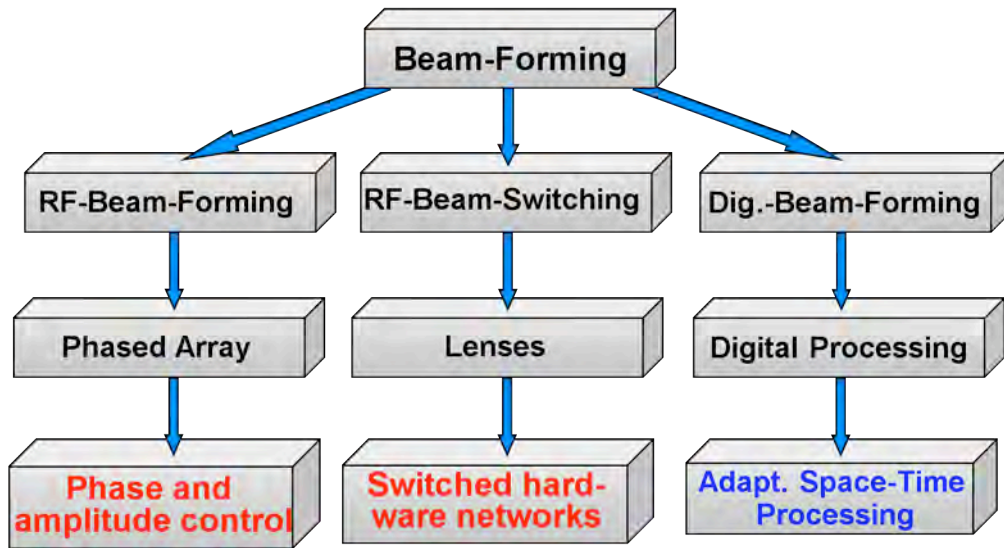


Figure 9.1 Beamforming concepts.

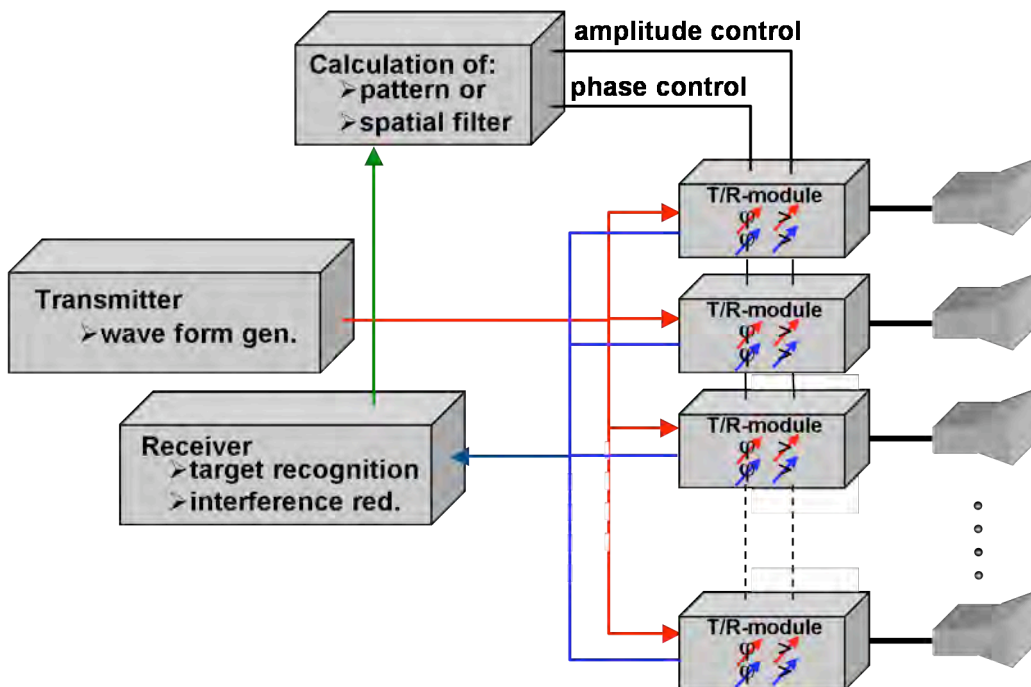


Figure 9.2 Single channel Phased Array.

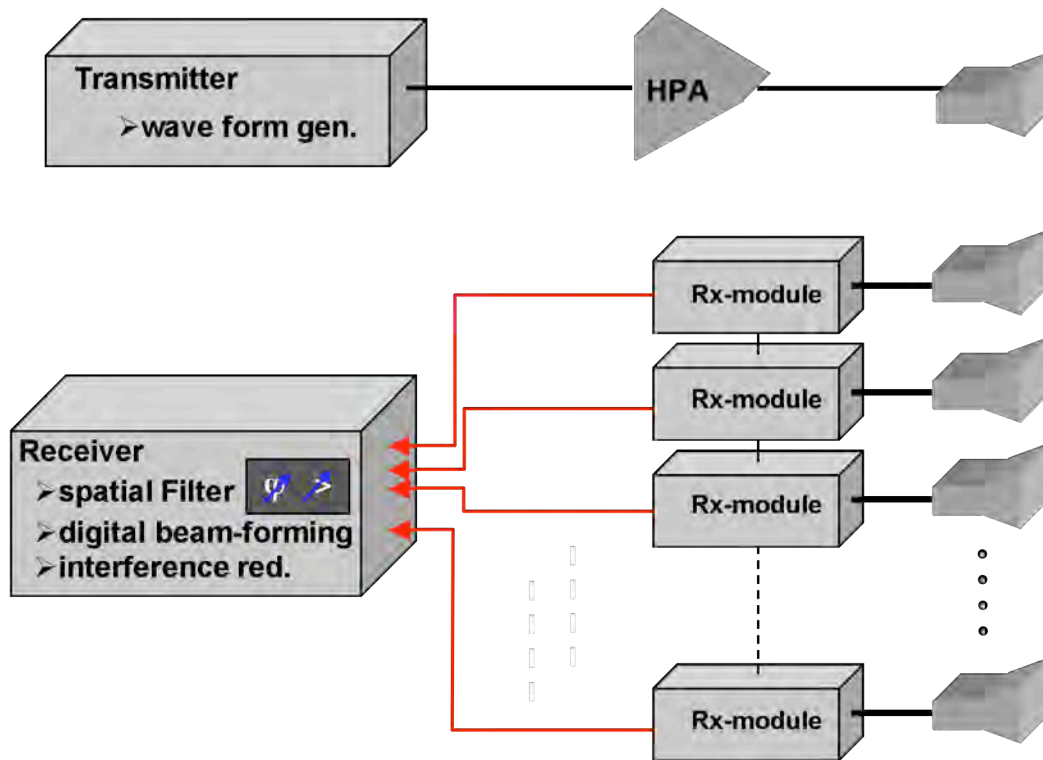
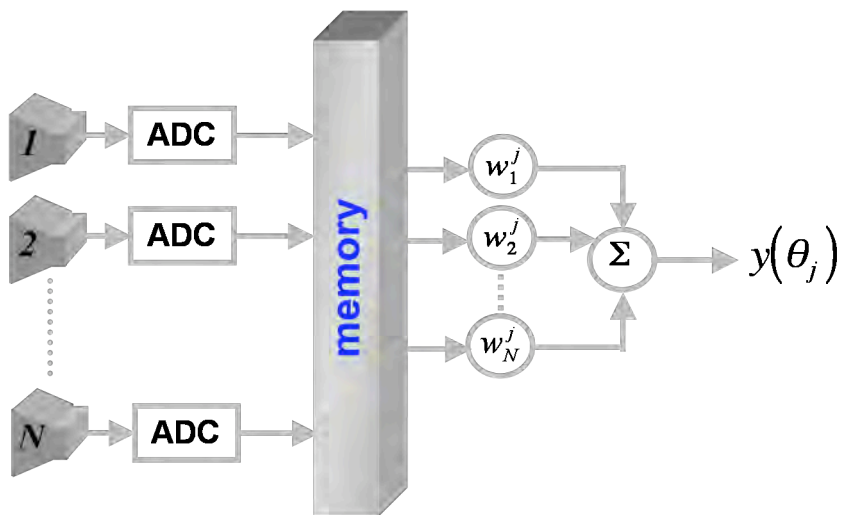


Figure 9.3 Digital Beam-forming on receive only.



- separate A/D-converter for each antenna element/sub array
- storage of all received signals
- digital processing of the beam-forming
- no T/R-Modules are required
- multiple beams can be processed simultaneously

Figure 9.4 Digital Beam-forming characteristics.

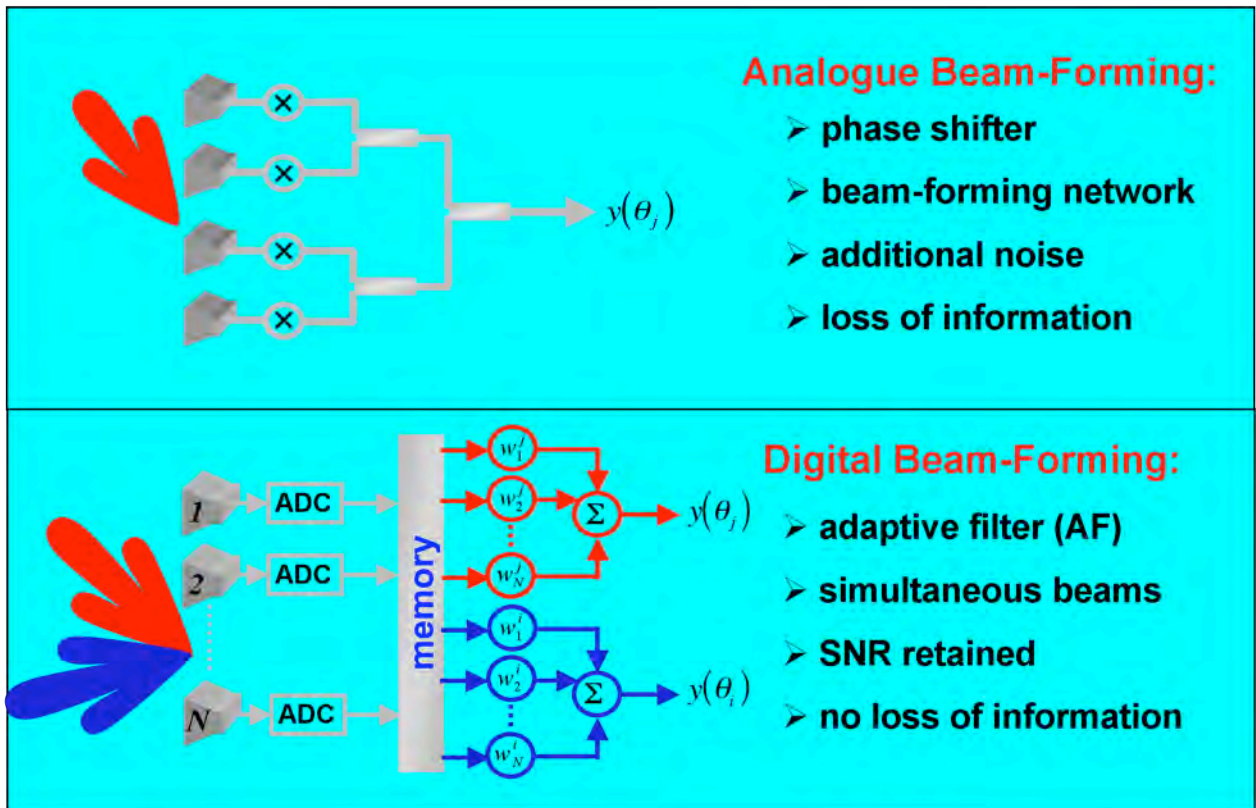


Figure 9.5 Comparison of analog and Digital Beam-forming.

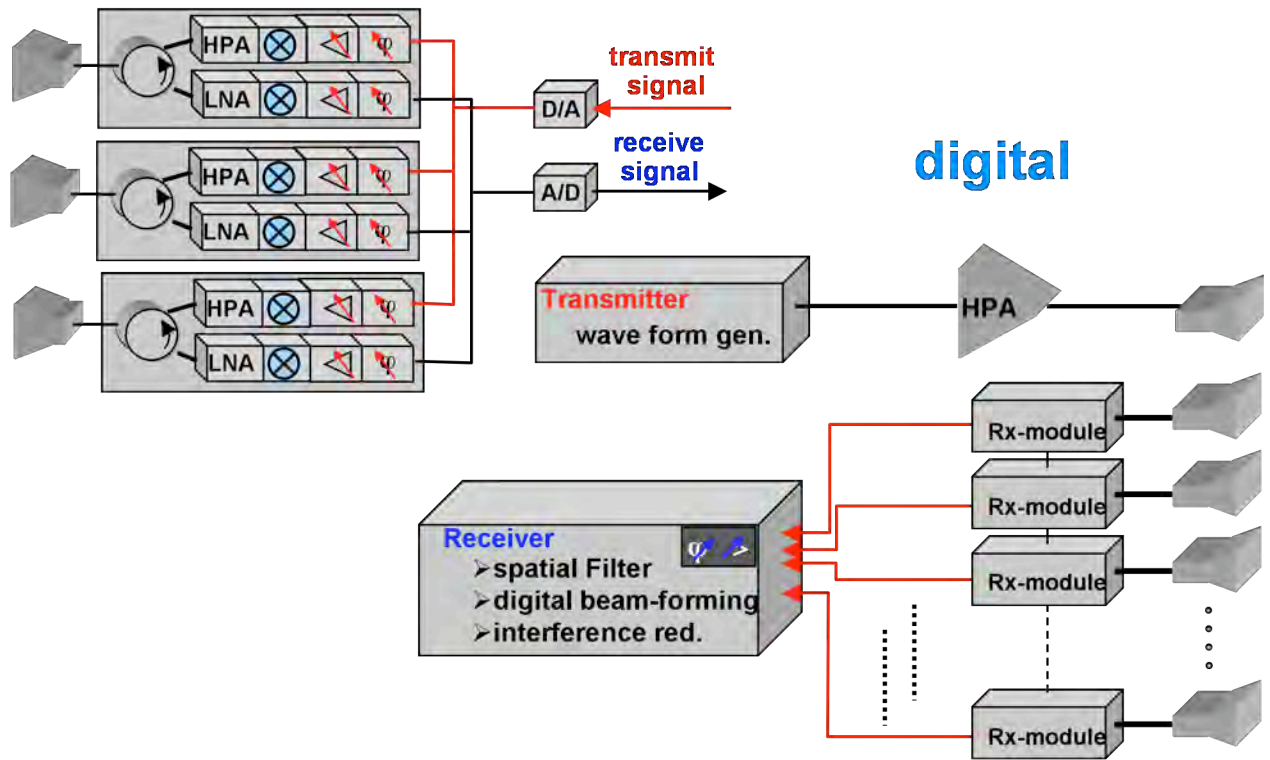


Figure 9.1 Comparison of analog and Digital Beam-forming system concepts.

10 Synthetic Aperture Radar

10.1 Resolution Limits of Conventional Radar Devices

The achievable resolution capability of conventional pulse Radar devices is, as already described, determined by:

- Pulse duration τ for range resolution
- Half-power bandwidth θ_H for the resolution of the angle

The resolution in the propagation direction, i.e. range, is approximately:

$$\Delta R \approx \frac{c_0 \tau}{2} \quad (10.1)$$

Then orthogonal to that in azimuth, i.e. cross range, is given with the half-power bandwidth:

$$\Delta z \approx \theta_{3dB} \cdot R; \left(\theta_{3dB} \approx 68^\circ \cdot \frac{\lambda}{a} \text{ for } \cos^2\text{-taper} \right) \quad (10.2)$$

Presently it is assumed that two targets can be separated if their echoes overlap at the 3 dB points (half power). With various new algorithms an increased resolution can be achieved. Normally the azimuth values are in particular dissatisfactory for large ranges, as they arise for Earth exploration by Radar from satellites. With a range of 300 km and a half-power bandwidth of 1° , the resolution is $\Delta z = 5,2$ km.

10.2 Procedures for Improving the Resolution

10.2.1 Range Resolution with Pulse Compression

The range resolution can be improved with shorter pulse duration and/or a larger FM bandwidth. Procedures for the synthetic shortening of the pulse duration have already been dealt with through digital and analog pulse compression and are used in practice. With this pulse times after compression of 1 ns or smaller can be achieved, meaning that the resolution ΔR amounts to around 15 cm. At the receiver and/or with signal processing there must then be an available bandwidth of >1 GHz. For Earth exploration a small degradation of the range resolution results from the angled or diagonal view as represented in Figure 9.1.

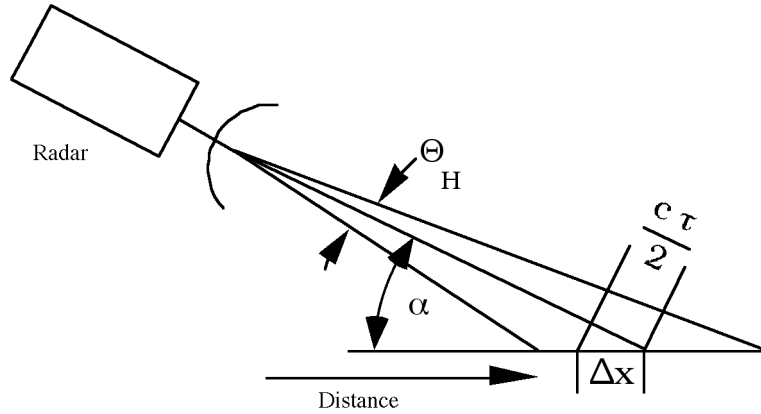


Figure 10.1 Range resolution of a Radar with a diagonal incident wave trajectory.

The range resolution from Equations (9.1) & (9.3) correspond to the notation and identifiers from Figure 9.1.

$$\Delta x = \frac{c\tau}{\cos\alpha} \cdot \frac{1}{\cos\alpha} = \frac{c\tau}{2} \cdot \sec\alpha \tag{10.3}$$

10.2.2 Improvement of the Azimuth Resolution

For the resolution of the azimuth according to Equation (9.2) only the range R and the half-power bandwidth θ_H are suggested. Consequently, with the search for possibilities for the improvement of the resolution orthogonal to the propagation direction, there remain no other alternatives than the reduction of θ_H . Figure 9.2 shows a surface, which is illuminated by Radar from an altitude or height h at an angled incidence. With pulse compression a region in the range can be resolved, from here according to Equation (9.3), as shown:

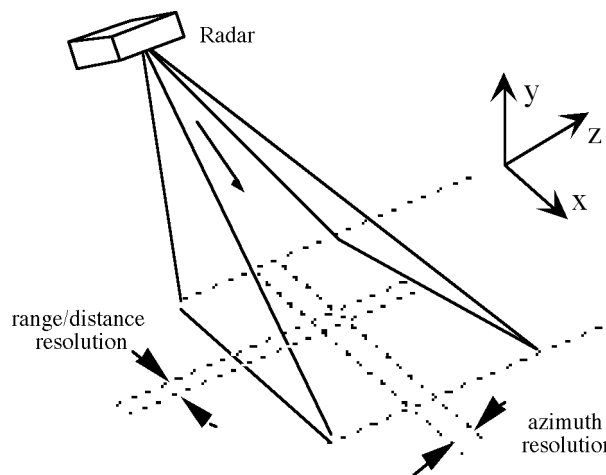


Figure 10.2 Illumination and region of resolution.

In order to achieve the azimuth resolution, as shown, θ_H must be decreased accordingly. From the aperture a , a good approximation of half-power bandwidth results:

$$\Theta_H = \frac{\lambda}{a} [\theta_H \text{ in rad}] \quad (10.4)$$

From here the azimuth resolution is

$$\Delta z - \theta_H R = \frac{\lambda}{a} R \quad (10.5)$$

If, for example, one would require a range resolution of 1,5 m at a range of 100 km, then the aperture for 10 GHz would result from:

$$a = \frac{\lambda}{\Delta z} R = \frac{3}{150} 10^7 \text{ cm} = 2 \text{ km} \quad (10.6)$$

It is not practically possible to realize an antenna of this size.

The fundamental idea for improvement is now a fixed flight route or zone with moving Radar, which itself is used as an aperture. Thus it is possible to create a very large aperture through the synthetic “stringing together” of the physical aperture as the Radar moves. This procedure is identified as SAR, which stands for "Synthetic Aperture Radar". The fundamentals of this procedure are described in more detail in the following sections.

10.3 Basic Principle of SAR

"Synthetic Aperture Radar" [24], henceforth referred to as SAR, operates from a moving carrier, which moves along or over the target area. An example “fly-by” is illustrated in Figure 9.3.

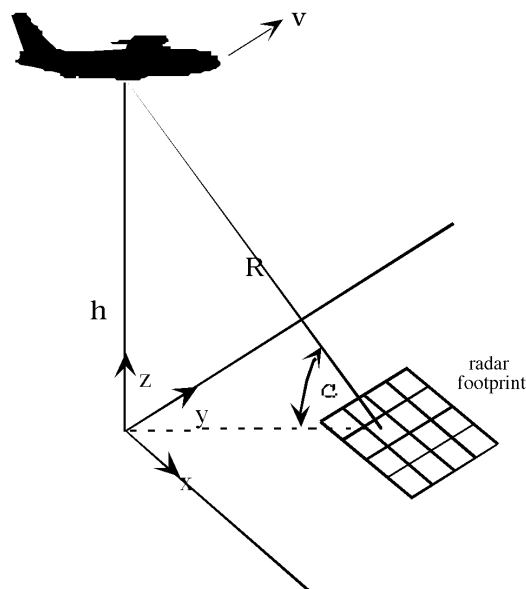


Figure 10.3 Three-dimensional representation of SAR geometry.

Point C of the illuminated target area, or foot print, is seen during the “fly-by” so long, as the carrier is within the half-power bandwidth of the directivity of the antenna. This means that information from the target point C can be collected over the entire time of the “fly-by”.

The actual problem exists in the synthesizing or the piecing together of the various parts of information. As the best criterion for this the phase gradient and/or the change of the phase of the Doppler frequency is used. In practice one speaks about the “Doppler history.” The change of the phase represents the relative velocity. Each object, which is acquired from moving Radar, delivers a defined progression of the Doppler frequency. From this the aspect angle θ_0 , the velocity of movements, the height h , and the range R are determined. Figure 9.4 shows the associated array of curves.

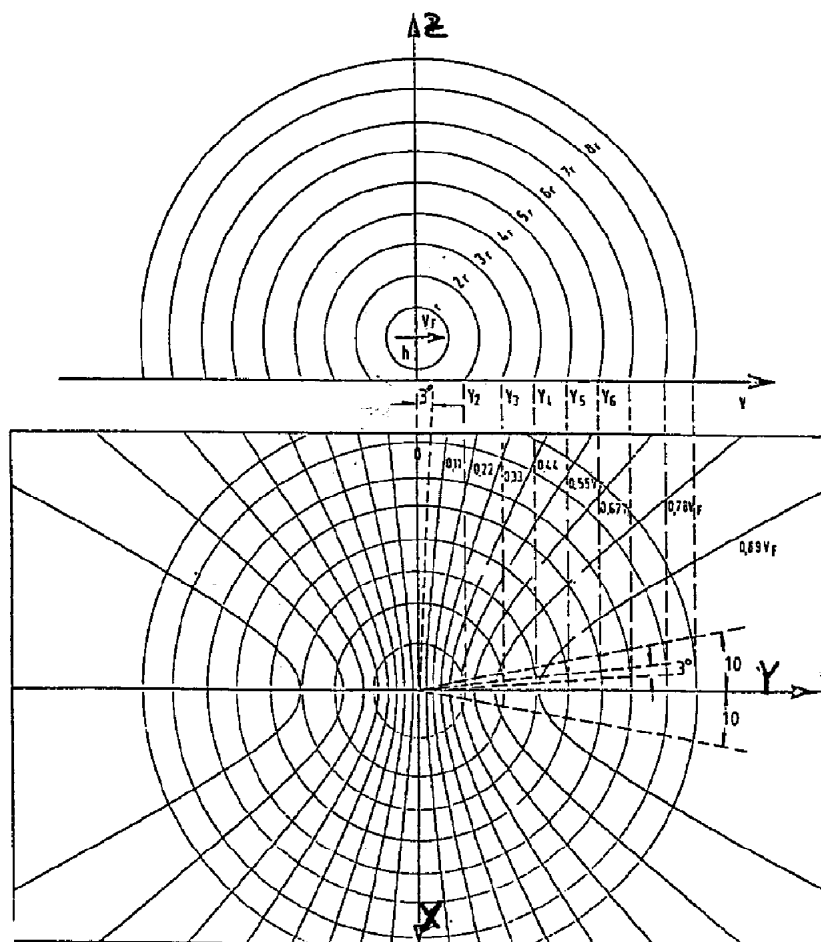


Figure 10.4 Curves of the same range (iso-range contours, circles) and relative velocity (iso-Doppler contours, hyperbolas).

The iso-Doppler contours are the places for all objects of the same Doppler frequency if the Radar is moving with the velocity v_F at a height h of above the ground. With a fixed place of an object in the x - y plane, the iso-Doppler contour moves away with the flying Radar. The iso-Doppler contours clusters are dependent on the height h ($h=1.5 R$ in Figure 9.4). The

smallest change of the relative velocity and therefore the Doppler frequency results for objects ahead. The largest relative Doppler frequency changes result from transverse objects.

The Doppler history for transverse objects is shown next to each other in Figure 9.5, as they result from a “fly-by”, for successive resolution regions. The lines begin, where the scatterer is seen first by the Radar antenna and end, when it leaves the antenna main beam.

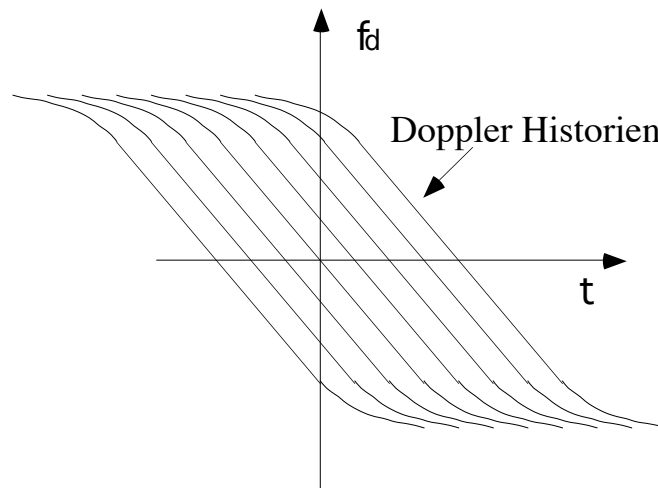


Figure 10.5 Progression of the Doppler frequency for successive resolution cells (Doppler histories).

Since the curvature of the iso-Doppler contours for transverse objects is very slight and the changes are almost linear, the Doppler history frequencies also progress linearly. The task of the analysis with SAR consists of separating the Doppler criteria, thereby to determine and represent the cell amplitudes.

10.4 Theoretical Basics of SAR

The mathematical treatment of the SAR characteristics result on the basis of Figure 9.6.

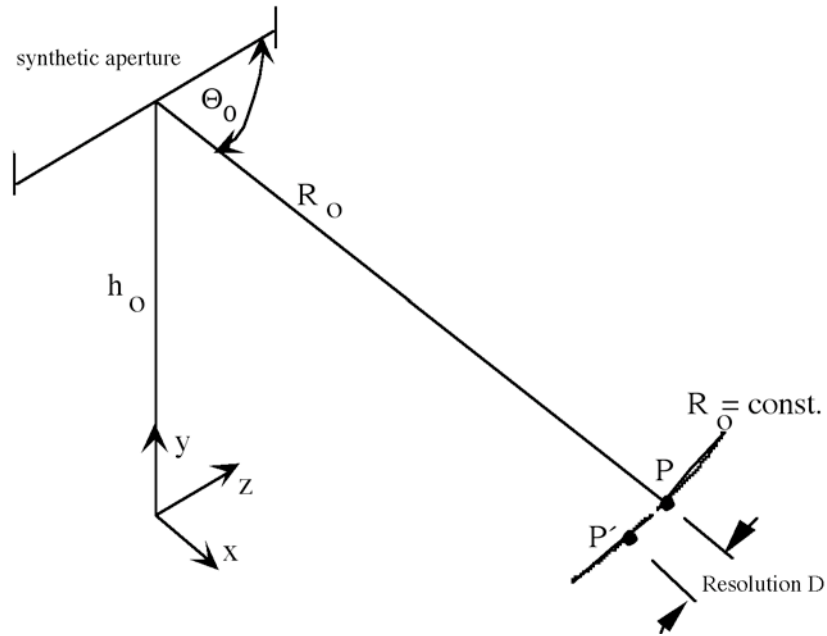


Figure 10.6 Identifiers for calculating SAR.

The Radar, at the height $y=h_0$ with $z=0$, $x=0$, illuminates a point P, whose coordinates are $(x_0, 0, z_0)$. The synthetic aperture should be determined for the region L, which is symmetric around $z=0$. L corresponds to the illumination width on the ground and is therefore the route of the Radar, while object P will be seen. The airplane flies over L with a constant velocity v . The flight time T is then:

$$T = \frac{L}{v}$$

The range R to the point P is calculated from the coordinates:

$$R = \sqrt{x_0^2 + (z_0 - vt)^2 + h_0^2} \tag{10.7}$$

$$\text{with } -\frac{T}{2} < t < +\frac{T}{2} \tag{10.8}$$

For large ranges or R, compared to synthetic aperture L ($L \ll R$), one can express R with the median range:

$$R = \sqrt{x_0^2 + z_0^2 + h_0^2} \tag{10.9}$$

$$\cos \theta_0 = \frac{z_0}{R_0} \tag{10.10}$$

After developing Equation (9.7) with a Taylor series for t:

$$R = R_0 \cdot \left(1 - \frac{vt}{R_0} \cos \theta_0 + \frac{v^2 t^2}{2R_0^2} \sin^2 \theta_0\right) \quad (10.11)$$

the Doppler frequency f_d is obtained from the change in range dR/dt :

$$v_d = \frac{dR}{dt} = -v \cos \theta_0 + \frac{v^2 t}{R_0} \sin^2 \theta_0 \quad (10.12)$$

$$f_d = -\frac{2v_d}{\lambda} \quad (10.13)$$

$$f_d = \frac{2v}{\lambda} \cdot \cos \theta_0 - \frac{2v^2 t}{\lambda R_0} \sin^2 \theta_0 \quad (10.14)$$

The first term in Equation (9.14) is the angle dependent Doppler frequency. The second term reproduces the change of the Doppler frequency. The progression of f_d is demonstrated in Figure 9.5. Two points P and P', which have the same distance R_0 from the Radar, distinguish themselves in azimuth are the route D. This route of the Radar is flown in the following time:

$$\Delta t = \frac{D}{v} \cdot \frac{1}{\sin \theta_0} \quad (10.15)$$

Substituted into Equation (9.14) the following Doppler frequencies for P and P' result:

$$f_d(P) = \frac{2v}{\lambda} \cos \theta_0 \quad (t = 0) \quad (10.16)$$

$$f_d(P') = \frac{2v}{\lambda} \cos \theta_0 - \frac{v^2 D}{\lambda R_0} \sin \theta_0 \quad (t = \Delta t) \quad (10.17)$$

The Doppler frequencies between P and P' amount to:

$$\Delta f_d = 2 \frac{vD}{\lambda R_0} \sin \theta_0 \quad (10.18)$$

The maximum sampling period T in order to separate these 2 targets with a distance D is calculated by:

$$T = \frac{1}{\Delta f_d} \quad (10.19)$$

In time T the Radar moves along the route, which corresponds to the synthetic aperture L:

$$L = vT = \frac{R_0 \lambda}{2D \sin \theta_0} \quad (10.20)$$

10.5 Maximum Resolution Capability

For consideration of the resolution capability D , it must be ensured that the Radar continuously illuminates the target, while it moves in the z direction for the length of the synthetic aperture L . From this the result according to Equation (9.5) is:

$$L = \frac{\Delta z}{\sin \theta_0} = \frac{\lambda}{a} \cdot \frac{R_0}{\sin \theta_0} = \theta_H \frac{R_0}{\sin \theta_0} \quad (10.21)$$

The requirement of the half-power bandwidth of the antenna θ_H is:

$$\frac{\lambda}{a} = \theta_H \geq \frac{L \sin \theta_0}{R_0} \quad (10.22)$$

The following is obtained by replacing L in Equation (9.22) with (9.20)

$$\frac{\lambda}{a} \geq \frac{\lambda}{2D}, D \geq \frac{a}{2} \quad (10.23)$$

The achievable resolution D is consequently equal to the half aperture of the real antenna. Worth noting here is that this is independent of all other parameters like frequency, range, aspect angle, and flying altitude. Since the range of coverage is dependent on the aperture with $1/a^2$, there are in practice, even aside from the complexity of the processing, limits placed upon the resolution. For the derivation of resolution there also exist other approximations.

10.6 Analysis Procedures

When describing possible analysis methods it is useful to regard the progression of the Doppler frequencies according to Equation (9.14). The change in the Doppler frequency leads to a linear frequency modulation (see Figure 9.5). In Sec. 8.8 it has been shown for analog pulse compression, that through the Fourier transformation of a linear FM signal in the time domain a compressed signal with the envelope $\sin x/x$ results. The FM-bandwidth B and the duration τ of the FM signal determine the compression. With SAR the duration is:

$$\tau = T \quad (10.24)$$

B from Equation (9.19):

$$\Delta f_{\max} = B = \frac{2v^2 T}{\lambda R_0} \sin^2 \theta_0 \quad (10.25)$$

The linear FM rate b arises from this as:

$$b = B \frac{2\pi}{T} = \frac{4\pi v^2}{\lambda R_0} \sin^2 \theta_0 \quad (10.26)$$

The time function of the received signal has the following phase:

$$\begin{aligned} \varphi(t) &= \omega_0 t - \varphi_0 + \frac{4\pi}{\lambda} vt \cos \theta_0 - \frac{2\pi v^2 t^2}{\lambda R_0} \sin^2 \theta_0 \\ &\quad \downarrow \quad \downarrow \quad \quad \downarrow \quad \quad \downarrow \\ &= 2\pi f_0 t - \frac{4\pi R_0}{\lambda} + 2\pi f_d t \cos \theta_0 - \frac{1}{2} b t^2 \end{aligned} \tag{10.27}(10.28)$$

The amplitude is:

$$x(t) = \cos \varphi(t) \tag{10.29}$$

If the signal passes through a matched filter, meaning a filter, which has the opposite frequency characteristic as the received frequency, the result is the function:

$$g(t) = \text{const} \cdot \cos\left(\omega_0 + \frac{\omega d}{2}\right)t \cdot \frac{\sin\left(\frac{1}{2} \frac{4\pi v^2 T}{\lambda R_0} t \sin^2 \theta_0\right)}{\frac{1}{2} \frac{4\pi v^2 T}{\lambda R_0} t \sin^2 \theta_0} \tag{10.30}$$

Here the matched filter has been tuned to $f_0 + f_d$. The power spectral density of the filter response is proportional to the square:

$$S(t) \sim \left[\frac{\sin(1/2bTt)}{1/2bTt} \right]^2 \tag{10.31}$$

Figure 10.7 shows the function.

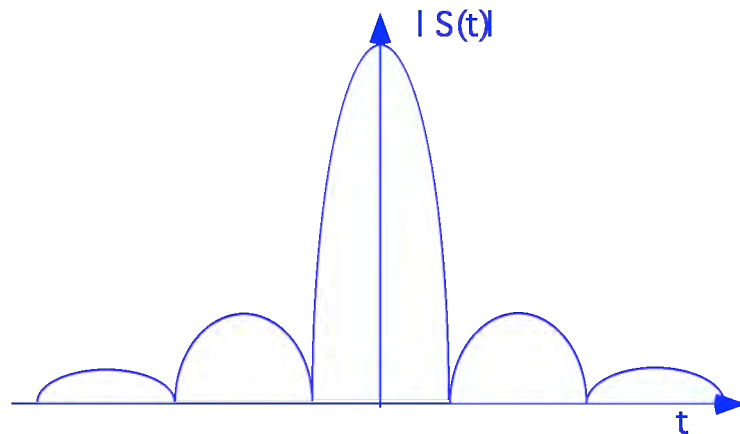


Figure 11110.7 Envelope of the receiving signal of SAR.

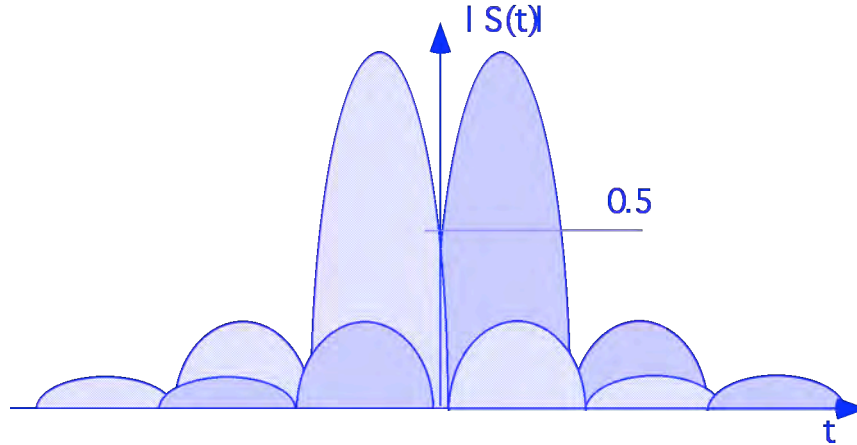


Figure 9.8 Resolution of two signals.

If two neighbouring points reproduce two $(\sin x/x)^2$ responses, then they can be directly resolved if the envelopes are “cut” within the 3 dB points. Here applies:

$$\left(\frac{\sin x}{x}\right)^2 = .5 \text{ with } x = 1.4[\text{rad}] \tag{10.32}$$

The distance of the maximums is $2x$:

$$\Delta t = \frac{2x}{\pi} \cdot \frac{\lambda R_0}{4v^2 T \sin^2 \theta_0} \tag{10.33}$$

Replace $v \cdot T = L$ and calculate the resolution to obtain the following:

$$\Delta t v = D = \frac{2.8}{\pi} \cdot \frac{\lambda R_0}{4L} \frac{1}{\sin^2 \theta_0} \tag{10.34}$$

Other results for the resolution D are stated in literature, for example in [24], which results from different approximations within the processing.

$$D_{\min} = \sqrt{\frac{R_0 \lambda}{2}} \tag{10.35}$$

The processing which has been illustrated until here, is in practice more difficult due to the pulsed transmitting signal. Each rectangular pulse has a spectrum, whose envelope is the Fourier transform of the pulse, and whose linear separation is the pulse sequence frequency. The middle frequency of the received signal has a constant offset around f_d for the transmitting signal:

$$f_d = \frac{2v}{\lambda} \cos \theta \tag{10.36}$$

To this is added the respective offset resulting from the linear FM modulation within the antenna beam-width, which contains the actual information. This means that the reception spectrum shifts towards the transmission spectrum, as shown in Figure 10.9.

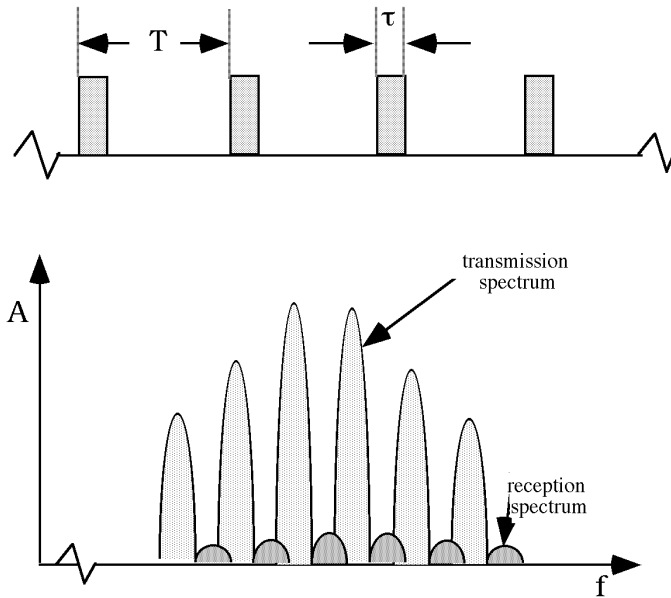


Figure 10.9 Transmission and reception spectrum.

Consequently, the analysis has the following tasks:

- To correctly filter the amplitude and phase of the reception spectrum,
- To apply a Fourier transform to the linear FM.

10.7 PRF Determination

The resolution D of SAR in azimuth is, as has been shown, equal to half of the antenna length $a/2$. For processing a pulse must be available for each resolution cell of the azimuth, since otherwise the optimal resolution cannot be achieved. From this results:

$$f_{p \min} = \frac{1}{T_p} = \frac{v}{D} \sin \theta_0 = \frac{2v}{a} \sin \theta_0 \tag{10.38}$$

To avoid ambiguities in range, the maximum PRF is:

$$f_{p \max} = \frac{c_0}{2\Delta R_{\max}}$$

ΔR_{\max} is the swath width. Thus the following is the range for f_p :

$$\frac{c_0}{2\Delta R_{\max}} > f_p > \frac{2v}{a} \sin \theta_0 \tag{10.40}$$

11 Characteristics of Radar Targets

In this section the characteristics of Radar targets are described for the impingement of electromagnetic waves. Plane waves, whereby only the far field characteristics will be dealt with, can be scattered more or less directed by dielectric or metallic bodies. This scattering is additionally dependent upon polarization. The amount and/or strength of this scattering is described by the RCS (*Radar Cross-Section*). Starting from the conventional definition of the scalar scattering cross-section the fundamentals of Radar polarimetry and the polarization scattering matrix will be entered in this chapter as well as will be introduced new, coherent polarimetric measuring methods, a revised definition of a complex scattering cross-section, a scattering cross-section matrix, and an object oriented polarization scattering matrix.

11.1 Definition of the Radar Backscattering Cross-Section

The common way to define the Radar cross-section is with use of the Radar equation. For a homogenous, loss-less, isotropic medium and a universally bistatic configuration according to Figure 11.1, the Radar cross-section σ is defined by:

$$\sigma = \frac{4\pi}{\lambda_0^2} \left(\frac{P_r L_r}{G_r} 4\pi R_r^2 \right) \left(\frac{L_t}{G_t P_t} 4\pi R_t^2 \right) L_p \quad (11.1)$$

Where r=receiving, t=transmitting, p=polarization, and L=losses.

With this R_r should be so large that the object lies in the far field of the impinging waves as well should $R_r \rightarrow \infty$ (approaching infinity) so that the receiving antenna lies in the far field of the scattering body. If one expresses σ from Equation (11.1) as a relationship of the electric field strength at the receiving antenna to the field strength of the incident plane wave front at the object, then the result is:

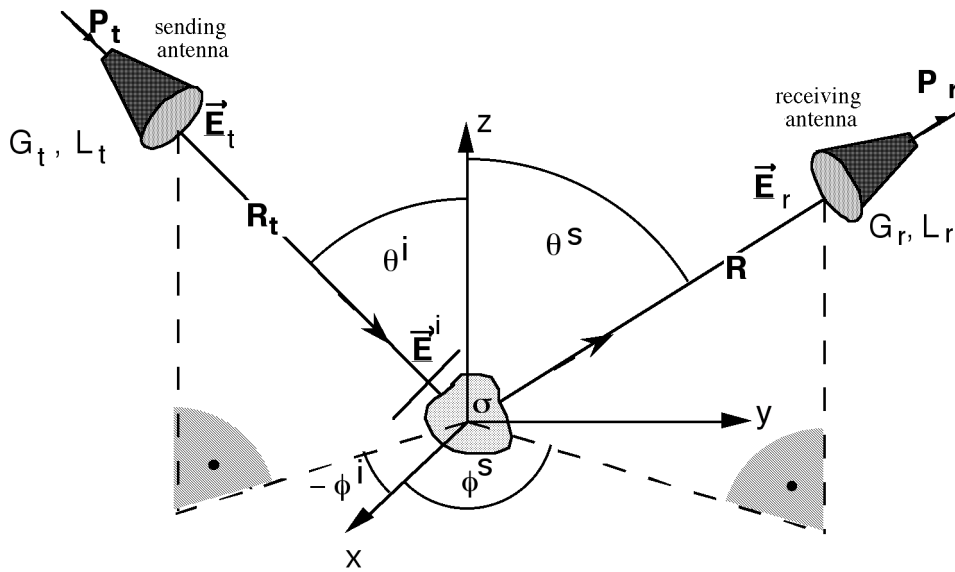
$$\sigma = 4\pi \cdot \lim_{R \rightarrow \infty} R^2 \cdot \frac{\vec{E}^S \cdot \vec{E}^{S*}}{\vec{E}^i \cdot \vec{E}^{i*}} \quad (11.2)$$

Where s=scattered and i=incident.

Usually the cross-section is based on an area of 1m^2 and is stated in dB as

$$\sigma/\text{dBm}^2 = 10 \log \left(\frac{\sigma}{1\text{m}^2} \right).$$

Stated clearly in words the Radar cross-section σ of a target is the projected area of metal sphere (where the projected area of a sphere is a circle with $A=\pi r^2$) which would return the same amount of power to the Radar as the actual target.



x, y, z Coordinates

θ^i, ϕ^i Azimuth and elevation angle of the incident wave front

θ^s, ϕ^s Azimuth and elevation angle of the scattered wave front

R_r Range from origin to the receiving antenna

R_t Range from origin to the transmitting antenna

\vec{E}_t Radiated electric field strength

\vec{E}^i Electric field strength of the incident wave front

\vec{E}_r Electric field strength at the receiving antenna

P_t, P_r Transmitting and receiving power

G_t, G_r Gain of the transmitting and receiving antennas

L_t, L_r Losses at the transmitter and receiver

L_p Losses due to polarization effect (not shown)

Figure 11.1 Transmission scheme and coordinate system with abbreviations for the illustration of the Radar equation for an object according to Equation (11.1).

The given definition applies for the general bistatic case ($\theta^i, \phi^i, \theta^s, \phi^s$ arbitrary). In practice receiving and sending antennas are often identical, meaning $\theta^i = \theta^s$ and $\phi^i = \phi^s$. σ can then be referred to as Radar Backscattering Cross-Section, the Radar geometry being monostatic. If the receiving and sending antennas are not the same, one then speaks of quasi-monostatic Radar if the antennas are close to one another, meaning $\theta^i \approx \theta^s$ and $\phi^i \approx \phi^s$. For further consideration it is important that σ characterizes the target for only one frequency and one polarization at given aspect angles ($\theta^i, \phi^i, \theta^s, \phi^s$) and it doesn't contain any phase information of the scattering.

11.2 Fundamentals of Radar polarimetry

11.2.1 Polarization

An important attribute of scattering, namely polarization and depolarization (the object conditional change of incident to scattered polarization), is only considered with the scalar Radar equation in the form of a general loss term. An arbitrary, polarized, plane wave can always be represented through the linear combination of two orthogonal fields. For example, a wave impinges, coming from $+\infty$ (direction of propagation z), on an object, then the incident electric field reads as a superposition of two linear, orthogonal polarized waves in the linear (horizontal-vertical) reference system.

$$\vec{E}^i = \vec{E}_h^i + \vec{E}_v^i = (\underline{E}_x^i \vec{e}_x + \underline{E}_y^i \vec{e}_y) \cdot e^{j(\omega t + \beta z)} \tag{11.3}$$

For representing a state of polarization the polarization ellipse is frequently used, as in Figure 11.2. It describes a curve, which the real part of the electrical field vector $\vec{E}^i(z,t)$ goes through, if either the position “ z ” is held constant ($z=\text{constant}$) and the time “ t ” runs or the time “ t ” is held constant ($t=\text{constant}$) and the position “ z ” changes. The angle τ between three-dimensional axes and the semi-major axis of the ellipse is called the rotation angle.

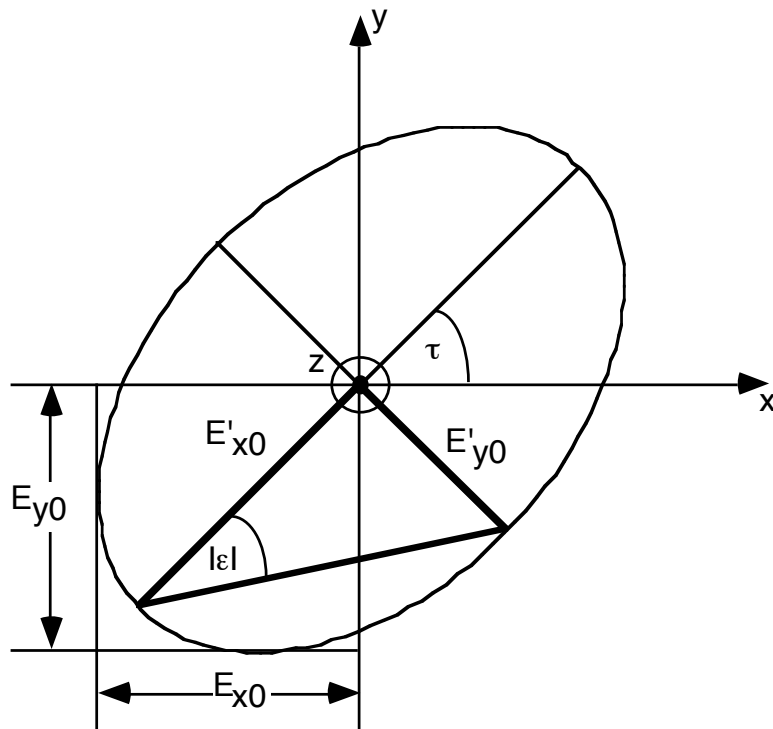


Figure 11.2 Polarization ellipse.

The angle of ellipticity ϵ is defined by the axial relationship m between the semi-major and semi-minor axes of the ellipse.

$$m = |\tan \epsilon| \text{ with } -45^\circ \leq \epsilon \leq +45^\circ$$

Thus waves without ellipticity ($\epsilon=0$) are linearly polarized. Those with $\epsilon=\pm\pi/4$ are circular. With the decision of the propagation direction and of the sign (+/-) the polarization will be defined as left- ($\epsilon>0$) or right-handed ($\epsilon<0$).

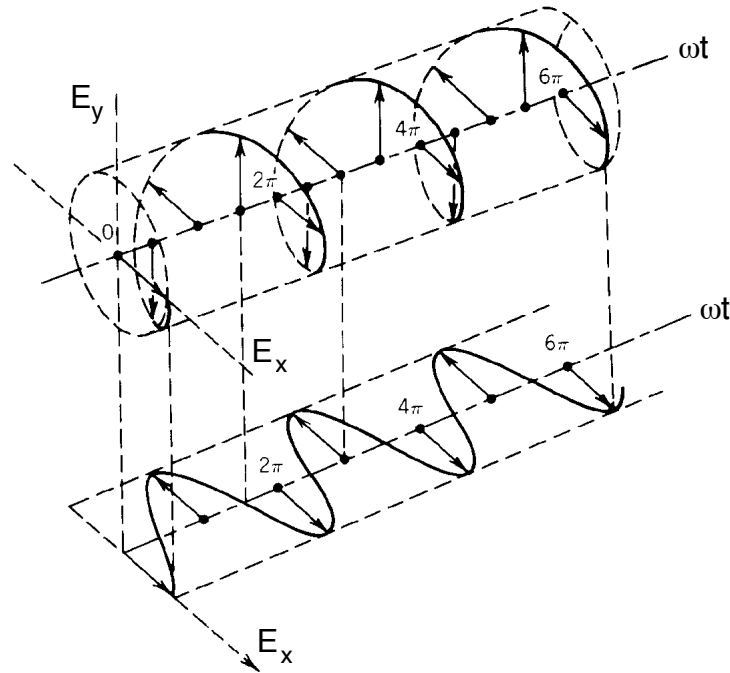


Figure 11.3 Circularly polarized wave.

Figure 11.3 shows the trajectory of an electrical field vector of a circularly polarized wave along the time axis, if a fixed position is considered.

11.2.2 Polarization Scattering Matrix

If one describes an incident wave on an object with “i” and the radiated wave at the receiver with “r” with the superposition of horizontal and vertical polarized electric fields according to

Equation (11.3) the result is:

$$\begin{bmatrix} \underline{E}_h^r \\ \underline{E}_v^r \end{bmatrix} = \begin{bmatrix} \underline{S}_{hh} & \underline{S}_{hv} \\ \underline{S}_{vh} & \underline{S}_{vv} \end{bmatrix} \cdot \begin{bmatrix} \underline{E}_h^i \\ \underline{E}_v^i \end{bmatrix} \quad (11.4)$$

The matrix $[\underline{S}]$ is called the Polarization Scattering Matrix. The four parameters are complex amplitudes, meaning that a scattering object is described by 8 scalar magnitudes. They contain all information about the scattering behaviour of an object with frequency, object orientation, sender and receiver position. Thus far the scattering matrix has been defined in a linear framework (in the following: ξ, η for h,v), since in practice linear polarized antennas are employed. Circular or elliptical “orthogonal” polarized antennas deliver the same information content.

11.3 Complex Radar Cross-Section and RCS Matrix

If $[S]$ and R are known, then σ can be calculated for any arbitrary sender and receiver polarization.

$$\sigma_{\xi\eta} = \lim_{R \rightarrow \infty} 4\pi R^2 \cdot |S_{\xi\eta}|^2 \tag{11.5}$$

The polarization scattering matrix additionally contains phase and polarization information. As is to see from Equation (11.4) and (11.5), the observation distance R is also a parameter, whereby in practice it is only possible to evaluate the parameters relative to each other. In order to eliminate the disadvantages of the conventional definitions of σ and $[S]$, which were introduced in the previous sections, in the following section 2 new terms will be derived, which more adequately fulfill the requirements of coherently measuring Radar systems. They can be looked upon as consequent enhancements of the old definitions and they don't contradict these old definitions. If one introduces a reference range R_0 from the coordinate origin, then reference planes for the incident and scattered wave can be defined according to Figure 11.4. R_0 is thereby an arbitrarily selectable, however fixed radius, which can, for example, coincide with the radius of a reference sphere.

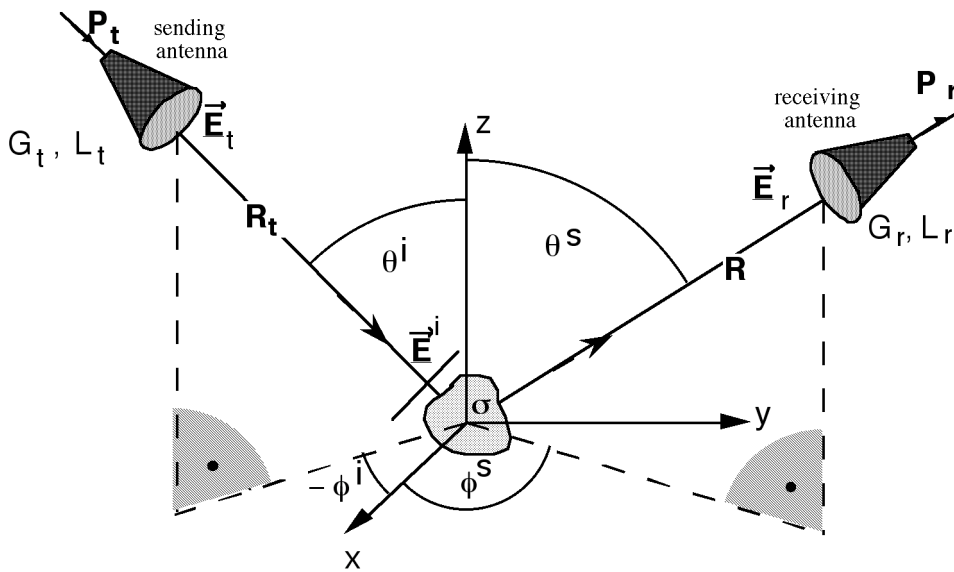


Figure 11.4 Introduction of reference planes with a distance of from the origin, with fixed scattered field.

The incident wave can actually be represented by a plane wave (for $R^i \rightarrow \infty$) at the reference plane R_0 , and consequently a phase and amplitude reference can be created through R_0 . The scattered field, however, can only be represented by a fictitious plane wave at R_0 , since the reference plane is not necessarily in the far-field of the scatterer. This fictitious plane wave-field \underline{E}^s can be defined by the following transformation via the receiving field strength:

$$\underline{\vec{E}}^s = \frac{\sqrt{4\pi R^2}}{\sqrt{4\pi R_0^2}} \cdot e^{j\beta(R-R_0)} \cdot \underline{\vec{E}}^r(R) \tag{11.6}$$

Note: R must lie in the far field of the emitter, however R_0 not.

Clearly is $\underline{\vec{E}}^s$ the field strength with R_0 , brought about by an isotropic emitter at the origin, which affects the receiving field strength $\underline{\vec{E}}^r$ with radius R. Starting from Equations (11.2) and (11.5), the **complex Radar cross-section** $\underline{\sigma}$ can be defined with the transformation from Equation (11.6).

$$\sigma_{\xi\eta} = \lim_{R \rightarrow \infty} 4\pi R^2 \cdot e^{j2\beta(R-R_0)} \cdot \left(\frac{E_{\xi}^r}{E_{\eta}^i} \right)^2 \tag{11.7a}$$

$$= 4\pi R_0^2 \cdot \left| \frac{E_{\xi}^s}{E_{\eta}^i} \right| \cdot e^{j2(\varphi_s - \varphi_i)} \tag{11.7b}$$

- R_0 Range from the origin to the reference planes,
- ξ, η Orthogonal polarizations (vertical or horizontal),
- φ_s Phase of the ξ -components of the scattered field with R_0 ,
- φ_i Phase of the η -components of the incident field with R_0 .

The definition is so chosen that the absolute of $\underline{\sigma}_{\xi\eta}$ coincides with the known Radar cross-section σ from Equation (11.2). The usefulness of the phase definition is most clearly explained by the example of the monostatic measurement. Thereby merge the two reference planes. The measurement of a metallic sphere with radius R_0 results in a phase shift of $\varphi=(\varphi_s-\varphi_i)=180^\circ$ at the sphere forefront. The phase φ behaves like one of the reflection factors by a short circuit and with it defines a unique reference phase. With the definition of the complex Radar cross-section from Equation (11.7) the scattering matrix, according to Equation (11.4), consequently results in a complex Radar cross-section matrix (RCS Matrix).

$$[\underline{\sigma}] = \begin{bmatrix} \sigma_{hh} & \sigma_{hv} \\ \sigma_{vh} & \sigma_{vv} \end{bmatrix} \tag{11.8a}$$

$$\text{with } \begin{bmatrix} E_h^s \\ E_v^s \end{bmatrix} = \frac{1}{\sqrt{4\pi R_0^2}} \cdot [\sqrt{\sigma}] \cdot \begin{bmatrix} E_h^i \\ E_v^i \end{bmatrix} \tag{11.8b}$$

The complex RCS Matrix contains the same information as the polarization scattering matrix, but is not dependent on the observation range, meaning that it is object specific. Correspond-

ingly an object oriented polarization scattering matrix $[\underline{S}^0]$ can be introduced by means of Equation (11.8b), for which applies:

$$[\underline{S}^0] = \left[\sqrt{\frac{\underline{\sigma}}{m^2}} \right] \quad (11.9)$$

11.4 RCS Measurement Techniques

It is possible to distinguish between the following principle procedures in RCS measurement techniques:

- Scalar RCS measurements $\Rightarrow \sigma, S$
- Complex RCS measurements $\Rightarrow \underline{\sigma}, \underline{S}$
- Polarimetric RCS measurements $\Rightarrow [\underline{\sigma}], [\underline{S}]$

These types of modulation have a considerable influence on the measurement system:

- Pulse modulation,
- FM-CW modulation,
- Stepped frequency (CW)

Measurements can be carried out in closed, low-reflective rooms, so-called anechoic chambers, and in open-air.

11.4.1 Measurement of the Scalar Radar Cross-Section σ

RCS measurements have been common since the introduction of Radar technology. They have been carried out for the determination of σ as well as scattering diagrams $\sigma = f(\Theta)$. For this conventional Radar devices are frequently used. The technology is comparable to the measurement of antennas; there are similar given technical requirements and legalities to consider. The primary difference is the increased attenuation over the range of the measurement signal, which travels twice along the path from the measurement antenna to the measurement object. Measuring paths in absorption chambers the attenuation is 100 dB to 150 dB for common measuring distances of 10 to 20 m. In large free-space test ranges the attenuation is considerable higher. This value, plus the required dynamic for the measurement of 30 dB to 60 dB, yield the required decoupling between the transmitting and receiving sectors of 130 dB to 200 dB. The procedures for measuring scalar RCS will not be further discussed, instead, in the following the concentration will be on polarimetric RCS determination.

11.4.2 Measurement of The Complex Polarization Scattering Matrix

The Radar signature of scattering objects, expressed by the complex RCS $\underline{\sigma}$, is a function of various parameters:

$$\underline{\sigma} = f(\text{frequency, polarization, aspect angle})$$

The requirements of the measuring system for an as complete as possible description of the scattering object result accordingly:

Broadband, if possible more than an octave,

Coherent, for measuring a complex Radar cross-section $\underline{\sigma}$

Measurement of the complex polarimetric RCS Matrix,

Variable aspect angle ($\theta^i, \phi^i, \theta^s, \phi^s$)

Additionally, possibilities for the separation of disruptive influences, for calibrating the RCS Matrix as well as for acquiring the measurement data, must be available. Present Radar systems inadequately fulfill these demands.

Since 1984 there has been a new generation of modern vector-network analyzers, conceived for the measurement of microwave components. Such vector-network analyzers (VNWA) can be employed as the core of a new type of RCS measurement system, especially for use in laboratories. The fundamental principle had been described for the first time in 1974 and the first realization was introduced in 1985. Already with the still simple and non-sophisticated structures advantages could be shown compared to conventional Radar systems, like linear FM Radar or pulse Radar. In this way the sum of such characteristics, as sensitivity, dynamic range, reproducibility, coherency, polarimetry and bandwidth, have been greatly advanced by new orders of magnitude.

Figure 11.5 shows a simplified block diagram of the Radar cross-section measurement procedure upon the basis of vector-network analysis for the case of a quasi-monostatic, polarimetric antenna configuration. A frequency synthesizer transmits discrete frequencies over the measuring bandwidth during a cycle. A part of the power is fed into a reference channel and builds the magnitude and phase reference. The passing signal is radiated from the transmitting antenna.

The polarimetric antenna system consists of 2 antennas, each with orthogonal polarization (vertical and horizontal). With a HF emitter successive horizontal and vertical polarized signals are sent, while both polarizations are simultaneously fed into the measuring channels. In the receiver the signals of the test and reference channel are converted to IF in a phase-preserving way. Then, the ratio of both signals according to magnitude and phase is calculated. This relationship yields the non-calibrated RCS of the measuring objects. With the VNWA principle it is important that the obtained phase information remains and the crucial noise bandwidth for the sensitivity is determined by the narrow filter width of the IF stage (in the order of a few kHz) and not by the full measuring bandwidth (typically some GHz).

In principle the RCS measuring system is a CW Radar, however with substantially extended abilities. Equipment of this kind is called instrumentation Radar. The Fourier transform of the signals, received in the frequency range, into the time domain corresponds to a pulse response with a resolution corresponding to the measuring bandwidth. This procedure is related to pulse compression.

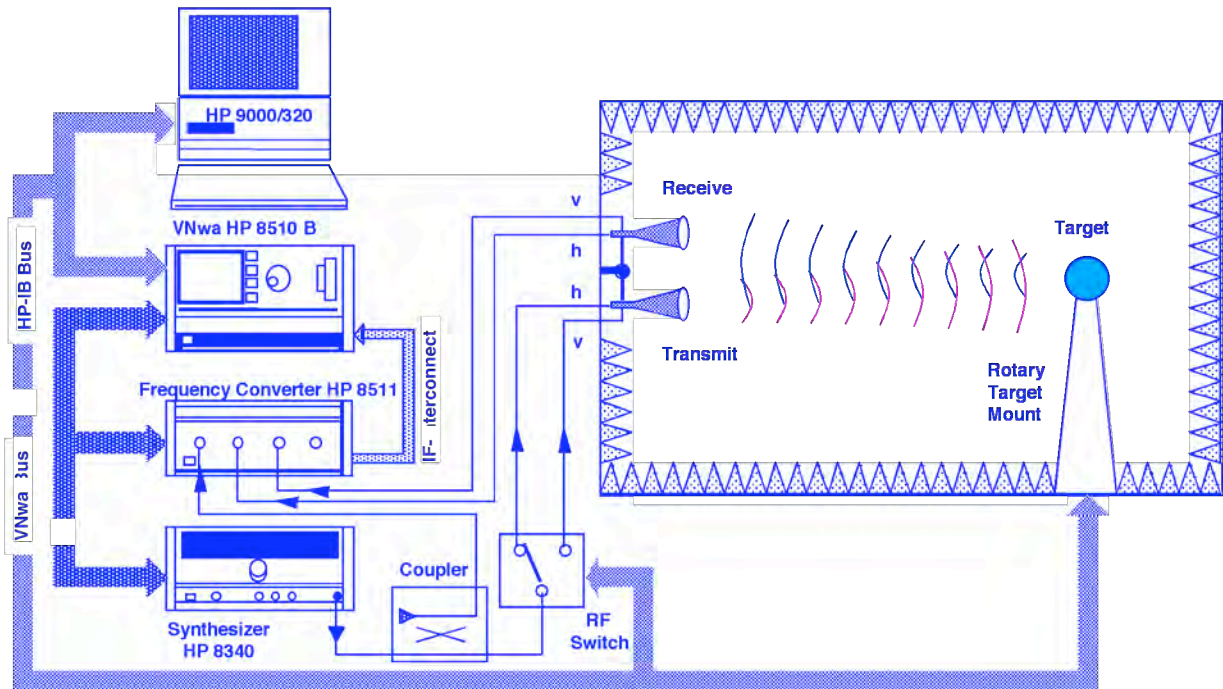


Figure 11.5 Wideband polarimetric RCS measurement station with a quasi-monostatic antenna system.

11.4.3 Calibration and Error Correction for Polarimetric RCS Measurements

In Figure 11.6 a typical polarimetric measurement system is schematically shown for RCS and antenna measuring technology. The measurement system is complete in block 1 of Figure 11.6. The measuring object of interest is represented in block 3, where the transmitting and receiving paths are shown respectively in block 2 and 4. In the available case the system is polarimetrically constructed with two linear, orthogonal polarizations. This will be maintained in the following without restriction of the general validity, since any other arbitrary orthogonal polarization can be derived from it.

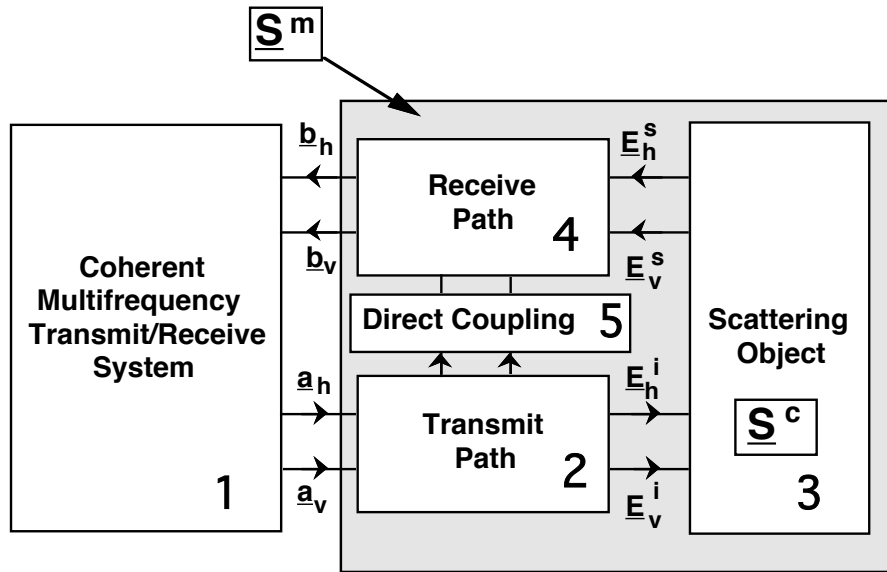


Figure 11.6 Schematic block diagram of a polarimetric RCS measurement system.

There are two distinguishable error categories with measurement systems: systematic errors and statistical errors. The following error model exclusively corrects the systematic errors, while the statistical errors can normally be reduced through integration. The error model considers the following contributions:

- Error due to the environment (e.g. non-ideal anechoic measurement chamber),
- Error due to the coupling of the transmitting into the receiving channel,
- Errors, which have been caused due to the coupling between the orthogonal receiving channels of the polarimetric measurement system (antenna as well as cables and electronics),
- Errors, which arise due to the coupling of the transmitting channel
- Errors, which arise along the transmission path.

The used measuring system measures complex voltages or power waves ($\sqrt{\text{Watt}}$). Therefore it is favourable to describe the behaviour of the object by its complex scattering matrix $[S^c]$. The measuring system doesn't have direct access to the object, as is obvious to see in Figure 11.6. It determines the incoming waves a_h & a_v and the outgoing waves b_h & b_v , whereby h and v respectively symbolize horizontal and vertical polarization. The correct scattering matrix $[S^c]$ can consequently not be directly determined. The matrix is measured $[S^m]$, which additionally to $[S^c]$ still considers the transmission and receiving paths $T_{\xi\eta}$ & $R_{\xi\eta}$, as well as the direct isolation $I_{\xi\eta}$. The entire measuring system can be described with the scattering matrices upon this basis:

$$[S^m] = [I] + [R][S^c][T] \tag{11.10}$$

In component form Equation (11.10) reads:

$$\begin{bmatrix} \underline{S}_{hh}^m & \underline{S}_{hv}^m \\ \underline{S}_{vh}^m & \underline{S}_{vv}^m \end{bmatrix} = \begin{bmatrix} \underline{I}_{hh} & \underline{I}_{hv} \\ \underline{I}_{vh} & \underline{I}_{vv} \end{bmatrix} + \begin{bmatrix} \underline{R}_{hh} & \underline{R}_{hv} \\ \underline{R}_{vh} & \underline{R}_{vv} \end{bmatrix} \begin{bmatrix} \underline{S}_{hh}^c & \underline{S}_{hv}^c \\ \underline{S}_{vh}^c & \underline{S}_{vv}^c \end{bmatrix} \begin{bmatrix} \underline{T}_{hh} & \underline{T}_{hv} \\ \underline{T}_{vh} & \underline{T}_{vv} \end{bmatrix}$$

$$\begin{aligned} [S^c] &= \text{correct, wanted magnitudes} & R_{\xi\eta} &= \text{receiving path} \\ T_{\xi\eta} &= \text{Transmission path} & I_{\xi\eta} &= \text{isolation} \\ [S^m] &= \text{measurable magnitudes} \end{aligned} \quad (11.11)$$

Indices describe the respective polarizations (horizontal and vertical). Same indices mean co-polarization and different indices mean cross-polarization. All terms $\underline{I}_{\xi\eta}$, $\underline{T}_{\xi\eta}$ and $\underline{R}_{\xi\eta}$ contribute to the determination of $\underline{S}_{\xi\eta}$ as complex magnitudes. The error model itself is constructed based upon this scattering parameter description of the signal path. The measured magnitudes (m) result from the corrected magnitudes (c) due to additive and multiplicative error influences. In Equation (11.11) the complete mathematical model is given in matrix form.

The Equation (11.11) is not suitable to demonstrate the physical interpretation of the errors, as well as the vectorial correction. A form often used in scattering parameter technology, as such to represent graphical relationships, is the signal flow graph according to Mason. With it the relationship between the measured scattering matrix $[\underline{S}^m]$ and $[\underline{S}^c]$ can be described. Because of the many crossovers of the paths, which arise with a polarimetric system, a three-dimensional representation is advantageous. In Figure 11.7 this 3-D signal flow graph is demonstrated by a cube, with which lie the signal paths on the edges and diagonals. It is in the coming text referred to as an error cube. The polarimetric in and output gates, which $[\underline{S}^m]$ and/or \underline{a}_h , \underline{a}_v and \underline{b}_h , \underline{b}_v demonstrates, are in the foremost 4 corners of the cube. The front surface of the cube is therefore identified as the Radar plane. This front surface contains the isolation errors $\underline{I}_{\xi\eta}$, which arise due to the over-coupling between the receiving and sending channels, as well as reflections from the environment. The transmitting and receiving paths ($\underline{T}_{\xi\eta}$ & $\underline{R}_{\xi\eta}$) are on the side surfaces of the cube and respectively represent the transmitting and receiving planes. The edges describe the desired direct co-polarization signal paths. The diagonals describe the unwanted cross-polarization effects, which are caused by the measuring system (e.g. polarization purity of the antenna). They link the horizontal plane (top surface of the cube) and the vertical plane (underside of the cube) across the transmitting and receiving path. The backside of the cube, the so-called object plane, describes the actual object scattering matrix $[\underline{S}^c]$. Input magnitudes of the object plane are the co- and cross-polarized signal paths of the transmitting plane. Output magnitudes are those scattered from the object into the receiving plane. The co-polarization scattering parameters \underline{S}_{vv} and \underline{S}_{hh} are on the upper and lower edges of the object plane, while the diagonals represent the cross-polarization parameters \underline{S}_{vh} and \underline{S}_{hv} . All signal paths are uni-directional.

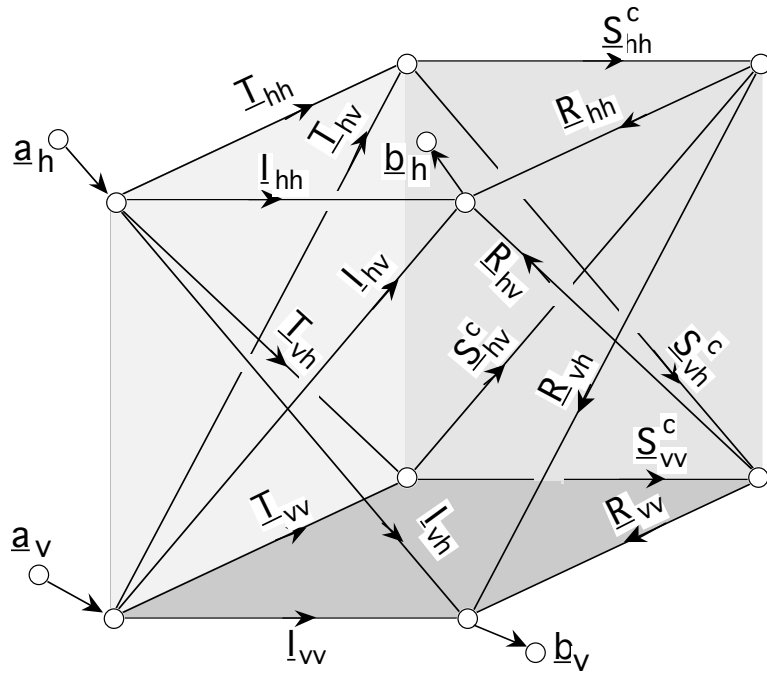


Figure 11.7 Three-dimensional, graphical error model (error cube).

The determination of the individual paths, meaning $\underline{I}_{\xi\eta}$, $\underline{T}_{\xi\eta}$ and $\underline{R}_{\xi\eta}$ are based on the measurement of reference objects, whose scattering matrix is exactly known. It is, however, not possible to individually determine $\underline{R}_{\xi\eta}$ and $\underline{T}_{\xi\eta}$. This is understandable, if one multiplies the matrix product in Equation (11.11) out and arranges the quadratic matrices in vector form, as is presented in Equation (11.12). All measurements result from a product $\underline{R}_{\xi\eta} \cdot \underline{T}_{\xi\eta}$ of the transmitting and receiving path.

$$\begin{bmatrix} \underline{S}_{vv}^m - \underline{I}_{vv} \\ \underline{S}_{hh}^m - \underline{I}_{hh} \\ \underline{S}_{vh}^m - \underline{I}_{vh} \\ \underline{S}_{hv}^m - \underline{I}_{hv} \end{bmatrix} = \begin{bmatrix} \underline{R}_{vv} \underline{T}_{vv} & \underline{R}_{vh} \underline{T}_{hv} & \underline{R}_{vv} \underline{T}_{hv} & \underline{R}_{vh} \underline{T}_{vv} \\ \underline{R}_{hv} \underline{T}_{vh} & \underline{R}_{hh} \underline{T}_{hh} & \underline{R}_{hv} \underline{T}_{hh} & \underline{R}_{hh} \underline{T}_{vh} \\ \underline{R}_{vv} \underline{T}_{vh} & \underline{R}_{vh} \underline{T}_{hh} & \underline{R}_{vv} \underline{T}_{hh} & \underline{R}_{vh} \underline{T}_{vh} \\ \underline{R}_{hv} \underline{T}_{vv} & \underline{R}_{hh} \underline{T}_{hv} & \underline{R}_{hv} \underline{T}_{hv} & \underline{R}_{hh} \underline{T}_{vv} \end{bmatrix} \begin{bmatrix} \underline{S}_{vv}^c \\ \underline{S}_{hh}^c \\ \underline{S}_{vh}^c \\ \underline{S}_{hv}^c \end{bmatrix} \quad (11.12)$$

The explicit formulation of Equation (11.12) introduces the formal coefficients \underline{c}_{ij} :

$$\begin{bmatrix} \underline{S}_{vv}^m - \underline{c}_{10} \\ \underline{S}_{vv}^m - \underline{c}_{20} \\ \underline{S}_{vh}^m - \underline{c}_{30} \\ \underline{S}_{hv}^m - \underline{c}_{40} \end{bmatrix} = \begin{bmatrix} \underline{M}_{vv} \\ \underline{M}_{hh} \\ \underline{M}_{vh} \\ \underline{M}_{hv} \end{bmatrix} = \begin{bmatrix} \underline{c}_{11} & \underline{c}_{12} & \underline{c}_{13} & \underline{c}_{14} \\ \underline{c}_{21} & \underline{c}_{22} & \underline{c}_{23} & \underline{c}_{24} \\ \underline{c}_{31} & \underline{c}_{32} & \underline{c}_{33} & \underline{c}_{34} \\ \underline{c}_{41} & \underline{c}_{42} & \underline{c}_{43} & \underline{c}_{44} \end{bmatrix} \begin{bmatrix} \underline{S}_{vv}^c \\ \underline{S}_{hh}^c \\ \underline{S}_{vh}^c \\ \underline{S}_{hv}^c \end{bmatrix} \quad (11.13)$$

These coefficients will be referred to as error coefficients in the coming sections. The four additive coefficients \underline{c}_{i0} are identical with $\underline{I}_{\xi\eta}$ and contain the isolation error and the room reflection. The 16 terms of \underline{c}_{ij} result from the transfer coefficients $\underline{T}_{\xi\eta}$ und $\underline{R}_{\xi\eta}$. The diagonal elements contain the frequency response error. The elements \underline{c}_{12} , \underline{c}_{21} , \underline{c}_{34} and \underline{c}_{43} result from

the final polarization purity of both orthogonal channels. The 16 coefficients can be expressed by 8 remaining coefficients through mutual sequential substitution, due to the relationship from Equation (11.14). A favourable solution is given with Equation (11.14).

$$[C] = \begin{bmatrix} c_{11} & \frac{c_{32} \cdot c_{42}}{c_{22}} & \frac{c_{32} \cdot c_{11}}{c_{22}} & \frac{c_{33} \cdot c_{42}}{c_{22}} \\ \frac{c_{31} \cdot c_{41}}{c_{22}} & c_{22} & \frac{c_{33} \cdot c_{41}}{c_{22}} & \frac{c_{31} \cdot c_{22}}{c_{22}} \\ c_{11} & c_{22} & c_{11} & c_{33} \\ c_{31} & c_{32} & c_{33} & \frac{c_{32} \cdot c_{31}}{c_{33}} \\ c_{41} & c_{42} & \frac{c_{42} \cdot c_{41}}{c_{44}} & c_{44} \end{bmatrix} \quad (11.14)$$

Beginning from equation (11.14) to (11.13) leads to a solvable homogeneous set of equations with 8 unknown quantities. This system can be solved according to the coefficients c_{ij} by the measurement of three reference objects with known scattering matrices $[S^{c1}]$, $[S^{c2}]$ and $[S^{c3}]$. The single assumption the calibration object, however not the eventual measuring object, should satisfy the requirement $S_{vh}^{ci} = S_{hv}^{ci}$. This is a very advantageous stipulation, since objects with defined $S_{vh} \neq S_{hv}$, are difficult to realize, at least with monostatic RCS. Nevertheless, the calibration is valid even when measuring objects with $S_{vh} \neq S_{hv}$, i.e. for anisotropic reflectors. The following objects have proven themselves as favourable, since they exhibit linear independent scattering matrices:

Metallic sphere $[S_{\text{sphere}}] = |S_{\text{sphere}}(f)| \cdot \begin{bmatrix} 1 & 0 \\ 0 & 1 \end{bmatrix}$

Vertical dihedral (two-plate) reflector $[S_{\text{DH}}^{0^\circ}] = |S_{\text{DH}}^{0^\circ}(f)| \cdot \begin{bmatrix} 1 & 0 \\ 0 & -1 \end{bmatrix}$

45° rotated dihedral (two-plate) reflector $[S_{\text{DH}}^{45^\circ}] = |S_{\text{DH}}^{45^\circ}(f)| \cdot \begin{bmatrix} 0 & 1 \\ 1 & 0 \end{bmatrix}$

The isolation error c_{i0} , which merely represents an additive term in Equation (11.13), can be determined by measuring for an empty room (no object in the measurement chamber):

- empty room $[S_{\text{empty room}}] = \begin{bmatrix} 0 & 0 \\ 0 & 0 \end{bmatrix}$

By inverting the system in Equation (11.12) one obtains the desired scattering matrix $[S^c]$ of an unknown object from the measurement $[S^m]$:

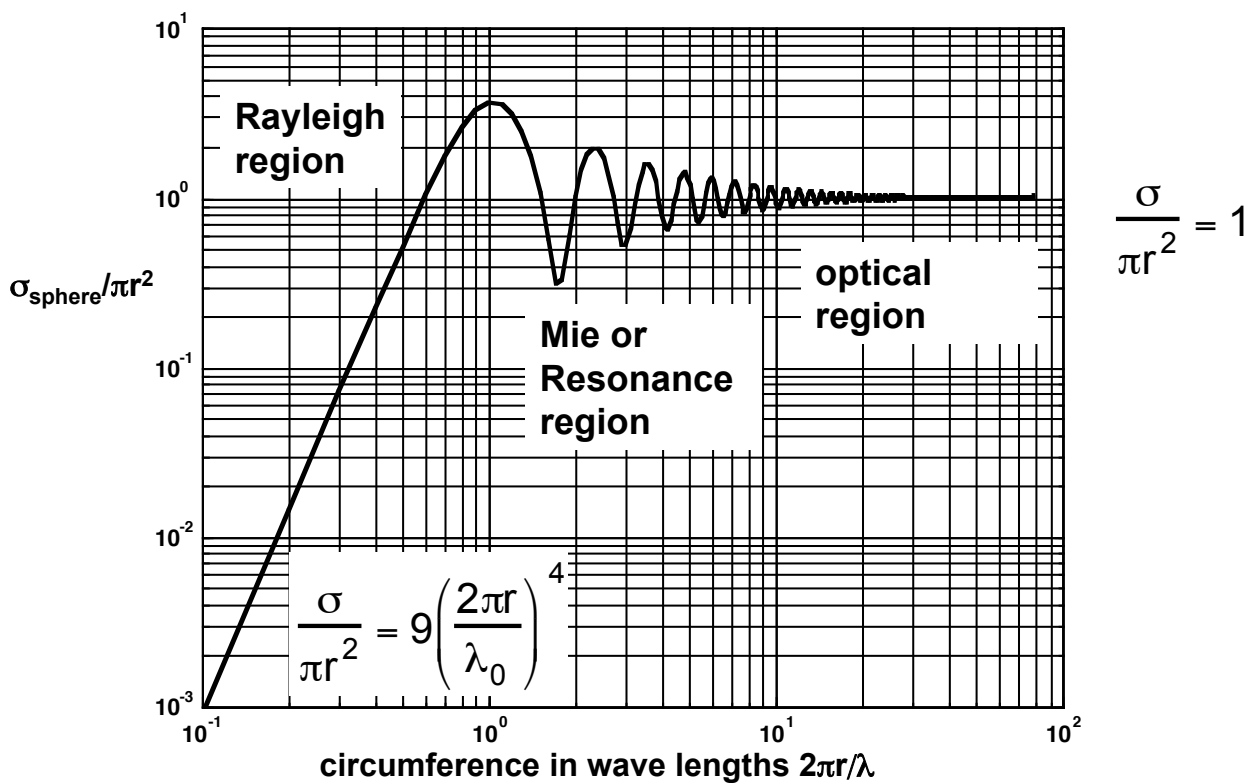
$$[S^c] = [C]^{-1} [S^m] \quad (11.15)$$

11.5 Radar Cross-Section of Simple Objects

The behaviour of the Radar backscattering cross-section as a function of the parameters listed in section 11.1 is best understood by the consideration of simple bodies, of which will be discussed in the following sections.

11.5.1 Sphere

In practice the sphere is the simplest available scattering body. Since the sphere offers the same view from all approaching directions, the back scattering is independent on the rotation of the sphere. The Radar backscattering cross-section of a sphere is represented in Figure 11.8



as a function of circumference normalized by the wavelength.

Figure 11.8 Radar backscattering cross-section of a sphere (r = sphere radius, λ = wavelength).

Three regions can be clearly distinguished:

$$2\pi r / \lambda \ll 1$$

The area, in which the sphere circumference is very small compared to the wavelength, is called the Rayleigh region. Lord Rayleigh investigated the scattering of light by precipitation in 1870. The results apply in the same manner for Radar technology. In the Rayleigh region the Radar backscattering cross-section, normalized by the geometric cross-sectional area, is proportional to r^4 and consequently squarely proportional to the cross-sectional area:

$$\frac{\sigma}{\pi r^2} = 9 \left(\frac{2\pi r}{\lambda_0} \right)^4 \quad (11.16)$$

For Radar technology this region is the most interesting, since there is scattering by precipitation of up to approximately 70 GHz in this region.

$$2\pi r / \lambda \gg 1$$

This region, in which the sphere circumference is much larger than the wavelength, is known as the optical region. In this region the Radar backscattering cross-section is proportional to the cross-sectional area $r^2\pi$.

$$\frac{\sigma}{\pi r^2} = 1 \quad (11.17)$$

For Radar technology this is of interest, since this result corresponds to the definition of the Radar cross-section. Theoretically the sphere thus would be the ideal calibration standard for Radar devices and Radar backscattering cross-sectional measurements. That it is still seldom used is due to the relatively low reflection capability compared to the physical size. The Radar backscattering cross-section of a sphere of 1 m diameter is .79 m² in the optical range.

$$2\pi r / \lambda \approx 1$$

The range between the two extremes is called the "Mie" or resonance region. Here the Radar backscattering cross-section is strongly dependent upon frequency. The largest maximum amounts to approximately 5.7 dB, and the lowest minimum is nearly 4 dB under $r^2\pi$. A simple relationship is however here not stated. The Radar backscattering cross-section is independent from the aspect angle, conditional upon the symmetry. The RCS Matrix of the sphere has the form:

$$\left[\underline{S}_{\text{sphere}} \right] = \left| \underline{S}_{\text{sphere}}(f) \right| \cdot \begin{bmatrix} 1 & 0 \\ 0 & 1 \end{bmatrix} \quad (11.18)$$

The time domain representation in Figure 11.9 shows the Radar pulse response calculated from the measurements for a sphere with a diameter of 3.6 cm and with 14 GHz bandwidth. The backscattered wave results from a portion, which is directly reflected on the forefront of the sphere (optical portion) – first maximum of the impulse response – as well as from a portion, which "creeps" around the sphere (creeping wave). The distance between both maxima is calculated to twice the radius of the sphere plus half of the circumference.

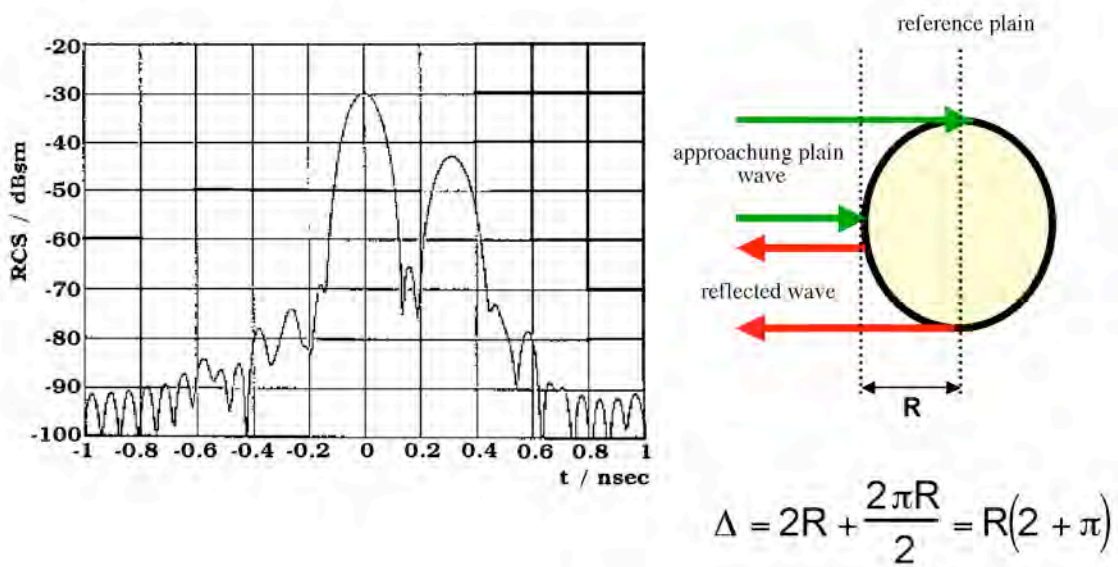


Figure 11.9 RCS $|\sigma|$ of a gold-plated metal sphere ($\varnothing=3.6\text{cm}$) in the time domain (measured frequency ranges is 3-17 GHz).

11.5.2 Circular Disks

Through the integration over the circular area (according to Figure 11.10) results the calculation of the Radar backscattering cross-section of a circular disk with $r \gg \lambda$, just as in antenna technology for homogenous arrangement.

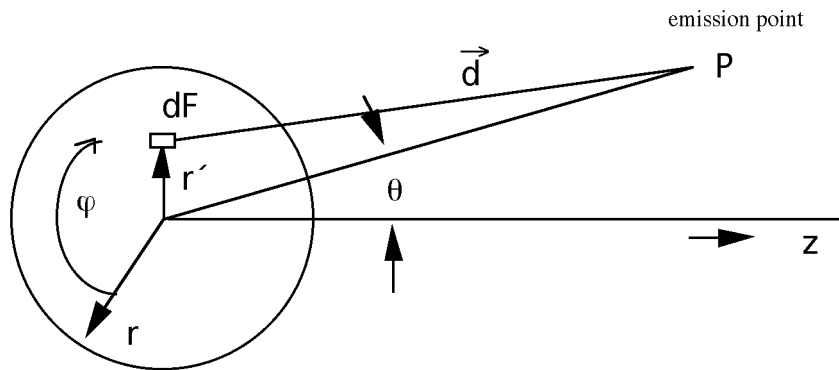


Figure 11.10 Geometry for calculating the Radar backscattering cross-section (Aufpunkt = emission point).

$$\sigma \propto \int_{r=0}^r \int_{\varphi=0}^{2\pi} \vec{d} d\varphi dr \tag{11.19}$$

$$\vec{d} = f(r', \varphi, \theta), \theta = \text{aspect angle}$$

The result of the integration reads:

$$\sigma = r^2 \pi \cos^2 \theta J_1^2 \left(\frac{4\pi r}{\lambda} \sin \theta \right) \quad (11.20)$$

For orthogonal incidence one obtains the following from Equation (11.20)

$$\sigma = \frac{4\pi^3 r^4}{\lambda^2} = G \cdot A_w \quad (11.21)$$

Where A_w = surface of the disk and the disk is assumed to be infinitesimally thin. A disk with a diameter of 1 m has a Radar backscattering cross-section of 8610 m² with a frequency of 10 GHz.

11.5.3 Arbitrary Flat Disk

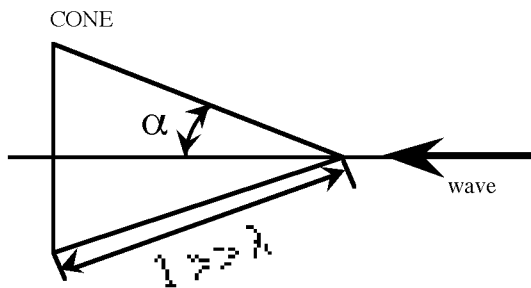
Again under the assumption that the dimensions are much larger than the wavelengths, one obtains the corresponding equation from Equation (11.21):

$$\sigma = \frac{4\pi A_w^2}{\lambda^2} = G \cdot A_w \quad (11.22)$$

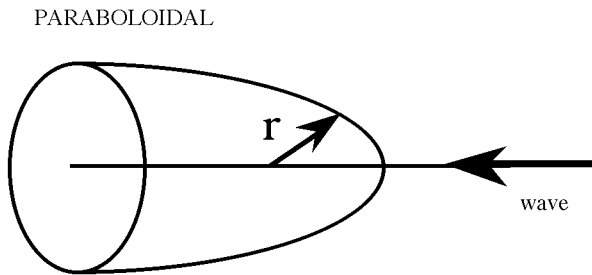
$$A_w = \text{disk surface}$$

The Radar backscattering cross-section of the disk can be obtained from the consideration that the gain is equal to $4\pi A_w / \lambda^2$ and this is to be multiplied with the area A_w , which is taken from the radiation field.

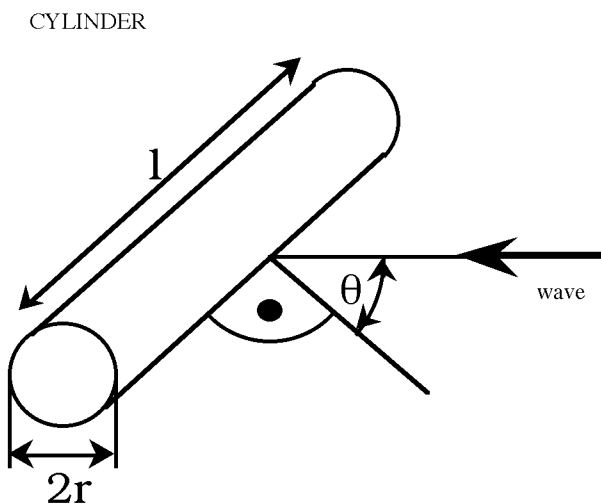
11.5.4 Radar Cross-Section of Further Simple Bodies



$$\sigma = \frac{\lambda^2}{\pi 16} \tan^4 \alpha$$



$$\sigma = r^2 \pi$$



$$\sigma = \frac{r \lambda \cos \theta \sin^2 (\beta l \sin \theta)}{2\pi \sin^2 \theta}$$

for $\theta=0$ $\sigma = \frac{2\pi r l^2}{\lambda}$

for θ small $\sigma = \frac{r \lambda}{2\pi \theta^2}$

11.6 Calibration Standards for Free Space Measurements

11.6.1 Luneburg Lenses

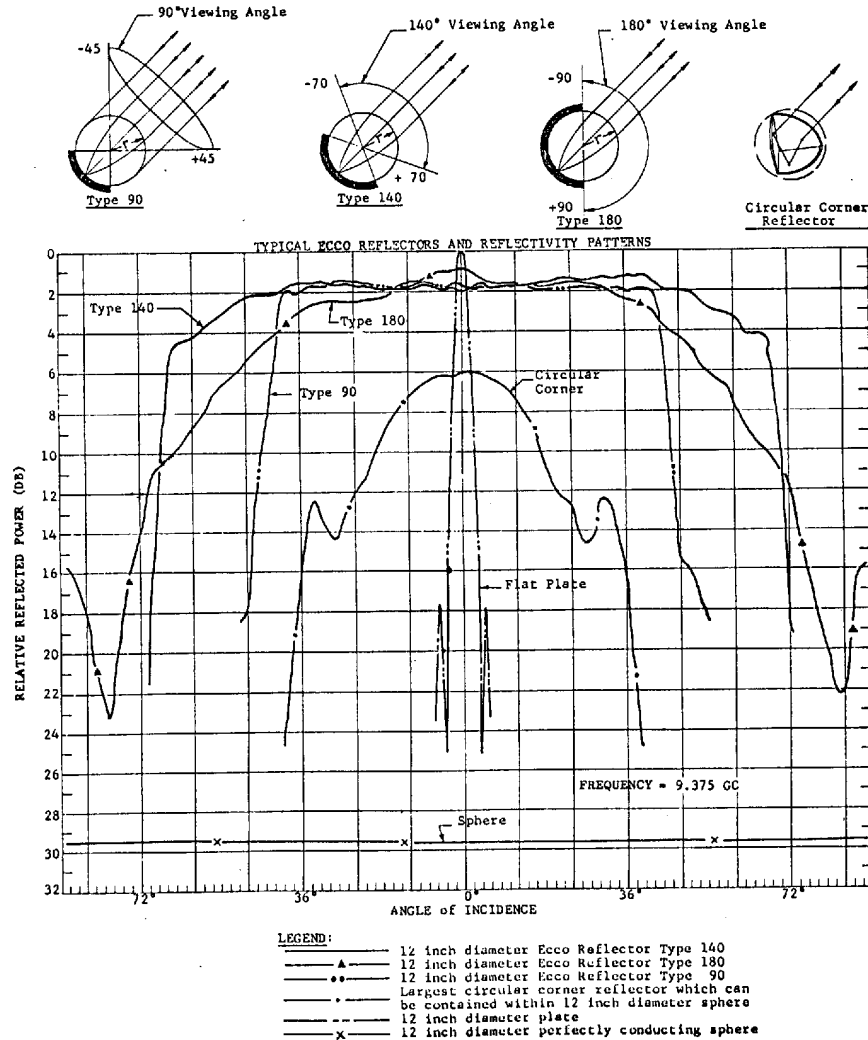


Figure 11.11 Reflection behaviour from Luneburg lens reflectors.

As mentioned earlier, spheres, which would be favourable from their characteristics, have Radar backscattering cross-sections, which are too small. However, reflectors from Luneburg lenses have similar characteristics with a considerably larger Radar backscattering cross-section. Luneburg lenses are spherical objects made from individual dielectric shells, whose refractive index n from outside inward is in accordance with the function:

$$n = \sqrt{2 - \left(\frac{r}{R_0}\right)^2} \tag{11.23}$$

$R_0 = \text{outer radius}$

These Luneburg lenses have the property to concentrate an incoming wave at a point of the opposite outer side. If one mounts a reflector there then the signal will be completely reflected in the incident direction. The losses are commonly very small and can be calculated. The described property is demonstrated in Figure 11.11.

11.6.2 Corner Reflectors

As for further calibration standards, so-called corner reflectors are becoming used for scalar RCS measurements:

Dihedral Corner,

Trihedral Corner.

With these corner reflectors the maximum of the re-radiation diagrams is broadly developed. σ can be calculated precisely and is large. Figure 11.12 shows a corner reflector with triangular side surfaces. In Figure 11.13 is a tabular summary of the data for a few reflectors. A Trihedral corner with an edge length of 1 m has a projection area of .58 m² and a σ of approximately 4500 m² with a frequency of 10 GHz.

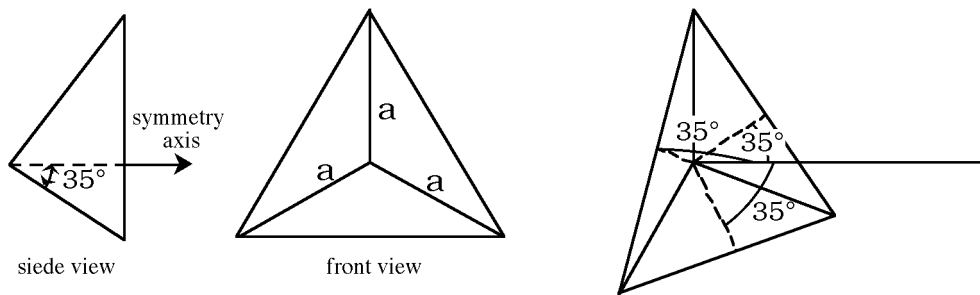


Figure 11.12 Trihedral corners.

The re-radiation characteristics are represented in Figure 11.14. Representative is the distinct broad maximum. This is clearly obvious in the three-dimensional representation.

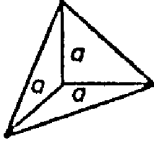
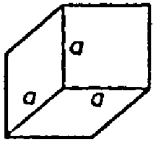
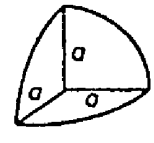
REFLECTOR TYPE	DIMENSION	MAX PROJECTION PLAIN F_p	REFLECTED RAY GAIN $G_{max} = \frac{4\pi F_w^2}{\lambda^2 F_p}$	RADAR CROSS SECTION $\sigma = GF_p = \frac{4\pi F_w^2}{\lambda^2}$
TRIPLE CORNER WITH TRIANGULAR SIDE WALLS		$\frac{\sqrt{3}a^2}{2}$	$4.9 \left(\frac{a}{\lambda}\right)^2$	$\frac{4}{3}\pi \frac{a^4}{\lambda^2}$
TRIPLE CORNER WITH SQUARE SIDE WALLS		$\sqrt{3}a^2$	$21.8 \left(\frac{a}{\lambda}\right)^2$	$12\pi \frac{a^4}{\lambda^2}$
TRIPLE CORNER WITH CIRCULAR SECTOR SIDE WALLS		$\frac{\sqrt{3}\pi a^2}{4}$	$13.1 \left(\frac{a}{\lambda}\right)^2$	$\frac{16}{3}\pi \frac{a^4}{\lambda^2}$

Figure 11.13 Corner reflectors.

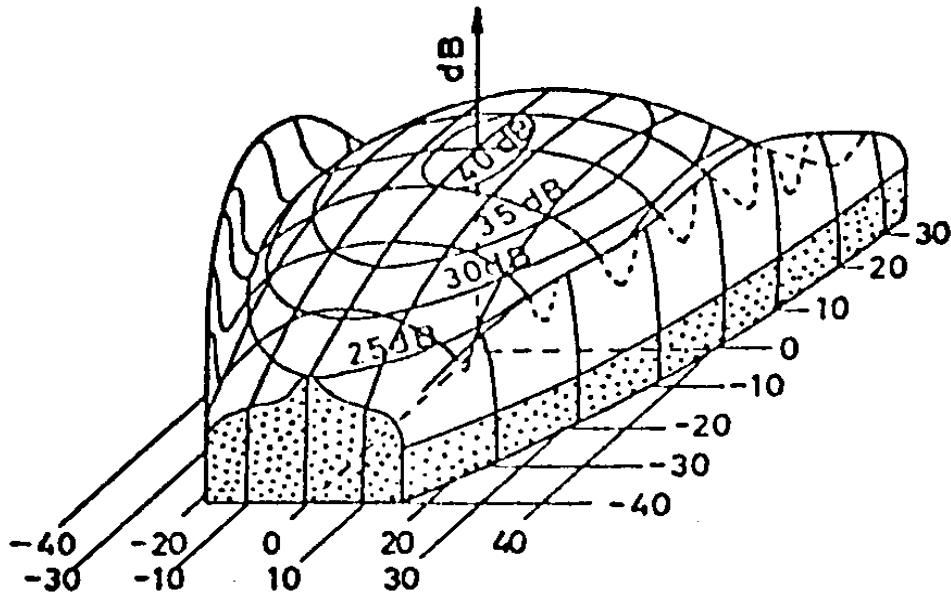


Figure 11.14 Three-dimensional representation of the Radar backscattering diagrams of a trihedral corner reflector.

The number of phase shifts of the reflection changes with trihedral corners dependent on the incidence angle of the wave, as shown in Figure 11.15.

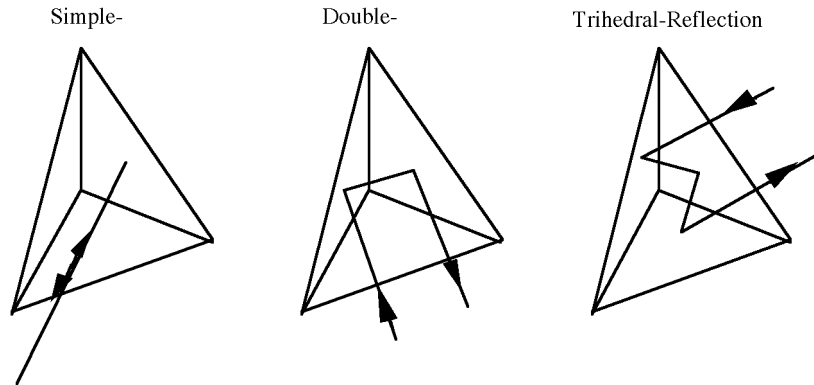


Figure 11.15 Types of reflections with trihedral corners.

For a circularly polarized wave the rotational direction changes with each phase shift of the electrical field strength between right-handed circularly and left-handed circularly polarized. For measurements over 360° corner reflectors are bundled into so-called clusters. Cluster reflectors are primarily employed for the marking of position (e.g. Ships, balloons, towers, etc.). Examples with the corresponding Radar backscattering diagrams are shown in Figure 11.16.

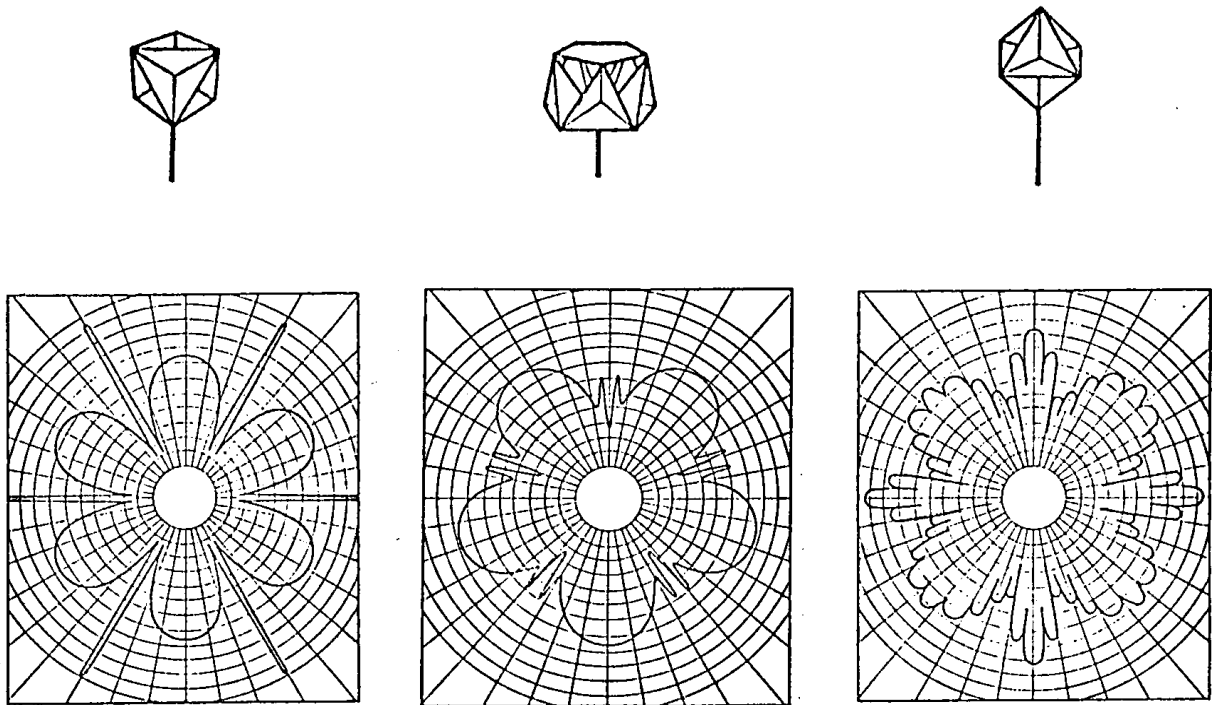


Figure 11.16 “Cluster” reflectors.

11.7 RCS of Complex Objects

For objects such as airplanes and ships (understood under the term “complex objects”), numerous, widespread from one another scattering centres contribute to the Radar scattering cross-section. Therefore, the RCS pattern can become very irregular. Presently, almost exclusively just the scalar Radar backscattering cross-section is determined from such objects. Since calculations are very elaborate, one normally decides for other ways:

- Original measurement,
- Model measurement,
- Simplification or concentration on area of interest for calculation.

A few figures and examples shall point out the mentioned relationships. Figure 11.17 represents the Radar backscattering diagram of an airplane.

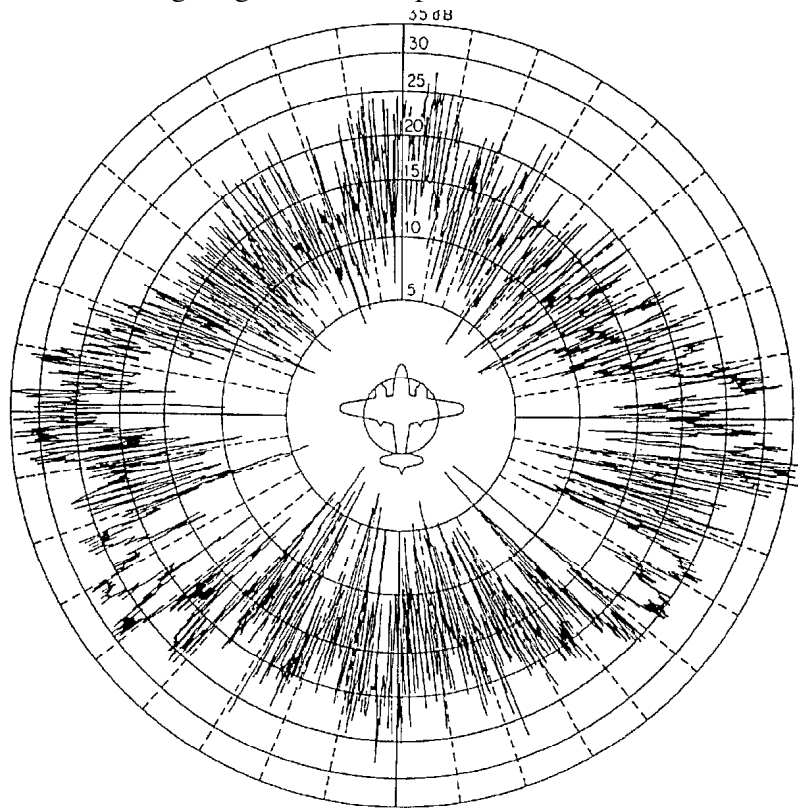


Figure 11.17 Measured Radar backscattering diagram of an airplane (B 26), $\lambda = 10$ cm, horizontal polarization. The fluctuations of σ amount up to 20 dB.

Even more striking than the Radar backscattering diagram from airplanes, are those from ships. At certain aspect angles huge metal surfaces are orthogonal to the incident waves and with other angles a mirror reflection results. The fluctuation levels of RCS are frequently over 30 dB. Typical Radar backscattering cross-sections for the X band (8 - 12 GHz) of various ships are:

Type	σ / m^2	BRT/to
------	----------------	--------

Sailing Yacht	10	1
Speedboat	500	400
Frigate	10.000	2000
Tanker	100.000	100.000

Especially interesting is the backscattering cross-section of people according to the table below. The size variations result from the chosen aspect angle and the polarization.

Frequency [GHz]	σ [m ²]
0,41	0,03 - 2
1,12	0,1 - 1
2,89	0,15 - 1
4,8	1,37 - 1,9
9,4	0,5 - 1,2
35	1-10

11.8 Reduction of the Radar Backscattering Cross-Section

The dream of ships and airplanes invisible to Radar is as old as Radar technology itself, known as stealth technology. Since it is known that one can locate objects with electromagnetic waves, especially in military applications, possibilities to reduce the Radar backscattering cross-section have been sought. Earlier even alchemy was looked to for a solution. Today the possibilities are simple to list after many disappointments due to disillusionment:

Optimization of the shape and style (wideband)

Covering with Radar absorbing material (wideband)

Layering of the outer-surface materials (narrowband)

These three possibilities will be further discussed in the coming sections.

11.8.1 Optimization of Shape and Style

It was shown by the representation of backscattering characteristics of simple bodies that, based upon the projection surface, the sphere had the smallest scattering cross-section, with:

$$\sigma_{Kugel} = r^2 \pi \quad (11.24)$$

For bodies with differing curvature in both planes the following applies, where r_1 and r_2 are the two radii of curvature:

$$\sigma = r_1 r_2 \pi \quad (11.25)$$

From this it follows that the radius of curvature is to be minimized. In these cases, in which not all aspect angles are expected, one can also consider working with mirrored reflection at diagonal angles of incidence, as Figure 11.18 shows.

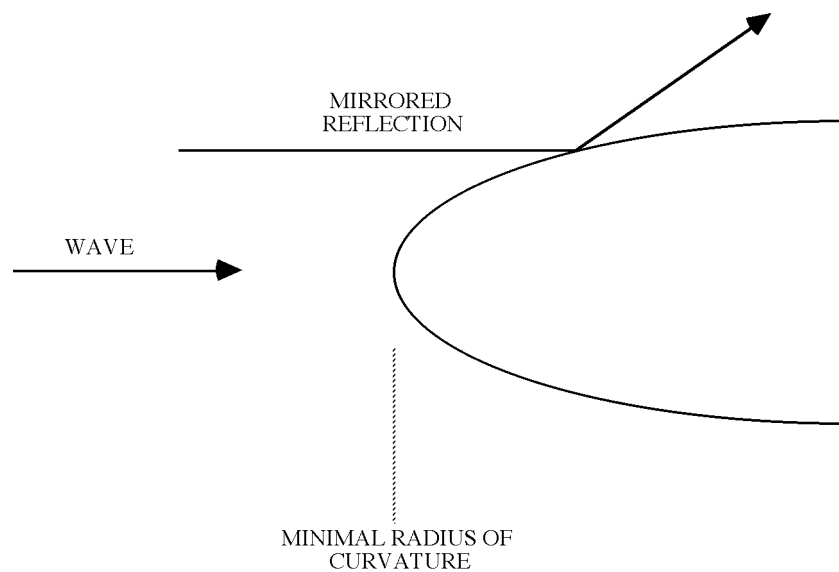


Figure 11.18 Example for the optimization of the shape.

The requirements, which are similar to those of good aerodynamics, were particularly realized with reconnaissance airplanes.

11.8.2 Covering with Radar absorbing material

Radar absorbing material (RAM), in order to have a good absorption characteristic, must have a minimum depth of approximately half of a wavelength. Thus this possibility doesn't exist for airplanes. Aboard ships the absorbing coverage is so extremely exposed to the environment that the characteristics are maintained for a longer period of time. Consequently this possibility remains almost exclusively for use on land. In practice reductions of 5 and 11 dB have been achieved.

11.8.3 Layering of the Outer-Surface Materials

On the boundary of two dielectrics arises a reflection due to the ϵ -discontinuity. The aim of the consideration is to minimize the sum of reflections through the existence of two or more layered reflection locations. Today in optics these procedures are commonly applied. It is assumed that:

The wavelength is known,

The wave incidence takes place at a defined angle.

Under these assumptions a reduction of up to 20 dB can be achieved. The creation of a stealth object with materials adapted to the free-space wave-impedance, according to Equation (11.26), offers no advantages for loss-less materials, since only the phase velocity in the material is lowered. Additionally would the material still have to absorb, since otherwise a reflection takes place on the other side.

$$r = 0 \Rightarrow \sqrt{\frac{\mu_0 \mu_r}{\epsilon_0 \epsilon_r}} = \sqrt{\frac{\mu_0}{\epsilon_0}} = 120\pi\Omega \quad (11.26)$$

$$\text{or } \epsilon_r = \mu_r$$

Coatings of this type have been used with airplanes for a few years. Ferrite (thin layer absorbing) is primarily used in the coating material. In the military this is known as “Stealth Technology.” Reductions of reflection up to 15 dB for a frequency range of 8 GHz to 15 GHz seem possible to be realized.

12 Selected Areas in Radar Signal Processing

In the beginning of Radar technology, signals were not processed in a sophisticated way. The ‘processing’ was accomplished by systems inherent in the RF- and video subsystems, for example by filters (integration) or in the display (storage). During the decades a special ‘culture’ in Radar signal processing was developed, mainly supported by the availability of digital hardware and during the last years by software. In state of the art Radar systems the amplified RF-signal is down converted, digitized, software processed and displayed or fed by automatic processes to other systems like missiles or automobile systems (e.g. throttle, break, and collision avoidance Radars). This chapter is intended to give a very short introduction to Radar signal processing. For special and more detailed information see the literature listed at the end.

12.1 Constant False Alarm Rate (CFAR)

12.1.1 Introduction

At the output of the signal processing of pulse compression and Doppler processing clutter and clutter residue can still appear. This interference can obscure target echoes and cause false alarms. Clutter signals result from, among other things, rain and snow echoes (i.e. rain clutter, sea clutter from rough sea surfaces) and from signal processing devices (processing clutter). For example, the range side-lobes from target echoes in pulse compression systems. These types of clutter can be eliminated by appropriate CFAR (Constant False Alarm Rate) methods. The basic feature of CFAR is that the false alarm probability remains approximately constant in clutter by a threshold, riding a definite value above clutter. Targets with an echo power exceeding the threshold level can still be detected. The CFAR is completely realized in digital signal processing. In the following sections different concepts of the CFAR processing will be shown.

An efficient CFAR circuit has to fulfill the following requirements:

- Efficient implementation regarding required processing power and production costs,
- Low CFAR-loss,
- Accurate fitting of the CFAR threshold to the clutter scenario,
- The CFAR threshold must pass point targets and extended targets,
- Closely spaced targets must not mask each other,
- The CFAR threshold must follow steep rises (or falls) in background clutter amplitude with as little lead (or lag) as possible

12.1.2 The CAGO-CFAR

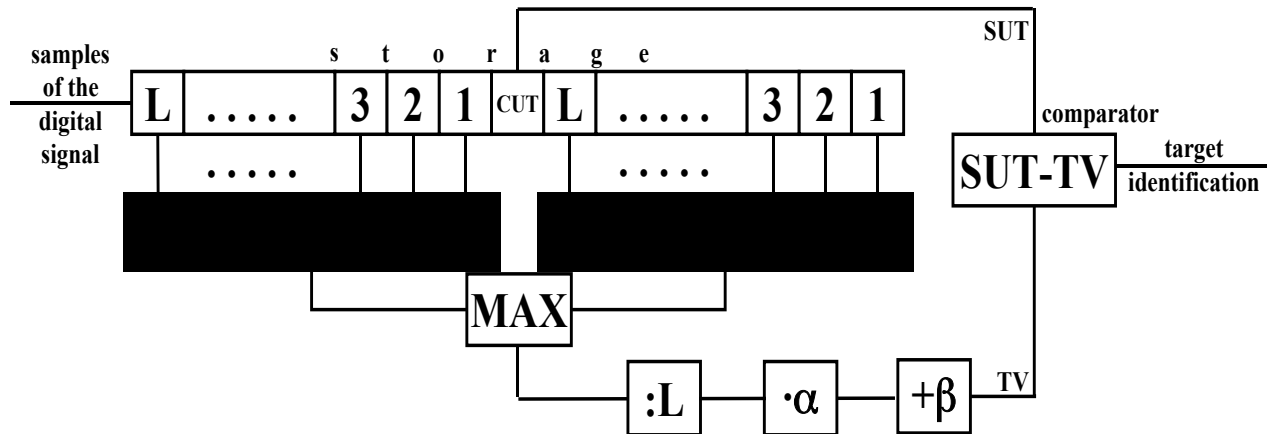


Figure 12.1 Principle of the CAGO-CFAR circuit.

The CAGO-CFAR (Cell Averaging Greatest Of-) comprises essentially a shift register consisting of two sub-registers, each containing L storage cells. Between the sub-registers, the so-called cell under test (CUT) is located. Each sub-register has its own adding circuit. The larger of the two sum-values (MAX) is normalized by dividing it by the number of cells in the sub-register, L . Using a multiplicative factor α for linear processing or an additive factor β for processing with a LOG-amplifier, the threshold value (TV) is calculated. Finally, the amplitude of the signal under test (SUT) is compared with the threshold value to decide whether the SUT belongs to a target or not.

The CAGO-CFAR has the advantages of requiring little processing power and having low CFAR loss. However, it also has the disadvantage that the thresholding is often ineffective. The reason for this is that the mean-value calculation inevitably raises the threshold in the neighbourhood of targets. Consequently, closely spaced targets can mask each other, particularly if a small target is located close to a large or extended target. Furthermore, because of the MAX-process, the CAGO threshold cannot immediately follow an abrupt rise or fall in clutter level, e.g. the front of a thunderstorm. Therefore the threshold will lead in time in case of a steep rise in clutter level and will lag in case of a steep fall. Both these effects can result in target losses. If a summing process (with division by 2) replaces the MAX-process of the CAGO-CFAR, then the CAGO-CFAR results in the so-called Cell Averaging CA-CFAR.

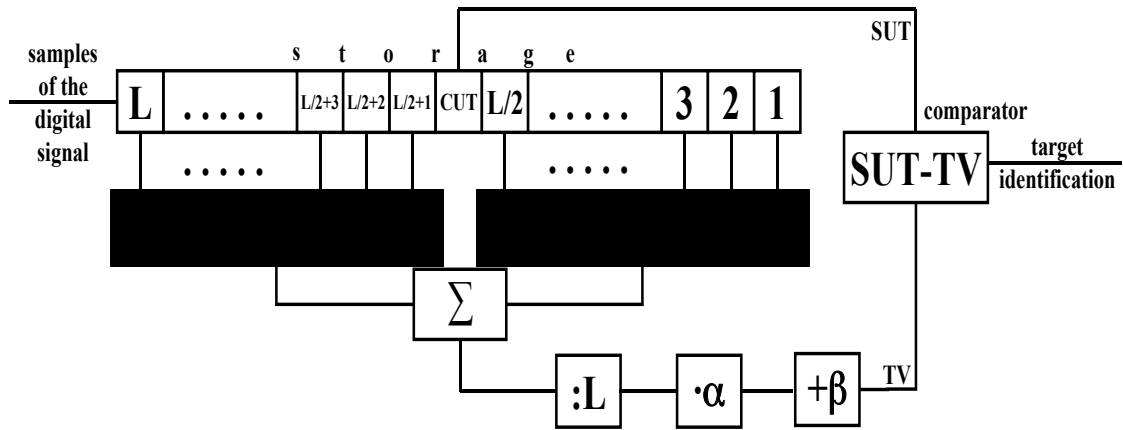


Figure 12.2 Principle of the CA-CFAR circuit.

12.1.3 The OS-CFAR

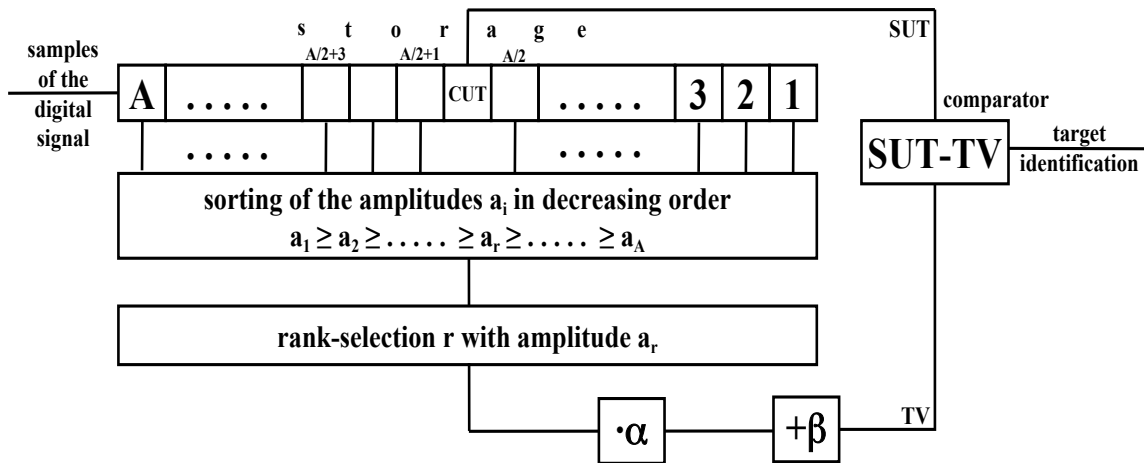


Figure 12.3 Principle of the OS-CFAR circuit.

The OS-CFAR (Ordered Statistic) comprises a shift register containing “A” storage cells, plus the CUT. A sorting algorithm arranges the amplitudes of the storage cells in order of decreasing magnitude. In a rank-selection process, the “r-th” largest amplitude is chosen as a representative of the clutter. The TV is calculated using a multiplicative α or additive factor β as described for the CAGO-CFAR above. Target detection is accomplished by comparing the SUT with the TV. In contrast to the CAGO-CFAR, the OS-CFAR has the advantage of effective threshold formation, allowing accurate fitting of the threshold in the clutter scenario. The OS-CFAR only shows inadequacies in the case of extreme scenarios, where the thresholding process is required to fulfil conflicting requirements. This is because on one hand, a timely following of jumps in clutter level without undue lead or lag can only be achieved by a rank-selection $r \leq A/2$. On the other hand, the threshold can only pass accumulations of (extended)

targets if the rank r is chosen high enough. The major disadvantage of the OS-CFAR is the high processing power required for performing the sorting algorithm.

The following section shows how the two quite differently structured CFAR algorithms: the CAGO-CFAR with its low processing requirements but often ineffective thresholding and the OS-CFAR with its effective thresholding, but heavy processing requirements for sorting, can be freely combined.

12.1.4 CAOS-CFAR

The CAGO-CFAR (or the CA-CFAR) can be freely combined with the OS-CFAR. The new circuit is then termed CAOS OFAR (Cell Averaging Orded Static).

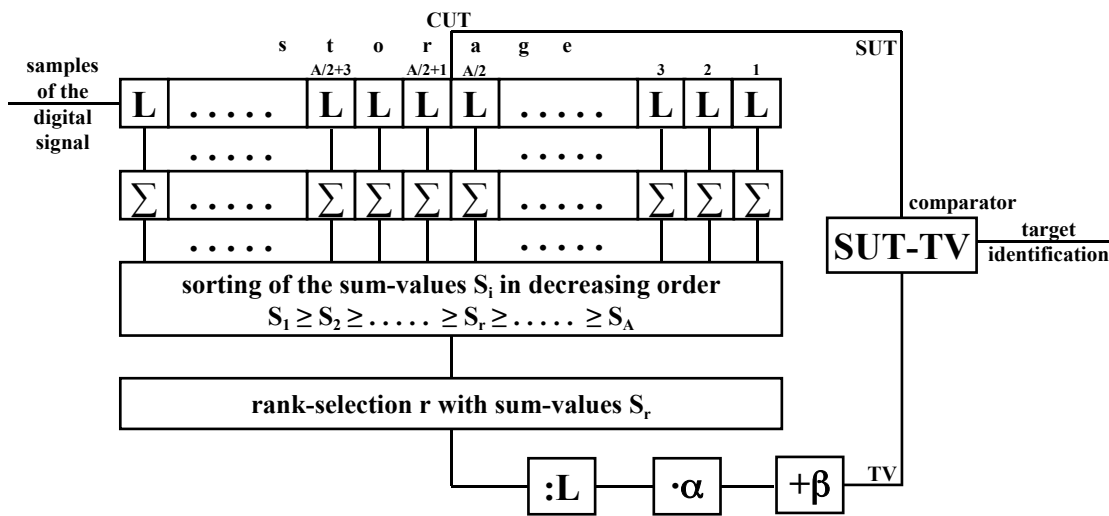


Figure 12.4 Principle of the CAOS-CFAR circuit.

The CAOS-CFAR comprises essentially a shift register with “A” sub-registers, each containing L storage cells. Each sub-register has its own adder. Thereafter the normal OS-CFAR algorithm is applied to the “A” sum-values:

- For $A=1$, one gets the CA-CFAR (without free cell),
- For $A=2$ and $r=1$ the CAGO-CFAR results (without free cell),
- For $L=1$ the OS-CFAR results.

Moreover, between the CAGO-CFAR and the OS-CFAR any number of intermediate variants is possible. With regard to the above techniques an optimal CFAR circuit would result if it would be possible to create a circuit with thresholding at least as effective as that of the OS-CFAR, but with essentially lower processing power requirements. The following CFAR methods are possible.

12.1.5 The CASH-CFAR

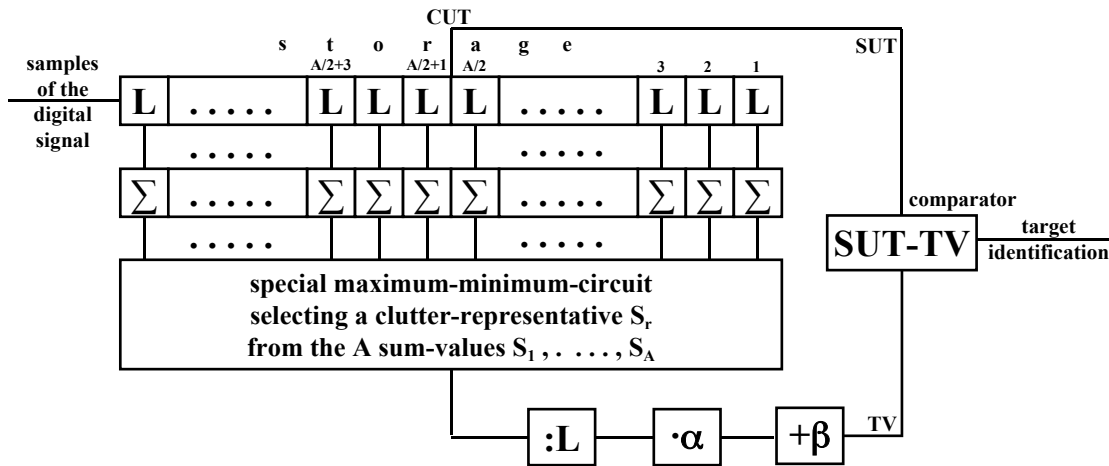


Figure 12.5 Principle of the CASH-CFAR circuit.

The CASH-CFAR (Cell Averaging Statistic Hofele [1-2]) comprises essentially a shift register configured by “A” sub-registers, each having its own adder and containing L storage cells. By means of a special maximum-minimum process a clutter-representative sum-value S_r , will be selected from the “A” sum-values S_1 to S_A . The threshold value is then calculated using a multiplicative (α/L) and/or additive (β/L) factor.

A number of possibilities are possible for implementing the maximum-minimum process. For the CASH-CFAR, a special maximum-minimum circuit is applied. Using this variant, the “A” sum-values are first halved by a special efficient pair-wise maximum calculation. Then (using α/L and or β/L the threshold value results as the smallest of the remaining sum-values.

This special maximum-minimum circuit has the favourable characteristic that the resulting CASH-CFAR threshold eliminates blocks of interference (rain clutter areas, blocks of pulse compression side lobes), exceeding $\geq A \cdot L/2 + L - 1 = b$, and completely passes point and extended targets of an extent $\leq A \cdot L/2 - 2L + 1 = a$, almost independently of the number of targets in the CFAR-window. This constitutes an enormous advantage of the CASH-CFAR as opposed to the rank-selection method of the OS-CFAR.

Consequently the use of the CASH-CFAR avoids mutual masking of targets, even taking target accumulations into consideration. The CASH-CFAR threshold very accurately fits the clutter scenario. Moreover, because of the special maximum-minimum process, the threshold follows steep jumps in clutter level with almost no time displacement. Finally, because of the selection of the clutter-representative by means of the special maximum-minimum process the CASHCFAR requires much less processing power than the OS-CFAR with its rank-selection method.

The processing power requirement can be reduced for the CASH-CFAR by using block processing in which the threshold is held constant for L values. Thus the threshold value calculation does not take place in the storage cell raster but only in the sum register raster.

12.1.6 MAMIS-CFAR

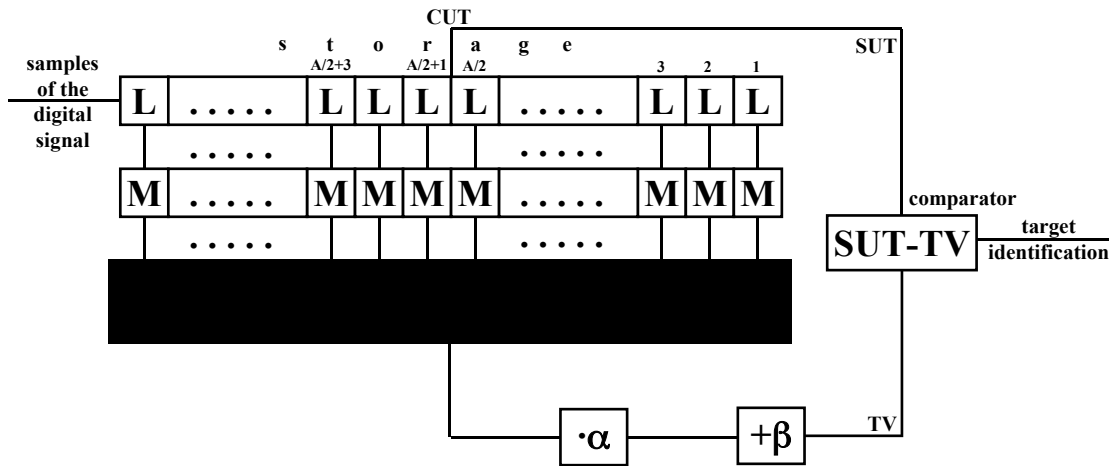


Figure 12.6 Principle of the MAMIS-CFAR circuit.

The MAMIS-CFAR (Maximum Minimum Static) is essentially the same as the CASH-CFAR, except that the special maximum-minimum circuit M replaces the adders of the CASH-CFAR. The characteristics of the MAMIS-CFAR are quite similar to those of the CASH-CFAR. For the CFAR-handling of block interference and of point- and extended targets, in analogy with the CASH-CFAR $a = A \cdot L/2 - L - 1$ and $b = A \cdot L/2 - 1$ are valid.

12.1.7 Quality of the CFAR Threshold and CFAR Loss

Now the quality of the several CFAR thresholds will be compared. For this purpose a simulated sea target scenario in the video domain, consisting of 15 targets, sea clutter and two rain areas are considered. In this example the length of the sea targets (ships) is between 20 and 200 m. After the A/D-conversion, the video signal is sampled at a rate of 50 ns, corresponding to a range resolution cell of 7.5 m. The scenario signals are passed through the following simple signal processing.

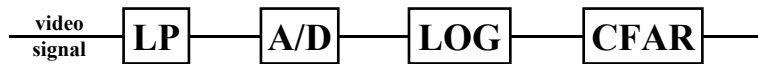


Figure 12.7 Signal processing chain for CFAR comparison (low-pass filter (LP), analog-to-digital converter (A/D) including magnitude calculation, logarithmic amplifier (LOG) and CFAR algorithm.

Figures 12.8-12.13 show a modeled sea target scenario after the LOG-process with potential CFAR thresholds for CAGO- (Figure 12.8), OS- (Figure 12.9), CASH- (Figure 12.10), CA- (Figure 12.11), CAOS- (Figure 12.12) and MAMIS- (Figure 12.13) CFAR. Adjusted to the given sampling rate and range resolution cell size, the length of the CFAR-window is chosen to be approximately 120.

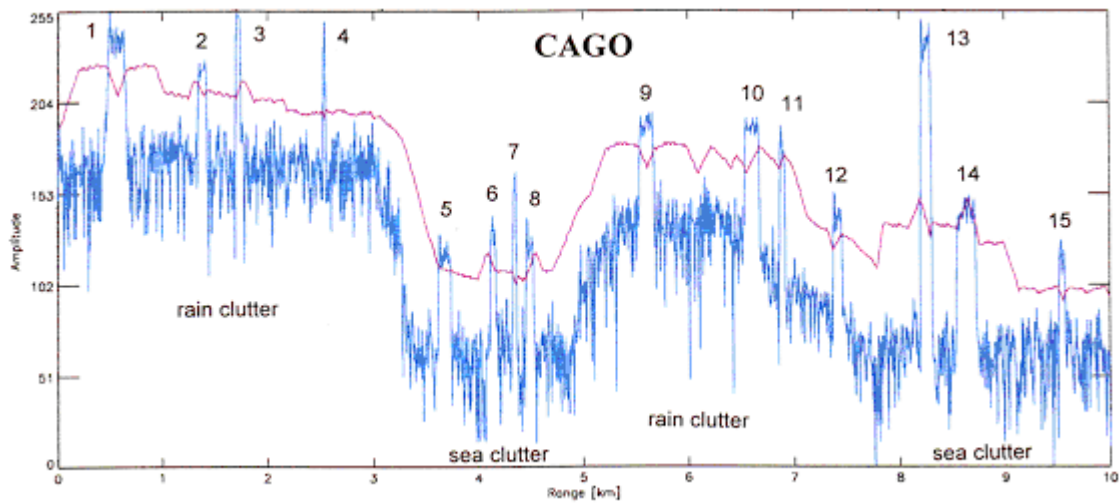


Figure 12.8 Sea target scenario and threshold, processed with CAGO-CFAR ($L=60$, $\alpha=1$, $\beta=30$).

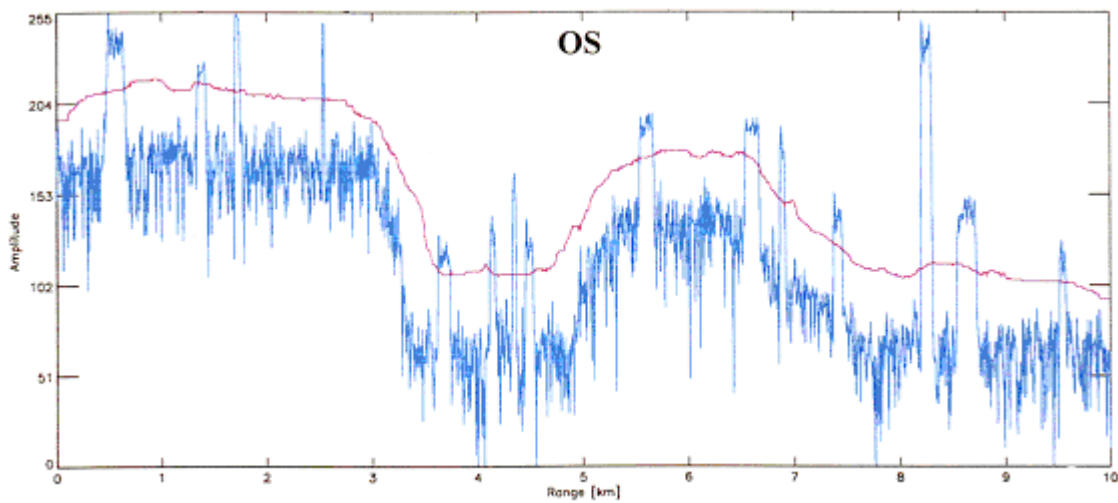


Figure 12.9 Sea target scenario and threshold, processed with OS-CFAR ($A=120$, $r=50$, $\alpha=1$, $\beta=35$).

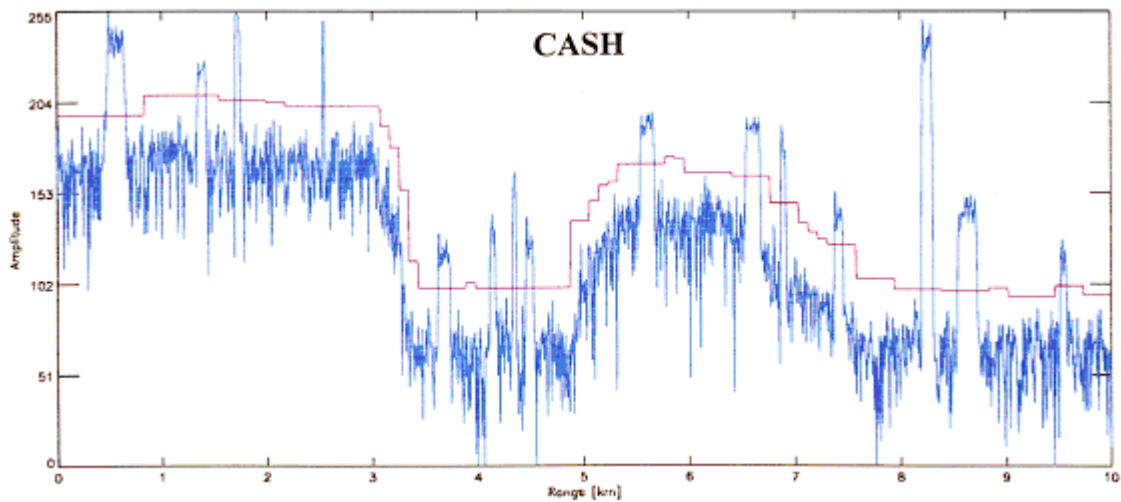


Figure 12.10 Sea target scenario and threshold, processed with the CASH-CFAR ($A = 10$, $L = 12$, $\alpha = 1$, $\beta = 37$).

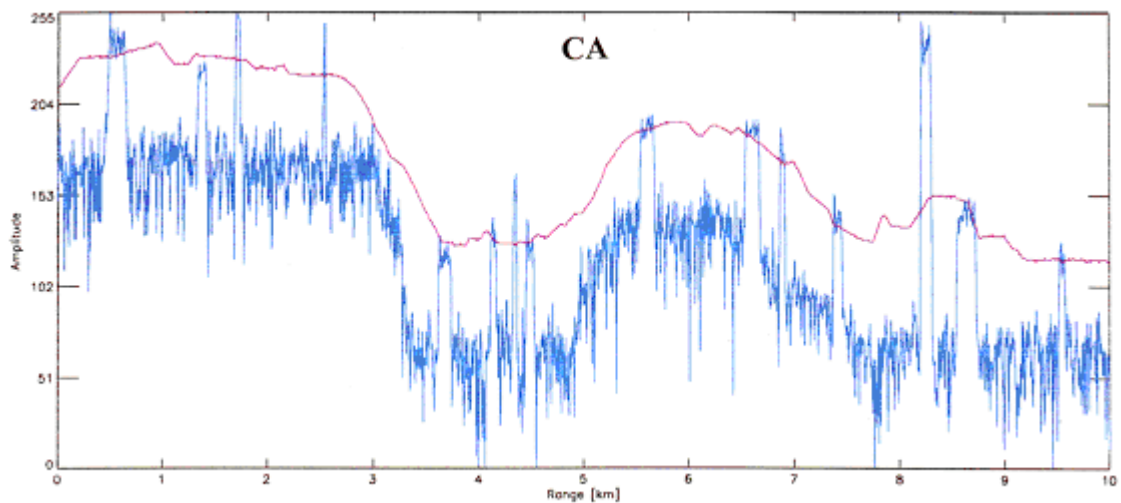


Figure 12.11 Sea target scenario and threshold, processed with the CA-CFAR ($L = 120$, $\alpha = 1$, $\beta = 53$).

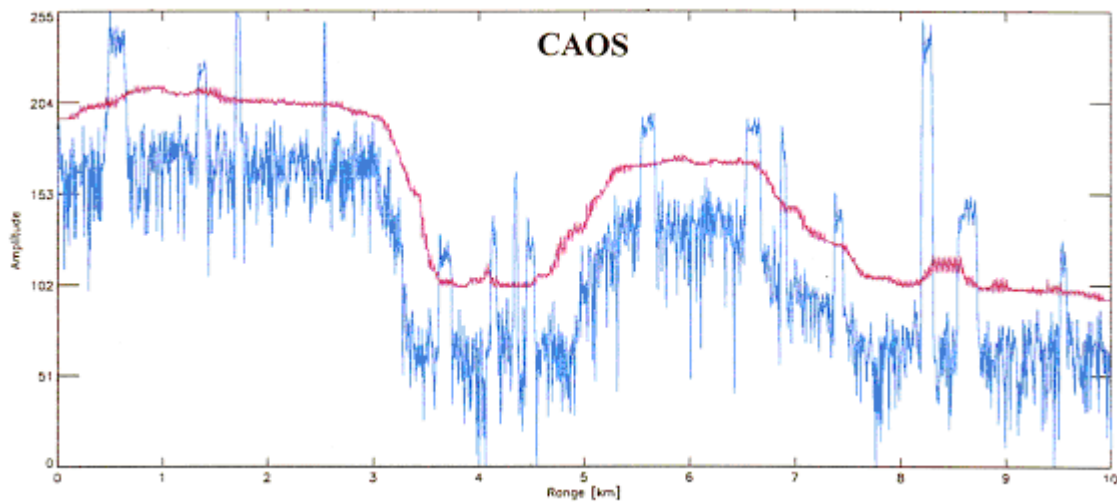


Figure 12.12 Sea target scenario and threshold, processed with CAOS-CFAR ($A = 30$, $L = 4$, $r = 13$, $\alpha = 1$, $\beta = 35$).

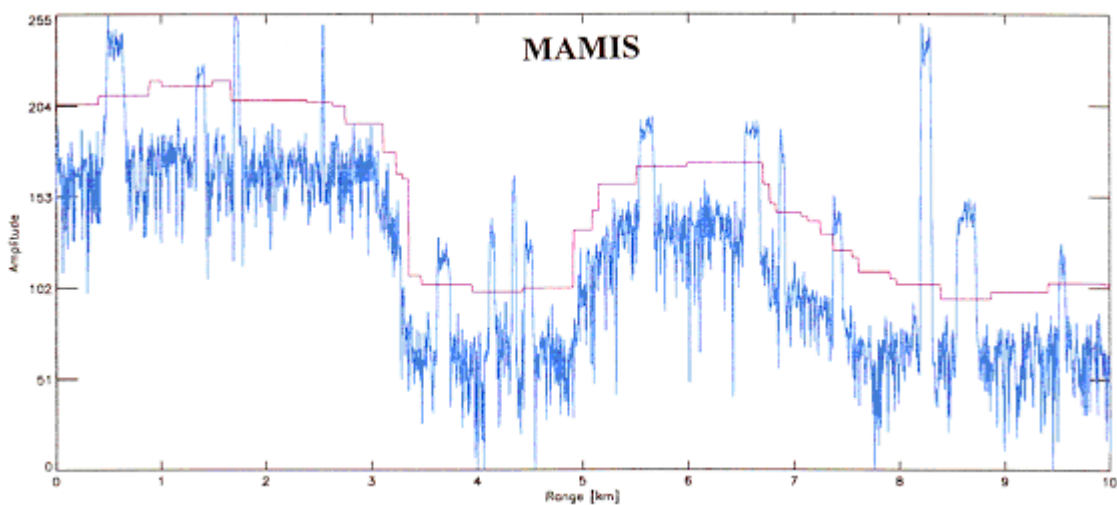


Figure 12.13 Sea target scenario and threshold, processed with MAMIS-CFAR ($A = 16$, $L = 8$, $\alpha = 1$, $\beta = 45$).

As a first step, the quality of a CFAR threshold is judged considering the above scenario with targets and clutter interference (sea clutter, rain areas). For this, we consider the sea target scenario and the CFAR thresholds documented in Figures 12.8-12.13. The thresholds of the individual CFAR algorithms (CFAR-parameter setting $\alpha = 1$ and $\beta > 0$ because of the LOG-amplifier) cause no false alarms, meaning that the signal amplitudes in the scenario exceed the CFAR threshold only for targets. Thus, a criterion for the quality of the CFAR threshold (i.e., the fit of the threshold to the clutter scenario) is given by summing the threshold crossings. These are defined as $q = \sum [s(i) - c(i)]$ for all i with $s(i) > c(i)$, where s is the scenario and c

is the CFAR threshold. The following table results for the individual CFAR algorithms with the CFAR-parameter settings applied in Figures 12.8-12.13.

CFAR Type	Quality q	q in %
CASH	6859	100
MAMIS	6117	89,2
CAOS	6016	87,7
OS	5187	75,6
CAGO	4002	58,3
CA	1998	29,1

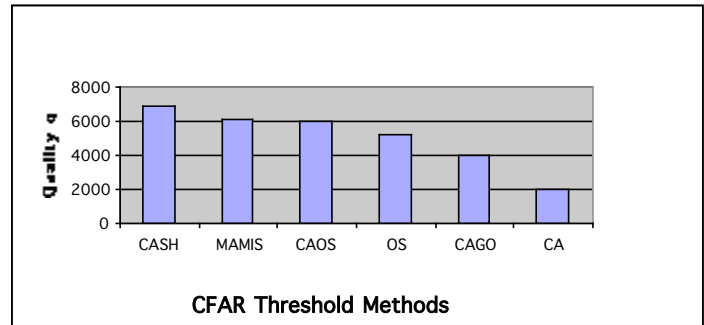


Figure 12.14 CFAR Threshold quality.

As a second step, the quality of a CFAR threshold considering a scenario without targets or clutter, implying a pure Rayleigh-distributed background (resulting in the parameter-settings $\alpha > 0$ and $\beta = 0$) is evaluated. A criterion for the quality of a CFAR threshold is then given by the so-called CFAR-loss (L_{CFAR}), defined in [3] as $L_{CFAR} [dB] = 20 \log_{10} (E(T_C) / T_{WC})$, where T_{WC} is the fixed threshold without CFAR, dependent on the false alarm probability (P_{fa}), and $E(T_C)$ is the mean-value of the CFAR threshold, also P_{fa} -dependent.

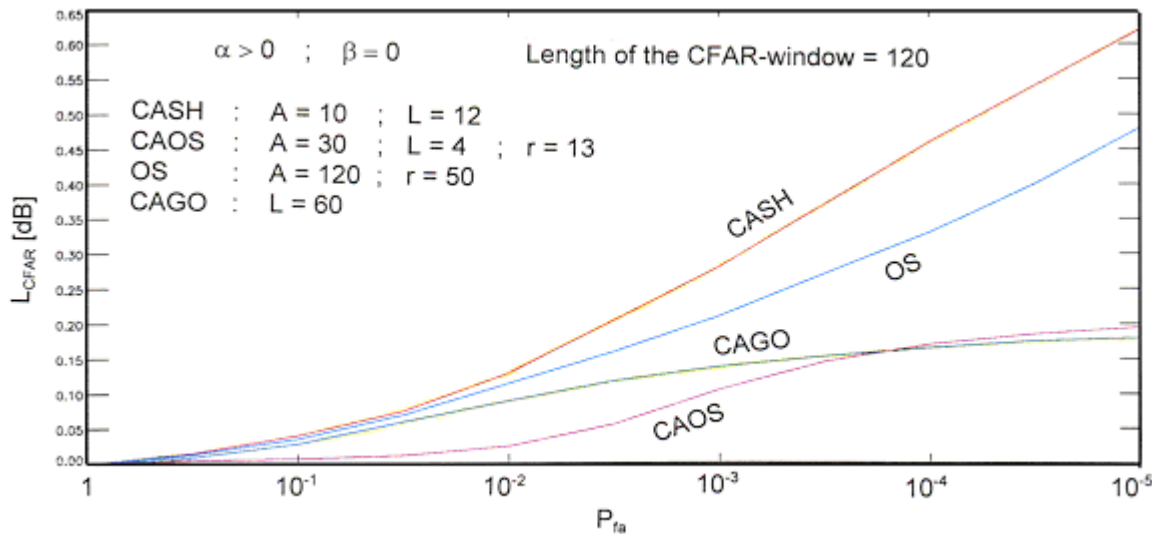


Figure 12.15 CFAR-Loss L_{CFAR} .

Consequently L_{CFAR} is dependent on the P_{fa} and on the CFAR-parameter settings and thus also on the length of the CFAR-window. According to the above Figure, the CFAR loss L_{CFAR} of the individual CFAR methods in dependence on the P_{fa} for a CFAR-window length of approximately 120. The CFAR loss of the MAMIS-CFAR is higher than that of the CASH-CFAR and L_{CFAR} of the CA-CFAR is insignificantly smaller than that of the CAGO-CFAR. In

general, L_{CFAR} decreases with an increasing CFAR-window length and L_{CFAR} increases with a decreasing CFAR-window length.

12.1.8 Conclusions

It is possible that the OS-CFAR is combined with the CAGO- and CA-CFAR in a wide range of ways. The resulting CAOS-CFAR provides a threshold with a quality q at least as high as that of the OS-CFAR and, moreover, the required processing power (for the CAOS-CFAR, we have a factor- L -reduced sorting algorithm) and the CFAR loss L_{CFAR} of the CAOS-CFAR are less than those of the OS-CFAR.

For the MAMIS-CFAR and, in particular, for the CASH-CFAR, the quality q of the CFAR threshold (threshold fit to the clutter scenario) is significantly higher than for CA-, CAGO-, OS- and CAOS-CFAR. The MAMIS- and CASHCFAR react to changes (rises, falls) in the interference background quickly and without delay. In comparison, the CA-, CAGO- and also, to some extent the OS- and the CAOS-CFAR, react essentially more delayed to these clutter level changes. This is the reason why the CFAR-loss of the CASH-CFAR is a little higher than that of the other CFAR methods. CFAR adder circuits favorably influence CFAR-loss. Since the MAMIS-CFAR includes no adding process its CFAR-loss (dependent on the CFAR-parameter settings) is higher than that of the CASH-CFAR. Finally, it is noted that the required processing power for the MAMIS- and CASH-CFAR is significantly less than that for the OS- and CAOS-CFAR.

References:

- [1] F.X. Hofele, Gell Averaging Statistic Hofele (CASH) CFAR, Impulshöhenanalyse (IHA) und Pulscompressions-Nebenzipfel-Maske (PNM), *Technical Report of Daimler-Benz Aerospace AG, Ulm*, February 11, 1997.
- [2] F.X. Hofele, Neue Verfahren zur Unterdrückung von Regen und von Pulscompressions-Nebenzipfeln und zur Berechnung der Schwellen für eine automatische Zielerkennung, *Proceedings of the 9th Radar Symposium of 'Deutsche Gesellschaft für Ortung und Navigation' (DGON)*, Stuttgart, April 8-10, 1997, pp. 209-220.
- [3] A. Ludloff, *Handbuch Radar und Radarsignalverarbeitung*, Vieweg-Verlag Braunschweig, Wiesbaden, 1993, pp. 9-3 and 9-4.
- [4] F.X. Hofele, A new class of CFAR Algorithms, *Proceedings of the International Radar Symposium IRS'98*, Munich, Sept. 1998. pp.

12.2 Design of Low Side Lobe Chirp Pulse Compression

12.2.1 Introduction

The increasing use of high duty cycle, solid-state transmitters in modern Radar systems is making a companion pulse compression subsystem mandatory. The availability of digital waveform synthesis when transmitting, and a digital matched filter approximation when receiving, are making it possible to synthesize a system with very low mismatch loss, low peak side lobes, low integrated side lobes, and good Doppler tolerance.

In this paper waveform design and signal processing, which will result in low range-time side lobes and a low mismatch loss, are addressed along with the practical constraints of the analog-to-digital (A/D) conversion process and digital filtering. The required A/D converter-sampling rate determines the feasibility and resulting dynamic range of the signal processor implementation and therefore requires careful attention. Other limitations, such as those caused by transmitter distortion, limited receiver dynamic range, and other implementation tolerances also play an important role in realizing a successful design, but these issues are beyond the scope of this paper.

While receiver and signal processor algorithms such as transversal equalizers (or the equivalent) can be used to suppress the range side lobes of almost any pulse compression system, such techniques usually bring with them an extended filter time-response and have a poor tolerance to Doppler shifts of the received returns. The use of single pulse filter banks can improve the Doppler tolerance but only at the cost of added processor complexity.

In this paper the need to design a transmit waveform, which results in a spectrum with low amplitude ripple, is emphasized. For chirp type waveforms such low ripple designs can be achieved either through the use of a non-linear chirp with a carefully chosen characteristic, or by slowing the rise- and fall-times of the transmitted chirp, or a combination of both. Accurate control of the rise- and fall-time of a solid-state transmitter is, however, often quite difficult. In the design of the receiver, A/D converter, and digital processing it is also important to perform the major portion of the spectral weighting in the receiver filters, since this will result in the lowest possible A/D converter-sampling rate. In the signal processor the phase portion of the "Matched Filter" operation is performed using either the fast Fourier transform (FFT) or a finite impulse response (FIR) filter.

Each of these design processes will be discussed and illustrated by examples. A specific design for an S-band Radar with a 100:1 (100 μ s to 1 μ s) non-linear pulse compression system is presented. For Doppler shifts up to 10 kHz (1000 knots radial velocity) this design maintains a peak side lobe level below -55 dB and an integrated side lobe level less than -37.9 dB with a mismatch loss of 0.6 dB. The receiver uses a 5-pole Bessel filter with a 0.7 MHz bandwidth, the A/D converter sampling rate is 2.5 MHz, and the FIR filter pulse compressor has an impulse response duration which exceeds the Radar pulse-length by only 35%. The mismatch loss is less than 0.1 dB at zero Doppler.

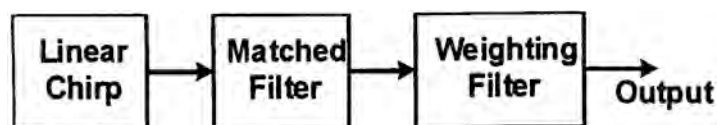


Figure 12.16 Linear Chirp pulse compression system.

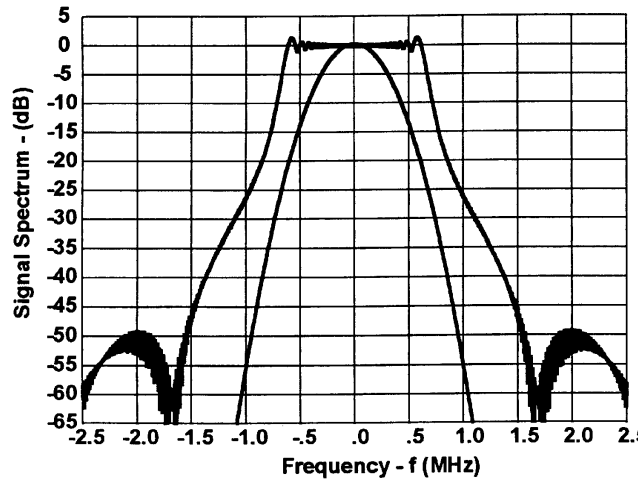


Figure 12.17 Spectrum of 1.37 MHz linear Chirp and Gaussian weighting function designed for 45 dB side lobes.

12.2.2 Linear and Nonlinear Chirp Waveforms

When the classical linear chirp waveform is used in Radar, additional weighting in the frequency or time domain must be added to the matched filtering, as shown in Figure 12.16, in order to obtain acceptable side lobes [1, 2]. As an example, the spectrum of a $100\mu\text{s}$ linear chirp is shown in Figure 12.17 together with a Gaussian weighting filter designed to provide 45 dB side lobes. A total chirp bandwidth of 1.37 MHz is used to obtain a compressed pulse-width of $1\mu\text{s}$ after weighting and rise- and fall-times of $1\mu\text{s}$ are assumed. Figure 12.18 shows the pulse compressed output for a matched filter receiver alone (gray curve) and with the additional Gaussian weighting filter added to the matched filter. At the frequency limits of the linear chirp (0.685 MHz) the required response of the Gaussian filter is -26 dB down. The need for a weighting filter is the result of the near-rectangular spectrum generated by the linear chirp. For the case described above, the use of weighting to reduce the pulse compression side lobes introduces a mismatch loss of 1.48 dB. The output side lobe levels can be improved somewhat if the matched filter in Figure 12.16 is replaced by the phase-only version (constant amplitude response) when used in conjunction with the Gaussian weighting filter (see [1], Figure 9 and 10). The compressed output for this case is shown in Figure 12.19 resulting in an improvement of about 6 dB. This example demonstrates that amplitude variations in the signal spectrum should not be replicated in the digital pulse compression filter.

Based on the principle of stationary phase, which states that for 'slow' sweep rates, the spectral energy due to a swept signal will be inversely proportional to the rate of sweep, numerous studies and implementations have been pursued, where the rate of sweep has been made to match the inverse of Taylor or Gaussian functions [3-6]. This approach is generally successful in reducing the amount of required weighting and therefore the resulting mismatch loss, but the residual Fresnel ripple in the spectrum often limits the resulting pulse compression side lobes [7].

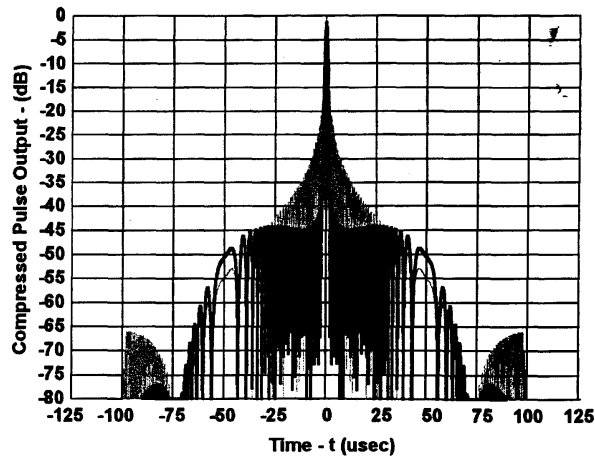


Figure 12.18 Matched filter compressed output (gray) and matched filter with added Gaussian weighting.

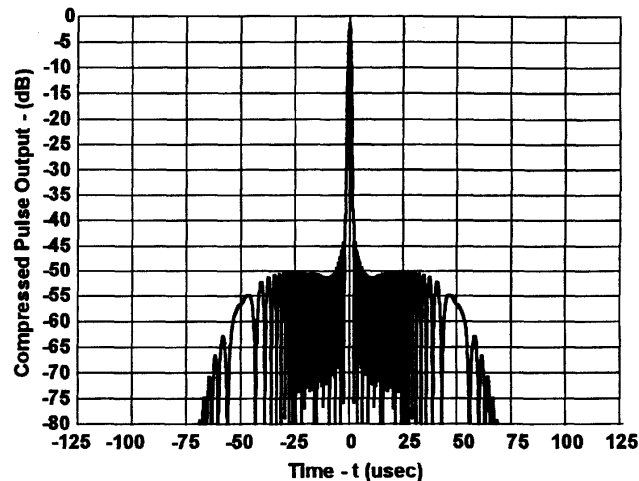


Figure 12.19 Compressed output using phase-only matched filter with Gaussian weighting filter.

It is well known that slowing the rise- and fall-times of the transmitted pulse envelope can reduce the amount of ripple in the signal spectrum, but this approach is often technologically difficult to implement in Radar transmitters, and will result in reduced transmitter efficiency. However, some slowing of the rise- and fall-times is always required to meet spectrum control requirements and for this reason a $1\mu\text{s}$ rise- and fall-time was assumed for the waveform designs presented in this paper. Several papers have recognized that low spectral ripple, nonlinear chirp waveform designs can be achieved for low time-bandwidth products by adding very rapid frequency excursions at the start and end of the chirp waveform [8-9]. In particular, the paper by Price [8] discusses the "circle- ϕ " nonlinear frequency modulation, which results in extremely low side lobes at the output of a matched filter. This paper uses this type of nonlinear frequency chirp, superimposed on a conventional linear chirp, as proposed by Price, to

achieve a practical compromise between mismatch loss, time side lobes, and spectral spreading of the transmitted signal.

12.2.3 Nonlinear Chirp Based on the Circle- ϕ Function

Based on the "circle- ϕ " nonlinear chirp proposed by Price [8] the class of waveforms considered in this paper have a frequency versus time characteristic given by the following equation:

$$f(t) = \frac{1}{2}B_L \cdot x + \frac{B_C}{2} \frac{x}{\sqrt{1-x^2}} \quad -1 < x < 1 \tag{12.1}$$

where $x = \frac{2t}{T} \quad -\frac{T}{2} < t < \frac{T}{2}$

In these equations B_L is the total sweep of the linear chirp component and B_C is the total frequency extent of a straight line which has the same slope as the circular term at $x=0$. An example of this type of non-linear chirp waveform is shown in Figure 12.20 for the specific parameters used later in this paper. The chirp duration is 100 μs with $B_L = 0.55 \text{ MHz}$ and $B_C = 0.18 \text{ MHz}$, and the rise- and fall-times are 1 μs .

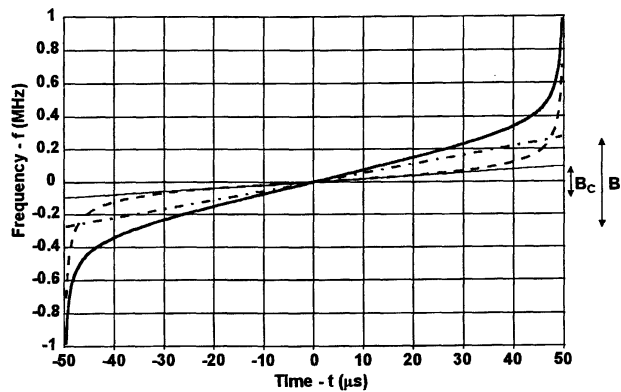


Figure 12.20 Non-linear chirp based on the sum of linear chirp and circle- ϕ chirp.

The corresponding signal amplitude spectrum is shown in Figure 12.21 along with the amplitude characteristic of a 5-pole Bessel filter having a 3-dB bandwidth of 0.7 MHz (dotted curve) as used in the pulse compression implementation example below. The matched filter output corresponding to this nonlinear chirp is shown in Figure 12.22 and the improvement relative to the linear chirp case in Figure 12.18 is substantial. When the matched filter is replaced with a combination of the 5-pole, 0.7 MHz Bessel filter and a phase-only matched filter, the output shown in Figure 12.23 is obtained. While the mismatch loss is slightly increased to 0.045 dB, the side lobe level beyond 4 μs from the peak is now below -50.9 dB. The integrated side lobe level outside $\pm 4 \mu\text{s}$ from the peak is less than -41.8 dB. The shoulders on the response with peaks at -32 to -33 dB would hardly affect any real aspect of Radar performance.

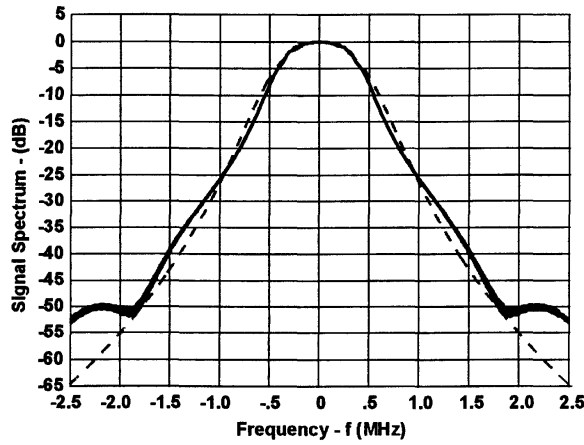


Figure 12.21 Spectrum of non-linear chirp using circle- ϕ function with response of 5-pole Bessel filter with $B_3=0.7$ MHz (dotted line).

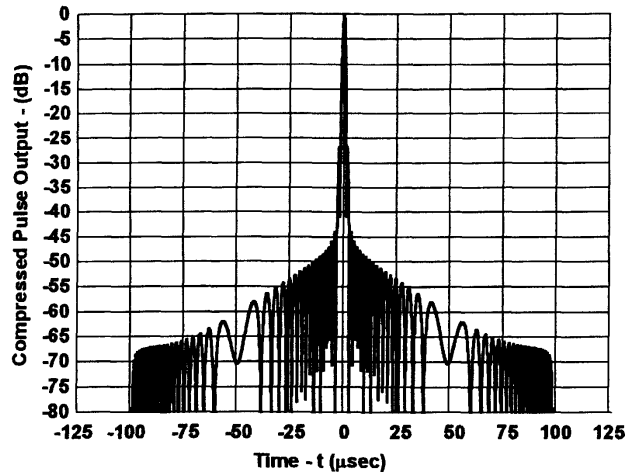


Figure 12.22 Matched filter output for non-linear chirp shown in Figure 12.21.

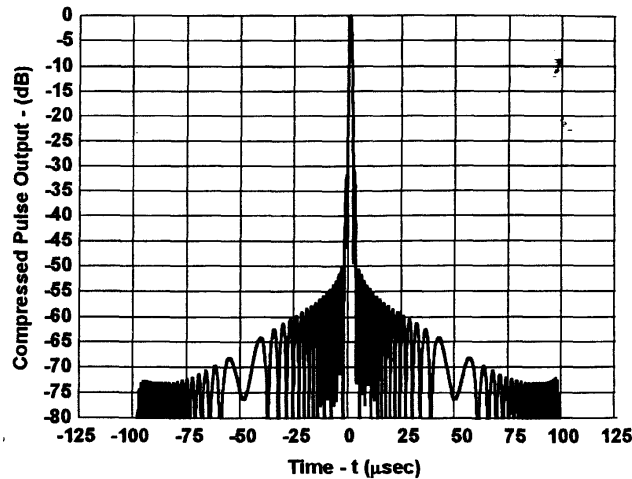


Figure 12.23 Non-linear chirp compressed output using Bessel filter and phase-only Matched filter.

12.2.4 Receiver and Signal Processor Considerations

Today most Radar receivers use digital signal processing. A generic block diagram of such a Radar receiver is shown in Figure 12.24.

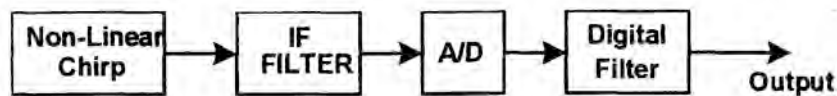


Figure 12.24 Digital implementation of non-linear chirp pulse compression.

As much as possible of the amplitude weighting should be placed in the analog filter in order to minimize the required A/D converter sampling rate and the pulse compression and any equalization should be performed by the digital signal processor after A/D conversion.

A digital implementation of pulse compression places a more stringent requirement on the A/D conversion rate than more conventional DSP applications (Even more difficult A/D sampling rate requirements are imposed by the use of direct sampling where aliasing must be kept at a very low level). In Figure 12.25 an example is shown, where a 1.5 MHz complex sampling rate is used between the Bessel filter and the phase-only Matched filter as considered in Figure 12.23. It is seen that this sampling rate is having a noticeable effect on the time response of the pulse compression system. From the Bessel filter response shown in Figure 12.21 it is seen that a 1.5 MHz sampling rate will result in aliasing at the -18 dB level. At an A/D sampling rate of 2.5 MHz the response would become almost the same as in analog processing case.

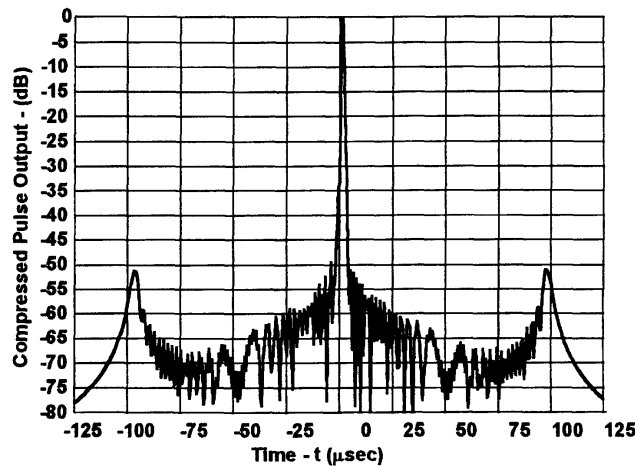


Figure 12.25 Non-linear chirp compressed output using Bessel filter, phase-only matched filter, and 1.5 MHz A/D conversion.

12.2.5 Design Example

When implementing digital filters it becomes possible to compensate for spectral ripples and thus to improve the resulting pulse compression side lobes. The characteristics of such "reciprocal ripple" filters [9-10] are most easily visualized in the frequency domain. The fundamental idea is to add a reciprocal ripple filter in series with the phase-only matched filter, such that spectral ripple in the signal is cancelled, as represented in Figure 12.26. The gray curve shows the signal spectrum and the black curve is the combined response of the Bessel filter and reciprocal ripple filter. It can be seen that the total filter response exactly counters the residual spectral ripple with the result that the signal spectrum at its output has a smooth characteristic as shown in Figure 12.27. While the compressed output obtained with the reciprocal ripple filtering, shown in Figure 12.26, would provide extremely low side lobe, this performance would be unachievable in practice, because the required filtering implies an infinite impulse response. The duration of this impulse response must be taken into account regardless of whether pulse compression is performed with a finite length FIR filter, or whether it is based on the FFT approach. Furthermore, as mentioned above, the use of a phase-only matched filter will also result in an extended duration impulse response. The FIR impulse response of the combination of the reciprocal ripple filter and the phase-only Matched filter as described above is shown in Figure 12.28 (gray curve) together with a version of this filter, which has been truncated to a total of 337 taps corresponding to a total response time of 135 μ s. This only exceeds the Matched filter implementation (250 taps) by 35%. The compressed output resulting from the use of this truncated filter is shown in Figure 12.29. A side lobe level less than -65 dB is realized and could be improved by an increased length FIR filter implementation. The 3-dB width of the compressed pulse is 0.941 μ s and the integrated side lobe level outside +4 dB is -50.3 dB. The mismatch loss is 0.063 dB.

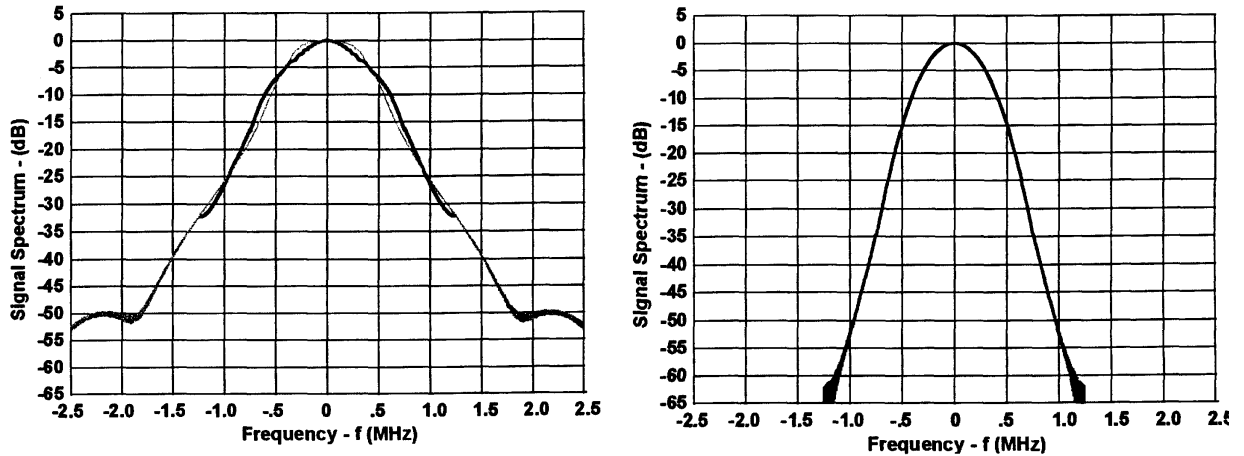


Figure 12.26 (Left) Original signal spectrum (gray) and total filter amplitude response with added digital reciprocal ripple compensation. (Right) Signal spectrum after Bessel and reciprocal ripple filtering.

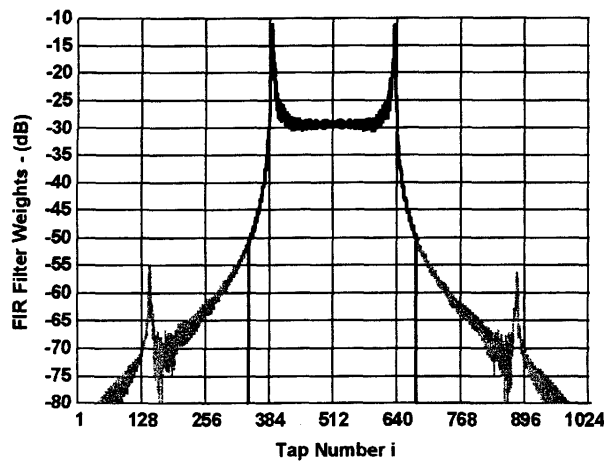


Figure 12.27 Amplitudes of FIR weights of exact phase-only Matched filter plus reciprocal ripple filter and truncated version used to obtain output response in Figure 12.29 and 12.30.

The issue of Doppler sensitivity was finally considered as shown in Figure 12.30 where a 10 kHz Doppler shift was added to the signal. At S-band this Doppler shift represents a radial target velocity of 1000knots. For this Doppler shift side lobes have increased but are still below the -55 dB level, while the mismatch loss has increased to 0.59 dB. In spite of its non-linear characteristic this waveform has retained the good Doppler tolerance of the linear chirp.

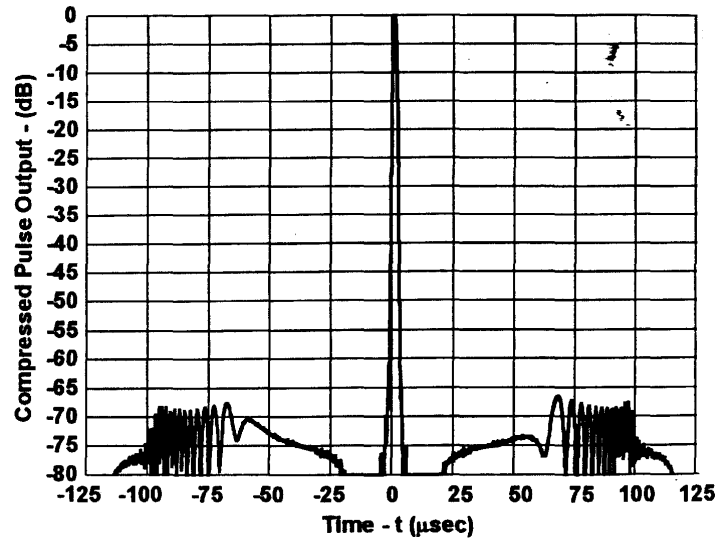


Figure 12.28 Compressed output of final pulse compression system design using 5-pole Bessel filter and 360 tap digital FIR filter.

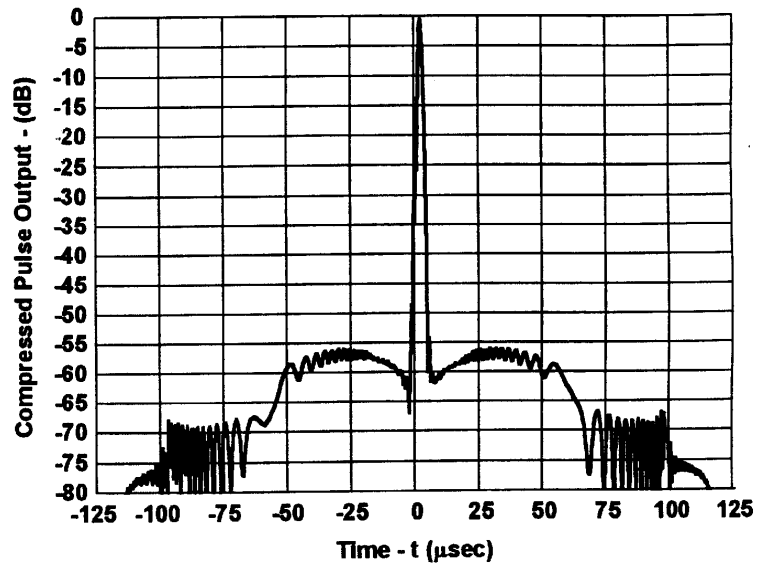


Figure 12.29 Compressed output as in Figure 12.28 but with 10 kHz Doppler shift.

12.2.6 Results

The design process of low-loss, low-side lobe, non-linear chirp pulse-compression systems, along with considerations for its practical implementation as part of a digital signal processing system, needs to include at least the following:

- Determine the necessary and achievable rise- and fall-times of the transmitted waveform, which will meet spectrum control requirements.
- Develop a signal design, which achieves the desired spectral shaping to minimize processing losses, while minimizing spectral ripple.

Design the receiver/processor using a close approximation to a Matched filter in order to minimize mismatch loss.

Place most (or all) of the amplitude weighting in the analog receiver portion of the system. This minimizes the required A/D converter-sampling rate.

Do not double the spectral ripple by including the amplitude characteristics of the matched filter. This could degrade the achievable time side lobes by as much as 6 dB. Use only the phase characteristic of the matched filter and replace its amplitude response with a smoothed function in the analog portion of the receiver. Perform trade-off of required digital filter transient response.

If necessary add a reciprocal ripple inverse filter to further reduce range time side lobes. Keep in mind that this may result in greater Doppler sensitivity. Re-consider the required digital filter transient response.

Determine required A/D converter sampling rate. Iterate the receiver filter design to reduce aliasing at a minimal cost in pulse compression performance.

Finally any such design needs to be evaluated relative to implementation tolerances and variations in transmitter distortion versus frequency, or from module to module, in order to verify the practicality of the design.

References:

- [1] Klauder, J.R., et al, "The Theory and Design of Chirp Radars", *Bell System Technical Journal*, Vol.XXXIX, No.4, pp.745-809, July 1960.
- [2] Cook, C.E., and Bernfeld, M., *Radar Signals - An Introduction to Theory and Application*, New York: Academic Press, 1969.
- [3] Cook, C.E., and Paolillo, J., "A Pulse Compression Predistortion Function for Efficient Side lobe Reduction in a High-Power Radar", *Proceedings IEEE*, vol. 52, pp.377-389, April 1964.
- [4] Brandon, P.S., "The design of a nonlinear pulse compression system to give a low loss high resolution Radar performance", *Marconi Review*, vol.36, pp.1-45, 1973.
- [5] Fowle, E.N., "The Design of FM Pulse Compression Signals", *IEEE Trans. on Information Theory*, vol. IT-10, pp.61-67, January 1964.
- [6] Key, E.L., Fowle, E.N., and Haggarty, R.D., "A Method of Designing Signals of Large Time Bandwidth Product", *IRE International Convention Record*, Part 4, pp.146-154,1961.
- [7] Worley, J.C., "Implementation of Nonlinear FM Pulse Compression Filters Using Surface Wave Delay Lines", *Proceedings IEEE*, vol. 59, pp. 1618-1619, November 1971.
- [8] Famett, E.C., and Stevens, G.H., *Pulse Compression Radar*, in Radar Handbook, M. Skolnik ed., McGraw-Hill, NY: 1990.
- [9] Price, R., "Chebyshev low pulse compression side lobes via a nonlinear FM", *National Radio Science Meeting of URSI* (Digest Abstract), Jun 18, 1979, Seattle, WA.
- [10] Johnston, J. A., et al, "Waveform Design and Doppler Sensitivity Analysis for Nonlinear FM Chirp Pulses", *IEE Proceedings*, vol.133, Pt. F, No.2, pp.163-175, April 1986.

- [11] Kowatsch, M., and Stocker, H.R., "Effect of Fresnel Ripples on Side lobe Suppression in Low Time-Bandwidth Product Linear FM Pulse Compression", *IEE Proceedings*, vol.129, Pt. F, No.1, pp.41-44, February 1982.

13 Selected Radar Applications

13.1 Tracking Radar

The exact position of the target is required for a few applications of Radar technology. Some examples are airspace surveillance, linking with spacecraft and/or satellites, or for use in military applications. The accuracy of the angle position ($\approx \theta_{HB}/2$), attainable with the directivity of the antenna, is not sufficient. The measurement of Δx of an object over the resolution at a range R , realizable by the half-power bandwidth Θ_{HB} of the antenna, is large for greater distances.

$$\Delta x = \theta_{HB} \cdot R \quad (13.1)$$

A value of $\Delta x \approx 17,3$ m results for $\Theta_{HB} = 1^\circ$ at a range of 1 km. To improve this various procedures for pivoting or rotating antennas have been developed for target scanning. This includes all scanning procedures, such as Conical Scanning, and directivity-switching procedures, such as Sequential Lobing. These procedures are relatively time consuming, since they are serially operated. A considerably faster procedure, which operates as a parallel process, is the Monopulse Procedure.

13.2 Monopulse Radar

The so-called Monopulse Procedure makes possible a considerable improvement. At first the name is somewhat misleading. It signifies the possibility to already determine the target with one pulse. As almost always there are, as normal, a vast number of pulses to integrate for improving the signal-to-noise ratio. Now and again this procedure is also referred to Simultaneous Lobing. From this it is possible to recognize the implementation: several directivity patterns are radiated at the same time. If this takes place with an antenna then one refers to the Amplitude Monopulse Procedure. If two locally separated antennas are used then one normally realizes the so-called Phase Monopulse Procedure. The Amplitude Monopulse Procedure will soon be described in more depth. The antenna of amplitude monopulse Radar radiates for determining the respective target angles θ and ψ of two separate, however correlated directivity patterns. This is illustrated in Figure 13.1.

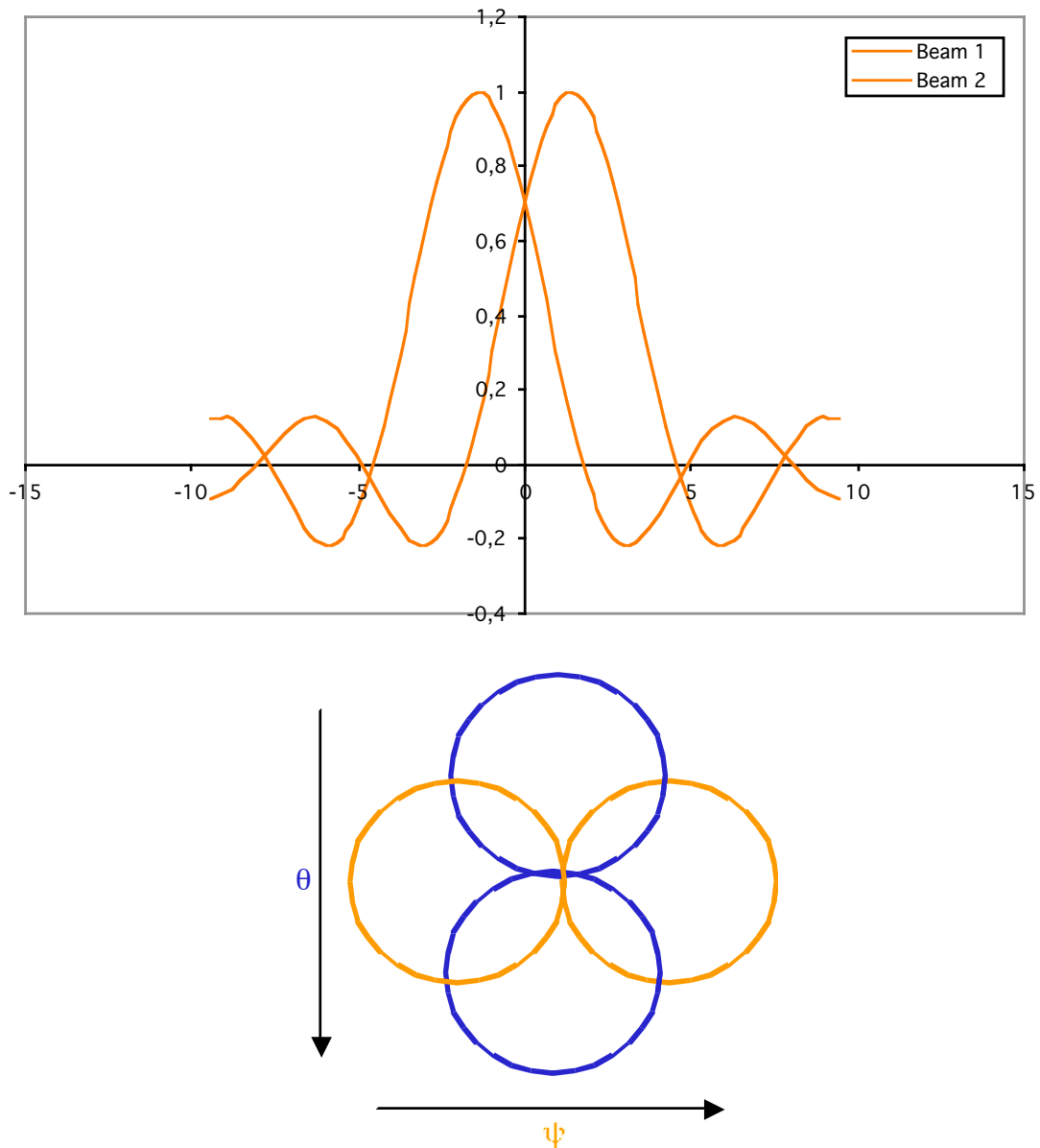


Figure 13.1 Example directivity patterns of monopulse Radar in the θ and ψ planes, intercept points 3 dB. Above: Horizontal characteristic. Below: Section through the 2x2 directivity patterns.

The antenna features four feeder antennas, e.g. Horn emitter, for the creation of these four individual directivity patterns with a reflector antenna. With phase controlled antennas the four patterns can be realized by four different, however, simultaneous allocations. Figure 13.2 shows a feeder system for a two-channel monopulse Radar consisting of eight log-periodic monopole arrays. These are combined into a beam-forming network of the type that form circularly polarized sum and difference patterns.

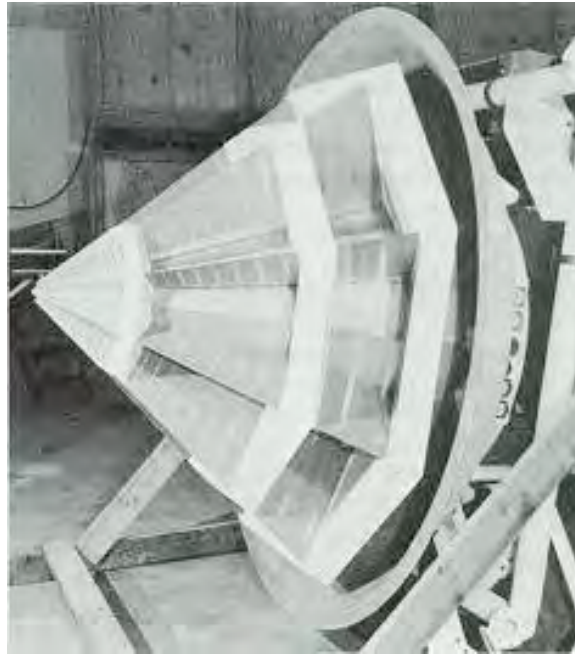


Figure 13.2 Two-channel monopulse antenna system.

The feed-ins of antennas of this type are created by $6 \times \lambda/4$ Hybrids (rat race ring) or “Magic Tee’s” (Figure 13.3).

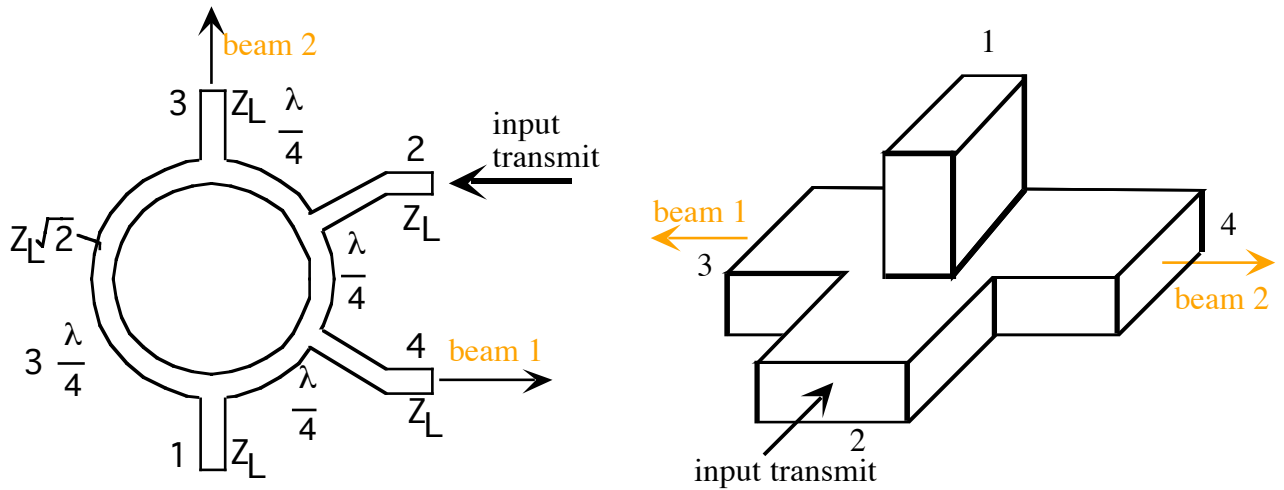


Figure 13.3 Transmit feeds of a monopulse antenna for the ψ -plane (equivalent θ -plane). Left: $6 \times \lambda/4$ Hybrid. Right: Magic Tee.

Since both feed-ins (beam 1 and 2) are of the same phase and are coherent, a summation pattern will be radiation, as represented in Figure 13.4.

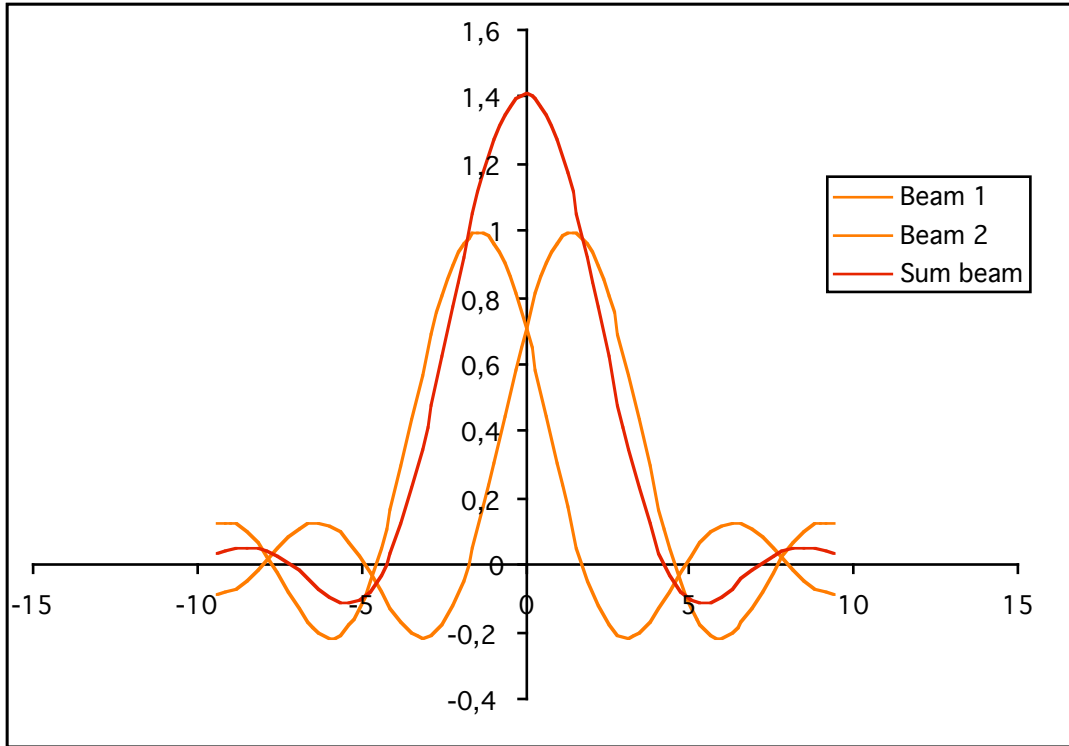


Figure 13.4 Transmitting monopulse directivity characteristic in the ψ -plane (equivalent θ -plane).

When receiving the reflected signals will be received over both gates. The hybrids each form sums and differences (Σ - Δ), as shown in Figure 13.5 and 13.6.

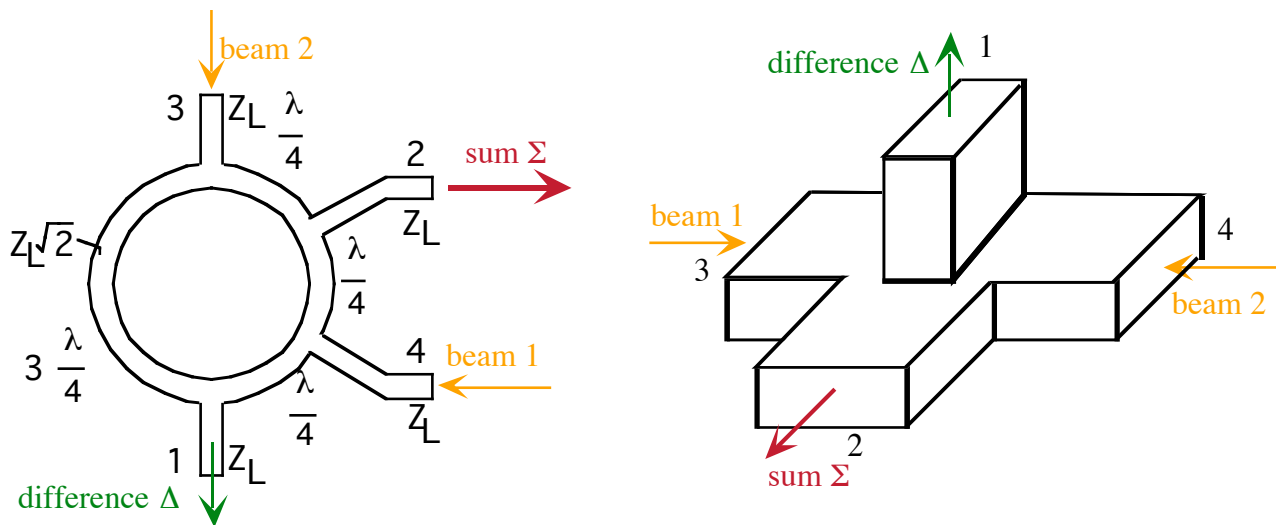


Figure 13.5 Reception with a monopulse antenna for the ψ -plane (equivalent θ -plane). Left: $6x\lambda/4$ Hybrid. Right: Magic Tee.

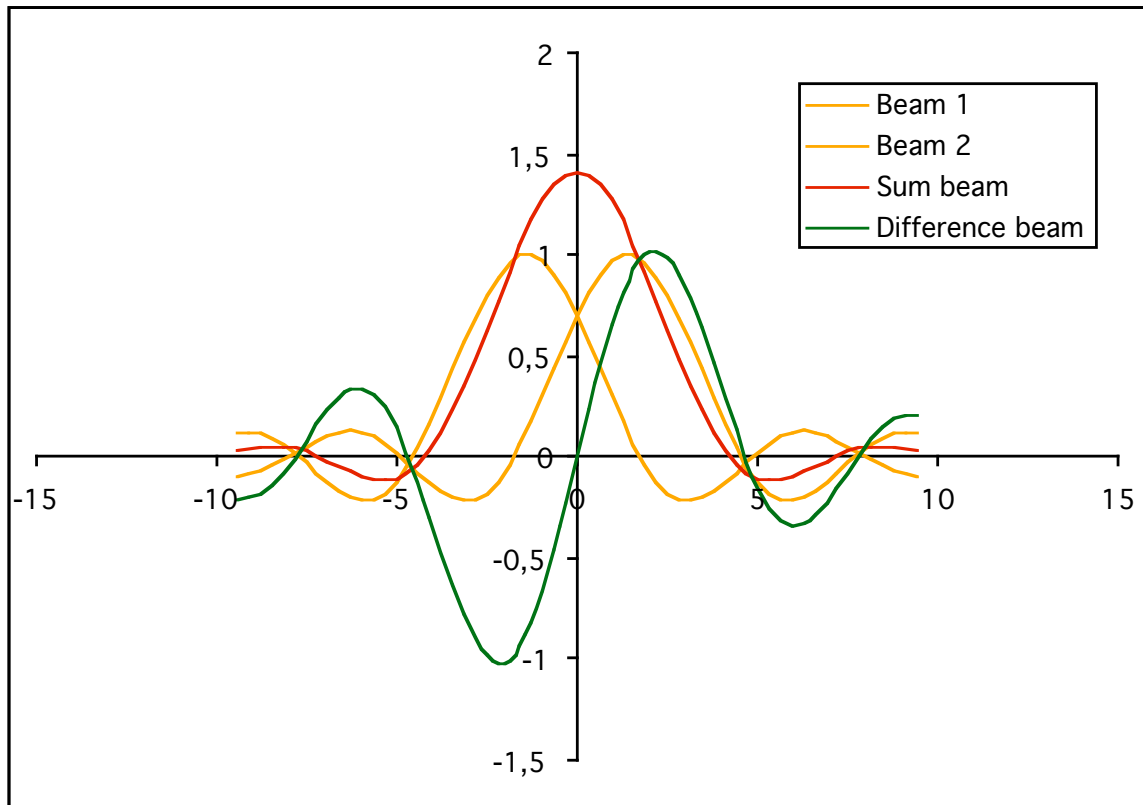


Figure 13.6 Receiving monopulse directivity characteristic in the ψ -plane (equivalent θ -plane).

The patterns in Figure 13.6 are normalized. By overlapping the individual directivity patterns at the 3 dB points, the achieved normalized sum is $\sqrt{2}$. The difference diagrams (beam 1 – beam 2) are of particular interest for the determination of the directivity. This has a nearly linear progression from -1 to $+1$ between both maximums of the individual directivity patterns. This range, with an example dynamic of $2 \times 25 \text{ dB} = 50 \text{ dB}$, is available for the higher resolution of the angle between both individual directivity patterns, e.g. 2° . Newer monopulse Radar devices have these difference curves stored in look-up tables. An improvement of the angle resolution of better than $.02^\circ$ is easily possible. For monopulse Radar in two plans (θ and ψ) the circuits of both single planes are merged over a further hybrid, shown in Figure 13.7.

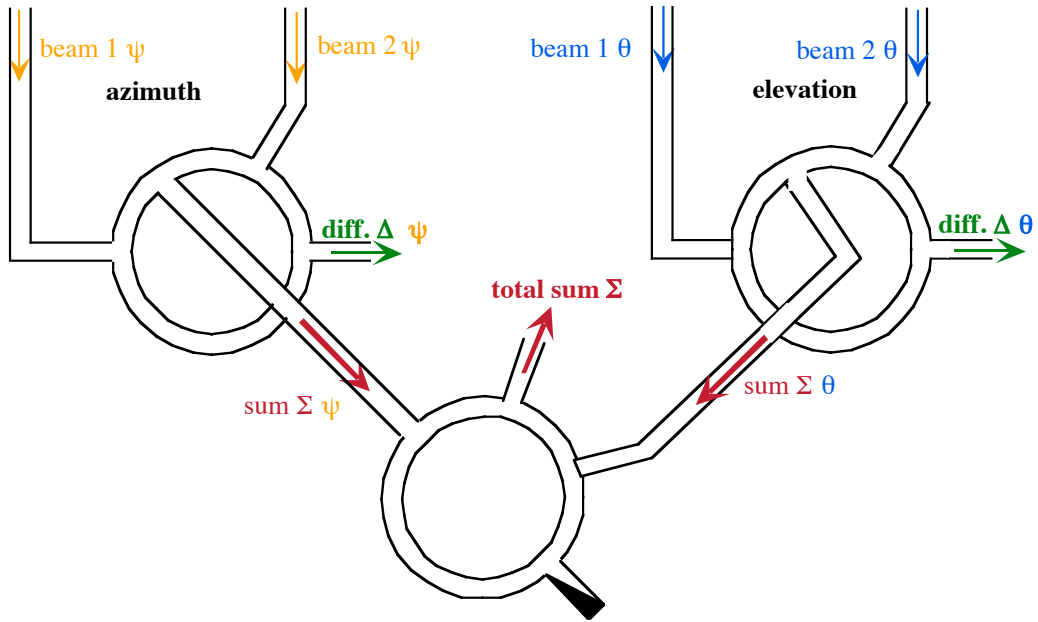


Figure 13.7 Two-plane (ψ - θ) receiving monopulse circuit.

The summation channel is evaluated as in normal pulse Radar for the measurement of the range and the velocity. Both difference channels determine the angles in azimuth and elevation. For the transmitting case (arrows in opposite directions), the power is fed into the summation channel and the difference channels are decoupled and remain without power. Three parallel receiving channels are required for monopulse Radar, which must be synchronized with one another. The block diagram of a monopulse Radar device is represented in Figure 13.8.

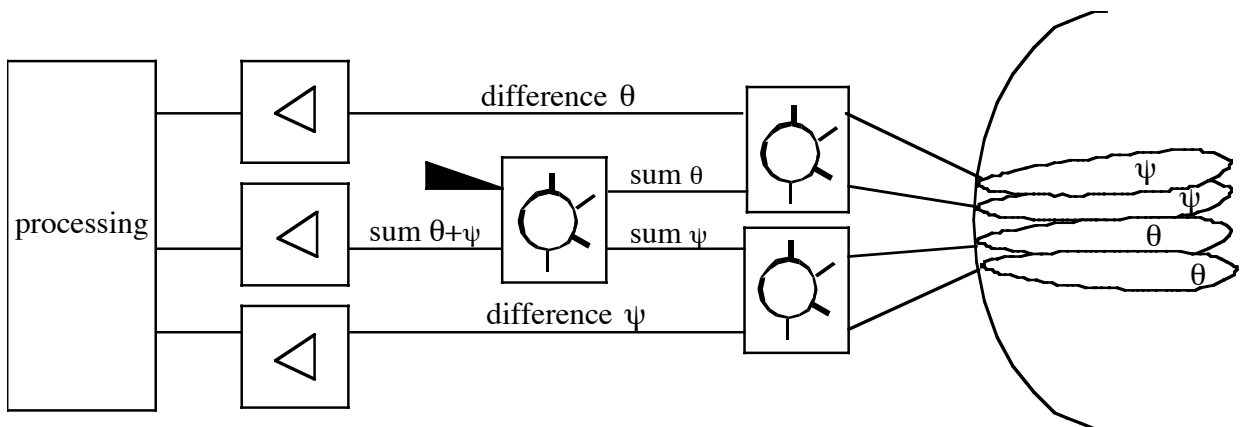


Figure 13.8 Block diagram of a monopulse Radar device.

13.3 Automotive Radar (ACC)

13.3.1 History

The first ideas to use Radar devices in vehicles date back to the 1950's. Radar devices are generally attractive for vehicles, since they are able to determine the distance and velocity of other objects, regardless of weather. General Motors realized the first integration in 1959 in the Cadillac Cyclone [GM], Figure 13.9. Behind the smooth, black plastic horns is hidden a modified airplane Radar. The distance to the approaching vehicle and the braking distance are indicated on the instrument panel.



Figure 13.9 Radar in the 1959 Cadillac Cyclone.

Radar was still constructed with tube technology and with very simple target extraction. The Microprocessors and digital signal processing of the mid 1970's brought about a boom in the development of Radar instrumentation. This made possible the considerable size reduction of instruments for microwave technology. The first Radar to be constructed completely with transistors is described in [LiW], and operated at 35 GHz. It operated in pulse mode with a resolution of approximately 2m. The frequency for this was internationally coordinated at the beginning of the 1970's. Gunn elements were used in the oscillators. The device had only one main beam direction. Sample lines were constructed on various occasions, but it was recognizable that no cost-effective manufacturing was to be expected.

This only came about in the mid 1990's with the availability of MMIC's (Monolithic Micro-wave Integrated Circuits), which allowed for higher level of integration. As a main application the automatic distance control appeared in the sense of an intelligent cruise control system (*AICC Autonomous Intelligent Cruise Control; ACC Adaptive Cruise Control; ICC Intelligent Cruise Control*).



Figure 13.10 ACC Radar sensors for highway and street traffic (Courtesy A.D.C.).

Since then the frequency range from 76 GHz to 77GHz has been licensed in Europe, the USA and in Japan (Technical Standard EN301091 V1.1.1, ETSI) for the use in ACC. The first series installation took place with the S-class from Mercedes at the beginning of 1999. Nearly all such Radar devices of this recent generation possess three horizontal antenna beams of around 3° each. The typical range is indicated as 150 m for objects with 1 m^2 Radar cross-section. The direction of the acquired target is determined with a mono-pulse procedure. The data processing is usually so applied that a certain number of point targets in the distance (> 32) and the stored angles (history) are tracked and are evaluated in their significance for the same lane as the traveling automobile. For range determination almost all well-known procedures are employed, such as Pulse Radar, FM-CW, Pseudo Noise and Multifrequency CW procedures, whereby the FM-CW is the most frequently used procedure. The antennas are usually quasi-optically formed and the individual directivities are switched electronically. The processing forms the main part of the devices. In 2000 their size was approximately $10 \times 10 \times 10 \text{ cm}^3$.

The vision for 2010 is one of transportation supported by several Radar sensors, as shown in Figure 13.10 and 13.11. Radar sensors are used apart from the distance and obstacle controls in the range up to 250 m and eventually will be used additionally for close-range sensing to approximately 5 m (city traffic, airbag sensors, etc.), used as impact sensors (airbags, seatbelt control), for complete angle sensing (lane changing), and so forth. It is anticipated that close-range sensing will be controlled with sensors operating at 24 GHz. A drastic drop in price is also expected in the coming years. It is expected that legal regulations for the installation of these systems in buses and heavy transport will be first. This is likewise expected with rail-mounted vehicles. It is also considered possible that the number of accidents will decrease

and the transport capability will increase with the equipment of all vehicles with such Radar sensors and systems. In the long-term prices will probably sink to the same price level as car radios.



Figure 13.11 Vision of transportation and traffic supported by Radar sensors (Courtesy A.D.C.).

13.3.2 Automobile Radar System Parameters

13.3.2.1 Coverage

The area in front of the vehicle, which is around 1.5 the breaking distance, is identified as the collision region. The neighbouring lanes, left and right, are also considered and the functioning of such a Radar system must also guarantee safety when driving in the curves. This is shown for a section of straight road in Figure 13.12. The lane width of streets is normally around 3 – 3.4 m. Thus there is an angular range of $\pm 5^\circ$, which must be additionally acquired during curving. Presently the antenna patterns are not adjusted with the turning of the steering wheel.

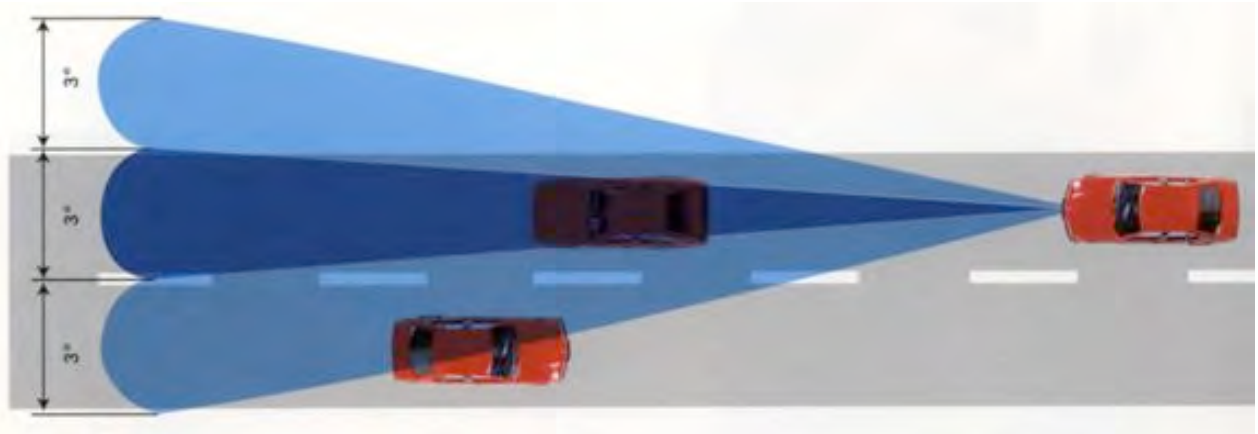


Figure 13.12 Coverage of an ACC sensor (Courtesy A.D.C.)

Today the collision region is normally covered by 3 radiated beams, which are sequentially switched. A further field of vision is required in the near region, e.g. during city driving for the acquisition and detection of incoming traffic from the sides and perpendicular directions. This near field sensing is illustrated in Figure 13.13. The near field is also referred as the cut-in zone and here a higher resolution is required than in the far field. At present the ACC Radar detectors do not provide special measures for a particular detection or acquisition at close range.

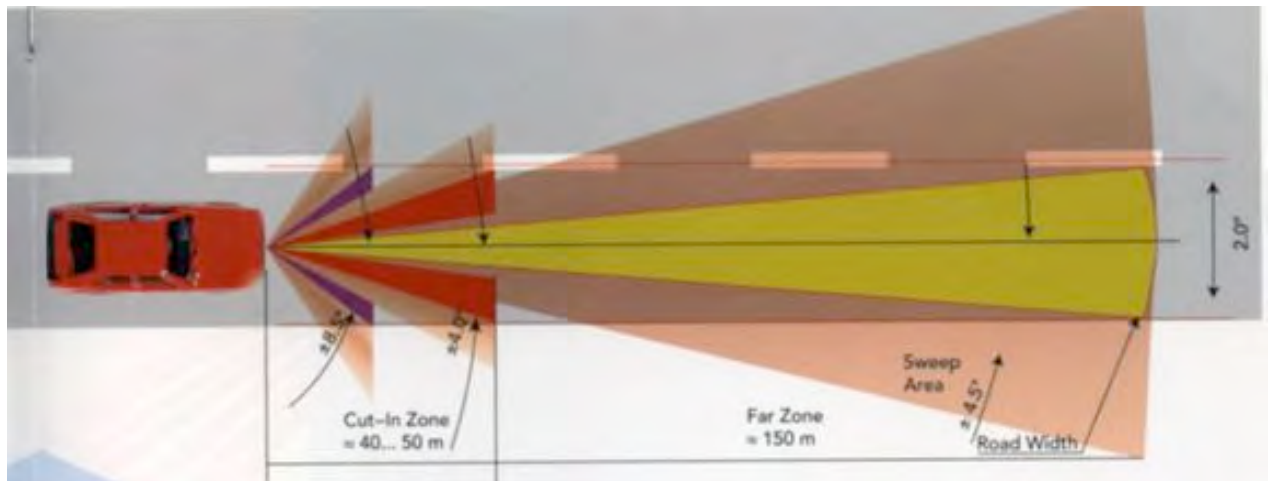


Figure 13.13 Coverage of an ACC sensor with close-range sensing (Courtesy A.D.C.)

13.3.2.2 Antenna Design

Today dielectric lenses are almost exclusively used for ACC Radar sensors. In a few cases are these full lenses and in other cases layered lenses. There are also well-known antennas with polarized lattices having double reflection at 45° . The price will be crucial for the future. The lenses are excited by patch-antennas ($\lambda/2$ emitter) or by dielectric shaft emitter. The polariza-

tion in normally chosen to be 45° in order to be stimulated by vertical as well as horizontal structures of the targets.

The 3 dB width of the antenna characteristic is today between 2° and 3°. The three directivities overlap each other at the 3 dB points. The correlation for a cos² allocation (side lobes < 32 dB) is represented in Figure 13.14. In practice side lobes < 25 dB are required. After an antenna width of approximately 110 mm a half-power bandwidth of around 3° results.

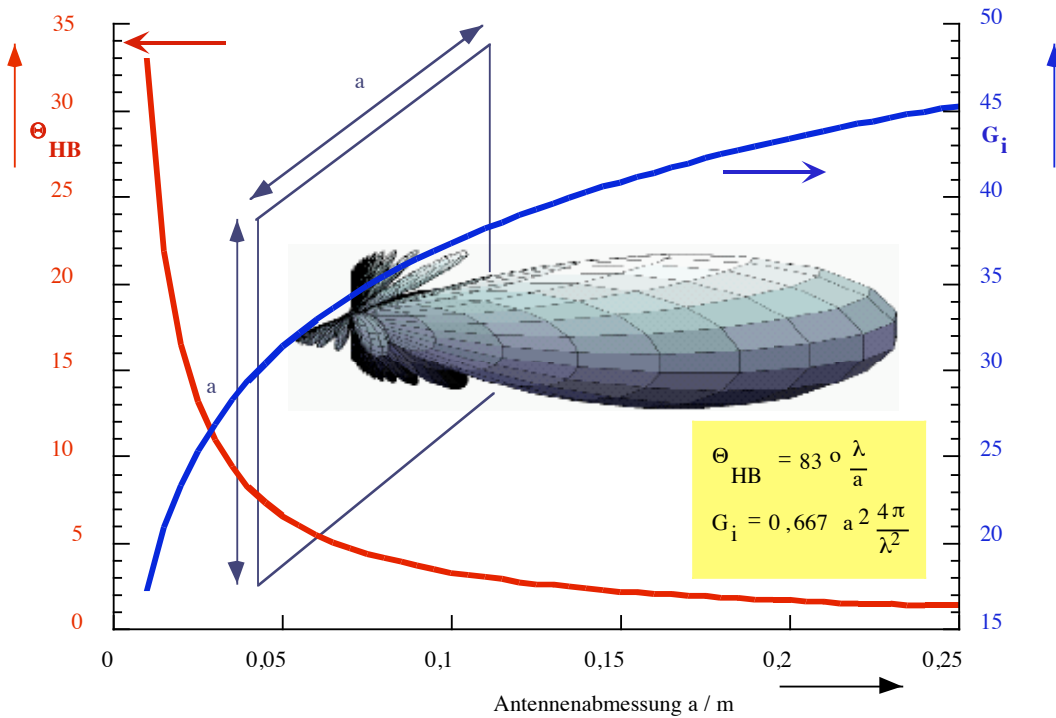


Figure 13.14 Antenna parameters at 76 GHz, half-power bandwidth Θ_{HB} , gain G_i , with \cos^2 alignment, and quadrature antenna (left Θ_{HB} , right G_i).

13.3.2.3 System Paramter Overview

Kriterium	Spezifikation	Zielspezifikation
Angle range	$\pm 4^\circ - \pm 5^\circ$	$\pm 8^\circ$
Half-power beamwidth	3°	1°
Angle precision	$0,2^\circ - 0,5^\circ$	
Angle resolution	$0,1^\circ - 0,25^\circ$	
Beam switching	elektronisch	elektronisch
Field of range	2 m - 150 m	1 m – 250 m
Range precision	0,5 m oder 5%	
Range resolution	0,05 m – 0,5 m	0,2 m
Velocity range	$\pm 2 - \pm 50$ m/s	$0 - \pm 60$ m/s
Velocity precision	0,25 - 0,4 m/s oder 5%	

Velocity resolution	0,1 m/s – 0,2 m/s	
Antenna size	8x8 cm ² bis 10 x 10 cm ²	
Bandwidth	> 100 MHz	> 300 MHz
Smallest target at 150 m	1 m ²	1 m ²
Reaction time	100 ms	30 ms
Interface	CAN	

Table 13.1 Typical specification for an ACC sensor.

13.3.3 Circuit and Switching Concepts

The main components of an ACC Radar sensor are:

- RF frontend
- Signal processing
- Vehicle interface

The RF frontend contains the oscillator, the transmitting/receiving duplexer and the receiver. Today the oscillators are normally constructed at frequencies of 19 GHz or 38 GHz with duplication or triplication. The pulse modulation takes place via the switching. With FM modulation the FM pass is added. For the transmitting/receiving duplexer $6x\lambda/4$ hybrids are used. These lead a priori to a loss of over 6 dB. The receiver is constructed as a “push-pull” mixer. The sample takes place in the baseband.

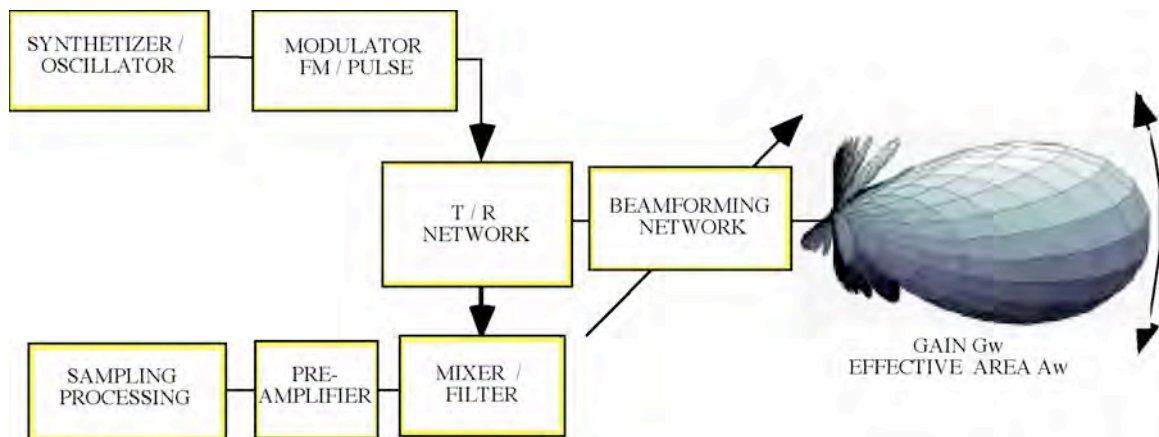


Figure 13.15 Block diagram of an ACC Radar sensor.

There are very differing implementations for the individual function blocks. Examples will be shown in the proceeding sections.

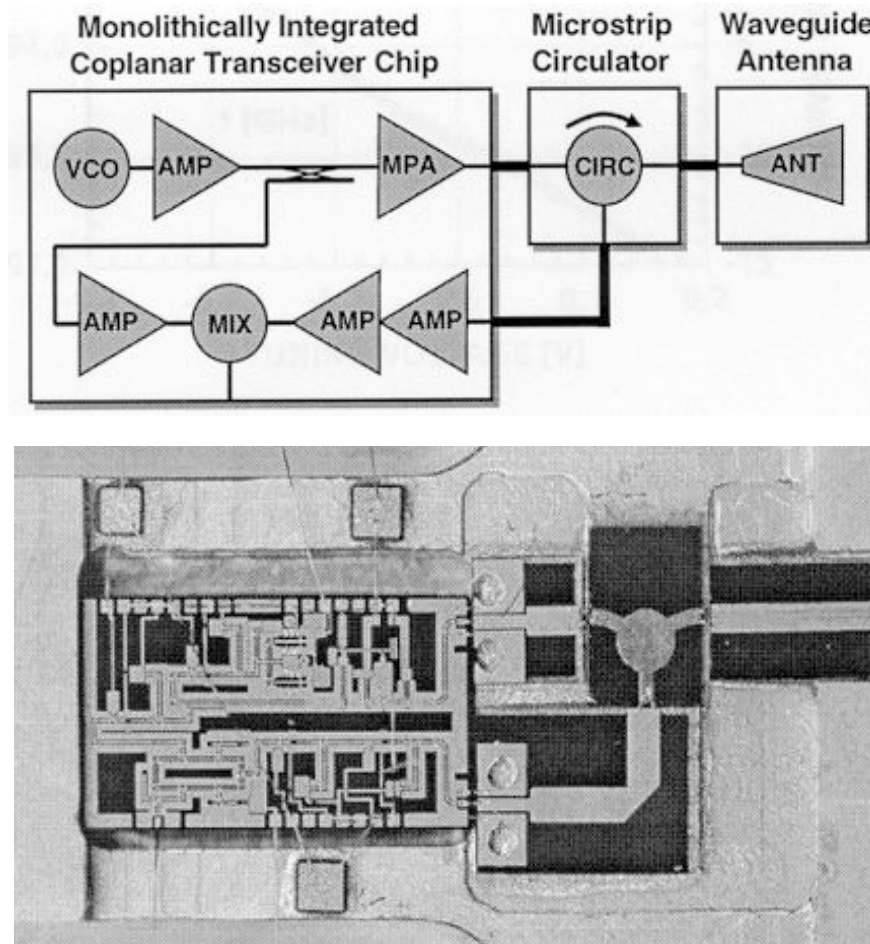


Figure 13.16 Block diagram and inner-view of a 94 GHz FM-CW ACC Radar sensor, IAF (Fraunhofer Institut Angewandte Festkörperphysik) ERA9401

MMICs of 76 GHz will be employed in the next generation, approximately 2003, as shown in Figure 13.17.

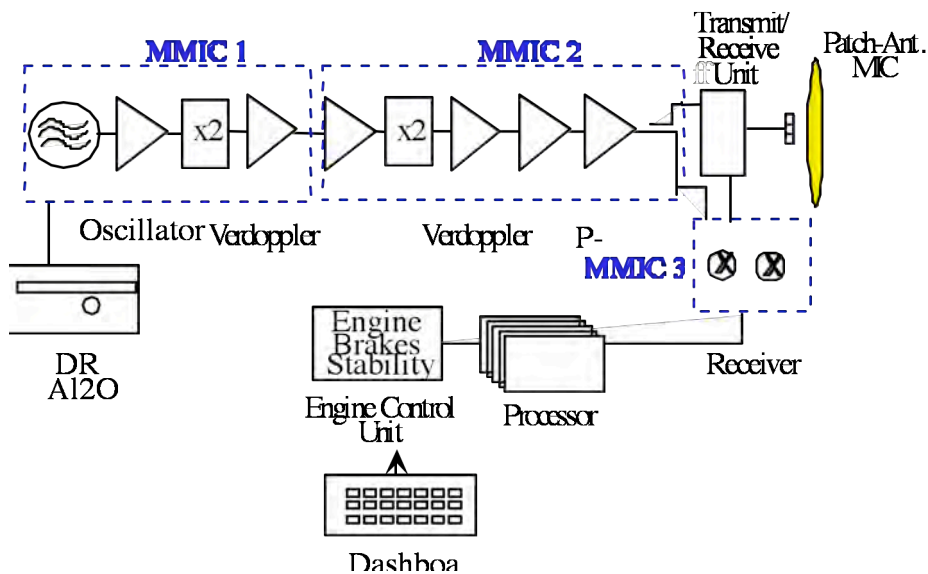


Figure 13.17 Concept of a highly integrated (3 MMIC) ACC Radar sensor.

A considerably higher integration can be achieved using MMICS. A large advantage is the reduction of the millimeter-wave connections. With that there is an increase in the reliability and a reduction of the line losses.

13.3.4 Modulation Procedures

As is represented above are presently very many different modulation procedures used. The most successful will be that form of modulation, which best handles multiple targets.

13.3.4.1 FM-CW Modulation Procedures

The most frequently used modulation procedure is FM-CW. As a rule a trapezoidal modulation is used, since it most simply allows for the determination of range and velocity. Since it, however, is not always unique, two or several different trapezoids are sent in succession. The varying edges are chosen to increase the uniqueness. This also results in various “beat frequencies” for identical targets, a fact that can also be exploited.

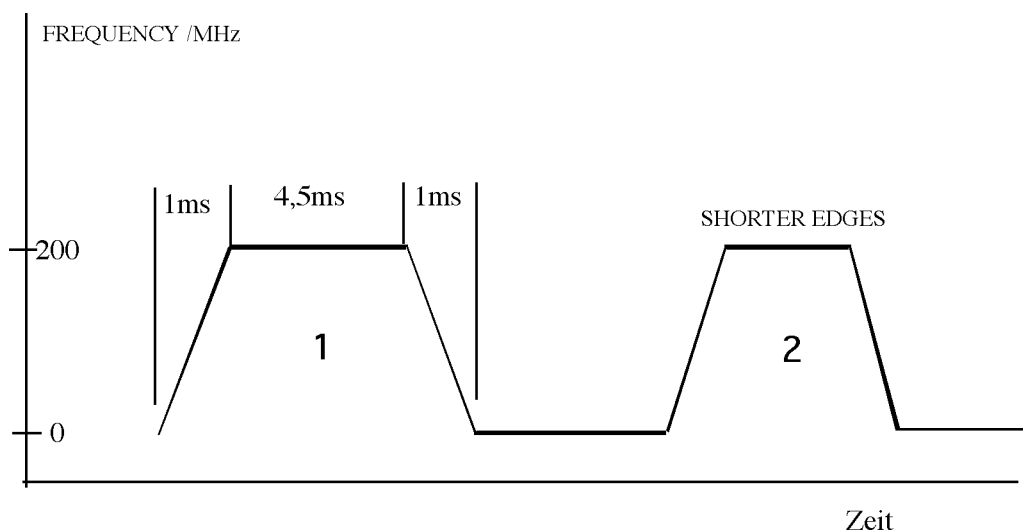


Figure 13.18 Typical double-trapezoidal modulation for ACC sensors.

13.3.4.2 FSK Procedure

FSK modulation procedures are similar to the instrumentation Radar procedure from Radar measuring technology. The large advantage is the extremely high sensitivity due to the narrow bandwidth. The analysis is almost exclusively based on phase and phase difference measurements. Problems can arise with targets having a velocity difference of zero.

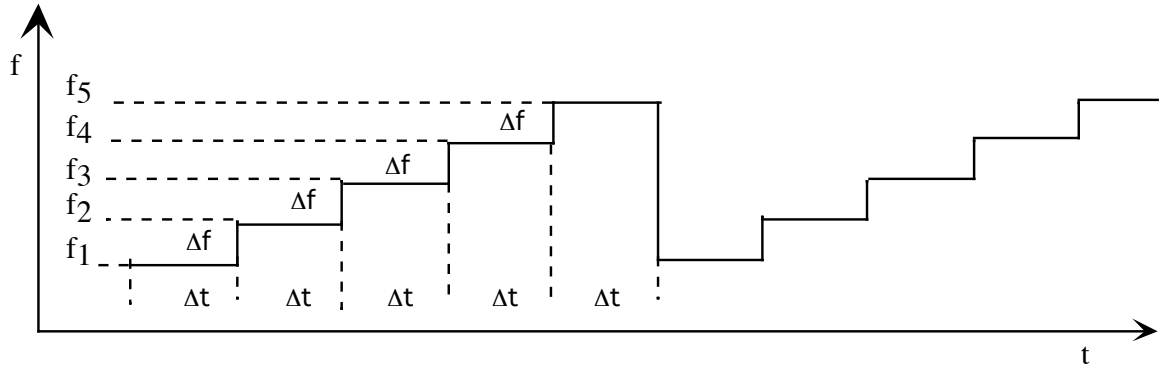


Figure 13.19 5-step FSK procedure (typically: $\Delta f = 150 \text{ kHz}$, $\Delta t = 2,4 \mu\text{s}$)

13.3.5 Processing

The effectiveness of an ACC sensor is decisively dependent on the processing. The core task emerges from the structure of the data history, somewhat of a development of the target or relevant object. Only with this can it be decided, for example, if there is an object on the road or perhaps on the side of the road during a curve. Bridges can also be distinguished as relevant objects. The resolution of an A/D converter could be around 12 bits. Depending on the procedure it is possible to carry out multiple transformations and filtrations.

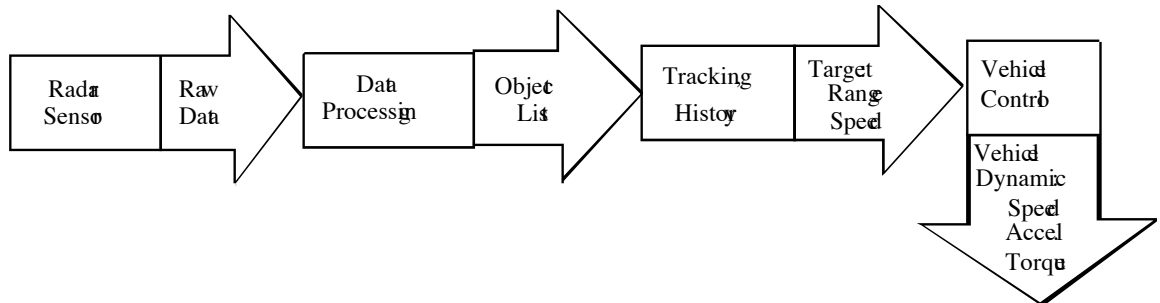


Figure 13.20 Scheme for processing with ACC Radar sensors.

13.3.6 Reflection Cross-Section in Street Traffic at 76 GHz

Obstacles in traffic can range from stones to trucks with flat, metallic rear walls. The reflection cross-section σ is defined in the respective far field. For a Radar with the aperture diameter $a=10 \text{ cm}$ of the antenna, this is:

$$R_{FF} = \frac{2 \cdot a^2}{\lambda} = 5m \tag{13.2}$$

For an object, e.g. a truck, with a width d the range becomes considerably larger:

$$R_{FF-LKW} = \frac{2 \cdot d^2}{\lambda} = 2km \tag{13.3}$$

Since large objects no longer find themselves in the far field, the calculational reflection cross-section cannot be achieved. The 76 GHz Radar with 1° half-power bandwidth and at a distance of 100 m only illuminates a circle with a diameter of 1.73 m. Figure 13.21 shows the typical reflection cross-section σ for 76 GHz.

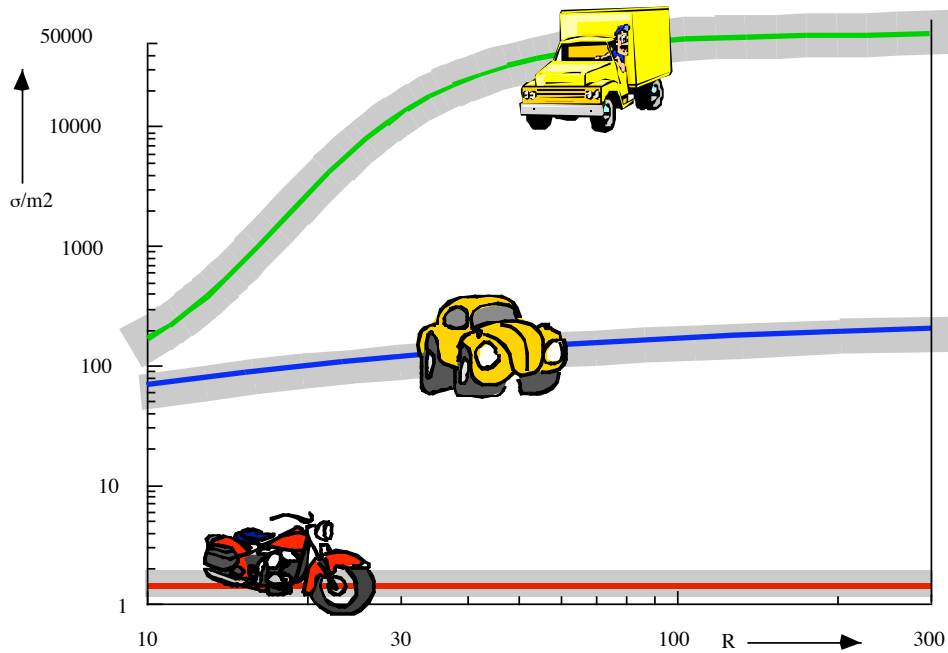


Figure 13.21 Typical reflection cross-section for a 76 GHz Acc Radar sensor.

In the literature [Cur, TaK] there are given the flowing values found in the table below.

Objekt	$\sigma_{\min}/\text{dBm}^2$	$\sigma_{\max}/\text{dBm}^2$
car (from the rear)	0	20
truck (from the rear)	0	40
motorbike	-10	10
bicycle	-10	5
person	-10	0
stone	-10	-

Table 13.2 Typical reflection cross-section values for 76 GHz ACC Radar.

The dynamic of the values can become somewhat compressed by the far field conditions.

13.3.7 Power Budget

Following is given a large estimation of the power budget. Also considered is the processing gain by integration or pulse compression, as well as losses. It is possible to estimate the following standard values:

Noise bandwidth	B_N	150 MHz
RF losses ¹	L_{RF}	13 dB
Phase noise (at 100 kHz)	PN	<-85dBc/Hz
Noise figure	F	12 dB
Processing gain ²	G_I	17 dB
Signal-to-Noise ratio ³	S/N	8 dB
Thermal noise	kTB_N	-92,5 dBm
Antenna gain	G_T, G_R	35 dB
Range	R	150 m
Reflection cross-section	σ	1 m ²

Table 13.3 Typical values of a power budget for a 76 GHz ACC sensor.

¹) Losses ~ 2*1,75 dB, T/R-Hybrid ~ 6.5 dB, power losses ~ 3 dB, total = 13 dB

²) Integration coherent over 512 pulses, processing losses accounted for to 10dB

³) (POD > 80%; POF < 2%)

The minimum receiving power $P_{R\min}$ is:

$$P_{R \min} = \frac{kTB_N \cdot (S/N) \cdot L_{RF} \cdot F}{G_I} \quad (13.4)$$

$$P_{R \min} = -92,5 + 8 + 13 + 12 - 17 \approx -76,5 \text{ dBm}$$

For further computation it is assumed that the phase noise does not continue to reduce the sensitivity. From this the minimum transmitting power results as follows:

$$P_{T \min} = P_{R \min} \frac{(4\pi)^3 \cdot R^4}{G^2 \cdot \lambda^2 \cdot \sigma} \quad (13.5)$$

$$P_{T \min} = -76,5 + 33 + 87 - 70 + 48 - 0 = 21,5 \text{ dBm}$$

Usually the transmitting power lies in the range of 100 mW. Vast improvements are expected in the sensitivity of the next generation of ACC sensors with integrated circuitry.

13.3.8 ACC Sensor System Specification

The following specifications for the frontends of future ACC Radar sensors are being strived for [Sch]:

Frequency	f	76,5 Ghz
Transmitting power	P_T	22,5 mW
Antenna gain	G	35 dB
No of beams		5
Pulse duration	τ	6,7 ns
IF bandwidth	B	150 MHz
Noise figure	F	7 dB
Pulse repetition frequency	PRF	71 kHz
Processing gain	N_{FFT}	512

Table 13.4 Sensor system specifications for 76 GHz ACC Radar.

13.3.9 MMIC Integration

In previous years there have been many high-integrated chips for ACC and other vehicle sensors developed by several companies. The construction of the millimeter wave integrated circuit has been still up to now developed almost exclusively with Gallium-Arsenate. With integration the following has been achieved:

Reduction of costs

Reduction of the sizes

Homogeneous devices

Individual MMIC chips (2000 relevant) will be shown in the following figures.

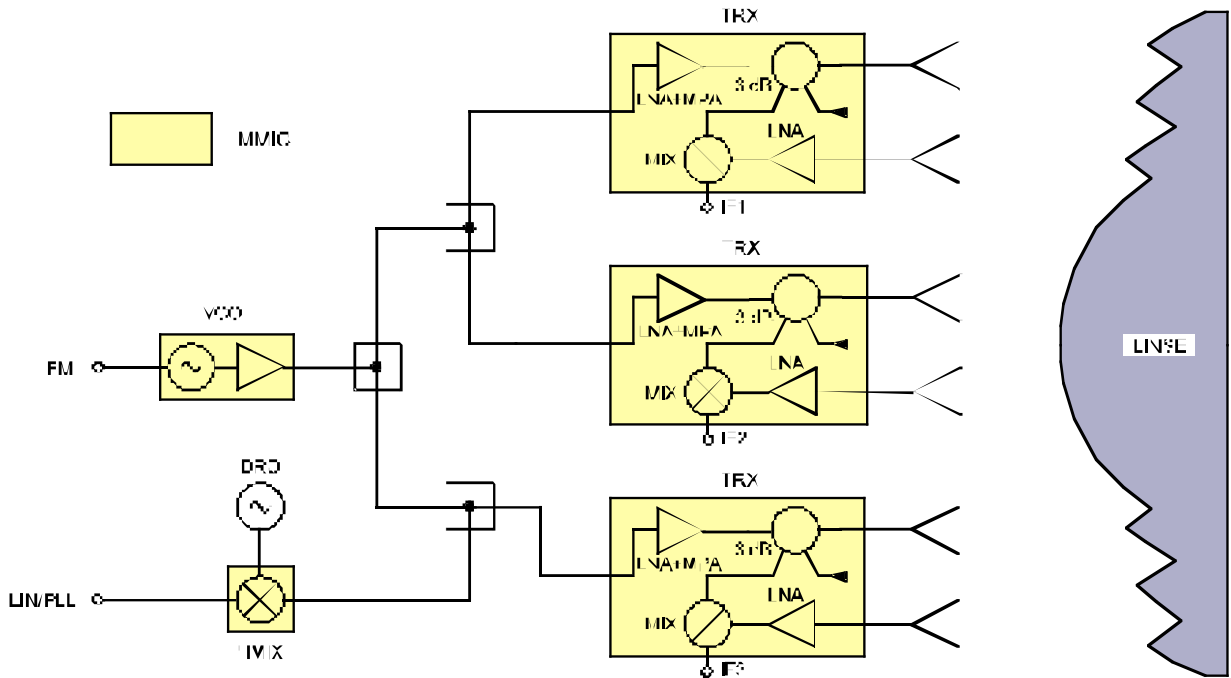


Figure 13.22 Block diagram of an integrated ACC (Infineon).

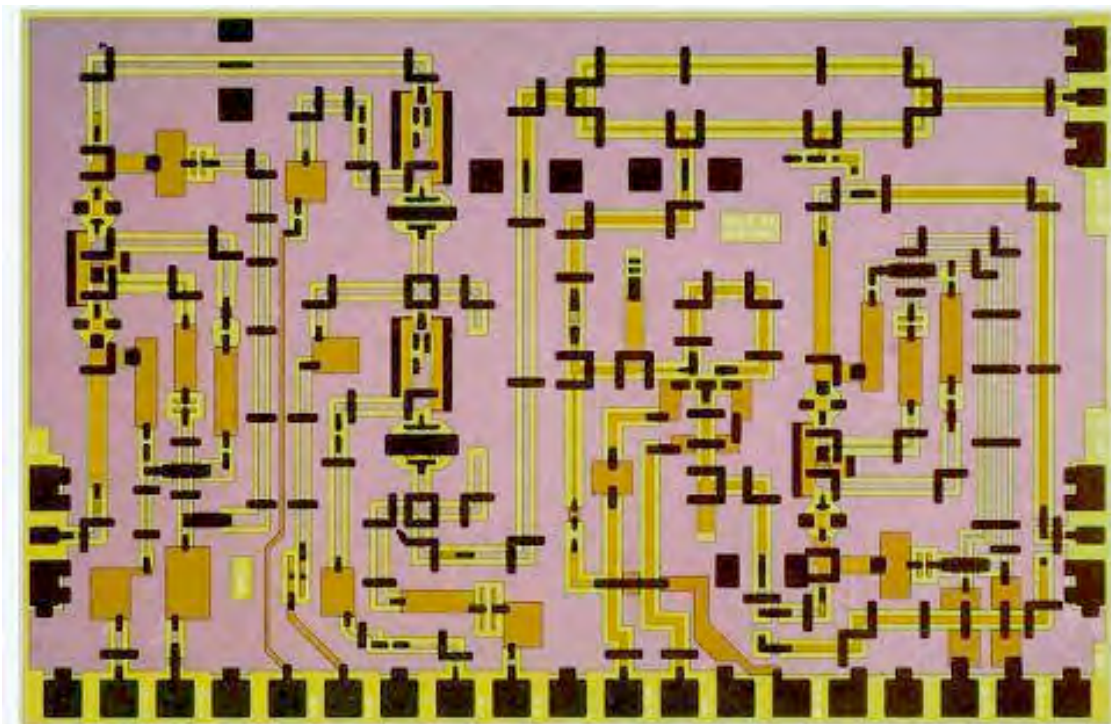


Figure 13.23 ACC on MMIC (Layout from Infineon).

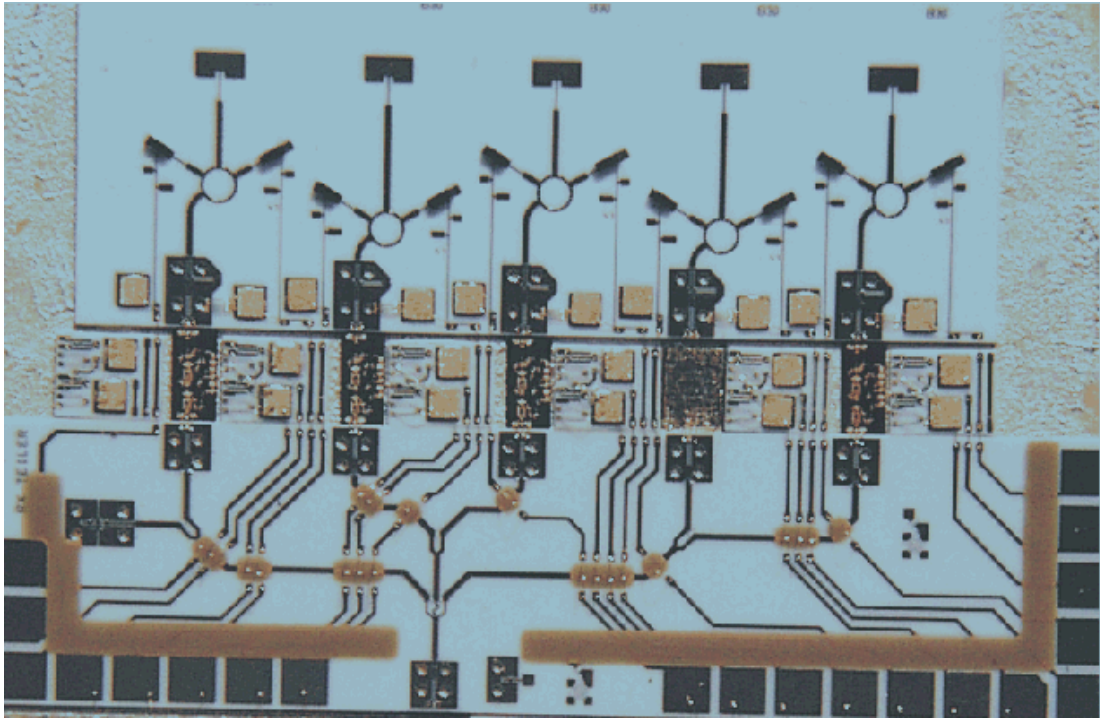


Figure 13.24 ACC on MMIC (Photo from Infineon).

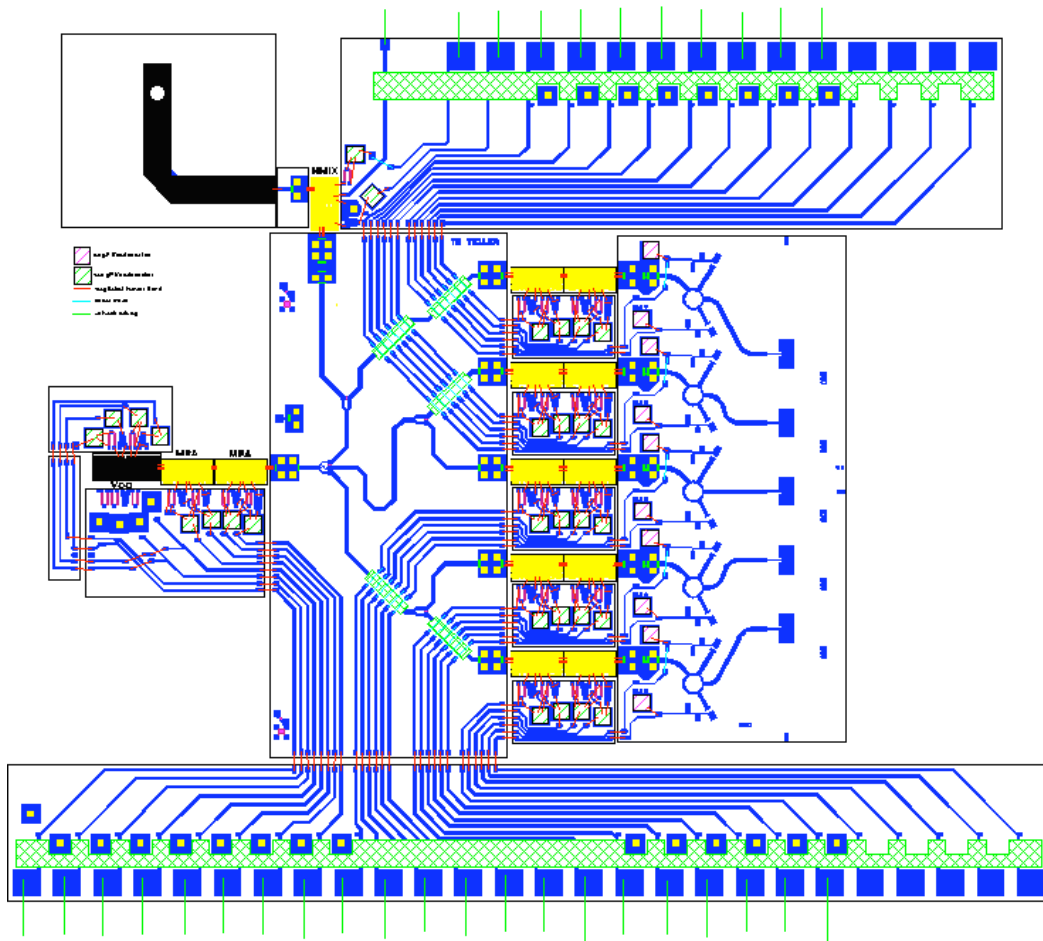


Figure 13.25 ACC on MMIC (Layout from Infineon).

13.3.10 Problem Areas

Despite the recognized effectiveness of Radar sensors in street traffic it may not be misconceived that there exist certain problems. A few are here listed:

Still Object Recognition: Stationary objects have the same characteristics as objects on the sides of the roads or bridges. They are distinguished only by their history, meaning that it is recognized somewhat late whether the objects represent dangers or not.

Detection with $v_{rel} = 0$: With FM-CW sensor there can be problems for objects which move very quickly, where $v_{rel} = 0$, since the velocity value zero is difficult to measure.

Multiple Objects: A large number of objects leads to “processing artifacts” for FM-CW sensors with FFT-Processing under certain conditions. Normally these can be identified and verified by using the history.

Mechanical Stability: The integration must have the necessary precision for millimetre wave technology. In particular this means that the alignment be exact by 0.1° .

Sensor Blindness Recognition: The function of the sensors must be continually checked to ensure the immediate detection of sensor blindness due to wetness, snow, dirt, pollution, defect, etc.

13.3.11 Literature

- [Cur] N.C. Currie, C.E. Brown (eds), Principles and application of millimeter-wave Radar, Aertech House, Norwood, MA, 1987
- [GM] --"Cars Detroit Never Built" (anitquarisch), Stirling Publishing Co. New York
- [GrD] H.P. Groll, J. Detlefsen, History of automotive anticollision Radars and final experimental results of a mm-wave car Radar, developed by the Techn. University of Munich, *IEEE Aerospace El. Systems Magazine*, pp. 13-18, Dec. 1995
- [GrJ] D.M. Grimes, T.O. Jones, Automotive Radar,; a brief review, *Proc. IEEE*, vol. 62, no. 6 pp. 804-822, 1974
- [LiW] K. Lindner, W. Wiesbeck, 35 GHz-ImpulsRadarsensor zur Verwendung in Abstandswarngeräten für Kraftfahrzeuge, *Nachrichtentechnische Zeitung*, Ausg. 26, no 9, pp. 667-672, 1976
- [Mei] H.H. Meinel, Commercial applications of millimeterwaves: history, present status and future trends, *IEEE Trans. On Microwave Theory and Techniques*, vol. 43, no. 7. pp. 1639-1653, July 1995
- [Sch] R. Schneider, Modellierung der Wellenausbreitung für ein bildgebendes Kfz-Radar, Dissertation an der Universität Karlsruhe, Mai 1998
- [TaK] Y. Takimoto, M. Kotaki, Automotive AnticollisionRadar, *Applied Microwave*, Fall 1992

13.3.12 Exercises for ACC Radar

Given specification:

$$\begin{aligned}
 R &= 100m \\
 F &= 75GHz \\
 \sigma &= 1m^2 \\
 \Delta R &= 1,5m \\
 \Delta x &= 1,75m \\
 \Delta y &= 1,75m \\
 R_{unamb} &= 1000m \\
 S/n &= 14dB \\
 NF &= 10dB \\
 L_{RF} &= 12dB
 \end{aligned}$$

Check whether all the required specifications are present. Expand the specification if necessary by assigning meaningful and appropriate values. Begin with the simple calculations.

Find: Radar parameters?

$$\lambda =$$

$$P_t =$$

$$P_{\min} =$$

$$G_T =$$

$$G_R =$$

$$G_I =$$

$$A_{\text{eff}} =$$

$$\tau =$$

$$PRF =$$

$$B =$$

$$\theta_{HB} =$$

$$\psi_{HB} =$$

$$POD =$$

$$PFA =$$

13.4 Phased-Array Radar

Phased arrays are groups of antenna with the possibility to electronically steer the directivity (beam forming). This is achieved by a feeding network, which allows a specific influence of the phase and/or the amplitude for each individual element and/or sub-array of the entire array. With the appearing monostatic Radar devices, since the same antenna groups for transmitting and receiving are predominantly used, the transmitting and receiving paths must be additionally separately switchable. The named functions are made available by the so-called Transmit/Receive (T/R) modules, which are embedded into the system according to Figure 13.26.

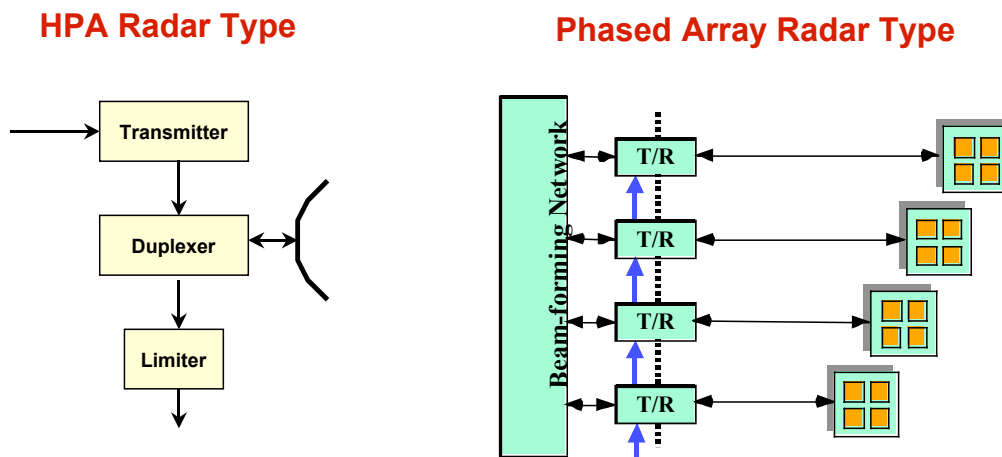


Figure 13.26 Conventional and phased-array Radar in comparison.

The typical requirements on a T/R module can be summarized as follows:

	2001	ab 2002
Output power:	4 – 10 W	> 16 W
Noise figure:	≤ 4 dB	< 2.5 dB
Region of adjustable phase	360 °	
Phase resolution	6 bit	
Region of adjustable amplitude	≥ 30 dB	
Amplitude resolution	6 bit	
Efficiency	> 18 %	> 35 %
Bandwidth	> 20 %	
Weight per module	≤ 120 g	
Dimensions per module	≤ 50 cm ³	

T/R modules can be realized by different methods. Figure 13.17 shows a full-polarimetric module. With which the deposited region, consisting of LNA (Low Noise Amplifier), PHS (Phase Shifter) and VGA (Variable Gain Amplifier), is used by corresponding changeover switches in transmitting and receiving mode.

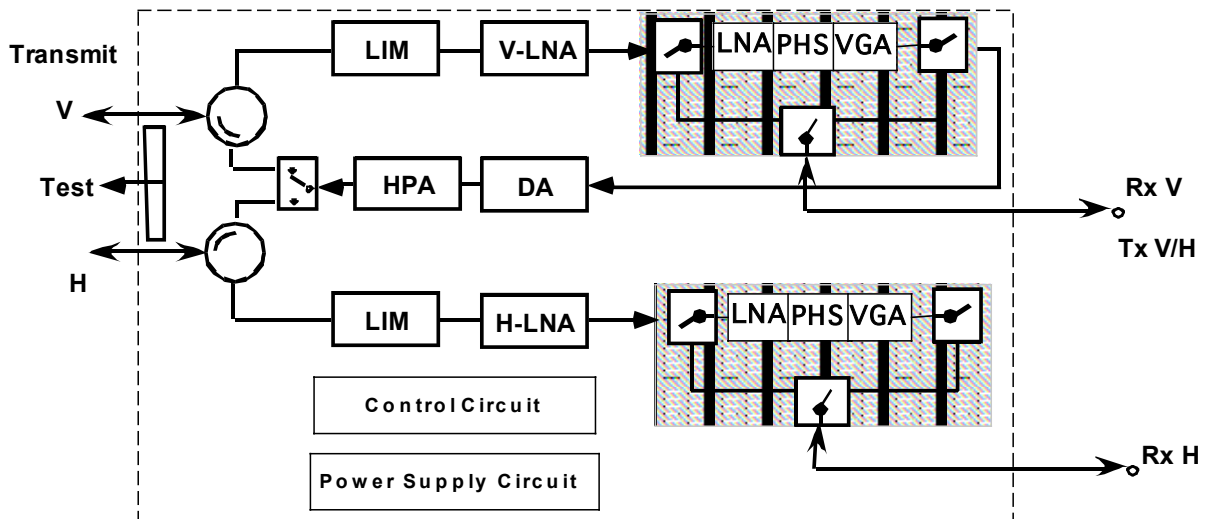


Figure 13.27 Full-polarimetric T/R module with high-power H/V changeover switch.

The realized system *DESA*, from the company Astrium GmbH, is shown in the Figures 13.28 and 13.29. It features the following specifications.

Center frequency	9.6 GHz
Bandwidth	≥150 MHz
Polarisation	horiz.; vert.
Transmit output power / TR-Module	≥ 7W; ≥ 3W
Pulse length	25 - 50μs
Pulse repetition frequency (PRF)	1 - 3 KHz
Receiver gain	15 - 30 dB

Panel noise figure	£ 4.4 dB
Phase stability (temperature range -20° - +60°C)	± 10°
Panel radiated power (peak)	138 W
Panel power consumption	£ 123 W
Panel mass	14.2 kg

Before deployment the components and the overall system must undergo extensive test procedures (e.g. EMC, thermal, and vibration tests), which verifies the systems electrical characteristics, as well as its resistance to environmental influences.

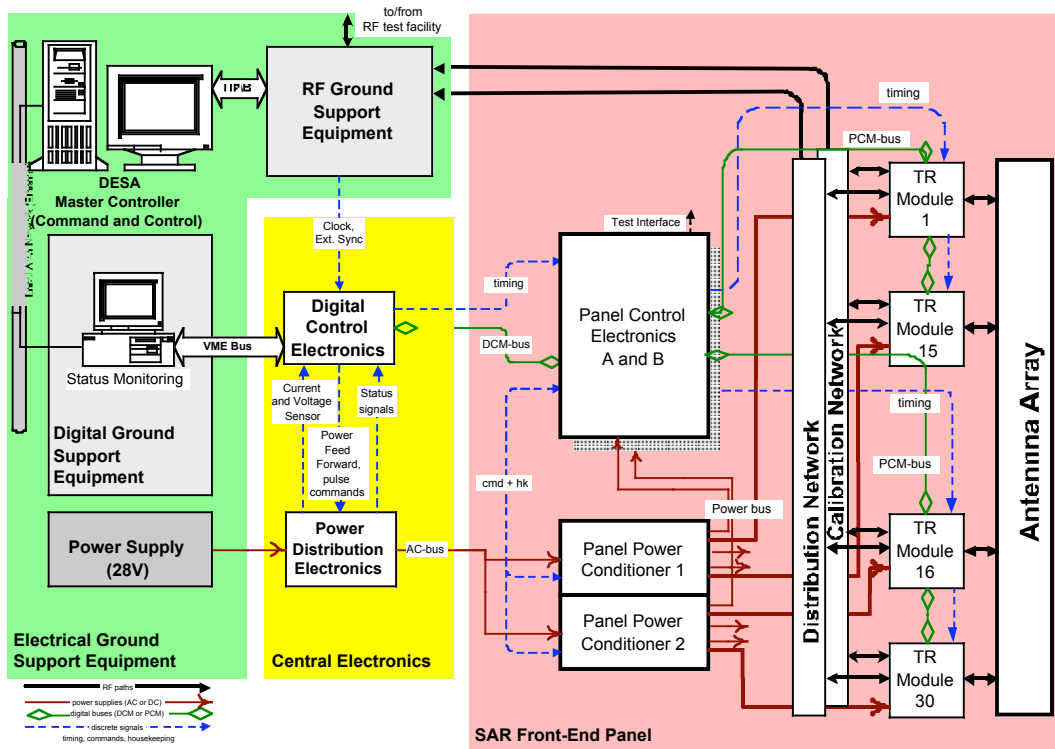


Figure 13.28 Block diagram of the phased-array Radar DESA, © Astrium GmbH

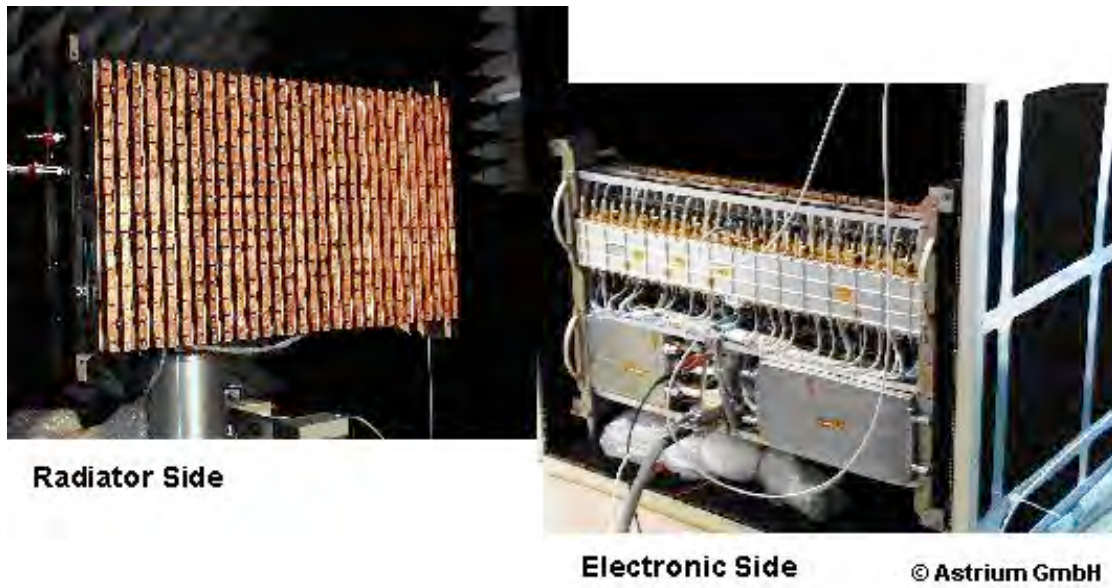


Figure 13.29 Phased-array Radar *DESA*, © Astrium GmbH

14 Future Radar Systems

Recent advances in RF, microwave, digital and software technology will allow the development of software-defined Radar sensors (SDRS) in the near future. The functionality and system parameters of Radar sensors for remote sensing applications will no longer be implemented in hardware, but instead in downloadable software. Software-defined SAR (SD-SAR) is especially suited for these developments. In this short article, I will outline the envisioned functionality, structure and features of software-defined Radar sensors. The vision is not new: Connect the antenna output to an A/D converter and process the signals digitally. This vision may now become possible and extend far beyond what was previously imagined. Synthetic aperture Radar is an especially appropriate candidate to explain and demonstrate the future.

14.1 The Transmit Subsystem

Currently transmit subsystems are mainly implemented using one of the following principles:

Pulsed-FM synthesizer - high power amplifier - reflector antenna

Pulsed-FM synthesizer - high power amplifier - beam forming network - fixed array

Pulsed-FM synthesizer - feed network - transmit/receive modules - radiating elements

The first two of these alternatives are completely inflexible. They seldom allow transmit frequency agility and changes in the radiated beam. Transmit/Receive (T/R) modules are typically associated with the use of phased arrays, spot beams and distributed power generation. Several feed or beam-forming networks are required. Spot beams inherently imply loss of coverage, and the overall power efficiency is quite low. The antenna systems have large space and weight requirements, and necessitate large-area solar panels for power generation. Nevertheless, SAR-systems with T/R modules are the best available with the present technology and will continue to be launched during the next few years.

The vision of the future is that Radar and synthetic aperture transmitters will be implemented as arrays of modules, each one composed of:

DDS (Direct Digital Synthesizer) up-converter, medium power amplifier antenna as shown in Figure 14.1

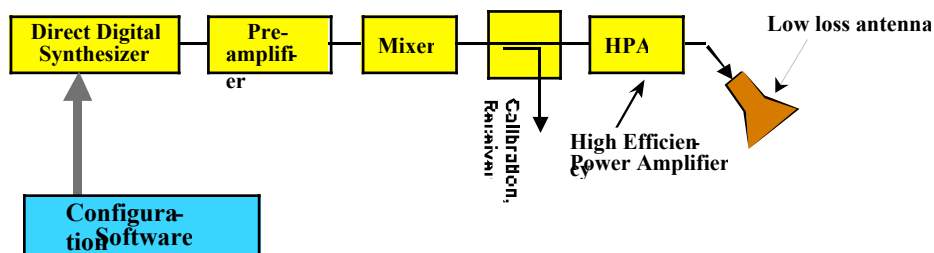


Figure 14.1 Block diagram of a single channel SDRS transmit subsystem

These modular transmit subsystems can be arranged to arrays much more flexible than Phased arrays because of the simple and only digital control. In addition a true time delay can easily be digitally controlled. An array is shown in the next figure.

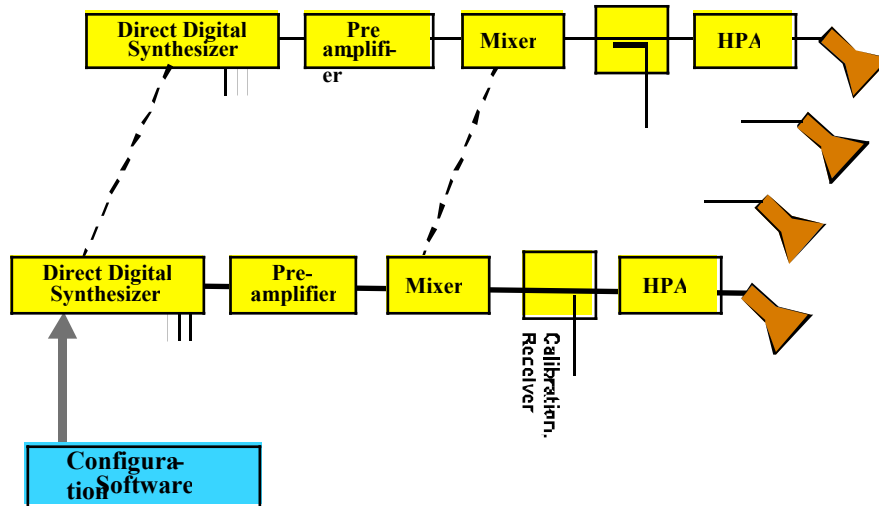


Figure 14.2 Block diagram for SDRS transmit subsystem.

DDSs are now available on the market with frequencies up to almost 1 GHz, more than sufficient for most applications. They can generate nearly any arbitrary waveform and provide full versatility in amplitude, phase, and spectrum. Complex waveforms can be with FM, PM, or AM modulation can be generated, as well as coding schemes such as pseudo noise (PN), CDMA, etc. Even multi-carrier waveforms are possible, all using only downloadable software. Spectrally efficient modulation and convolutional codes are of special interest. The SDRS implementation makes sensor transmitters highly flexible and modular. Using an up-converter, the DDS frequency range can be transposed to any frequency band used by SAR for remote sensing. The limiting components will be the medium power amplifier and the antenna elements. Using wideband components (antennas, mixers, amplifiers, etc.), a wide variety of spectral transmit modes, e.g. narrow-band, wideband, and multi-carrier, are possible. In the same manner single-beam, wide-beam, spot-beam, and multi-beam are possible. Because of modularity, transmitters of different sizes as well as different number of elements can easily be configured baseband signals. Control and power supply lines are the only connections to each module. Conformal schemes and adaptation to satellites, aircraft and other platforms are more readily realizable.

14.2 The Receiver Subsystem

The receivers of software defined Radar sensors have similar configurations and structures to that of the transmitters. Both may use the same antenna. The configuration of one channel is rather simple. Figure 14.3 shows the configuration.

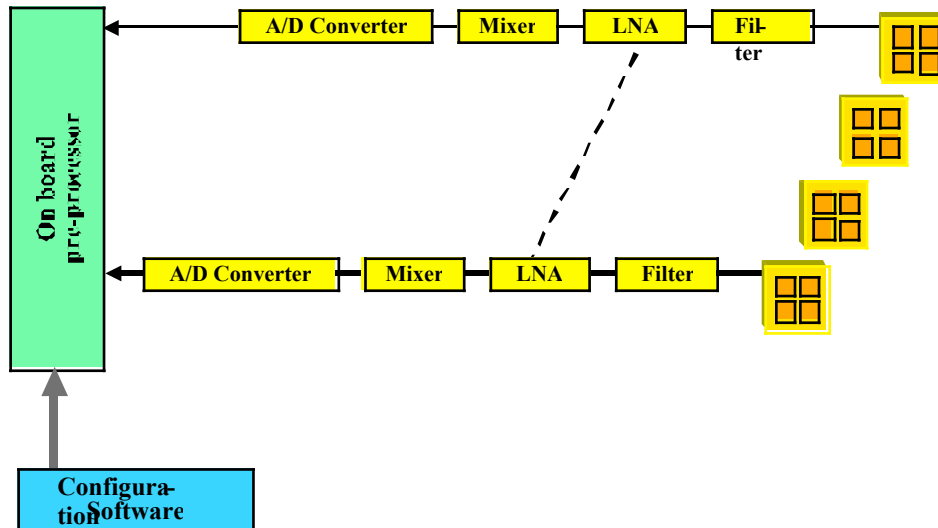


Figure 14.3 Receiver block diagram for digital beam forming on receive only.

The sub-system is comprised of:

- Antenna
- Filter
- Low-noise amplifier
- Downconverter
- A/D converter

The entire antenna consists of an array of these channels. The same flexibility that applies to the transmit elements also applies to the receiver. Amplitude, phase and, to a limited extent, coupling can be corrected during the processing. The restrictions that usually apply to phased arrays will be relaxed, because the coherence and phase relationships will be during post-processing and calibration. These receive systems will have a lower noise figure than standard phased array receivers, because the phase shifters are eliminated. The necessity of a down-converter is determined by the available A/D-converter. The digital output of each receiver channel is directly fed to dedicated processors. The processing modes are adapted to the transmit modes by downloadable software and they can be modified with changes in the sensor/target positions, the required specifications in resolution, and the depth of processing. Radar engineers can learn a great deal from their communications colleagues who realize similar concepts for software-defined radios (SDR). In the future, the processing needs for communications are comparable to remote sensing or even higher.

14.3 SDRS and SD-SAR System Aspects

Because the entire functionality of this new type of software-defined Radar sensors can be downloaded, their operating modes may be multifunctional, selective, active, passive and corrective. In addition to their typical Radar function, they may operate as radiometers, for communication or even as electronic warfare transmitters. Several components and subsystems of these envi-

sioned software-defined Radar sensors are already under development. Prices and power consumption are still high, but, like those of most digital hardware, they will plummet. Appropriate antennas with excellent features, wide bandwidths, dual polarization and low loss are under development. Digital beam forming on receive only is one of the top R&D areas for the third and fourth generations of mobile communications. Similarly, multifunctional software-defined radios (SDR), fulfilling the processing needs of different mobile communications standards and services, are under development at many places worldwide. SDRS and SD-SAR will benefit from them.

The future of Radar remote sensing hardware will be digital. Several key digital projects in the past have been successful. The functionality of software-defined sensors will be downloaded or stored according to the actual requirements. Because of their modular structure, these systems will be more readily available, with shorter production times and by far lower prices. Software-defined Radar sensors will make microwave remote sensing more affordable in the future. The functionality may even be user-implemented. One should not be afraid of this dramatic yet expected change in our research field in the future. There will be still the need for scientists, RF, microwave, digital and software engineers. Also required will be antennas, microwave semiconductors, digital hardware and software, and last but not least, platform development.

15 Bibliography

15.1 Fundamental Literature

- Skolnik, M.; *Introduction to Radar Systems, McGraw Hill Text; ISBN: 0072909803; 3rd edition (August 15, 2000)*
- Detlefsen J.; *Radartechnik; Springer-Verlag, 1989*
- Skolnik, M.; *Radar handbook; McGraw-Hill; 1990; UB-Ka [71A1195(2)]*
- Baur, E.; *Einführung in die Radartechnik; Teubner-Studienskripten ; 106: Elektrotechnik; UB-Ka [85A1809]*
- Brookner E.; *Radar Technology.; Artech House; 1988*
- Barton, David K.; *Radars (Band 1-7); Artech House; 1977; UB-Ka [80E84]*
- *Radar Handbook; McGraw-Hill, New York; ISBN 0-07-057913-X*

15.2 Automotive Radar

- J. Kehrbeck, E. Heidrich, W. Wiesbeck, "Planar microwave doppler-sensors for car speed monitoring", *Proc. of the 21st Europ. Microwave Conference, EuMC*, pp. 129-134, Stuttgart, Sept. 13 ,1991
- K. Schuler, M. Younis, R. Lenz, and W. Wiesbeck, "Array Design for Automotive Digital Beamforming Radar System". *Proceedings International Radar Conference IEEE Radar 05*, pp. 435 – 440, Arlington, VA, USA, May 2005
- K. Schuler, M. Younis, R. Lenz, and W. Wiesbeck, "Array Design for Automotive Digital Beamforming Radar System". *Proceedings International Radar Conference IEEE Radar 05*, pp. 435 – 440, Arlington, VA, USA, May 2005

15.3 Synthetic Aperture Radar

- J. Kim, M. Younis, and W. Wiesbeck, "Implementation of Digital Beam forming for Synthetic Aperture Radar", *Proceedings International ITG/IEEE Workshop on Smart Antennas, CD-ROM, Duisburg, Germany, April 2005*

15.4 Antennas general

- *Antenna Theory, Analysis and Design; Constantine A. Balanis; John Wiley & Sons Publication; ISBN 0-471-66782-X*
- *Antenna Engineering Handbook; Richard C. Johnson, McGraw-Hill, New York; ISBN 0-07-032381-X*
- *Antenna Handbook, Vol. I – III; Y. T. Lo, S. W. Lee; Chapman & Hall; ISBN 0-442-01592-5, ISBN 0-442-01593-3, ISBN 0-442-01594-1*
- *Rothammels Antennenbuch, DARC Verlag Baunatal, ISBN 3-88692-033-X*

- E. Heidrich; W. Wiesbeck, "Features of advanced polarimetric RCS-antenna measurements," in Proc of the IEEE AP-S Int. Symp. & URSI Radio Science Meeting, San Jose, pp. 1026-1029, June 26-30, 1989

15.5 Antennearrays

- Phased Array Antennas; R. C. Hansen; John Wiley & Sons Publication; ISBN 0-471-53076-X
- Phased Array Antenna Handbook; Robert J. Mailloux; Artech House Inc.; ISBN 0-89006-502-0
- Practical Phased Array Antenna Systems; Eli Brookner; Artech House Publishers; ISBN 0-89006-563-2
- Antennas for Radar and Communications- A Polarimetric Approach; Harold Mott; John Wiley & Sons; ISBN 0-471-57538-0

15.6 RCS

- Radar Cross Section Handbook Vol. 1&2; Ruck, Barrick, et al.; Plenum Press New York ; ISBN: 306-30343-4
- Microwave Remote Sensing; Active and Passive; Vol. 1 & 2; Ulaby, Moore, Fung; Addison- Wesley Publishing Company, ISBN 0-201-10759-7 (Vol1), ISBN 0-201-10760-0 (Vol2)
- Wiesbeck, W.; Riegger, S.: Measurement of the complex RCS-Matrix for small metallic and dielectric objects, RADAR 87, IEE-Conference Proc., pp. 360-364, London, Oct. 87
- S. Riegger; W. Wiesbeck, "Wide - band polarimetry and complex radar cross section signatures," in Proc. of the IEEE, Invited Paper, vol. 77, no. 5, pp. 649-658, May 1989
- E. Heidrich; W. Wiesbeck, "Features of advanced polarimetric RCS-antenna measurements," in Proc of the IEEE AP-S Int. Symp. & URSI Radio Science Meeting, San Jose, pp. 1026-1029, June 26-30, 1989
- E. Heidrich; S. Riegger; W. Wiesbeck, "The signal flow error cube for polarimetric antenna and RCS measurements," in Proc. of the IEEE AP-S Int. Symp. & URSI Radio Science Meeting, San Jose, pp. 1042 - 1045, June 26-30, 1989
- D. Kähny; S. Riegger; W. Wiesbeck, "Fundamentals of broad - band polarimetric radar metrology," in PIERS (Progress in Electromagnetics Research symposium) NSF Workshop, Boston, Massachusetts, USA, p. 164, July 25-27, 1989
- W. Wiesbeck, D. Kähny, "Comparison of dual polarization RCS-measurement facilities", Proc. of the Progress In Electromagnetics Research Symposium, PIERS, pp. 806, Cambridge, Massachusetts, USA, July 1-5, 1991
- W. Wiesbeck, S. Riegger, "A complete error model for free space polarimetric measurements", IEEE Transactions on Antennas and Propagation, vol. 39, no. 8, pp. 827-844, Aug. 1991

- W. Wiesbeck, D. Kähny, "Single reference, three target calibration and error correction for monostatic, polarimetric free space measurements", Proceedings of the IEEE, vol. 79, no. 10, pp. 1551-1558, Oct. 1991
- K. Schmitt, E. Heidrich, W. Wiesbeck, "A new calibration technique for bistatic RCS-measurements", Proc. of the 13th Antenna Measurement Techniques Association Meeting and Symposium, AMTA, pp 2-25 & pp. 2-29, Boulder, Colorado, USA, Oct. 7-11, 1991
- S. Riegger, W. Wiesbeck, D. Kähny" "Basic polarimetric measurements on monostatic or bistatic radar images", W.-M. Boerner et al. (eds.) : Direct and Inverse Methods in Radar Polarimetry, Part 1, pp. 739-772, Kluwer Academic Publishers, Jan. 1992
- W. Wiesbeck, "A complete error model for polarimetric RCS- and antenna measurements", W.-M. Boerner et al. (eds.) : Direct and Inverse Methods in Radar Polarimetry, Part 1, pp. 793-807, Kluwer Academic Publishers, Jan. 1992
- K. Schmitt, D. Kähny, W. Wiesbeck, " Reduced calibration procedure for multiple bistatic RCS-measurements", Proceedings of the IEEE International Geoscience and Remote Sensing Symposium, IGARSS'92, pp. 1201-1203, Houston, Texas, USA, May 25-29, 1992

15.7 Digital Beamforming

- Digital Beamforming in Wireless Communications; J. Lithva, T. Kwok, Y. Lo; Artech House Publishers; ISBN 0-89006-712-0
- Digital Beamforming for high Resolution Wide Swath Real and Synthetic Aperture Radar; Marwan Younis, Forschungsberichte aus dem Institut für Höchsthfrequenztechnik und Elektronik der Universität Karlsruhe, Band 42, ISSN 0942-2935
- C. Fischer, W. Wiesbeck, A. Moreira, "Versatile receiver subsystem with digital beamforming on receive only", Proc. 5th International Conference on Radar Systems, Brest, France, Poster Session, May 18-20, 1999
- Y. Venot, M. Younis, W. Wiesbeck, "Realisation of a Compact Forward Looking SAR with Digital Beamforming on Receive Only", Frequenz, vol. 55, pp. 85-90, March/Apr. 2001
- M. Younis, C. Fischer and W. Wiesbeck, "Digital beamforming in SAR systems", IEEE Transactions on Geoscience and Remote Sensing, vol. 41, no. 7, pp. 1735-1739, July 2003

15.8 General and Supporting Literature

- Wiesbeck, W.; Hochfrequenztechnik; Skriptum zur Vorlesung
- Wiesbeck, W.; Antennen und Antennensysteme; Skriptum zur Vorlesung
- Grau, G.; Ausgewählte Kapitel aus der Hochfrequenztechnik; Skriptum zur Vorlesung
- Bosch, B. G.; A very early RADAR pioneer: Christian Hülsmeier in 1904; RADIO BYGONES No. 54, Aug./Sept. 1998

- Hovanessian, S. A.; Radar systems design and analysis; Artech House; 1984; UB-Ka [85A3012]
- Schleher, D. C.; MTI Radar; Artech House; 1978 ; UB-Ka [80E26]
- Currie, N. C.; Techniques of Radar reflectivity measurement; Artech House; 1984 ; UB-Ka [85A3011]
- Ruck, G. et al; Radar Cross Section Handbook (Band 1-2); *Plenum Press NY*; 1970
- Ulaby, F. T. et al; Microwave remote sensing, active and passive (Band 1-4); *Addison-Wesley*; 1981; UB-Ka [88A762]
- Maurice W. Long Ph. D., Radar Reflectivity of Land and Sea, Hardcover 400 Seiten, ISBN 0.89006.130-6, 1983
- Sherman, S.; Monopulse Principles and Techniques; Artech House; 1984
- Mensa, D.L; High Resolution Radar Imaging; *Artech House*; 1982; UB-Ka [82A2418]
- Swerling, P.; Probability of detection for fluctuating targets; IRE Trans.; Vol. IT-6; pp.269-308; 1960
- Hovanessian, Synthetic Array & Imaging Radars, ISBN 0-89006-082-7
- Johnston, ed. Millimeter Wave Radar, ISBN 0-89006-095-9
- Hovanessian, Radar Detection & Tracking System, ISBN 0-89006-018-5.
- Wiley, R.G.; Electronic Intelligence: The Analysis of Radar Signals; Artech House; 1982